



|        |  |     |
|--------|--|-----|
| 3.     | Anisotropic chemical shifts  | 196 |
| 3.1.   | CSAs of nuclei in peptides and proteins  | 196 |
| 3.1.1. | $^{13}\text{C}$ CSA  | 196 |
| 3.1.2. | $^{15}\text{N}$ CSA  | 197 |
| 3.1.3. | $^{17}\text{O}$ CSA  | 202 |
| 3.1.4. | $^1\text{H}$ CSA   | 205 |
| 3.1.5. | CSA can reveal the geometry of hydrogen bonding  | 205 |
| 3.2.   | CSA values of nuclei in solid-state globular and fibrous proteins                                  | 206 |
| 3.3.   | CSA values for $^{13}\text{C}$ , $^{15}\text{N}$ and $^1\text{H}$ in globular proteins in solution | 207 |
| 4.     | Insights into biological problems  | 210 |
| 4.1.   | CSA versus secondary structure   | 210 |
| 4.1.1. | Unoriented samples   | 210 |
| 4.1.2. | Oriented samples   | 211 |
| 4.2.   | CSA and dynamics   | 213 |
| 4.2.1. | Solution NMR   | 213 |
| 4.2.2. | Solid-state NMR  | 215 |
| 4.3.   | $^{31}\text{P}$ CSA of phospholipids in biomembranes   | 220 |
| 4.3.1. | Unoriented lipid bilayers  | 220 |
| 4.3.2. | Oriented lipid bilayers  | 220 |
| 4.3.3. | Polymorphism: non-bilayer lipids   | 221 |
| 4.3.4. | Lipid–protein or peptide interactions  | 222 |
| 5.     | Concluding remarks   | 223 |
|        | Acknowledgements   | 223 |
|        | References   | 223 |

## 1. Introduction

### 1.1. A brief account of the chemical shift

The chemical shift of a nucleus,  $i$ , in a molecule arises from the nuclear shielding effect of an applied magnetic field, caused by an induced magnetic field resulting from circulation of surrounding electrons [1–6]. The magnitude of such an induced magnetic field is proportional to the strength of the applied external magnetic field  $\mathbf{B}_0$ , so that the effective field  $\mathbf{B}_{\text{eff}}$  at the nucleus is given as

$$\mathbf{B}_{\text{eff}} = \mathbf{B}_0(\mathbf{1} - \boldsymbol{\sigma}_i), \quad (1)$$

where  $\boldsymbol{\sigma}_i$  is the second-rank nuclear shielding tensor and  $\mathbf{1}$  is the unit matrix. In normal NMR experiments  $\mathbf{B}_0$  is a uniform field along the  $z$ -axis; therefore,  $\sigma_i = \sigma_{izz}$ . The resonance NMR frequency,  $\nu_i$ , of a given nucleus in a molecule is thus related to its gyromagnetic ratio,  $\gamma_i$ , as given by:

$$\nu_i = (\gamma_i/2\pi)\mathbf{B}_0(\mathbf{1} - \boldsymbol{\sigma}_i). \quad (2)$$

The most commonly used isotropic chemical shift (ppm)  $\delta_i$  parameter is defined as the difference between the resonance frequency of a nucleus of interest,  $\nu_i$ , and that of a reference nucleus,  $\nu_{\text{ref}}$  [1–4,6]:

$$\delta_i = 10^6(\nu_i - \nu_{\text{ref}})/\nu_{\text{ref}}. \quad (3)$$

In normal NMR experiment  $\mathbf{B}_0$  is uniform field along  $z$ . Only one term survives so that  $\nu_i = (\gamma_i/2\pi)\mathbf{B}_0(\mathbf{1} - \boldsymbol{\sigma}_{izz})$ . In an isotropic, liquid sample we can replace  $\boldsymbol{\sigma}_{izz}$  by  $\sigma_i$  and  $\delta_i$  is a scalar quantity due to the fast tumbling of molecules as shown below by an average parameter,  $\delta_{\text{iso}}$ . In a solid or oriented samples (such as a liquid crystalline or single crystalline sample), the chemical shift is not an isotropic parameter but is a second-rank tensor. The components of the anisotropic chemical shift tensor in these samples can be specified by  $\delta_{ij}$ , where  $i, j = x, y$  or  $z$  in a reference frame fixed on the nucleus in a molecule. A transformation of the shielding tensor to a frame of reference defined by axes  $X, Y$  and  $Z$  [in the principal axis system (PAS)] diagonalizes the matrix to give the three principal components ( $\delta_{XX}, \delta_{YY}, \delta_{ZZ}$ ). The isotropic average of the tensor is given by:

$$\delta_{\text{iso}} = \frac{1}{3}(\delta_{XX} + \delta_{YY} + \delta_{ZZ}). \quad (4)$$

In the “Haeberlen notation”, each of the three principal components is related to  $\delta_{\text{iso}}$  by [7,8]:

$$|\delta_{ZZ} - \delta_{\text{iso}}| \geq |\delta_{XX} - \delta_{\text{iso}}| \geq |\delta_{YY} - \delta_{\text{iso}}|, \quad (5)$$

where  $\delta_{ZZ}$  is the principal component farthest from the isotropic value, and  $\delta_{YY}$  is the component closest to  $\delta_{\text{iso}}$ : the ordering of the components can be either  $\delta_{ZZ} \geq \delta_{YY} \geq \delta_{XX}$  or  $\delta_{ZZ} \leq \delta_{YY} \leq \delta_{XX}$ , depending on the chemical structure in question. Therefore, the “reduced anisotropy” is defined as

$$\Delta\delta = \delta_{ZZ} - \frac{1}{2}(\delta_{XX} + \delta_{YY}) \quad (6)$$

or

$$\delta = \delta_{ZZ} - \delta_{\text{iso}}. \quad (7)$$

These two definitions are related by:

$$\Delta\delta = (3/2)\delta. \quad (8)$$

The shielding asymmetry  $\eta$  is defined as

$$\eta = (\delta_{YY} - \delta_{XX})/\delta \equiv 3(\delta_{YY} - \delta_{XX})/2\Delta\delta. \quad (9)$$

In the “Mehring notation”, the principal components,  $\delta_{11}$ ,  $\delta_{22}$  and  $\delta_{33}$ , are defined as [9],

$$\delta_{33} \leq \delta_{22} \leq \delta_{11}. \quad (10)$$

Analogous to Eq. (4), the definition of an isotropic shielding is given as

$$\delta_{\text{iso}} = \frac{1}{3}(\delta_{11} + \delta_{22} + \delta_{33}) \quad (11)$$

but the relationships for anisotropy and asymmetry are more difficult to express than that under the Haeberlen convention, since they depend on the position of  $\sigma_{22}$  between  $\sigma_{11}$  and  $\sigma_{33}$  [7,9]. These anisotropy/asymmetry conventions can be replaced by span ( $\Omega$ ) and skew ( $\kappa$ ) parameter with the following definitions [7,10]:

$$\Omega = \delta_{11} - \delta_{33}, \quad (12)$$

$$\kappa = 3(\delta_{22} - \delta_{\text{iso}})/\Omega. \quad (13)$$

In the case of a symmetric nuclear site, however, those components may be expressed relative to the symmetry axis,  $\delta_{\parallel}$  ( $\delta_{11}$ ) and its per-

pendicular axes  $\delta_{\perp}$  ( $\delta_{22}$  and  $\delta_{33}$ ), with the chemical shielding (or shift) anisotropy

$$\Delta\delta = \delta_{\parallel} - \delta_{\perp}. \quad (14)$$

The magnitude of the anisotropy  $\Delta\delta$  and the asymmetric parameter  $\eta$  are also defined as

$$\Delta\delta = \delta_{11} - (\delta_{22} + \delta_{33})/2 \quad (15)$$

and

$$\eta = (\delta_{22} - \delta_{33})/(\delta_{11} - \delta_{\text{iso}}). \quad (16)$$

Here,  $\delta_{\parallel} = \delta_{11}$  and  $\delta_{\perp} = (\delta_{22} + \delta_{33})/2$ .

Undoubtedly, the nomenclature based on the chemical shift parameter  $\delta_{ii}$  is directly related to the chemical shift anisotropy (CSA) which is one of the main topics discussed in this article. Nevertheless, there are many previous papers utilizing shielding constants  $\sigma_i$ 's, instead chemical shifts  $\delta$ 's. In such cases, it should be bore in mind that  $\Delta\delta = -\Delta\sigma$  and  $\sigma_{33} \geq \sigma_{22} \geq \sigma_{11}$ .

Isotropic chemical shifts of nuclei in different chemical groups of a molecule, are usually available from a solution sample [1–6] where there is motional averaging of the anisotropic shielding tensor. They are undoubtedly one of the most important NMR parameters measured from high-resolution NMR experiments, besides other parameters such as spin coupling constants and nuclear relaxation times, for determining primary or secondary structures of molecules, their dynamics, intermolecular interactions, etc. The chemical shift anisotropy (CSA) is usually obtained from NMR experiments on a solid or a liquid crystalline sample; the corresponding isotropic chemical shifts can also be measured from solid samples [11–15]. It should be mentioned that CSA is an important source of spin–lattice ( $T_1$ ) and spin–spin ( $T_2$ ) relaxation at high magnetic fields even for solution samples, although not affecting the shapes of solution NMR spectral lines. The contribution of the CSA to  $T_2$ , and hence the width of the resonance increases with magnetic field strength leading to broad, unresolved lines.

Under such circumstances, transverse relaxation-optimized spectroscopy (TROSY) [16–20] can be utilized to record well-resolved spectra of large proteins or protein complexes with molecular weight on the order of 100 kDa, with the advantage of an attenuated  $T_2$  relaxation by mutual cancellation of dipole–dipole coupling and CSA under the proton-coupled condition. For this purpose, it is essential to have a prior knowledge of the magnitude of the CSA values for nuclei under consideration to optimize the condition for TROSY-type experiments. This has stimulated much interest in evaluating the CSA values of nuclei in individual amino acid residues of large globular proteins in aqueous solutions or micelles. Determination of residue-specific  $^{15}\text{N}$  CSA for proteins in solution is now feasible by careful evaluation of  $T_1$  and  $T_2$  values at various external magnetic fields [21]. Such data are currently available from the literature. It is emphasized here that we are now in an era when solid-state and solution NMR approaches are frequently utilized in the analyses of CSA parameters and their applications for structural and dynamical studies of biomolecules.

It is therefore very important to gain insights into how and to what extent the isotropic or anisotropic chemical shift of a nucleus under consideration are related to molecular and electronic structure. The existence of conformation-dependent chemical shifts was initially recognized for a variety of biological molecules by solid-state NMR studies on polypeptides, polysaccharides, antibiotics and so on [22–24] and later by a careful examination of a robust database of chemical shifts available from multidimensional NMR studies of globular proteins in aqueous solution [25–28]. Detailed analyses of such data showed that these chemical shift parameters are indispensable restraints for determining 3D structures of large proteins with or without the usual NOE constraints. Chemical shift anisotropies (CSAs) of individual nuclei were initially obtained by solid-state NMR studies on single crystalline, static or slowly rotat-

ing samples. These CSA parameters for nuclei in challenging proteins are now also available from samples using fast magic angle spinning (MAS) experiments [29].

The values of isotropic and anisotropic chemical shift parameters accumulated so far have been utilized to reveal either secondary or 3D structures of fibrous, membrane and globular proteins in solid-state or aqueous solution-state [22–30]. Further, CSA parameters are essential to characterize atomic-level dynamics in the solid-state, or to search for an optimal condition for obtaining TROSY spectra on globular proteins of larger molecular weight, and also to determine relaxation mechanisms in solution. In particular, the chemical shifts are now utilized as a means to reveal 3D structures of large globular proteins, in the absence of NOE constraints which are difficult to obtain because of broad resonances with low signal-to-noise ratio.

Because of the increasing interest in utilizing CSA parameters, there has been a plethora of studies determining CSA values of nuclei in different types of samples. There are several excellent review articles that deal with the topics of isotropic [22–28] and anisotropic [29–39] chemical shifts. In this review, it is our intention to deal equally with these topics from both solid-state and solution NMR studies based on the recent progress in the field, especially dealing with these studies from a historical point of view. Emphasis, however, is also made on how to reveal necessary chemical and biological insights into a variety of biological molecules, including peptides, proteins, lipids, etc. using isotropic or anisotropic chemical shift data. However, we believe that our treatment can also be extended to other areas of chemistry. In the solid-state, unlike in solution, the chemical shielding experienced by a nucleus depends on the direction of the applied magnetic field in the molecule frame. Therefore, the Hamiltonian for the Zeeman interaction,  $H_{\text{CSA}}$ , in the solid-state is given by:

$$H_{\text{CSA}} = \gamma(h/2\pi)[B_{0x}, B_{0y}, B_{0z}] \begin{bmatrix} \delta_{xx} & \delta_{xy} & \delta_{xz} \\ \delta_{yx} & \delta_{yy} & \delta_{yz} \\ \delta_{zx} & \delta_{zy} & \delta_{zz} \end{bmatrix} \begin{bmatrix} I_x \\ I_y \\ I_z \end{bmatrix}. \quad (17)$$

Thus, the chemical shift tensor component  $\delta_{zz}$  as stated above is related to components  $\delta_{11}$ ,  $\delta_{22}$  and  $\delta_{33}$  in the molecular principal axis system (PAS) frame by,

$$\delta_{zz} = \lambda_1^2 \delta_{11} + \lambda_2^2 \delta_{22} + \lambda_3^2 \delta_{33}, \quad (18)$$

$$\lambda_1 = \cos \alpha \sin \beta,$$

$$\lambda_2 = \sin \alpha \sin \beta, \quad (19)$$

$$\lambda_3 = \cos \beta,$$

where  $\alpha$  and  $\beta$  are the polar angles that the field  $B_0$  makes in the PAS (X, Y and Z) molecular frame (Fig. 1a) for single crystals or oriented samples [1,2]. An NMR signal from microcrystalline or powder samples arises from the sum of all possible contributions of  $\alpha$  and  $\beta$  angles (powder pattern), for either axially symmetric (left) ( $\delta_{11} = \delta_{22} \neq \delta_{33}$ ) or (axially) asymmetric (right) ( $\delta_{11} \neq \delta_{22} \neq \delta_{33}$ ) as illustrated in Fig. 2. The principal components of the CSA tensor can be obtained from the peak at  $\delta_{22}$  as well as the two edges at  $\delta_{11}$  and  $\delta_{33}$  of the powder pattern signal.

The chemical shift of an nucleus depends on its electronic and molecular environment [2] and can be given in terms of various contributions by the following equation.

$$\sigma = \sigma^d + \sigma^p + \sigma', \quad (20)$$

where  $\sigma^d$  is known as the diamagnetic term,  $\sigma^p$  the paramagnetic term, and  $\sigma'$  is a term from neighbors which accounts for the magnetic anisotropy effect, polar effect, ring current effect, etc. Intrinsically,  $\sigma$  is a tensor quantity, from a theoretical point of view, which depends on its electronic and molecular environments [1,3,4,7]. Indeed, by placing the nucleus of interest and the zero point of the vector potential due to the external magnetic field at the origin, the contributions to  $\sigma^d$  and  $\sigma^p$  are given by:

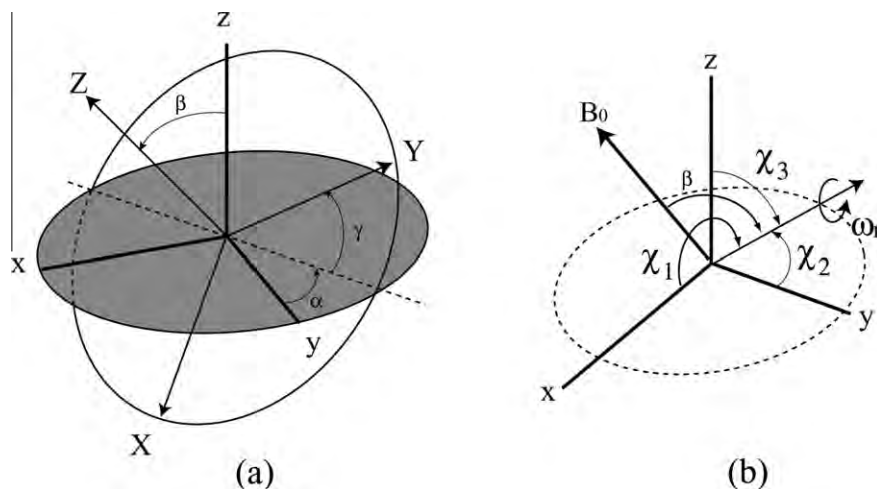


**Fig. 1.** (a) Euler angles which relate principal axis system (X, Y and Z) in a molecule and laboratory frame (x, y and z), in which z is taken along the direction of applied field. (b) Sample is rotated with angular velocity of  $\omega_r$  about an axis inclined at an angle of  $\beta$  to the applied field  $B_0$  at angles  $\chi_1$ ,  $\chi_2$  and  $\chi_3$  to the principal axes of  $\sigma$ . Magic angle for  $\beta = 54^\circ 44'$ .

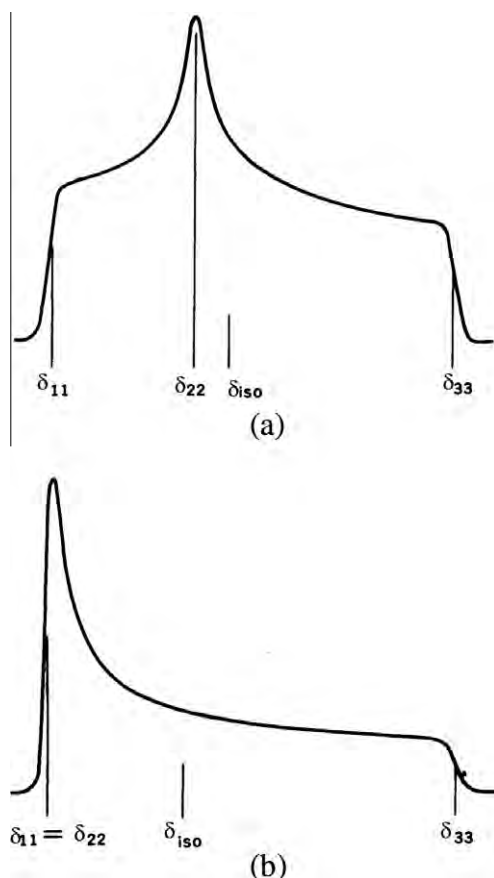


**Fig. 2.** Powder pattern spectra for spin 1/2 nuclei. (a) axially asymmetric ( $\delta_{11} \neq \delta_{22} \neq \delta_{33}$ ), (b) axially symmetric ( $\delta_{11} = \delta_{22} \neq \delta_{33}$ ).  $\delta_{iso} = (1/3)(\delta_{11} + \delta_{22} + \delta_{33})$ .

$$\sigma_{\alpha\beta}^d = (\mu_0 e^2 / 8\pi m) \langle 0 | \sum_k r_k^{-3} (r_k^2 \delta_{\alpha\beta} - r_{k\alpha} r_{k\beta}) | 0 \rangle,$$

$$\sigma_{\alpha\beta}^p = -(\mu_0 e^2 / 8\pi m) \sum_n (E_n - E_0)^{-1} \left[ \langle 0 | \sum_k r_k^{-3} L_{k\alpha} | n \rangle \langle n | \sum_k L_{k\beta} | 0 \rangle \right. \\ \left. + \langle 0 | \sum_k L_{k\beta} | n \rangle \langle n | \sum_k r_k^{-3} L_{k\alpha} | 0 \rangle \right], \quad (21)$$

where  $\alpha$  and  $\beta$  are subscripts labeling the Cartesian components (x, y or z),  $\mu_0$  is the vacuum permeability,  $e$  is the elementary charge and  $m$  is the electron mass,  $r_k$  is the position of the  $k$ th electron compared to the nucleus of interest.  $L_k$  is the corresponding orbital angular momentum operator,  $\delta_{\alpha\beta}$  is the Kronecker delta function.  $|0\rangle$  and  $|n\rangle$  refer to the electronic ground and excited states of molecules with energies  $E_0$  and  $E_n$ , respectively.

The paramagnetic term in the case of a nucleus for  $^{13}\text{C}$ ,  $^{15}\text{N}$  and  $^{17}\text{O}$  atoms having 2, 3 and 4  $2p$  electrons considered here, in particular, is expressed as a function of excitation energy, bond order and electron density according to the sum-over-states method in a simple form as follows [40]

$$\sigma_{\alpha\beta}^p = -C \sum_{m,n} \langle r^{-3} \rangle_{2p} (E_m - E_n)^{-1} Q_{\alpha\beta}, \quad (22)$$

where  $(E_m - E_n)$  is the singlet–singlet excitation energy between the  $n$ th occupied orbital and the  $m$ th unoccupied orbital, and  $Q_{\alpha\beta}$  is a factor including the bond order and the electron density. The quantity  $\langle r^{-3} \rangle_{2p}$  is the spatial dimension for a  $2p$  electron, and  $C$  is the coefficient incorporating the universal constants. The term  $\sigma_{\alpha\beta}^p$  can be evaluated by a variety of molecular orbital calculations, such as semi-empirical, non-empirical, or *ab initio* MO methods. It should be noted that a quantum chemical calculation gives all nine chemical shielding tensor components of the CSA tensor. The isotropic chemical shielding constant is obtained as an average of the magnitudes of the three principal components of the chemical shielding tensor. The chemical shielding anisotropy, therefore, arises from the distortion from symmetry of the distribution of electrons around a nucleus in molecules in the presence of the applied magnetic field. Using these procedures, it is possible to calculate the chemical shielding tensor components of a nucleus in a molecule with any specified conformation.

As mentioned above, the CSA originates from a distortion from a spherical distribution of  $2p$  electrons around a nucleus. Each of the three diagonal shielding tensor components is more sensitive to structural changes such as torsion angle and hydrogen bonding as compared to the average isotropic shielding constant. Also, the directions of the principal axes of the shielding tensor depend on the molecular structure. Therefore, the determination of the orientation of the principal axes in the molecular frame gives us detailed information about the molecular structure.

For atoms with  $2p$  electrons such as  $^{13}\text{C}$ ,  $^{15}\text{N}$  and  $^{17}\text{O}$  considered in polypeptides and proteins, the relative chemical shift is predom-



inantly contributed by  $\sigma^p$  and is little contributed by  $\sigma^d$  and  $\sigma'$ . Thus, it is very important to estimate  $\sigma^p$  values with good precision for these nuclei. On the other hand, for a  $^1\text{H}$  nucleus the relative chemical shift is more significantly determined by contributions from  $\sigma^d$  and  $\sigma'$  as compared to  $\sigma^p$ . The  $\sigma^d$  can be easily estimated from the calculated electron density. Using these procedures, one can calculate the chemical shift tensor components of a nucleus in a molecule with any specified conformation [41–54]. A negative sign of the chemical shielding constant  $\sigma$  indicates deshielding and so shielding variations can be compared with the observed chemical shift  $\delta$  where a positive sign denotes deshielding.

## 1.2. Determination of CSA values

Several approaches have been proposed to determine CSA tensors: (1) static NMR measurements on a single crystal or an oriented liquid crystalline sample, (2) simulations of static powder pattern spectra obtained from polycrystalline samples, (3) analysis of spinning sidebands in MAS spectra obtained under slow-spinning conditions, (4) CSA recoupling procedures based on multidimensional, fast-spinning MAS NMR. All six CSA parameters, including the three principal values  $\delta_{11}$ ,  $\delta_{22}$  and  $\delta_{33}$  and three direction cosines specifying the principal axis system, can be unambiguously determined by performing NMR experiments on single crystals. Some of direction cosines are also available from experimental measurements on uniaxially oriented samples. Further, relative orientations of such principal axes with respect to the  $^{13}\text{C}$ – $^{15}\text{N}$  bond axis can be also determined from [ $^{13}\text{C}$ ,  $^{15}\text{N}$ ]-doubly labeled polycrystalline samples. In many cases, isotope enrichment by  $^{13}\text{C}$ ,  $^{15}\text{N}$  and  $^{17}\text{O}$  nuclei is essential in order to determine reliable and precise CSA parameters.

### 1.2.1. Single crystal or aligned samples

The experimental procedures to determine CSA values from single crystals by a stepwise rotation of a sample holder attached to a goniometer are well documented [9,31,55]. Static NMR signals available from a single crystal in the laboratory frame as shown in Eq. (17) should be converted into the principal values (Eq. (18)) through transformations of coordinate frames: from laboratory frame  $\rightarrow$  goniometer frame  $\rightarrow$  crystal frame  $\rightarrow$  principal axis frame. For this purpose, it is essential to have a prior knowledge of the 3D structure of the molecule under consideration in the crystal frame determined either by X-ray or neutron diffraction study. The magnitudes of the principal values and direction cosines can be determined by fitting the observed chemical shift frequencies, obtained by stepwise rotation of the direction of a crystalline sample relative to the applied magnetic field, to Eqs. (18) and (19).

Such analyses, however, can be more complicated for quadrupolar nuclei such as  $^{17}\text{O}$  (spin number 5/2), since the central ( $1/2 \leftrightarrow -1/2$ ) transition signal becomes broad by the second-order perturbation by the very large quadrupolar interaction [11]. The quadrupolar interaction ( $\nu_Q$ ) in addition to the chemical shift tensor interaction ( $\nu_{\text{CS}}$ ) is expressed by:

$$\nu_Q = (\nu_Q^2/6\nu_0)(I(I+1) - 3/4)(A(\phi)\cos^4\theta + B(\phi)\cos^2\theta + C(\phi)), \quad (23)$$

where

$$\nu_Q = 3e^2qQ/[2I(2I-1)h], \quad (24)$$

$$A(\phi) = -27/8 - (9/4)\eta\cos 2\phi - (3/8)\eta^2\cos^2 2\phi, \quad (25)$$

$$B(\phi) = 30/8 + \eta^2/2 + 2\eta\cos 2\phi + (3/4)\eta^2\cos^2 2\phi, \quad (26)$$

$$C(\phi) = -3/8 + \eta^2/3 + (1/4)\eta\cos 2\phi - (3/8)\eta^2\cos^2 2\phi, \quad (27)$$

$$\eta_Q = (V_{xx} - V_{yy})/V_{zz}, \quad 0 \leq \eta_Q \leq 1. \quad (28)$$

Here,  $\theta$  and  $\phi$  are the polar and azimuthal angles, respectively, in the principal axes of the electric field gradient tensor,  $e^2qQ/h$  is the

quadrupolar coupling constant, and  $\eta_Q$  is the asymmetry factor of the electric field gradient defined by its principal components  $V_{xx}$ ,  $V_{yy}$  and  $V_{zz}$ . Recording  $^{17}\text{O}$  spectra at the highest magnetic field currently available is essential in order to minimize the relative contributions of the quadrupolar interaction which is decreased at a higher field, as seen from the  $\nu_Q^2/\nu_0$  factor in Eq. (23). It is also important to measure static spectra at several magnetic field strengths, in order to determine the total eight parameters including the quadrupolar coupling constant and asymmetry factor  $\eta_Q$ .

Next, we are concerned with aligned samples. For example, orientation-dependent  $^{15}\text{N}$  and  $^{13}\text{C}$  solid-state static NMR spectra of [ $^{15}\text{N}$ ]- or [ $^{13}\text{C}$ ]-labeled silk fibroin fibers were observed when the fiber axis was arranged at various angles between  $0^\circ$  and  $90^\circ$  relative to the external magnetic field direction [56,57]. A 1D spectrum convoluted with  $^1\text{H}$ – $^{15}\text{N}$  dipolar coupling and  $^{15}\text{N}$  chemical shift interactions has been obtained from a [ $^{15}\text{N}$ ]Gly–collagen fiber with the fiber axis oriented parallel to the external magnetic field [58]. Orientation-dependent spectra of lipid bilayers are discussed below in Section 4.3.2.

### 1.2.2. Static powder pattern spectra

While static solid-state NMR measurements from a high quality single crystal are the best way of determining accurate CSA tensors, obtaining single crystals is extremely difficult and sometimes impossible for biological systems. In addition, a single crystal study is very time-consuming in spite of some fast approaches to reduce the number of experiments [59]. The three principal values alone, however, are available from the analysis of the powder pattern spectra (see Fig. 2). Following Eq. (19), the observed frequency of spectral lines can be expressed in terms of Euler angles ( $\alpha, \beta$ ) which relate the principal axes of the CSA tensor to the laboratory frame. As a result,  $\delta_{11}$ ,  $\delta_{22}$  and  $\delta_{33}$  can be determined from the peak at  $\delta_{22}$  of the divergence of the line-shape function and two edges at  $\delta_{11}$  and  $\delta_{33}$  of the shoulder [9,31]. More accurately, these parameters can be determined by line-shape analyses of the experimental spectra based on a treatment by Bloembergen and Rowland [60]; discussions about the line-shape analysis can be found in the literature [9,15,31].

It is possible to determine the orientation of a  $^{15}\text{N}$  or  $^{13}\text{C}$  CSA tensor in the molecular frame by measuring the correlated/convoluted chemical shift spectra with  $^{13}\text{C}$ – $^{15}\text{N}$  or  $^{15}\text{N}$ – $^1\text{H}$  dipolar interactions. Several studies have reported  $^{15}\text{N}$  and  $^{13}\text{C}$  CSA tensors of peptides and proteins selectively labeled with these isotopes [61–64]. For example, the orientation of the  $^{15}\text{N}$  chemical shift tensor relative to the molecular frame was determined from a polycrystalline L-[ $^{13}\text{C}$ ]alanyl-L-[ $^{15}\text{N}$ ]alanine sample using a  $^{13}\text{C}$  chemical shift spectrum convoluted with the  $^{13}\text{C}$ – $^{15}\text{N}$  dipolar coupling interaction. The reported angles are  $\beta_{\text{CN}} = 106^\circ$ ,  $\alpha_{\text{CN}} = 5^\circ$  and  $\beta_{\text{NH}} = -19^\circ$ ,  $\alpha_{\text{NH}} = 12^\circ$  [65].

### 1.2.3. Spinning side-band analysis

The free induction decay from a spinning sample having inhomogeneous anisotropic interactions takes the form of a train of rotational spin echoes. The Fourier transform of these rotational spin echoes results in a spectrum with spinning side bands which contain information concerning the CSA. Maricq and Waugh [66] showed that the second ( $M_2$ ) and third ( $M_3$ ) moments [67] of such NMR spectra can be used to obtain the CSA from the side-band intensities. Thus,

$$M_2 = (\delta^2/15)(3 + \eta^2), \quad (29)$$

$$M_3 = (2\delta^3/35)(1 - \eta^2). \quad (30)$$

Herzfeld and Berger showed that the principal CSA values can be derived from the intensities of a relatively small number of sidebands, based on general integral and series expansions for sideband

intensities [68]. The expressions are evaluated for a wide range of shift parameters and the results are commonly used to construct graphical and numerical methods for extracting the principal values of chemical shift tensors from the intensities of just a few spinning sidebands. To accurately measure CSA parameters, Fenzke et al. [69] developed an alternative approach to determine the principal values of a CSA tensor from MAS sideband intensities, in which one attempts to minimize the mean square deviation between the calculated and experimental sideband intensities. Another approach was proposed for the analysis of MAS NMR spectra which combines nonlinear and linear analytical procedures for fitting sideband spectra [70]. This method is particularly useful for the analysis of spectra with lower S/N ratio or overlapping lines.

The reliability of the determination of the anisotropy and the asymmetry parameter of the chemical shift interaction was calculated using the Cramér-Rao lower bounds [71]. Based on numerous studies, it is realized that CSA tensors can be more accurately determined from a spinning sample experiment than from a static experiment on a powder sample.

#### 1.2.4. CSA recovery under MAS

While MAS averages CSA, a number of multidimensional separation and correlation techniques have been utilized to recover CSA interactions [15]. Magic angle hopping is a 2D technique which utilizes a mechanical device for rotating the sample in discrete 120° jumps, during the 120° jump time interval between the jumps with a “hop” about the magic angle axis, with the proton decoupling switched off during the “hop” period [72]. The CSA is averaged to zero by allowing the magnetization to evolve at three suitable orientations of the sample relative to the magnetic field. The static anisotropic pattern is observed in the detection period, after such an effective isotropic evolution. This technique was further modified by replacing the discrete magic angle hopping technique which requires special flip apparatus with a continuous slow MAS experiment, yielding similar result [73]. The sensitivity of this method (magic angle turning (MAT)) was increased by this modification due to acquisition of the full echo rather than only half of the echo. Alternatively, the switched-angle sample-spinning (SASS) method allows the  $^{13}\text{C}$  magnetization to evolve under the sample spinning at an off-magic-angle and under proton decoupling, and then makes measurements at the magic angle [74].

A phase corrected MAT (PHORMAT) technique has been developed to overcome the shortcomings of the previous version of the MAT experiment [75]. An excellent spectrum of methyl- $\alpha$ -D-glucopyranoside free of baseline artifact provided the principal values of  $^{13}\text{C}$  CSA with an accuracy comparable to the values obtained from a single crystal study. A complete separation of isotropic and anisotropic chemical shifts was established by a 2D MAS experiment, relying on the fact that the magnetization evolution under the TOSS sequence [76] can be reversed by the application of a “mirror image” sequence [77]. A 2D phase adjusted spinning sideband (PASS) method was developed to separate anisotropic and isotropic chemical shift interactions under MAS using sequences of five  $\pi$  pulses [78,79].

One revolutionary technique, polarization inversion spin exchange at magic angle (PISEMA), that correlates  $^{15}\text{N}$  CSA and  $^1\text{H}$ – $^{15}\text{N}$  dipolar coupling greatly improves the resolution and sensitivity of separated-local-field (SLF) spectroscopy [61]. The PISEMA sequence was combined with the MAT technique, taking advantages of high-resolution and high-sensitivity of PISEMA and the ability to resolve isotropic resonances using MAT [62]. 1D magic-angle decoupling and magic-angle turning (MADMAT) NMR was also developed by combining the magic-angle rf decoupling in one time period and the MAT pulse sequence in another time period [63]. Application of the 1D dipolar-shift method under

MAS was used to determine the  $^{15}\text{N}$  CSA and  $^1\text{H}$ – $^{15}\text{N}$  dipolar interaction tensors from a powder sample of a model peptide [64].

Another experiment was introduced to obtain undistorted CSA lineshape under MAS [80]. This utilizes the time dependence of the resonance frequency of an isolated spin under MAS  $\omega(t)$  [66], which can be written as

$$\omega(t) = C_1(\Omega)\cos(\omega_r t) + C_2(\Omega)\cos(2\omega_r t) + S_1(\Omega)\sin(\omega_r t) + S_2(\Omega)\sin(2\omega_r t). \quad (31)$$

Here,  $C_i(\Omega)$  are coefficients that depend on the molecular orientation relative to the rotor axis  $\Omega$  at time 0. For a stationary sample, the  $C_1(\Omega) + C_2(\Omega)$  term gives rise to the usual CSA pattern. By means of four rotor-synchronized  $\pi$  pulses under fast MAS in a 2D experiment, the anisotropy effects of  $C_1(\Omega)$  and  $C_2(\Omega)$  are reintroduced with equal prefactors, while those of  $S_1(\Omega)$  and  $S_2(\Omega)$  remain equal to zero over a rotor period. This 2D iso-aniso experiment was further developed (and named as RAI, recoupling of anisotropy information) to produce the static chemical shift spectra in the indirect dimension and isotropic chemical shift spectra in the direct dimension [81,82]. This approach decreases the influence of finite pulse length effects in the original sequence by recoupling the CSA over three rotor periods instead of one. Then, it is even possible to use a spinning speed as fast as 10 kHz. Cogwheel (COG) phase-cycled, constant time, and optimized implementations of the CSA recoupling experiment demonstrated that the modifications give reliable, undistorted CSA powder patterns using a standard experimental hardware and methods [83]. The constant time (CT-2DCSA (COG)) variant was shown to give optimum lineshapes of the powder patterns while the optimized (OPT-2DCSA(COG)) version of the experiment maximized the signal-to-noise ratio as illustrated in Fig. 3.

No significant artifacts, with standard rf power levels and spinning speeds between 2.5 and 5 kHz, were observed using the SUPER (separation of undistorted powder patterns by effortless

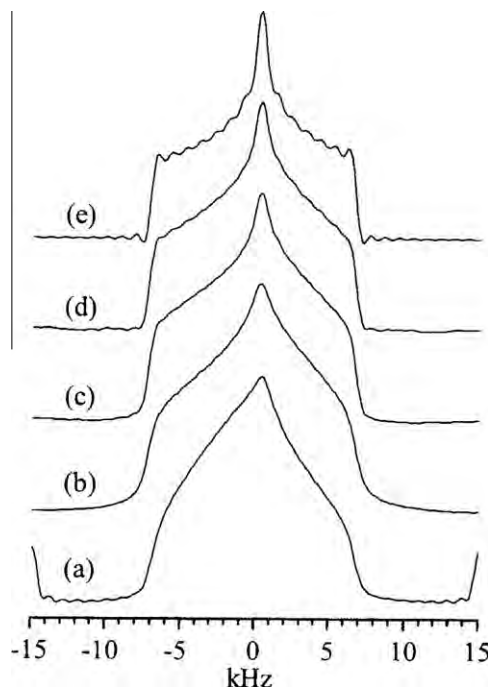


**Fig. 3.** F1 slices of the  $^{13}\text{C}$  resonance of carbonyl site of glycine extracted from the 100.56 MHz 2D spectra for (a) the conventional implementation of the 2DCSA experiment, (b) the 2DCSA(COG) implementation, (c) the OPT-2DCSA(COG) implementation, (d) the CT-2DCSA(COG) implementation, (e) a simulated powder pattern. Reproduced with permission from Orr and Duer [83]. Copyright 2006 Elsevier.

recoupling) approach [84] which utilizes  $360^\circ$  instead of  $180^\circ$  pulses in the above-mentioned iso-aniso 2D MAS experiment [80]. The SUPER method has been applied to samples containing various  $sp^2$ - and  $sp^3$ -hybridized carbon sites. A variant of this technique was proposed to recover the CSA by combining a pair of selective and non-selective  $\pi$  pulses to suppress the  $^{13}\text{C}$ – $^{13}\text{C}$  scalar and dipolar interactions [85]. Another approach was proposed for the recovery of CSA under MAS while retaining a static CSA powder pattern line shape and simultaneously attenuating homonuclear dipole–dipole interactions [86]. This was accomplished by a rotor-synchronized rf pulse sequence with symmetry properties that permit static CSA line shapes to be obtained by a pulse sequence called ROCSA (recoupling of chemical shift anisotropy), with the scaling factors of 0.272 for CSA, and approximately 0.05 for homonuclear dipole–dipole interactions. Analysis of the CSA patterns in N-acetyl-D, L-Valine (Fig. 4) and the A $\beta_{11-15}$  (a 15-residue peptide fragment of amyloid peptide from Alzheimer's disease in which four amino-acid residues (Val 18, Phe 19,20 and Ala 21) were uniformly  $^{13}\text{C}$  and  $^{15}\text{N}$  labeled) demonstrated the utility of ROCSA measurements for probing peptide conformations in noncrystalline solids.

#### 1.2.5. Solution NMR experiments

NMR signals split by CSA in the solid are time-averaged in solution by fast isotropic tumbling motions, yielding narrow spectral lines. Nonetheless, the CSA information is present in the individual isotropic signals through their nuclear spin relaxation times  $T_1$  or  $T_2$ , especially when solution NMR spectra of globular proteins are examined at a high magnetic field when the contribution of the

CSA relaxation mechanism becomes dominant as compared to that of the dipole–dipole interaction. Therefore, it is possible to retrieve CSA data from the spin–spin relaxation rates by careful examination of relaxation data available from solution NMR, as will be described in more detail in Section 3.3. For this reason, a prior knowledge of the magnitude of the CSA values in solution is essential to optimize the experimental condition to record high-resolution TROSY spectra for large proteins or protein complexes with a molecular weight of  $\sim 100$  kDa [16–20].

#### 1.2.6. Quantum chemical calculations

Quantum chemical methods have been used to calculate CSA tensors for nuclei in a variety of molecules. The accuracy of such calculated nuclear shielding constants and the orientations of the principal axes depends strongly on the quantum chemical calculations used, for example semiempirical, *ab initio* or DFT (density functional theory) [40,47,50–52,87,88]. These calculations have proved to be very useful for providing insights into the underlying mechanism of nuclear shielding, including the dependence on molecular conformational changes and intermolecular interactions such as hydrogen bonding, even though such calculations have long remained qualitative for prediction of the experimental data. Currently, more accurate data are available from *ab initio* Hartree–Fock theory using perturbation methods with the inclusion of the electronic correlation, or DFT theory [87,88]. Studies have shown that these calculations are useful in understanding the variation of CSA tensors from one molecule to another, and one amino acid residue to another in a given protein. Some of these studies are highlighted later in this review.

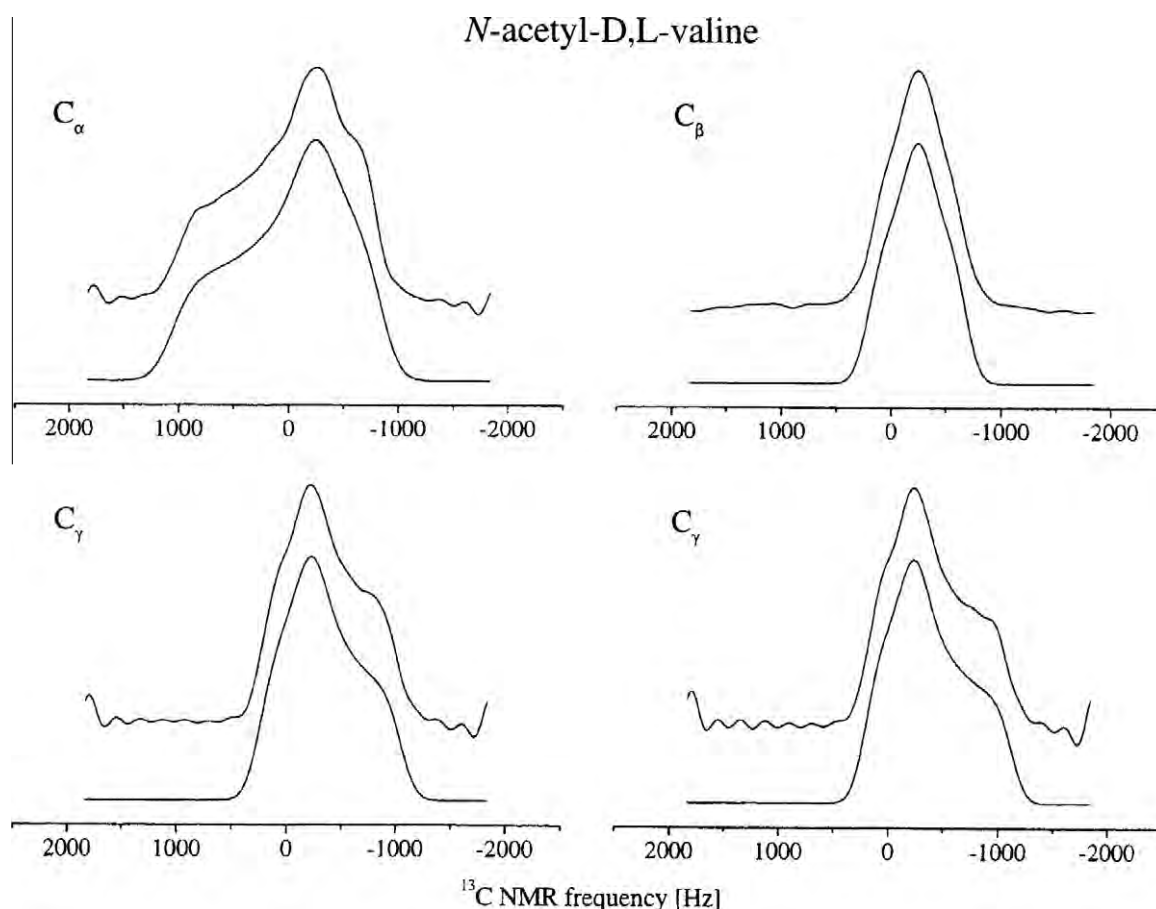


**Fig. 4.**  $^{13}\text{C}$  ROCSA spectra for  $C_\alpha$ ,  $C_\beta$  and  $C_\gamma$  of  $[\text{V-}^{13}\text{C}, ^{15}\text{N}]$ -N-acetyl-D, L-Valine at  $\nu_R = 11$  kHz and 14.09 T. Upper traces are experimental spectra. Lower traces are best-fit simulations for a one-spin system. Reproduced with permission from Chan and Tycko [86].

## 2. Isotropic chemical shifts

### 2.1. Referencing chemical shifts

A IUPAC recommendation proposed to delete the factor of  $10^6$  in Eq. (3), and to express the numerator in Hz and the denominator in MHz [7,89]. Tetramethylsilane (TMS) in dilute solution in organic solvents such as  $\text{CDCl}_3$  or 2,2-dimethylsilapentane-5-sulfonic acid (DSS) in aqueous solutions are commonly used as *internal* reference compounds for reporting  $^1\text{H}$  and  $^{13}\text{C}$  NMR spectra. Without significant differences in chemical shifts between these references, chemical shifts can also be given by “ $\Xi$ ” which is defined as the resonance frequency in a magnetic field in which TMS has a resonance frequency of 100.0 MHz,

$$\Xi = \nu(\chi)/\nu_{\text{TMS}}(^1\text{H}). \quad (32)$$

The data, however, must be reported to eight or nine significant figures as shown in Table 1 and therefore it is cumbersome for discussion. Hence, chemical shifts of any nuclei are commonly expressed relative to secondary references by the  $\delta$  scale as discussed above. It should be taken into account, however, that  $^{13}\text{C}$  chemical shifts based on DSS and TMS differ by about 2 ppm, which can cause confusion if not clarified [4].

In contrast, reporting  $^{13}\text{C}$  chemical shifts obtained from high-resolution solid-state NMR is more complicated as compared to solution NMR results based on an internal reference, because referencing for solids is usually done by a *substitution* method using a secondary reference compound, such as the carboxyl peak of glycine (176.03 ppm from neat TMS) or  $\text{CH}_2$  carbon of adamantane (29.50 ppm from the high-field doublet from a neat TMS). Chemical shifts with respect to other reference systems such as TMS in a sealed capillary of 1%  $\text{CDCl}_3$  solution or DSS should be compared with the data after subtracting or adding the correction factors given in Table 2 [90]. The following conversion scheme has also been proposed [7,91]:

$$\begin{aligned} \delta_{\text{MAS}} (1\% \text{ TMS in } \text{CDCl}_3) &= \delta_{\text{MAS}} (\text{neat TMS}) - 0.71 \text{ ppm} \\ &= \delta_{\text{MAS}} (0.5\% \text{ DSS in } \text{D}_2\text{O}) - 2.72 \text{ ppm} \\ &= \delta_{\text{MAS}} (\text{solid adamantane}) + 37.77 \text{ ppm} \end{aligned} \quad (33)$$

In order to retrieve any meaningful results from experimental data, a careful check on the reference system is also essential. Here we have dropped the label ‘iso’ on  $\delta$  when isotropic terms alone are concerned.

**Table 2**

Correction of  $^{13}\text{C}$  chemical shifts primarily referenced to glycine or adamantane (italic) and then secondarily referenced to TMS or DSS (ppm).

| Standard reference      | Primary reference (with reference to the respective standard reference) |                      |                       | Chemical-shift correction <sup>a</sup> |
|-------------------------|---|----------------------|-----------------------|--|
|                         | Glycine C=O   | Adamantane low field | Adamantane high field |  |
| TMS neat                | 176.03  | 38.04                | 29.00                 | 0                                      |
| TMS neat                |   | 38.5                 | 29.5                  | −0.5                                   |
| TMS 1% $\text{CDCl}_3$  |   | 37.8                 | 28.8                  | +0.2                                   |
| DSS solid               |   | 38.1                 | 29.1                  | −0.1                                   |
| 5% $\text{D}_2\text{O}$ |   | 40.4                 | 31.4                  | −2.4                                   |
| 1% $\text{D}_2\text{O}$ |   | 40.6                 | 31.5                  | −2.5                                   |

<sup>a</sup> Chemical shifts were calibrated by the peak position expressed by italic as the primary reference. Chemical shift correction should be made to compare the data based on different reference system to each other, after adding or subtracting “chemical shift correction”. Reproduced with permission from Saitô and Naito [90].

### 2.2. Isotropic chemical shifts

#### 2.2.1. $^{13}\text{C}$ chemical shifts

In the solid-state, displacements of  $^{13}\text{C}$  NMR peaks as large as 8 ppm are noticed between different conformations in polysaccharides, polypeptides, proteins and several types of ionophores [22–24]. Even though the magnitude of these displacements is still small compared with the total chemical shift spread of 200 ppm, it is sufficiently large to provide a convenient intrinsic probe for conformational characterization. In particular,  $^{13}\text{C}$  chemical shifts of the backbone  $\text{C}_\alpha$  and  $\text{C}=\text{O}$ , as well as the side-chain  $\text{C}_\beta$  signals, are significantly displaced for a variety of amino acid residues in polypeptides, depending on their local conformation such as  $\alpha$ -helix,  $\beta$ -sheet,  $3_1$  helix, silk I, collagen type triple helix, random coil, etc [22–24,92–101]: the  $\text{C}_\alpha$  and  $\text{C}=\text{O}$   $^{13}\text{C}$  chemical shifts of all residues in an  $\alpha$ -helix are displaced downfield by 3.5–8.0 ppm with respect to those of a (antiparallel)  $\beta$ -sheet form, while the  $\text{C}_\beta$  shifts in an  $\alpha$ -helix are displaced upfield by 3.4–5.2 ppm with respect to those of a  $\beta$ -sheet, as summarized in Table 3 (referenced to neat TMS, through the chemical shift of  $\text{C}=\text{O}$  carbonyl peak of Gly). The *transferability* of these parameters for particular residues, from simple model peptides to more complicated proteins, has proved to be an excellent diagnostic means of determining local conformations of specific amino acid residues in proteins such as silk fibroin [102,103], collagen [104–106] and transmembrane peptides [107]. This is a consequence of a dominant contribution from the paramagnetic term of the shielding constant in Eq. (21).

The  $^{13}\text{C}$  chemical shift peaks of polypeptides, involved in a random coil form in  $\text{CF}_3\text{COOH}$  or aqueous solution, always appear between the peaks of  $\alpha$ -helix and  $\beta$ -sheet conformations, as a consequence of time-averaging of the shifts of the allowed confor-

**Table 1**  
Alternative secondary references.

| Isotope         | Alternative secondary references    |                       |                         | Recommended secondary references |                   |                         |
|-----------------|-------------------------------------|-----------------------|-------------------------|----------------------------------|-------------------|-------------------------|
|                 | Reference compound                  | Sample conditions     | NMR frequency $\Xi$ (%) | Reference compound               | Sample conditions | NMR frequency $\Xi$ (%) |
| $^1\text{H}$    | DSS                                 | Internal              | 100.000 000             | TMS <sup>a</sup>                 | Internal          | 100.000 000             |
| $^2\text{H}$    | DSS                                 | Internal              | 15.350 608              | TMS <sup>a</sup>                 | Internal          | 15.350 609              |
| $^{13}\text{C}$ | DSS                                 | Internal              | 25.144 953              | TMS <sup>a</sup>                 | Internal          | 25.145 020              |
| $^{31}\text{P}$ | $(\text{CH}_3\text{O})_3\text{PO}$  | Internal              | 40.480 864              | $\text{H}_3\text{PO}_4$ (85%)    | External          | 40.480 742              |
| $^{15}\text{N}$ | $\text{NH}_3$ (liquid)              | External              | 10.132 912              | $\text{CH}_3\text{NO}_2$         | External          | 10.136 767              |
| $^{15}\text{N}$ | $[(\text{CH}_3)_4\text{N}]\text{I}$ | Internal <sup>b</sup> | 10.133 356              |                                  |                   |                         |
| $^{14}\text{N}$ | $[(\text{CH}_3)_4\text{N}]\text{I}$ | Internal              | 7.223 885               | $\text{CH}_3\text{NO}_2$         | External          | 7.226 717               |

<sup>a</sup> Volume fraction 1% in  $\text{CDCl}_3$ .

<sup>b</sup> 0.075 M in  $\text{DMSO}-d_6$ .

Reproduced from R.K. Harris, E.D. Becker, S.M.C. de Menezes, R. Goodfellow, F. Granger, Pure Appl. Chem. 73 (2001) 1795–1918.



**Table 3**<sup>13</sup>C chemical shifts characteristic of the  $\alpha$ -helix,  $\beta$ -sheet and random coil forms (ppm from TMS).

| Amino acid residues in polypeptides | $C_\alpha$        |                |                          |            | $C_\beta$         |                |                          |            | C=O                |                |                          |            |
|-------------------------------------|-------------------|----------------|--------------------------|------------|-------------------|----------------|--------------------------|------------|--------------------|----------------|--------------------------|------------|
|                                     | $\alpha$ -Helix   | $\beta$ -Sheet | Random coil <sup>b</sup> | $\Delta^a$ | $\alpha$ -Helix   | $\beta$ -Sheet | Random coil <sup>b</sup> | $\Delta^a$ | $\alpha$ -Helix    | $\beta$ -Sheet | Random coil <sup>b</sup> | $\Delta^a$ |
| Ala                                 | 52.4              | 48.2           | 51.1                     | 4.2        | 14.9              | 19.9           | 15.7                     | −5.0       | 176.4              | 171.8          | 176.1                    | 4.6        |
|                                     | 52.3              | 48.7           |                          | 3.6        | 14.8              | 20.0           |                          | −5.2       | 176.2              | 171.6          |                          | 4.6        |
|                                     | 52.8              | 49.3           |                          | 3.5        | 15.5              | 20.3           |                          | −4.8       | 176.8              | 172.2          |                          | 4.6        |
| Leu                                 | 55.7              | 50.5           | 55.2                     | 5.2        | 39.5              | 43.3           | 39.7                     | −3.8       | 175.7              | 170.5          | 175.7                    | 5.2        |
|                                     | 55.8              | 51.2           |                          | 4.6        | 43.7 <sup>c</sup> | 39.6           |                          | (4.1)      | 175.8              | 171.3          |                          | 4.5        |
| Val                                 | 65.5              | 58.4           | 61.2                     | 7.1        | 28.7              | 32.4           | 31.7                     | −3.7       | 174.9              | 171.8          | 174.4                    | 3.1        |
|                                     |                   | 58.2           |                          |            |                   | 32.4           |                          |            |                    | 171.5          |                          |            |
| Ile                                 | 63.9              | 57.8           | 61.1                     | 6.1        | 34.8              | 39.4           | 37.1                     | −4.6       | 174.9              | 172.7          | 175.8                    | 2.2        |
|                                     |                   | 57.1           |                          |            |                   | 33.1           |                          |            |                    | 171.0          |                          |            |
| Glu(OBzl)                           | 56.4              | 51.2           |                          | 5.2        | 25.6              | 29.0           |                          | −3.4       | 175.6              | 171.0          |                          | 4.6        |
|                                     | 56.8              | 51.1           |                          | 5.7        | 25.9              | 29.7           |                          | −3.8       | 175.4              | 172.2          |                          | 3.2        |
| Asp(OPBzl)                          | 53.4              | 49.2           |                          | 4.2        | 33.8              | 38.1           |                          | −4.3       | 174.9              | 169.8          |                          | 5.1        |
|                                     | 53.6 <sup>d</sup> |                |                          |            | 34.2 <sup>d</sup> |                |                          |            | 174.9              |                |                          |            |
| Lys <sup>e</sup>                    | 57.4              |                |                          |            | 29.9              |                |                          |            | 176.5              |                |                          |            |
| Lys(Z)                              | 57.6              | 51.4           |                          | 6.2        | 29.3              | 28.5           |                          | −0.8       | 175.7              | 170.4          |                          | 5.3        |
| Arg <sup>e</sup>                    | 57.1              |                |                          |            | 28.9              |                |                          |            | 176.8              |                |                          |            |
| Phe                                 | 61.3              | 53.2           |                          | 8.1        | 35.0              | 39.3           |                          | −4.3       | 175.2              | 169.0          |                          | 6.2        |
| Met                                 | 57.2              | 52.2           |                          | 5.0        | 30.2              | 34.8           |                          | −4.6       | 175.1              | 170.6          |                          | 4.5        |
| Gly                                 |                   | 43.2           |                          |            |                   |                |                          |            |                    | 168.4          |                          |            |
|                                     |                   | 44.3           |                          |            |                   |                |                          |            |                    | 169.2          |                          |            |
|                                     |                   |                |                          |            |                   |                |                          |            | 171.6 <sup>f</sup> | 168.5          |                          | 3.1        |

Reproduced with permission from Saitô et al. [24].

<sup>a</sup> Difference in the <sup>13</sup>C chemical shifts of the  $\alpha$ -helix form relative to those of the  $\beta$ -sheet form.<sup>b</sup> In CF<sub>3</sub>COOH solution. A few drops of H<sub>2</sub>SO<sub>4</sub> were added in the cases of (Ile)<sub>n</sub> and (Leu)<sub>n</sub>.<sup>c</sup> This assignment should be reversed.<sup>d</sup> Erroneously assigned from the left-handed  $\alpha$ -helix.<sup>e</sup> Data taken from the data of salt-induced  $\alpha$ -helix in neutral aqueous solution.<sup>f</sup> Averaged values from the data of polypeptides containing <sup>13</sup>C-labeled glycine residues.

mations. In some instances, however, the <sup>13</sup>C chemical shifts of the  $\alpha$ -helix are very close to those of a random coil as encountered for Ala and Leu residues (Table 3). This is also the case for a variety of membrane proteins, for instance, [3-<sup>13</sup>C]Ala-labeled bacteriorhodopsin (bR) in which an  $\alpha$ -helical Ala C<sub>β</sub> from the flexible C-terminal region resonates at the lowest boundary position accidentally overlapped at the frequency typical of a random coil [24,108]. Even in such cases, a distinction between  $\alpha$ -helix and random coil peaks can be made, by taking into account that the signal from the  $\alpha$ -helix under consideration can be recorded only by a CPMAS experiment in the presence of persistent C–H dipolar interactions, but the peak from random coil can be obtained by either solution NMR or by DD (direct-detection or dipolar-decoupled, without cross-polarization) MAS because of averaged such dipolar interactions. Even though the antiparallel structure is known as the major form in the  $\beta$ -sheet form, the parallel  $\beta$ -sheet form [109,110] plays an important role in the secondary structure of amyloid peptides [111] and silk fibroin from *S.c. ricini* [112]. In reflecting the presence of different types of hydrogen bonding between the two types of  $\beta$ -sheet forms, more wide spread of Ala C<sub>β</sub> <sup>13</sup>C chemical shifts (16.1–22.8 ppm, with reference to a neat TMS) in N- and C-terminal Ala residues in a parallel  $\beta$ -sheet (Ala)<sub>3</sub> and (Ala)<sub>4</sub>, as confirmed by X-ray diffraction studies, turned out to be an excellent means to distinguish the types of both conformations as compared with those of an antiparallel form (18.9–21.1 ppm) [112]. Consequently, the <sup>13</sup>C chemical shifts as measured in the solid-state with reference to those from model polypeptides in Table 3 and parallel  $\beta$ -sheet form turned out to be a very valuable means as intrinsic probes to determine the secondary structure of peptides and proteins, irrespective of neighboring amino acid residues.

Further, it is interesting to note that carbonyl <sup>13</sup>C chemical shifts (C') in peptides and proteins are also related to the nature of participating hydrogen bonds. In particular, it was empirically shown that the observed isotropic <sup>13</sup>C' chemical shifts in Gly, Ala, Leu, Val and Asp residues move linearly downfield with a decrease

in the hydrogen-bonding length  $R_{N...O}$ , according to Eq. (34) [113–115],

$$\delta_{iso} \text{ (ppm)} = a - bR_{N...O} \text{ (Å)}, \quad (34)$$

where  $a$  and  $b$  are 206.0 (ppm) and 12.4 (ppm/Å) for Gly residue, 237.5 (ppm) and 21.7 (ppm/Å) for Ala residue, 215.4 (ppm) and 14.2 (ppm/Å) for Val residue, 202.2 (ppm) and 10.0 (ppm/Å) for

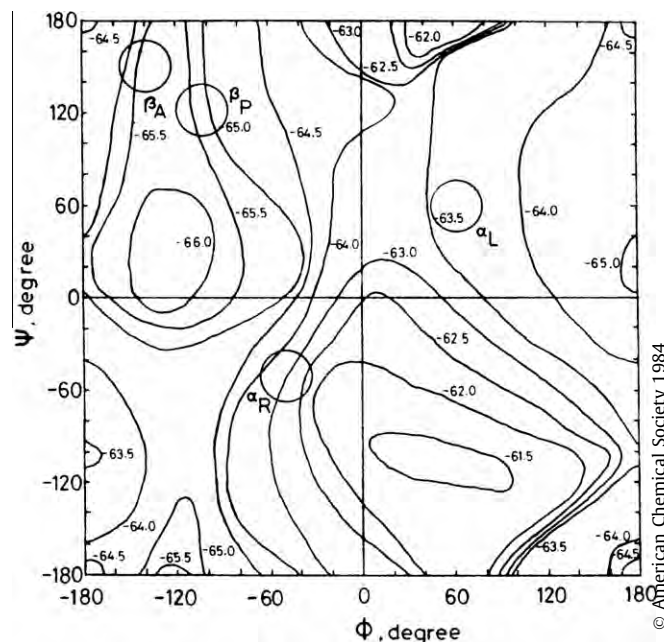


**Fig. 5.** The calculated <sup>13</sup>C chemical shift (shielding constant) map of the C<sub>β</sub> carbon of N-acetyl-N'-methyl-L-alanine amide obtained by using the FPT-INDO method. The chemical shielding constants were calculated at 15° intervals for the torsion angles ( $\phi$ ,  $\psi$ ). Reproduced with permission from Ando et al. [41].

Leu residue, and 199.0 (ppm) and 9.6 (ppm/Å), respectively. Alternatively, the  $R_{N\cdots O}$  values of some polypeptides in the crystalline state can be evaluated by these relations from the observed amide C' chemical shifts.

The above-mentioned conformation-dependence of  $^{13}\text{C}$  chemical shifts in polypeptides or proteins has been explained theoretically by calculation of the  $^{13}\text{C}$  shielding constants of Ala fragment (N-acetyl-N'-methyl-L-alanine amide; Ac-L-Ala-NHMe) as a function of the torsion angles (dihedral angles) ( $\phi, \psi$ ) by means of the FPT-INDO method [41]. The  $^{13}\text{C}$  chemical shift for the Ala  $\text{C}_\beta$  carbon, for instance, in any specified conformation can be found from the calculated contour map of the shielding constant as illustrated in Fig. 5 [41]. These calculations verified that  $^{13}\text{C}$  chemical shifts of Ala residues in polypeptides and proteins vary with conformation and can be utilized as convenient probes for predicting conformation. However, for the interpretation of  $\text{C}_\alpha$  and  $\text{C}=\text{O}$   $^{13}\text{C}$  chemical shifts, however, it turned out to be essential to include hydrogen bonds at N-H and C=O in addition to the effects of the torsion angles, although the  $\text{C}_\beta$  chemical shift is not affected by such hydrogen bonds. Instead of this fragment approach, calculation of  $\text{C}_\alpha$ ,  $\text{C}_\beta$  and  $\text{C}=\text{O}$   $^{13}\text{C}$  chemical shifts of  $(\text{Gly})_n$ ,  $(\text{Ala})_n$  and  $(\beta\text{-benzyl-L-Asp})_n$ , have been made which take tight-binding MO theory suitable for treating infinite molecular chain into account of the infinite chain-length of peptides including appropriate intramolecular hydrogen bond network and these are consistent with the experimental data [116,117]. Consistent results were further obtained by more elaborate calculations of  $^{13}\text{C}$  chemical shifts for Ac-L-Ala-NHMe and Ac-Gly-NHMe on the basis of *ab initio* MO approaches [43,44,117,118].

Average  $^{13}\text{C}$  chemical shifts obtained by multidimensional solution NMR experiments for  $\text{C}_\alpha$  and  $\text{C}=\text{O}$  carbons of all 20 amino acid residues taking  $\alpha$ -helix,  $\beta$ -sheet and random coil forms have been reported [25,120]. Both the  $^{13}\text{C}$  resonances experience downfield shifts in the  $\alpha$ -helix and upfield shifts in the  $\beta$ -sheet forms with respect to those in a random coil. Solution NMR structural studies have extended this approach to formulate a chemical shift index (CSI) to identify the secondary structure of proteins [28,121,122]. This method can be thought of as a filtration procedure to separate out spurious chemical shift signals, by assigning an index value of +1, 0 or -1 for the  $\alpha$ -helix, random coil and  $\beta$ -sheet structures, respectively. The CSI values which are graphically represented against the amino acid sequence were originally developed for the analysis of  $\text{H}_\alpha$  signals and extended to include  $^{13}\text{C}_\alpha$ ,  $^{13}\text{C}_\beta$  and  $^{13}\text{C}=\text{O}$  chemical shifts to identify and locate the secondary structure of proteins without recourse to NOE measurements by utilizing these four independent chemical shift measurements [122]. For example, the secondary structure of the first 65 residues of interleukin 4 experimentally determined by the CSI values are consistent with the secondary structure determined by X-ray and NOE data, as depicted by the arrows ( $\beta$ -strand) and coils (helices) in Fig. 6 [28].

$^{13}\text{C}$  chemical shifts of the  $\text{C}_\alpha$  and  $\text{C}_\beta$  carbons of individual residues can be used to obtain the corresponding torsion angles  $\phi$  and  $\psi$  of the peptide unit, whose values available from high-resolution X-ray diffraction studies in which their 3D structures have been resolved at 1.0–2.2 Å [25]. Average secondary shifts of  $\Delta(\phi, \psi)$  as a function of the torsion angles ( $\phi, \psi$ ) were calculated by convolution of each of the deviation from random coil chemical shift as a secondary shift of residue  $k$ ,  $\delta(\phi_k, \psi_k)$ , with a Gaussian function

$$\Delta(\phi, \psi) = \frac{\sum \delta(\phi_k, \psi_k) \exp[-((\phi - \phi_k)^2 + (\psi - \psi_k)^2)/450]}{\sum \exp[-((\phi - \phi_k)^2 + (\psi - \psi_k)^2)/450]} \quad (35)$$

Plots of these functions for  $\text{C}_\alpha$  and  $\text{C}_\beta$  signals are illustrated in Fig. 7a and b, respectively, together with histograms of secondary shift dis-

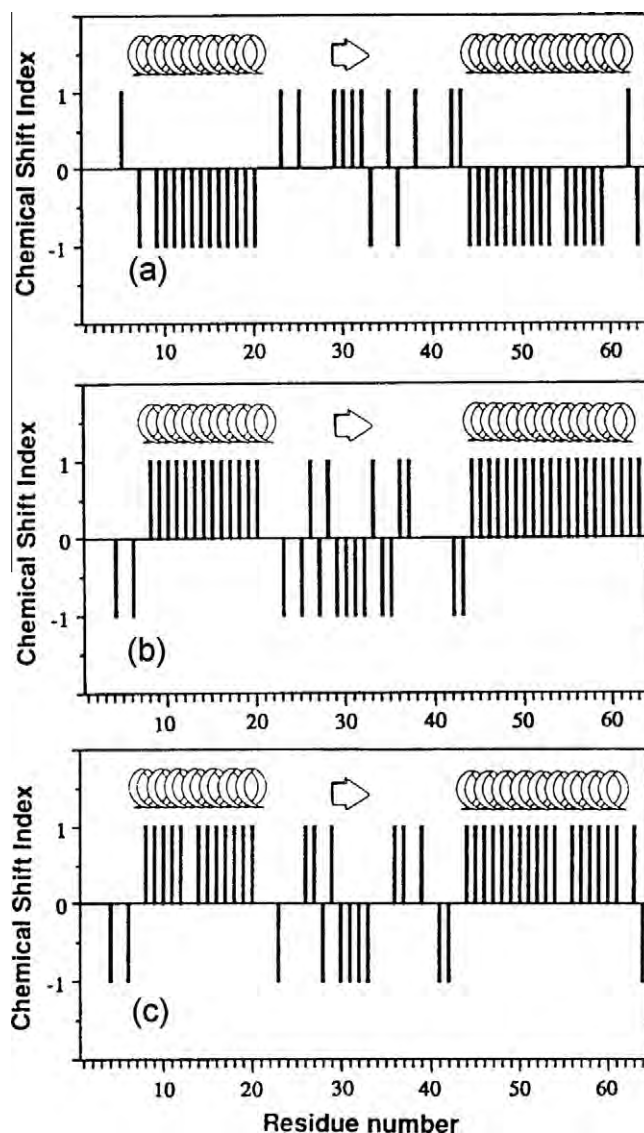


Fig. 6. Chemical shift index plotted for the first 65 residues of interleukin four using assignments supplied by Powers et al. [123]. (a)  $\text{H}_\alpha$ , (b)  $\text{C}_\alpha$  and (c) carbonyl resonances. Reproduced with permission from Wishart and Sykes [28]. Copyright 1994 Elsevier.

tribution in  $\alpha$ -helix and  $\beta$ -sheet forms (C). This is consistent with the data obtained from polypeptides in the solid-state as summarized in Table 3 and in Fig. 5. An extensive database of  $\text{C}_\alpha$  and  $\text{C}_\beta$  chemical shifts of proteins in solution has been generated, for which high-resolution crystal structures exist and they have been shown to be essentially identical to the solution structures [124]. The effects of backbone dihedral angles, side-chain dihedral angle  $\chi^1$  and hydrogen bonding on the  $\text{C}_\alpha$  and  $\text{C}_\beta$  chemical shifts were analyzed. These chemical shift data, together with those of  $^{15}\text{N}$  and  $^1\text{H}$  chemical shifts, are currently utilized as most important structural restraints for 3D construction as discussed in Section 4.1.

## 2.2.2. $^{15}\text{N}$ chemical shifts

It was also anticipated that amide- $^{15}\text{N}$  chemical shifts of polypeptides and proteins would also be sensitive to their secondary structures. In studies of  $^{15}\text{N}$ -labeled homo- and copolypeptides in the solid-state [30,125–127], the conformation-dependency of  $^{15}\text{N}$  chemical shifts is found to be not so simple as compared to the above-mentioned  $^{13}\text{C}$  chemical shifts, because  $^{15}\text{N}$  chemical shifts depend mainly on the conformation and side-chain structure of

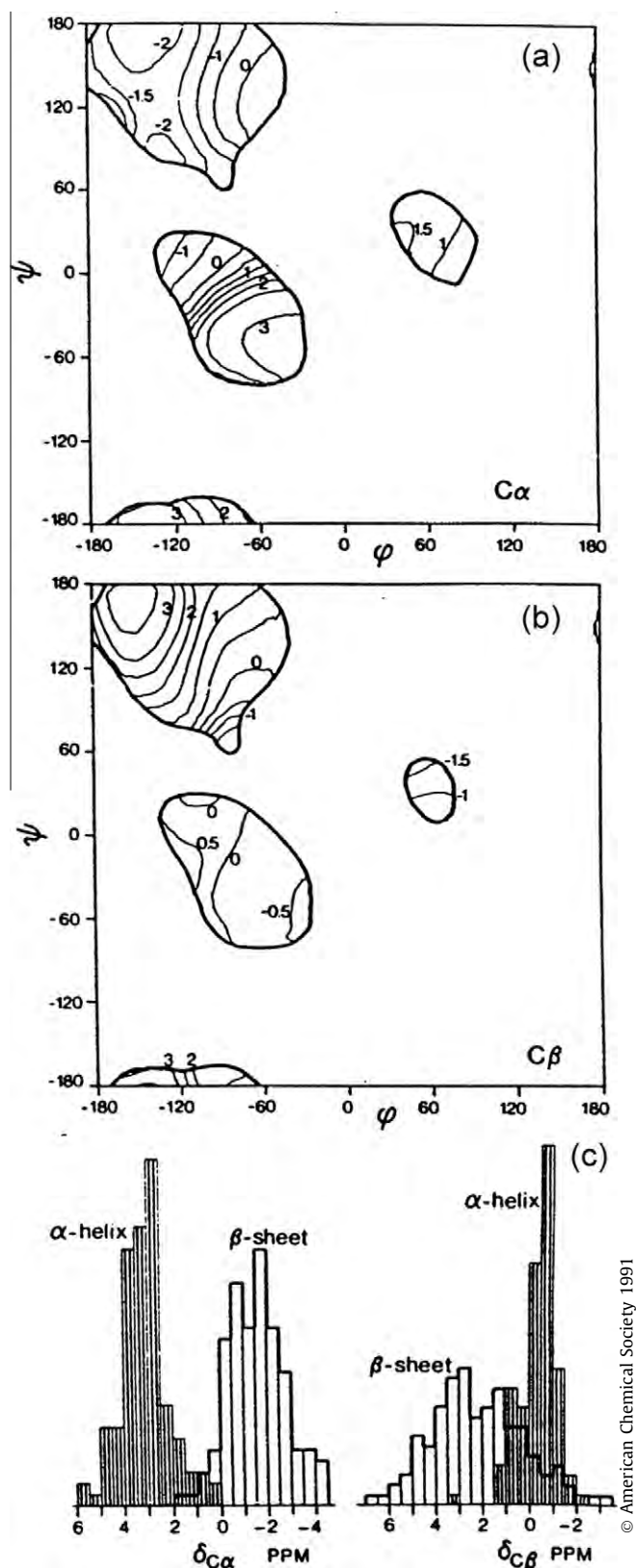


Fig. 7. Contour plots of the average secondary shift  $\Delta(\phi, \psi)$  of (a)  $C\alpha$  and (b)  $C\beta$  resonances and histogram (c) of secondary shift distribution in  $\alpha$ -helix and  $\beta$ -sheet form. Reproduced with permission from Spera and Bax [25].

an individual amino acid residue [30]. In fact, the amide- $^{15}\text{N}$  signals of  $\alpha$ -helical homopolypeptides (97.0–99.2 ppm) are found at a higher field than that of the  $\beta$ -sheet conformation (99.5–

107.0 ppm), as demonstrated in Fig. 8, consistent with the isotropic and  $\delta_{22}$  component of the  $^{15}\text{N}$  shielding map calculated for poly( $\beta$ -benzyl L-aspartate) [128]. The  $\delta_{22}$  component of the  $^{15}\text{N}$  shielding tensor, which lies perpendicular to the H–N–C plane as illustrated in Fig. 9 for the amide- $^{15}\text{N}$  nuclei, can be utilized as a good parameter for distinguishing  $\alpha$ -helix and  $\beta$ -sheet conformations. In Fig. 8,  $^{15}\text{N}$  chemical shifts of other conformations including forms I and II of (Pro) $_n$  [PP] and (Gly) $_n$  [PG],  $\alpha_L$  (left-handed  $\alpha$ -helix) and  $\omega_L$  (omega) helix are also included. It is also noted that the  $^{15}\text{N}$  chemical shifts of the  $\beta$ -sheet form of Leu, Val or Ile residues with alkyl side-chains appear at a lower field than that of an Ala residue, while the  $^{15}\text{N}$  chemical shifts of the  $\beta$ -sheet forms of Asp(OBzl), Glu(OBzl) or Glu(OMe) residues appear at higher fields than that of an Ala residue. In fact,  $^{15}\text{N}$  chemical shifts are strongly influenced by the side-chain bulkiness of residue  $i-1$  affecting the backbone  $^{15}\text{N}$  shift of the  $i$ th residue [30].

In a similar manner, a 3–4 ppm difference in amide- $^{15}\text{N}$  chemical shift was observed between the  $\alpha$ -helix and  $\beta$ -sheet residues from various globular proteins in aqueous solution [118]. In relation to the neighboring effect as described above, an empirical correlation between  $^{15}\text{N}$  chemical shifts, in BPTI and apamin, and the torsion angle of the preceding residue  $\psi_{i-1}$  was proposed for the  $\beta$ -sheet residues [129]. Empirical correlation between  $^{15}\text{N}$  chemical shifts and the torsion angles  $\phi_i$  and  $\psi_{i-1}$  was searched for a variety of proteins with known 3D structures [130]; on average, the rms error between experiment and prediction is about 3.5 ppm, although results for Thr, Val and Ile residues are worse ( $\sim 4.8$  ppm). *Ab initio* calculations were performed for several peptide fragments in order to estimate the contributions to  $^{15}\text{N}$  chemical shifts of peptide residues such as the torsion angles ( $\phi_{i-1}$ ,  $\psi_{i-1}$ ,  $\phi_i$ ,  $\psi_i$  and  $\chi^1$ ) and hydrogen bond [43,131]. It was shown that the two backbone torsion angles closest to the peptide group ( $\psi_{i-1}$  and  $\phi_i$ ) have the largest effects up to 20 ppm on  $^{15}\text{N}$  chemical shifts. The adjacent (preceding) torsion angles  $\phi_{i-1}$  and  $\psi_i$  have a smaller contribution up to 8 ppm. Different side chain conformations produced chemical shift variations of only 4 ppm [131].

Further, it should be taken into account that  $^{15}\text{N}$  chemical shifts are very sensitive to the nature of hydrogen bonding: the  $^{15}\text{N}$  signal of a proton donor (N–H) is displaced downfield by about 15 ppm, while the  $^{15}\text{N}$  shift of a proton acceptor (tertiary nitrogen atom) is shifted upfield by about 20 ppm [132–136]. Therefore, displacement of  $^{15}\text{N}$  chemical shifts arising from hydrogen bonds may surpass the effect due to the above-mentioned conformational changes. In addition to the isotropic  $^{15}\text{N}$  chemical shifts, the three principal tensor components were measured for Gly residue in a variety of peptides with a terminal Boc group in order to clarify the relationship between the  $^{15}\text{N}$  shifts and  $R_{\text{N}\dots\text{O}}$  distances: the isotropic  $^{15}\text{N}$  chemical shifts ( $\delta_{\text{iso}}$ ) of the glycine residues move downfield with a decrease of hydrogen bond lengths ( $R_{\text{N}\dots\text{O}}$ ) between the nitrogen and oxygen atoms in the amide groups, and that the principal value of  $\delta_{33}$  moves linearly downfield with a decrease of  $R_{\text{N}\dots\text{O}}$ . There is no relationship, however, between the principal value of  $\sigma_{11}$  or  $\sigma_{22}$  and  $R_{\text{N}\dots\text{O}}$ , although the decrease of the N–H bond length ( $R_{\text{N}\dots\text{H}}$ ) leads to a linear increase in the  $^{15}\text{N}$  chemical shift value [137,138]. Nevertheless, Gly N–H  $^{15}\text{N}$  chemical shifts of collagen (Gly- $X_{\text{aa}}$ - $Y_{\text{aa}}$  repeating units) and its model polypeptides [(Pro-Ala-Gly) $_n$  or (Pro-Pro-Gly) $_{10}$ ] were found to be very sensitive probes for locating the interchain (Gly)N–H...O=C ( $X_{\text{aa}}$  or Pro) hydrogen bond which is believed to be essential for the stabilization of the coiled-coil triple-helix conformation [139]. In particular, the  $^{15}\text{N}$  peak of the Gly N–H group and the high-field (low-frequency) shoulder peak of Pro nitrogen signals in (Pro-Pro-Gly) $_{10}$  are shifted downfield (4.9 and 6.8 ppm, respectively) with increasing relative humidity by forming N–H...O=C hydrogen bonds, while the corresponding peaks for collagen and (Pro-Ala-Gly) $_n$  are unchanged and close to the  $^{15}\text{N}$  chemical shift



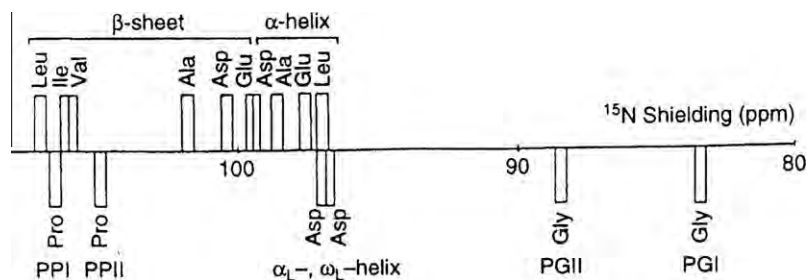


**Fig. 8.** The diagram of the observed isotropic  $^{15}\text{N}$  chemical shifts of some homopolypeptides ( $\text{X}_n$ ) with various conformations [ $\alpha$ -helix,  $\beta$ -sheet,  $\alpha_L$ -helix,  $\omega_L$ -helix, ( $\text{Gly}_n$ ) I (PGI), ( $\text{Gly}_n$ ) II (PGII), ( $\text{Pro}_n$ ) I (PPI) and ( $\text{Pro}_n$ ) II (PPII) forms]. Reproduced with permission from Shoji et al. [30]. Copyright 1993 Elsevier.

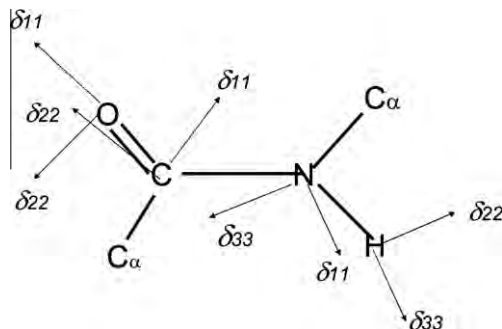


**Fig. 9.** Orientations of the principal axes for the  $^{13}\text{C}$ ,  $^{17}\text{O}$ ,  $^{15}\text{N}$  and  $^1\text{H}$  CSA tensors for an amide fragment. The most shielded component  $\delta_{33}$  for the  $^{13}\text{C}$  and  $^{17}\text{O}$  tensors is located perpendicular to the peptide plane. The  $\delta_{22}$  and  $\delta_{11}$  components for the  $^{15}\text{N}$  and  $^1\text{H}$  Tensors, respectively, are also located perpendicular to the peptide plane.

of (Pro-Pro-Gly) $_{10}$  in the hydrated state. For establishment of the above-mentioned relationship between the  $^{15}\text{N}$  chemical shifts and  $R_{\text{N} \cdots \text{O}}$  distances, it is more preferable to use the tensor component  $\delta_{33}$  (approximately, parallel to the C–N bond) (see Fig. 9) rather than the isotropic peak [140]. In addition, the N–H bond lengths determined from the N–H dipolar interaction, when the amplitude of a thermal vibration of N–H moiety is significantly enhanced as encountered for weakly hydrogen bonded systems.

This means that special care should be exercised when one uses the NMR-derived N–H distances involved in different types of hydrogen bonded systems as parameters for characterizing hydrogen bonded systems.

Naturally, the  $^{15}\text{N}$  chemical shift is also strongly affected by electrostatic interactions such as effects of electronic charge or counter ion in the vicinity of the nitrogen atom under consideration [135,136]. Thus, the  $^{15}\text{N}$  chemical shift of the Schiff base nitrogen in retinylidenes bacteriorhodopsin can be used to identification and detailed characterization of individual photo intermediates [141–145]. The frequencies of the maximum visible absorbance and the  $^{15}\text{N}$  chemical shifts of the 13-*cis* and all *trans* retinylidene compounds are found to be linearly related to the strength of the protonated Schiff base (pSB)–counterion (CI) interaction as measured by  $(1/d^2)$ , where  $d$  is the center-to-center distance between the pSB and the CI, as illustrated in Fig. 10 [143]. With these calibrations,  $d = 4.0, 3.9, 3.7, 3.6$  and  $3.8 \text{ Å} (\pm 0.3 \text{ Å})$  distances were estimated for the J $_{625}$ , K $_{590}$ , L $_{550}$ , N $_{520}$  and bR $_{555}$  states for 13-*cis*-compounds of bR, respectively. These distances are comparable with similarly determined values of about  $4.16 \pm 0.03 \text{ Å}$  and  $4.66 \pm 0.04 \text{ Å}$  for the all-*trans* bR $_{568}$  and O $_{640}$  states, respectively. The effective SB counter ion distance in regenerated bovine rhodopsin expressed by using suspension cultures of HEK293S cells was estimated by means of  $^{15}\text{N}$  chemical shift consideration using the empirical relationship as shown in Fig. 10 [146].

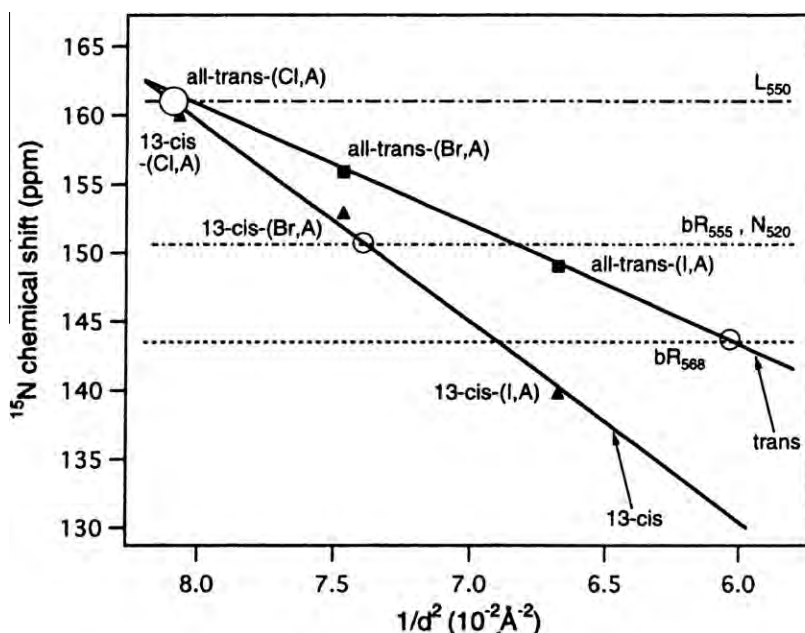


**Fig. 10.** Correlation between the  $^{15}\text{N}$  chemical shift for protonated 6-*s-trans*-retinal Schiff bases (SB) and the counterion strength measured by  $1/d^2$ , where  $d$  is the center-center distance between the SB nitrogen and the counterion. Reproduced with permission from Hu et al. [144].



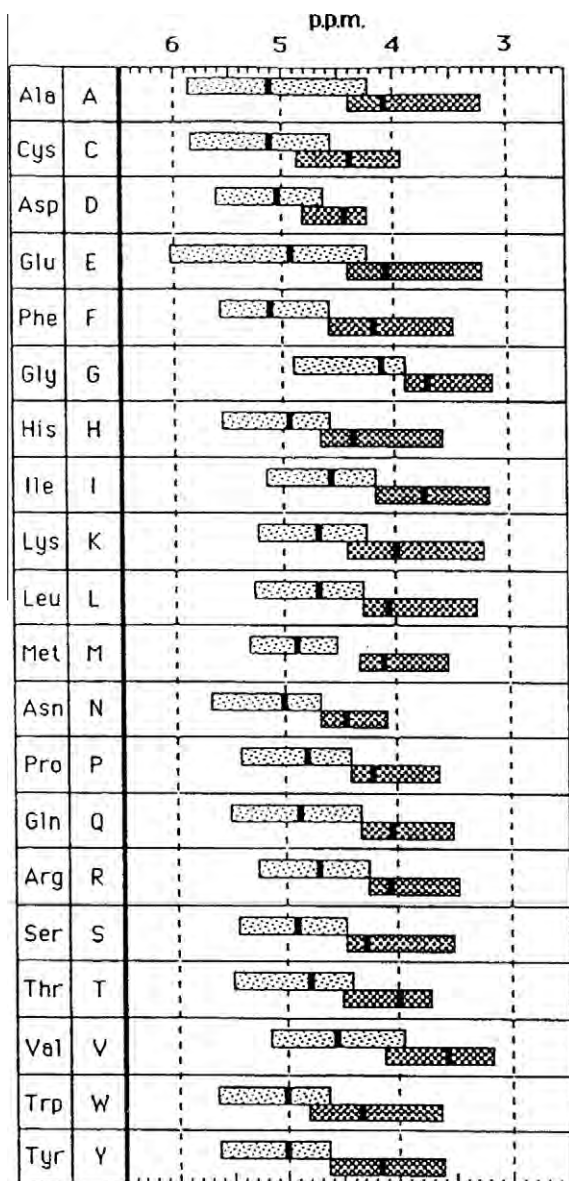


**Fig. 11.** Distribution of  $\alpha$ -proton chemical shifts in helices and  $\beta$ -strands. The black vertical bar indicates the median chemical shift. Reproduced with permission from Wishart et al. [26]. Copyright 1991 Elsevier.

### 2.2.3. $^1\text{H}$ chemical shifts

Conformation-dependent  $^1\text{H}$  chemical shifts, if any, can be caused by the last term in Eq. (20), consisting of neighboring group effects such as magnetic anisotropy, hydrogen bonding, electric field effects, etc. An attempt to evaluate such effects from protein data of known 3D structures showed that  $\text{H}_\alpha$  protons in the  $\beta$ -sheet regions experience downfield secondary shifts, whereas  $\text{H}_\alpha$  protons in  $\alpha$ -helix regions experience upfield secondary shifts with respect to those of the random coil form. Correlations between the chemical shifts of amide and  $\text{C}_\alpha$  protons and the length of hydrogen bonds formed by these groups have been made [119,147–152]. The existence of such close correlations between  $^1\text{H}$  chemical shifts and local secondary structure has been recognized for a variety of proteins of known 3D structures as demonstrated in Fig. 11 [26]. Semi-empirical quantum chemical calculations have been made in attempts to evaluate the contribution of the magnetic anisotropy and electric field effects besides the diamagnetic shielding to  $^1\text{H}$  chemical shifts of  $\alpha$ -helical polypeptide (initially for  $(\text{Ala})_n$ ) and the calculated chemical shifts agree fairly well with

the observed values [150]. An empirical analysis of proton chemical shifts referenced to the chemical shift values in random coil protein from a variety of proteins of known structure [151–155] was made to decompose the last term in Eq. (20) into the following contributions:

$$\sigma' = \sigma_{rc} + \sigma_m + \sigma_{el} + \sigma_s, \quad (36)$$

where the individual terms are contributions from aromatic ring currents, magnetic anisotropy effects from the peptide groups, electric fields from distant polar groups which can polarize the C–H bond, and solvent effects, respectively. The term for the ring current contributions in [155] is

$$\sigma_{rc} = iBG(\mathbf{r}), \quad (37)$$

where  $\mathbf{r}$  is the vector from the observed proton to the aromatic ring,  $G(\mathbf{r})$  is a geometric factor, and  $i$  and  $B$  are constants [156]. The magnetic anisotropy contribution is given by [157]:

$$\sigma_m = (3L_0R^3)^{-1}\Delta\chi(3\cos^2\theta - 1) \quad (38)$$

where  $L_0$  is the Avogadro constant,  $R$  is the distance from the proton to the amide group which has the magnetic anisotropy  $\Delta\chi = -5.1 \pm 0.6 \times 10^{-6} \text{ erg}/(\text{G}^2 \text{ mol})$  (formamide) [158]. The term for the electrostatic contribution is

$$\sigma_{el} = AE(\text{C}–\text{H}) \quad (39)$$

based on the charge model from the CHARMM (version 19) parameters. The parameter fitting of chemical shifts for 5678 protons bonded to carbon into these classical contributions yielded a linear correlation coefficient of 0.88 between calculated and observed structural shifts, with a root mean square error of 0.23 ppm: contributions from the peptide group are especially noticeable for protons at the  $\text{C}_\alpha$ , although predictions for protons bonded to nitrogen are much worse [152]. Various models for calculating the above-mentioned contributions have been compared [159] and also their relative proportions as illustrated in Fig. 12. The success of such an empirical treatment of  $^1\text{H}$  chemical shifts of a variety of proteins from the database is promising and further extends to the base of chemical shift restraints for revealing unknown 3D structures of proteins.

As compared with  $^{13}\text{C}$  and  $^{15}\text{N}$  NMR spectra, recording  $^1\text{H}$  NMR spectra of polypeptides and proteins in the solid-state is not an easy task because of the large line broadening caused by dipolar interactions among dense  $^1\text{H}$  spins. Nevertheless, it was shown that  $\text{H}_\alpha$   $^1\text{H}$  NMR signals of the  $\beta$ -sheet form of  $(\text{Ala})_n$  and  $(\text{Leu})_n$  resonate downfield as compared to their signals from the  $\alpha$ -helical form as recorded by a combined rotational and multipulse spectroscopy (CRAMPS) method [160,161], consistent with the data from proteins in aqueous solution. Well-resolved N–H proton signals in solid-state are observed either by CRAMPS of  $^{15}\text{N}$ -labeled polypeptides [162] or high field/fast MAS measurements [163–165], in order to avoid  $^{14}\text{N}$ – $^1\text{H}$  dipolar splitting caused by the effect of the  $^{14}\text{N}$  quadrupole coupling [166]. The measured  $^1\text{H}$  chemical shift values ( $\delta_{\text{iso}}$ ) of hydrogen-bonded Gly amide-protons of Gly-containing peptides and polyglycines in the solid-state have been plotted against the hydrogen-bond lengths between amide nitrogen and oxygen atoms ( $R_{\text{N} \cdots \text{O}}$ ) determined by X-ray diffraction studies, as illustrated in Fig. 13 [164]. The bars indicate the experimental errors in the spectra. It was found that as  $R_{\text{N} \cdots \text{O}}$  is decreased from 3.12 to 2.72 Å, the amide- $^1\text{H}$  chemical shift moves downfield by 2.46 ppm from 7.76 to 9.04 ppm. Well-resolved  $^1\text{H}$  NMR signals including those of amide-NHs were observed for anti-parallel and parallel alanine tripeptide  $(\text{Ala})_3$  by high-field (930 MHz) MAS (20 kHz) NMR [165]. In particular, amide-NH and  $\text{NH}_3^+$   $^1\text{H}$  NMR signals of parallel  $(\text{Ala})_3$  were well resolved at 7.5 and 8.9 ppm, respectively, whereas amide-NH and  $\text{NH}_3^+$  signals of

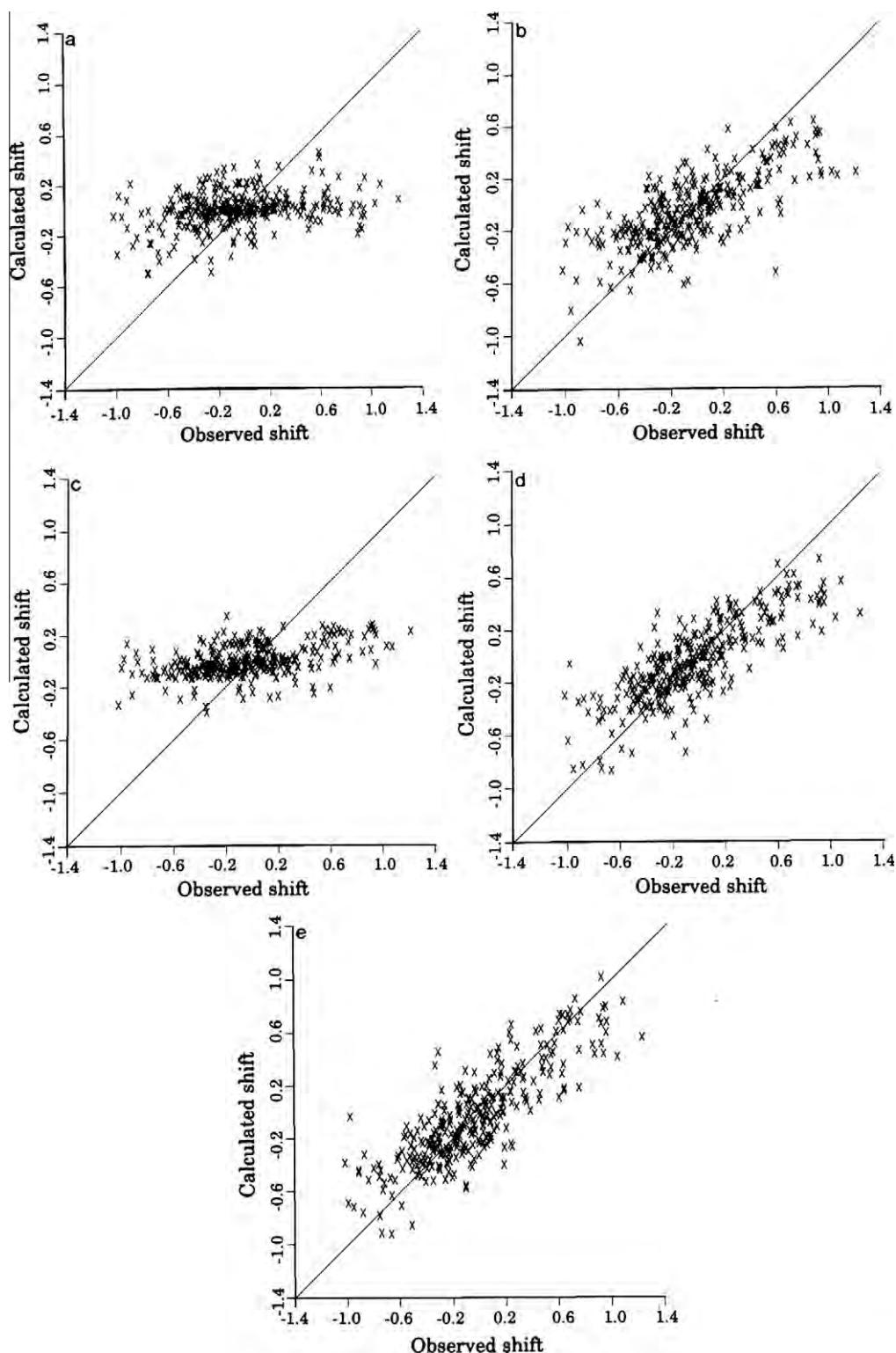


**Fig. 12.** Comparison of calculated and observed  $H_{\alpha}$  secondary structure shifts. (a) ring current only, (b) magnetic anisotropy only, (c) electric field only, (d) ring current plus magnetic anisotropy, (e) using all three. Values for ubiquitin, turkey ovomucoid third domain, human lysozyme and BTP1 are plotted. Reproduced with permission from Williamson and Asakura [159]. Copyright 1991 Elsevier.

antiparallel (Ala)<sub>3</sub> resonated at the same frequency (9.5 ppm) which is at lower field than that of the parallel peptide. In a similar manner, amide- $^{15}\text{NH}$  signals of antiparallel (Ala)<sub>3</sub> resonate at a lower field by 2–5 ppm than those of parallel (Ala)<sub>3</sub>, although the  $^{15}\text{NH}_3^+$  signal of the former resonates at the peak-position between

the two  $^{15}\text{N}$  peaks of the latter. These findings based on the  $^1\text{H}$  and  $^{15}\text{N}$  hydrogen bond shifts are consistent with the relative hydrogen bond lengths of inter-strand  $\text{N}-\text{H} \cdots \text{O}=\text{C}$  bonds as evaluated by X-ray diffraction studies, and are also consistent with DFT calculations for antiparallel and parallel (Ala)<sub>3</sub> [165].

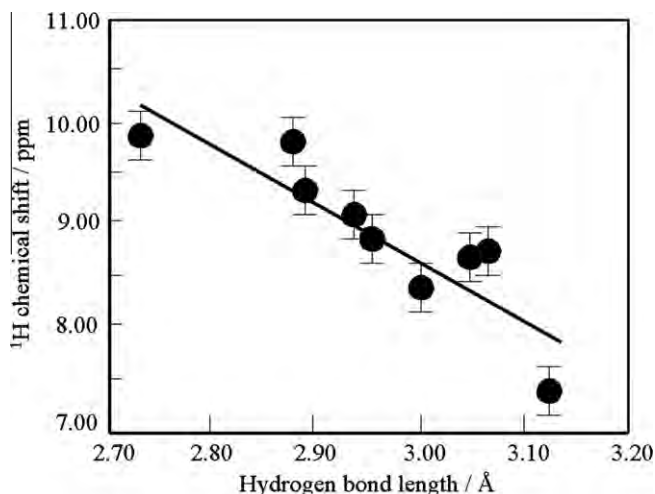


**Fig. 13.** Plots of the observed  $^1\text{H}$  chemical shift values ( $\delta$ ) of hydrogen-bonded Gly amide protons of Gly-containing peptides and polyglycines in the solid against the hydrogen bond lengths between amide nitrogen and oxygen atoms ( $R_{\text{N}\cdots\text{O}}$ ). Reproduced with permission from Yamauchi et al. [164]. Copyright 2002 Elsevier.

The  $^1\text{H}$  chemical shielding calculations of hydrogen-bonded Gly amide-protons of two hydrogen-bonded GlyGly molecules have been made using the Gaussian 96 HF program with *ab initio* 6-31G\*\* basis set by changes of  $R_{\text{N}\cdots\text{O}}$  from 3.5 to 2.6 Å as referred to its crystal structure determined by X-ray diffraction. The calculated chemical shifts move to downfield by 2.5 ppm from 6.9 to 9.4 ppm as  $R_{\text{N}\cdots\text{O}}$  is decreased from 3.30 to 2.72 Å [167].

#### 2.2.4. Chemical shifts can provide torsion angles

Incorporation of both  $^1\text{H}$  and  $^{13}\text{C}$  chemical shift as additional restraints into the refinement of protein structures using the simulated annealing protocol with NOE and  $J$  coupling data has been achieved [168,169]. An approach to obtain the most probable  $\phi$  and  $\psi$  angles from multidimensional hypersurface correlations of backbone chemical shifts ( $^{13}\text{C}_\alpha$ ,  $^{13}\text{C}_\beta$ ,  $^1\text{H}_\alpha$ ,  $^1\text{H}_\text{N}$  and  $^{15}\text{N}$ ) of a given residue with its backbone torsion angles was proposed [170]. It was claimed that this information considerably improves the structural quality when used for cases where only a very small number of NOE restraints is available. Indeed, the use of chemical shifts is now recognized as important tool in understanding, generating or refining macromolecular structures: chemical shift refinement options are now available in the simulated annealing protocols, AMBER, XPLOR and CNS [171]. To this end, a computer program (SHIFTY) was developed to accurately and automatically predict the  $^1\text{H}$  and  $^{13}\text{C}$  chemical shifts of unassigned proteins on the basis of sequential homology of proteins against the database from BioMagResBank [172].

A hybrid approach, [called TALOS (Torsion Angle Likelihood Obtained from Shifts and sequence similarity), <http://spin.niddk.nih.gov/bax>], which searches a database for triplets of adjacent residues with secondary chemical shifts and sequence similarity, in order to provide the best match to the query triplet of interest to predict the most likely backbone angles for a given residue of unknown structure [173]. For each query triplet of consecutive residues, the similarity to a triplet with center-residue  $j$  in the database is evaluated by computing a similarity factor,  $S(i,j)$  given by:

$$S(i,j) = \sum_{n=-1}^{+1} \left[ k_n^0 \Delta_{\text{ResType}}^2 + k_n^1 (\Delta\delta\text{C}_\alpha^{i+n} - \Delta\delta\text{C}_\alpha^{j+n})^2 + k_n^2 (\Delta\delta\text{N}^{i+n} - \Delta\delta\text{N}^{j+n})^2 + k_n^3 (\Delta\delta\text{C}_\beta^{i+n} - \Delta\delta\text{C}_\beta^{j+n})^2 + k_n^4 (\Delta\delta\text{C}^{i+n} - \Delta\delta\text{C}^{j+n})^2 + k_n^5 (\Delta\delta\text{H}_\alpha^{i+n} - \Delta\delta\text{H}_\alpha^{j+n})^2 \right] \quad (40)$$

and the value of  $S(i,j)$  is evaluated for all triplets  $j$  in the database.  $\Delta\delta$  denotes the secondary shifts of the  $^{13}\text{C}_\alpha$ ,  $^{13}\text{C}_\beta$ ,  $^{13}\text{C}$ ,  $^1\text{H}_\alpha$  and  $^{15}\text{N}$  nuclei. Using the empirical weighting factors  $k_n^0$  through  $k_n^5$  values and the residue similarity factors  $\Delta_{\text{ResType}}$ , the values of  $S(i,j)$  typically range from 5 to 600. As demonstrated in Fig. 14 for comparison of the torsion angles between predicted and observed values in the crystal structure, it appears that the accuracy of the TALOS prediction exceeds that of even some of the best solution structures calculated on the basis of NOEs and  $J$  coupling [173]. Alternatively, a computer program (SHIFTX, <http://redpoll.pharmacy.ualberta.ca>) uses a hybrid predictive approach that employs precalculated, empirically derived chemical shift hypersurfaces in combination with classical or semi-classical equations (for ring current, electric field, hydrogen bond and solvent effects) to calculate  $^1\text{H}$ ,  $^{13}\text{C}$  and  $^{15}\text{N}$  chemical shifts from atomic coordinates [174]. Data mining techniques were used to extract the largest pairwise contributor (from a list of ~20 derived geometric, sequential and structural parameters) to generate the necessary hypersurfaces which capture dihedral angle, sidechain orientation, secondary structure and nearest neighbor effects. The program was able to attain a correlation coefficient ( $r$ ) between observed and calculated shifts of 0.911 ( $^1\text{H}_\alpha$ ), 0.980 ( $^{13}\text{C}_\alpha$ ), 0.996 ( $^{13}\text{C}_\beta$ ), 0.863 ( $^{13}\text{CO}$ ), 0.909 ( $^{15}\text{N}$ ),

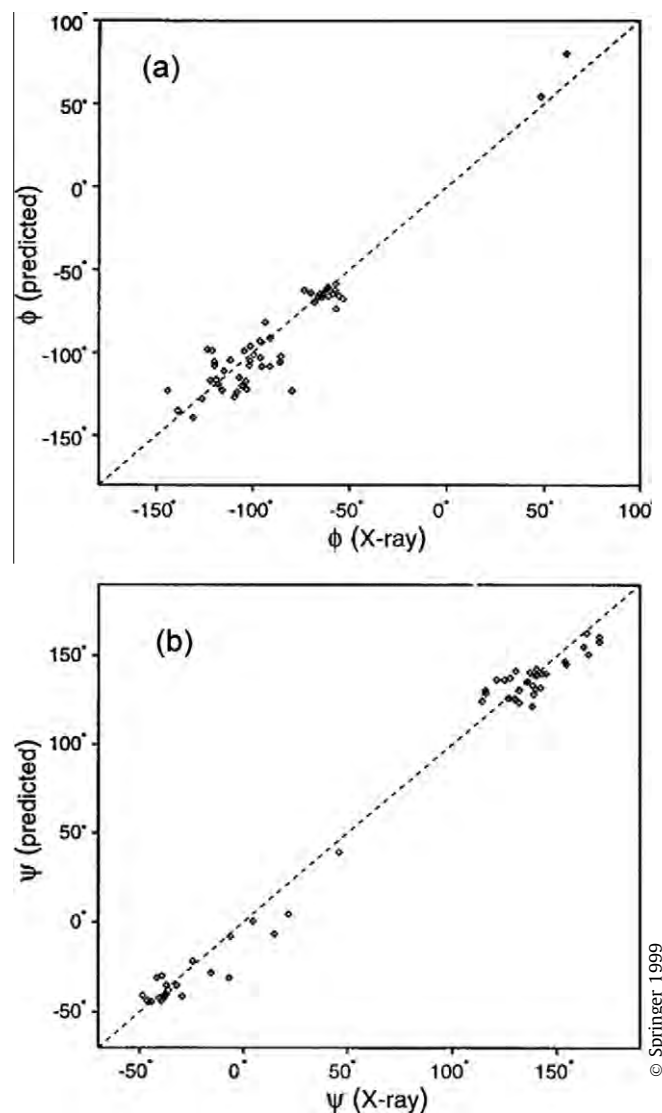


**Fig. 14.** Plots of the backbone angles (a)  $\phi$ , and (b)  $\psi$  predicted by TALOS, versus those observed in the crystal structure for ubiquitin. Reproduced with permission from Cornilescu et al. [173].



0.741 ( $^1\text{HN}$ ) and 0.907 (sidechain  $^1\text{H}$ ) with RMS errors of 0.23, 0.98, 1.10, 1.16, 2.43, 0.49 and 0.30 ppm, respectively. A TALOS-like database searching procedure, which utilizes both the protein sequence and the structural homology, was used after the inclusion of the nearest neighbor, ring current and hydrogen bond effects to predict the backbone  $^{15}\text{N}$ ,  $^1\text{H}_\text{N}$ ,  $^1\text{H}_\alpha$ ,  $^{13}\text{C}_\alpha$ ,  $^{13}\text{C}_\beta$  and  $^{13}\text{C}'$  chemical shifts for a protein of known structure, as a computer program SPARTA (Shift Prediction from Analogy in Residue type and Torsion angle) [175]. The predicted and experimental shifts were shown with a standard deviation of 2.52, 0.51, 0.27, 0.98, 1.07 and 1.08 ppm for  $^{15}\text{N}$ ,  $^1\text{H}_\text{N}$ ,  $^1\text{H}_\alpha$ ,  $^{13}\text{C}_\alpha$ ,  $^{13}\text{C}_\beta$  and  $^{13}\text{C}'$ , respectively.

The following three computer packages that are currently available on the internet are useful for protein structure determination using chemical shifts: CHESHIRE (CHEMical Shift Restraints) [176], CS-ROSETTA [177] and CS23D (Chemical Shift to 3D structure) [178].

### 3. Anisotropic chemical shifts

#### 3.1. CSAs of nuclei in peptides and proteins

It is expected that CSA tensors can provide insights into the local secondary structure and dynamics for individual residues in peptides and proteins, as well as their inter-residual besides their

inter-residual interactions through  $\text{N}-\text{H}\cdots\text{O}=\text{C}$  hydrogen bond networks. Both principal components and orientations of CSA tensors are straightforwardly obtained in the solid-state, as described in Section 1.2. The orientation information can also be derived from polycrystalline samples through the interactions between X CSA and X–Y dipolar tensors, where spins X and Y are dipolar coupled.

#### 3.1.1. $^{13}\text{C}$ CSA

The Gly  $^{13}\text{C}'$  principal values ( $\delta_{11}$ ,  $\delta_{22}$  and  $\delta_{33}$ ) for  $^{13}\text{C}'$  nuclei in Gly and their orientations for several single crystalline [179,180] and polycrystalline [42,113,181,182] peptides reported in the literature are summarized in Table 4. The frequency values of many of the principal components are converted and reported with reference to TMS. These values span a wide range of 242–88 ppm. It is noted that the orientations of the principal component  $\delta_{22}$  for  $^{13}\text{C}'$  is not always collinear with the  $\text{C}=\text{O}$  bond [179–182] although the  $\delta_{33}$  axis is perpendicular to the peptide plane [42,113,179–182], except for [ $1\text{-}^{13}\text{C}$ , 10%]  $^1\text{Gly}^2\text{Gly}\cdot\text{HCl}\cdot\text{H}_2\text{O}$  (tilt angle of  $85^\circ$ ) [180], as illustrated in Fig. 9. It is also noteworthy that the peak positions corresponding to  $\delta_{22}$  differ substantially among the peptides, although the peak positions of  $\delta_{11}$  and  $\Delta\delta$  are almost unchanged. The  $^{13}\text{C}'$   $\delta_{11}$  of [ $1\text{-}^{13}\text{C}$ ]Gly [ $^{15}\text{N}$ ]Gly·HCl·H<sub>2</sub>O lies in the peptide plane and forms an angle of  $77^\circ$  relative to the  $\text{C}=\text{O}$  bond

**Table 4**  
The amide  $^{13}\text{C}$  chemical shift tensors of peptides in the solid state.

| Peptides   | Angle between $\delta_{ii}$ and X–Y bond axis                                | $\delta_{11}^a$ (ppm) | $\delta_{22}^a$ (ppm) | $\delta_{33}^a$ (ppm) | $\Delta\delta^b$ (ppm) | $\delta_{\text{iso}}$ (ppm) | Remarks   | Reference |
|--|--|-----------------------|-----------------------|-----------------------|------------------------|-----------------------------|---|-----------|
| [ $1\text{-}^{13}\text{C}$ ]Gly [ $^{15}\text{N}$ ]Gly HCl<br>H <sub>2</sub> O | $\delta_{22}$ : $13^\circ$ from $\text{C}=\text{O}$ bond axis                | 244.1                 | 177.1                 | 87.9                  | 111.6                  | 169.7                       | Single crystal. $\delta$ converted <sup>c</sup>                               | [179]     |
| Ac [ $1\text{-}^{13}\text{C}$ ]Gly [ $^{15}\text{N}$ ]GlyNH <sub>2</sub>       | $\delta_{22}$ : parallel to $\text{C}=\text{O}$ bond axis                    | 243.0                 | 184.9                 | 91.2                  | 105.0                  | 172.8                       | $^{15}\text{N}$ -dipole coupled powder. $\delta$ converted                    | [181]     |
| Ac [ $1\text{-}^{13}\text{C}$ ]Gly [ $^{15}\text{N}$ ]AlaNH <sub>2</sub>       | $\delta_{22}$ : parallel to $\text{C}=\text{O}$ bond axis                    | 242.1                 | 184.9                 | 90.0                  | 104.7                  | 172.3                       | $^{15}\text{N}$ -dipole coupled powder. $\delta$ : converted                  | [181]     |
| Ac [ $1\text{-}^{13}\text{C}$ ]Gly [ $^{15}\text{N}$ ]TyrNH <sub>2</sub>       | $\delta_{22}$ : $-6^\circ$ from $\text{C}=\text{O}$ bond axis                | 242.5                 | 165.5                 | 95.3                  | 112.1                  | 167.8                       | $^{15}\text{N}$ -dipole coupled powder. $\delta$ : converted                  | [181]     |
| Ac [ $1\text{-}^{13}\text{C}$ ]Gly [ $^{15}\text{N}$ ]Gly HCl                  | $\delta_{22}$ : $-12^\circ$ from $\text{C}=\text{O}$ bond axis               | 243.8                 | 177.2                 | 89.1                  | 110.7                  | 170.0                       | $^{15}\text{N}$ -dipole coupled powder. $\delta$ : converted                  | [181]     |
| [ $1\text{-}^{13}\text{C}$ ]Ala [ $^{15}\text{N}$ ]Ala                         | $\delta_{22}$ : $3.6^\circ$ from $\text{C}=\text{O}$ bond axis               | 244                   | 170.8                 | 95                    | 111.1                  | 169.9                       | $^{13}\text{C}$ - $^{15}\text{N}$ dipole coupled powder. $\delta$ : converted | [182]     |
| Ac [ $1\text{-}^{13}\text{C}$ ]Gly [ $^{15}\text{N}$ ]AlaNH <sub>2</sub>       | $\delta_{11}$ : $-36.6^\circ$ from $\text{C}'\text{-N}$ bond axis            | 242.1                 | 184.9                 | 90.0                  | 104.7                  | 172.3                       | $^{13}\text{C}$ - $^{15}\text{N}$ dipole coupled powder. $\delta$ : converted | [182]     |
| Ac [ $1\text{-}^{13}\text{C}$ ]Gly [ $^{15}\text{N}$ ]TyrNH <sub>2</sub>       | $\delta_{11}$ : $-40.7^\circ$ from $\text{C}'\text{-N}$ bond axis            | 242.5                 | 165.5                 | 95.3                  | 112.1                  | 167.8                       | $^{13}\text{C}$ - $^{15}\text{N}$ dipole coupled powder. $\delta$ : converted | [182]     |
| [ $1\text{-}^{13}\text{C}$ ]Gly [ $^{15}\text{N}$ ]Gly HCl                     | $\delta_{11}$ : $-46.6^\circ$ from $\text{C}'\text{-N}$ bond axis            | 243.8                 | 177.2                 | 89.1                  | 110.7                  | 170.0                       | $^{13}\text{C}$ - $^{15}\text{N}$ dipole coupled powder. $\delta$ : converted | [182]     |
| Ac [ $1\text{-}^{13}\text{C}$ ]Gly [ $^{15}\text{N}$ ]GlyNH <sub>2</sub>       | $\delta_{11}$ : $-34.5^\circ$ from $\text{C}'\text{-N}$ bond axis            | 243                   | 184.2                 | 91.2                  | 105.3                  | 172.8                       | $^{13}\text{C}$ - $^{15}\text{N}$ dipole coupled powder. $\delta$ : converted | [182]     |
| [ $1\text{-}^{13}\text{C}$ , 10%]GlyGly HCl<br>H <sub>2</sub> O                | $\delta_{22}$ : $13^\circ$ from $\text{C}=\text{O}$ bond axis                | 242.1                 | 177.1                 | 87.9                  | 109.6                  | 169.7                       | Single crystal  | [180]     |
| [ $1\text{-}^{13}\text{C}$ , 10%]GlyGly HNO <sub>3</sub>                       | $\delta_{22}$ : $5^\circ$ from $\text{C}=\text{O}$ bond axis                 | 248.1                 | 167.8                 | 89.1                  | 119.7                  | 168.3                       | Single crystal  | [180]     |
| [ $1\text{-}^{13}\text{C}$ , 10%]GlyGly  | $\delta_{22}$ : $10^\circ$ from $\text{C}=\text{O}$ bond axis                | 242.3                 | 173.8                 | 88.2                  | 111.3                  | 168.1                       | Single crystal  | [180]     |
| [ $1\text{-}^{13}\text{C}$ , 99%]AlaGly H <sub>2</sub> O                       |  | 245                   | 179                   | 93                    | 109                    | 172.6                       | Polycrystalline; spinning side bands  | [42]      |
| [ $1\text{-}^{13}\text{C}$ , 99%]AlaSer  |  | 249                   | 172                   | 89                    | 118.5                  | 170.1                       | Polycrystalline; spinning side bands  | [42]      |
| [ $1\text{-}^{13}\text{C}$ , 99%]AlaProGly<br>H <sub>2</sub> O                 |  | 235                   | 178                   | 95                    | 98.5                   | 169.3                       | Polycrystalline; spinning side bands  | [42]      |
| [ $1\text{-}^{13}\text{C}$ , 90%]ValGlyGly                                     |  | 245                   | 170                   | 93                    | 113.5                  | 169.2                       | Polycrystalline; spinning side bands  | [114]     |
| BocPro [ $1\text{-}^{13}\text{C}$ , 90%]IleGly                                 |  | 249                   | 183                   | 88                    | 113.5                  | 173.0                       | Polycrystalline; spinning side bands  | [114]     |
| D,L-[ $1\text{-}^{13}\text{C}$ , 90%]LeuGlyGly                                 |  | 246                   | 178                   | 92                    | 111                    | 172.0                       | Polycrystalline; spinning side bands  | [114]     |
| [ $1\text{-}^{13}\text{C}$ , 90%]AspGly  |  | 242                   | 175                   | 93                    | 108                    | 170.3                       | Polycrystalline; spinning side bands  | [114]     |
| N <sup>+</sup> H <sub>3</sub> CH(CH <sub>3</sub> ) COO <sup>−</sup>            | 1. $\delta_{11}$ : $9.4^\circ$ from $\text{C}'\text{-C}\alpha$ bond axis     | 242.9                 | 183.5                 | 106.7                 | 97.8                   | 177.7                       | Single crystal. $\delta$ : converted  | [55]      |
| 1. COO <sup>−</sup><br>2. CH <sub>3</sub> (C <sub><math>\beta</math></sub> )   | 2. $\delta_{33}$ : $4.3^\circ$ from $\text{C}\alpha\text{-C}\beta$ bond axis | 30.3                  | 21.4                  | 8.3                   | 15.5                   | 20.0                        |   |           |

<sup>a</sup>  $\delta_{11} > \delta_{22} > \delta_{33}$ ,  $\delta_{11}$  is most deshielded component and  $\delta_{33}$  the most shielded component.  $\delta$ : Relative to TMS.

<sup>b</sup>  $\Delta\delta = \delta_{33} - (1/2)(\delta_{11} + \delta_{22})$ .

<sup>c</sup>  $\delta$ : Converted from liq. benzene reference to TMS reference [ $\delta$  for liq. benzene: 128.5 ppm relative to TMS].



**Table 5**Conformation-dependent changes in the  $^{13}\text{C}$  principal values of some polypeptides.

| Sample                | Conformation    | Amino-acid residues | Carbons         | $\delta_{11}$ (ppm) | $\delta_{22}$ (ppm) | $\delta_{33}$ (ppm) | $\Delta\delta$ (ppm) | $\delta_{\text{iso}}$ (ppm) | Reference |
|-----------------------|-----------------|---------------------|-----------------|---------------------|---------------------|---------------------|----------------------|-----------------------------|-----------|
| (Gly) $_n$ I          | $\beta$ -Sheet  | Gly                 | C'              | 243                 | 174                 | 88                  | 121                  | 168.3                       | [183]     |
| (Gly) $_n$ II         | $3_1$ -Helix    | Gly                 | C'              | 243                 | 179                 | 94                  | 117                  | 171.8                       | [183]     |
| (Gly) $_n$ I          | $\beta$ -Sheet  | Gly                 | CH <sub>2</sub> | 60                  | 45.0                | 28                  | 25                   | 44.3                        | [184]     |
| (Gly) $_n$ II         | $\alpha$ -Helix | Gly                 | CH <sub>2</sub> | 61                  | 45.7                | 25                  | 28                   | 43.7                        | [184]     |
| (Asp(OBzl), Gly) $_n$ | $\alpha$ -Helix | Gly                 | CH <sub>2</sub> | 65                  | 44.1                | 25                  | 29.6                 | 44.8                        | [184]     |
| (Asp(OBzl), Gly) $_n$ | $\omega$ -Helix | Gly                 | CH <sub>2</sub> | 65                  | 46.5                | 24                  | 31.8                 | 45.1                        | [184]     |
| (Ala, Gly) $_n$       | $\alpha$ -Helix | Gly                 | C'              | 244                 | 178                 | 94                  | 116                  | 176.4                       | [183]     |
| (Leu, Gly) $_n$       | $\alpha$ -Helix | Gly                 | C'              | 242                 | 179                 | 94                  | 117                  | 175.7                       | [183]     |
| (Glu(OBzl), Gly) $_n$ | $\alpha$ -Helix | Gly                 | C'              | 243                 | 178                 | 95                  | 116                  | 172.0                       | [183]     |
| (Asp(OBzl), Gly) $_n$ | $\alpha$ -Helix | Gly                 | C'              | 243                 | 178                 | 95                  | 116                  | 172.0                       | [183]     |
| (Asp(OBzl), Gly) $_n$ | $\omega$ -Helix | Gly                 | C'              | 242                 | 178                 | 93                  | 117                  | 171.1                       | [183]     |
| (Val, Gly) $_n$       | $\beta$ -Sheet  | Gly                 | C'              | 242                 | 171                 | 93                  | 114                  | 168.5                       | [183]     |
| (Ala) $_n$            | $\alpha$ -Helix | Ala                 | C'              | 247.1               | 192.5               | 93.8                | 104.0                | 177.8                       | [186]     |
| (Ala) $_n$            | $\alpha$ -Helix | Ala                 | C $\alpha$      | 72.1                | 54.3                | 31.7                | 29.2                 | 52.7                        | [186]     |
| (Ala) $_n$            | $\alpha$ -Helix | Ala                 | C $\beta$       | 25.3                | 19.5                | 0.6                 | 15.3                 | 15.1                        | [186]     |
| (Ala) $_n$            | $\alpha$ -Helix | Ala                 | C'              | 243                 | 194                 | 99                  | 177                  | 178.7                       | [42]      |
| (Ala) $_n$            | $\beta$ -Sheet  | Ala                 | C'              | 245.4               | 173.2               | 95.3                | 111.2                | 171.3                       | [186]     |
| (Ala) $_n$            | $\beta$ -Sheet  | Ala                 | C $\alpha$      | 59.7                | 54.6                | 31.6                | 16.6                 | 48.6                        | [186]     |
| (Ala) $_n$            | $\beta$ -Sheet  | Ala                 | C $\beta$       | 37.7                | 16.1                | 5.3                 | 27.0                 | 19.7                        | [186]     |
| (Ala) $_n$            | $\alpha$ -Helix | Ala                 | C $\alpha$      | 72.0                | 51.9                | 39.0                | 26.6                 | 53.3                        | [185]     |
| (Ala) $_n$            | $\alpha$ -Helix | Ala                 | C $\beta$       | 23.4                | 18.1                | 2.3                 | 13.2                 | 15.8                        | [185]     |
| (Ala) $_n$            | $\beta$ -Sheet  | Ala                 | C $\alpha$      | 64.6                | 49.7                | 32.4                | 23.6                 | 48.9                        | [185]     |

[179]. Measurements have been made of the magnitudes of the deviation of the bond axis for single crystalline samples of [1- $^{13}\text{C}$ , 10%]GlyGly, [1- $^{13}\text{C}$ , 10%] GlyGly·HNO<sub>3</sub> and [1- $^{13}\text{C}$ , 10%]  $^1\text{Gly}^2\text{-Gly}\cdot\text{HCl}\cdot\text{H}_2\text{O}$  for various hydrogen bond angles in O—H...O=C< type was examined [180]. For the  $^{13}\text{C}'$  principal values of Ala residue in some peptides, see Table 4 [42,114].

Magnitudes of displacements of chemical shifts accompanying conformational changes were examined for Gly  $^{13}\text{C}'$  CSAs of [2- $^{13}\text{C}$ , 8%] (Gly) $_n$ , taking I ( $\beta$ -sheet) and II ( $3_1$ -helix) forms, and the guest [2- $^{13}\text{C}$ , 8%] Gly incorporated into host ( $\beta$ -benzyl L-aspartate) $_n$  or ( $\beta$ -benzyl L-glutamate) $_n$  [127,183,184], and also for Ala C', C $\alpha$  and C $\beta$  CSAs [185]. Magnitudes of displacement upon conformational changes are larger for  $\delta_{22}$  and  $\delta_{33}$ , while  $\delta_{11}$  is almost unchanged (Table 5). Ala  $^{13}\text{C}_\alpha$  and  $^{13}\text{C}_\beta$  CSAs of (Ala) $_n$  with the  $\alpha$ -helix and  $\beta$ -sheet forms indicate that the most deshielded value of  $\delta_{11}$  for Ala C $\alpha$  and C $\beta$  are very sensitive to conformational changes and are responsible for the observed conformation-dependent isotropic chemical shifts [186]. The  $^{13}\text{C}_\alpha$  CSAs of Ala, Val and Leu in a series of various crystalline peptides of known structure have also been determined [187]. The magnitudes and orientations of the principal components of  $^{13}\text{C}_\alpha$  and  $^{13}\text{C}_\beta$  CSAs of a L-alanine single crystal have been reported and these tensors are not axially symmetric but their values are very small [55]. The direction of the most shielded  $\delta_{33}$  axis for C $\beta$  and C $\alpha$  carbons is almost parallel to the C $\alpha$ –C $\beta$  bond within  $\pm 5^\circ$  and is tilted by  $25^\circ$  from the C $\alpha$ –N bond, respectively.

FPT-INDO MO calculations have been performed for Gly and Ala residues having torsion angles of an  $\alpha$ -helix taken from N-acetyl-N'-methyl glycine amide and N-acetyl-N'-methyl L-alanine amide, respectively, both of which are hydrogen bonded to two formamide molecules to reveal the directions of principal components of  $^{13}\text{C}$  CSA tensors [113,114]. More accurate predictions for the directions of  $^{13}\text{C}$  chemical shift tensor components for Ala C $\alpha$  and C $\beta$  from the latter were carried out by the GIAO-CHF method with the 4-31 basis set, as illustrated in Fig. 15 [118]. It was shown that the direction of the most shielded  $\delta_{33}$  axis of Ala C $\beta$  lies almost along the C $\alpha$ –C $\beta$  bond for  $\alpha$ -helix,  $\beta$ -sheet,  $3_1^R$ -helix and the helix near the  $3_1$ -helix with small deviations of  $7.4^\circ$ ,  $11.0^\circ$ ,  $5.8^\circ$  and  $7.4^\circ$ , and also that the  $\delta_{11}$  axis is nearly perpendicular to the plane defined by C $\beta$ , C $\alpha$ , and N atoms in Ala residue and  $\delta_{22}$  is parallel to the plane [118]. These results agree with the experimentally determined direction of  $\delta_{33}$  of the  $^{13}\text{C}_\beta$  CSA of L-alanine [50].

### 3.1.2. $^{15}\text{N}$ CSA

$^{15}\text{N}$  CSA principal components and their orientations for a variety of single crystalline [188–190] and polycrystalline [58,62–65,126,127,181,182,191–204] peptides reported in the literature are summarized in Table 6. It is seen that the orientation of  $\delta_{11}$  lies approximately close to the N–H bond with a deviation of up to  $25^\circ$ ,  $\delta_{33}$  lies approximately along the N–C(=O) bond, and  $\delta_{22}$  is aligned in the direction perpendicular to the peptide plane (see Fig. 9). The orientation of the tensor can be also described by the angle that  $\delta_{11}$  makes with the C'–N bond axis. The  $\delta_{11}$  axis of Ala-[ $^{15}\text{N}$ ]Pro-Gly in a single crystal, deviates  $23^\circ$  from the N–C $\alpha$  bond and lies  $5^\circ$  below the peptide plane, whereas the orientation of  $\delta_{22}$  is  $4^\circ$  away from the peptide plane normal and  $\delta_{33}$  lies approximately in the peptide plane [189]. The  $\delta_{11}$  of Ala-[ $^{15}\text{N}$ ]Gly-Gly is  $11^\circ$  out of the peptide plane defined by accurate heavy atom positions N(Gly-2), C $\alpha$ (Gly-2), and C(=O)(Ala-1), and  $\delta_{22}$  is rotated by  $15^\circ$  away from the peptide plane normal. The most deshielded  $\delta_{11}$  axis of Gly-[ $^{15}\text{N}$ ]Gly-Val is  $1^\circ$  out of the peptide plane and is tilted by  $23^\circ$  from the N–H bond, but the  $\delta_{22}$  and  $\delta_{33}$  axes are substantially rotated about  $\delta_{11}$  such that  $\delta_{22}$  is off from the peptide plane normal by  $36^\circ$ . The possibility of conformation-dependent  $^{15}\text{N}$  CSA principal values for  $\alpha$ -helix,  $3_1$ -helix and  $\beta$ -sheet structures has been examined for (Ala) $_n$ , (Gly) $_n$  and Ala- or Gly-residues involved in polypeptides (Table 7). It appears that the values of  $\delta_{22}$  of Ala residues, and  $\delta_{11}$  of Gly residues are sensitive parameters for distinguishing between  $\alpha$ -helix and  $\beta$ -sheet conformations, but the rest of the components including  $\Delta\delta$  are insensitive. In contrast, only the  $\delta_{11}$  values are sensitive differences between  $\alpha$ -helix and  $\beta$ -sheet conformations. It is not easy, however, to distinguish the  $3_1$ -helix from the  $\alpha$ -helix and  $\beta$ -sheet conformations by using  $^{15}\text{N}$  CSA information.

The orientations of principal axes for  $^{15}\text{N}$  CSA of Boc-GlyGly-[ $^{15}\text{N}$ ,  $^2\text{H}$ ]Gly benzyl ester in triclinic and monoclinic crystalline phases have been determined from the measured  $^{15}\text{N}$ – $^2\text{H}$  dipolar coupling [191]. Roberts et al. have determined  $^{15}\text{N}$  CSA tensor values and N–H bond lengths for a few peptides and amino acids using MAS dipolar/chemical shift experiments as given in Table 6, and found that N–H distances measured from NMR experiments are uniformly  $\sim 0.035 \text{ \AA}$  longer than those determined from neutron diffraction studies [192]. The principal values of the amide  $^{15}\text{N}$  CSA for [ $^{15}\text{N}$ ]labeled Gly in BocGly, BocGlyAla, Boc GlyPhe, BocGlyAib and BocGlyProOBzl have been examined in relation to >N–H...O=C< hydrogen bonding [193]. The principal axes of the  $^{15}\text{N}$  CSA for the amide nitrogen were obtained by FPT calcu-

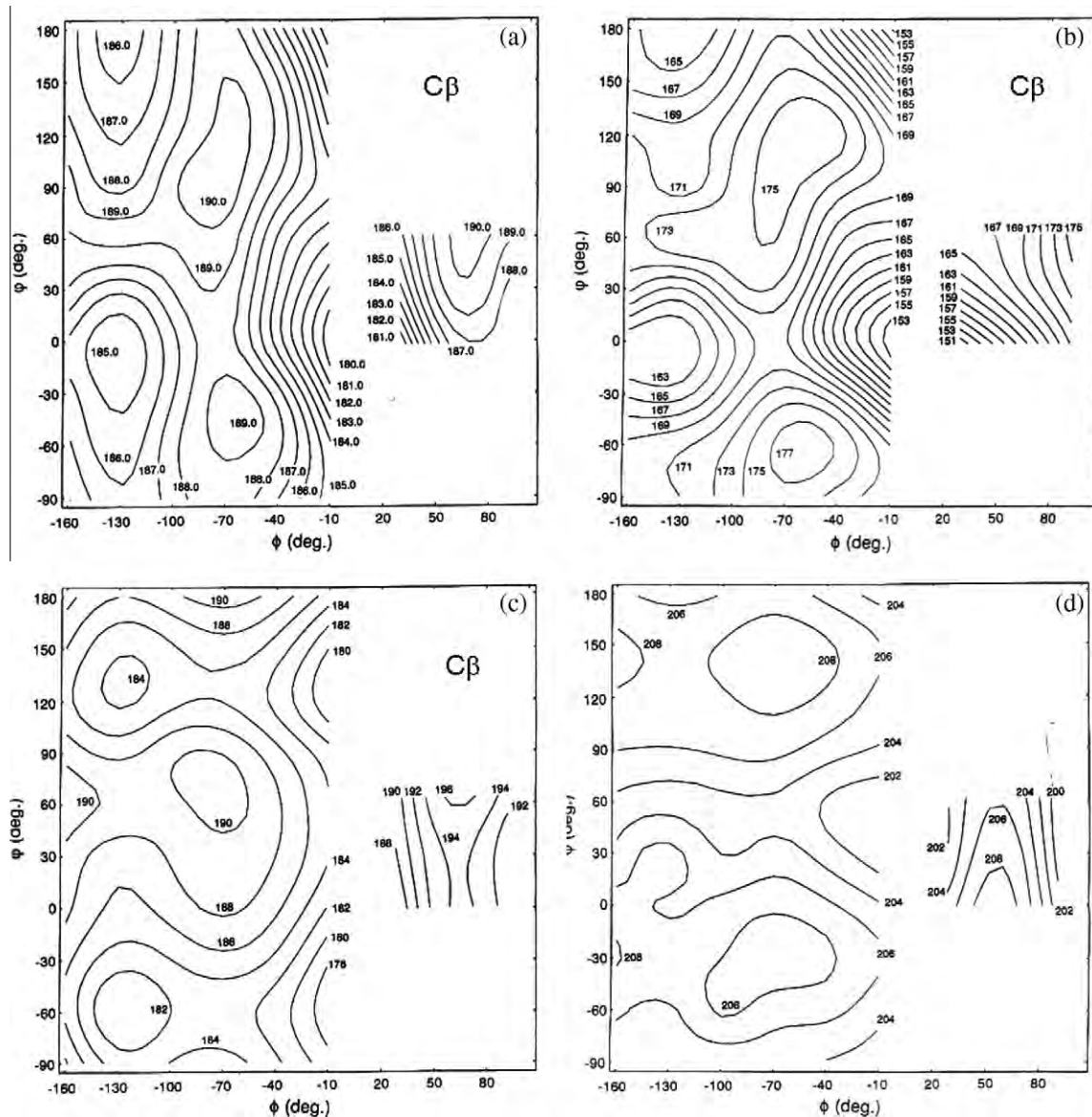


**Fig. 15.** The calculated  $^{13}\text{C}$  chemical shift map of the  $\text{C}_\beta$  and  $\text{C}_\alpha$  carbons of *N*-acetyl-*N'*-methyl-L-alanine amide calculated by using the GIAO-CHF method with a 4-31G *ab initio* basis sets. The 4-31G optimized geometries for the peptide were employed. (a)  $\sigma_{\text{iso}}$ , (b)  $\sigma_{11}$ , (c)  $\sigma_{22}$ , and (d)  $\sigma_{33}$  for the  $\text{C}_\beta$  carbon (in ppm), and (e)  $\sigma_{\text{iso}}$ , (f)  $\sigma_{11}$ , (g)  $\sigma_{22}$ , and (h)  $\sigma_{33}$  for the  $\text{C}_\alpha$  carbon (in ppm). A positive  $\sigma$  means shielding. Reproduced with permission from Asakawa et al. [118]. Copyright 1994 Elsevier.

lations on *N*-acetyl-*N'*-methylglycine hydrogen-bonded to a formamide molecule. The  $\delta_{22}$  axis lies approximately along the N–C(=O) bond and  $\delta_{33}$  is aligned in the direction perpendicular to the peptide plane, which is opposite to the previous assignment [138] but close to the reported experimental data [188]. Indeed, the  $\delta_{22}$  and  $\delta_{33}$  axes can be substantially rotated about the  $\delta_{11}$  axis.

It was also shown that  $\delta_{33}$  in Ala-[ $^{15}\text{N}$ ]Leu is tilted by  $17^\circ$  away from the N–H bond, and any deviation of the direction of  $\delta_{33}$  from the peptide plane would result in an equivalent rotation of the other two principal components of CSA about the N–H bond axis, and that  $\delta_{11}$  is tilted by about  $20^\circ$  from the peptide plane [194].  $^{15}\text{N}$  CSAs of a synthetic peptide c(Gly-D-Pro-Gly-Ala-D-Pro), labeled with  $^{15}\text{N}$  at both the Gly-1 and Ala-4 amide sites were examined using the 2D PISEMAT technique [62]. These experiments revealed that isotropic  $^{15}\text{N}$  resonances of both the Gly-1 and Ala-4 residues are well-resolved in one frequency dimension of the 2D spectrum while the full CSA powder patterns can be directly measured in the other dimension.

The relative orientation of a  $^{15}\text{N}$  CSA tensor and the N–H bond vector can be obtained by the 1D MADMAT technique from heteronuclear dipolar-coupled powder patterns [63]. This method was demonstrated on a  $^{15}\text{N}$  labeled polycrystalline *N*-acetylvaline (NAV) sample, and the simulation of the dipolar-shift powder pattern giving the  $^{15}\text{N}$  CSA tensor parameters of  $\delta_{11} = 235.1 \pm 1$  ppm,  $\delta_{22} = 78.3 \pm 0.5$  ppm, and  $\delta_{33} = 56.9 \pm 0.5$  ppm, and the angle between the N–H bond and the least shield axis =  $19 \pm 2^\circ$ , assuming an N–H bond length of 1.07 Å. This method has also been applied to  $^{15}\text{N}$  labeled *N*-acetyl glycine (NAG), in both unoriented and oriented [ $^{15}\text{N}$ -Gly] collagen samples, and in [ $^{15}\text{N}$ -Gly-18] [58] and [ $^{15}\text{N}$ -Phe-16] [195] magainin 2 samples. These studies demonstrated that the  $\delta_{33}$  axis is tilted away from the peptide plane ( $\alpha = 25\text{--}45^\circ$ ). This simple 1D method was applied under MAS conditions, and the dipolar-shift sidebands were analyzed to yield the orientation of the  $^{15}\text{N}$  CSA tensors [64]. A  $^{15}\text{N}$ -labeled NAV polycrystalline sample was studied under various MAS speeds ranging from 0.5 to 2.5 kHz. It was found that the errors in determining the  $\alpha$  angle increased with the spinning speed, which could be attrib-

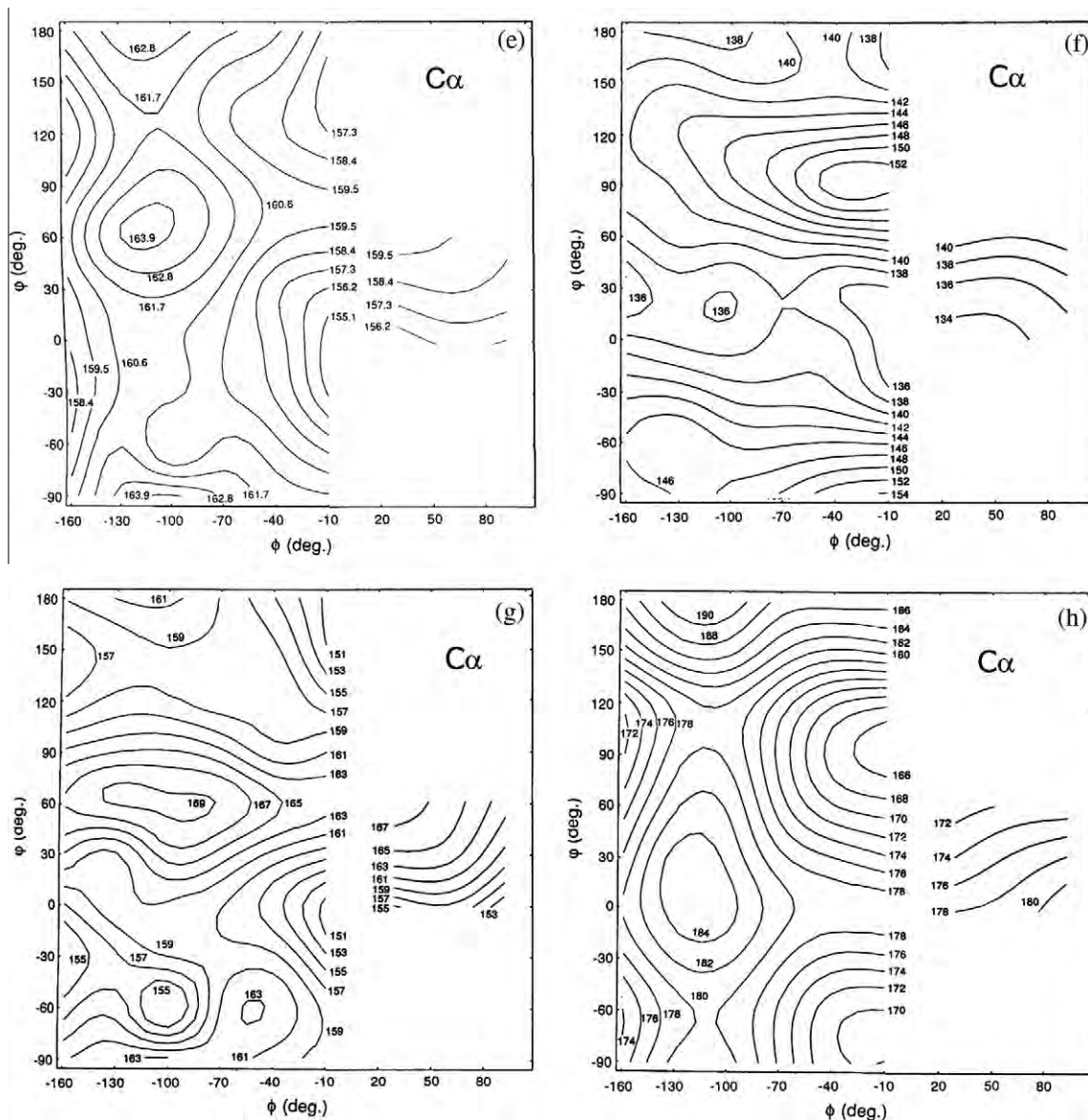


Fig. 15 (continued)

uted to the smaller number of sidebands present at a higher spinning speed, while the measured  $\beta$  angle was essentially unchanged at different spinning speeds (Table 6), where  $\alpha$  and  $\beta$  are defined to be the angle between  $\delta_{11}$  and the projection of the N–H bond on the  $\delta_{11}$ – $\delta_{22}$  plane, and the angle between the  $\delta_{33}$  axis and the N–H bond.

$^{15}\text{N}$  CSA tensors have been determined for the amide fragment of (Z)-acetanilide and (E)-N-methylacetanilide, revealing striking variations due to the difference in the orientation of the N-phenyl substituent with respect to the amide plane [196]. Recently, the amide- $^{15}\text{N}$  CSA tensor of GlyGly was determined by spectral simulation of the observed  $^{15}\text{N}$  chemical shift and  $^{15}\text{N}$ – $^1\text{H}$  dipolar-chemical shift powder patterns, and its backbone dynamics was examined by analyzing the  $^{15}\text{N}$  line shapes and  $^{13}\text{C}$  relaxation rates [197]. An analytical approach to determine the orientation of the  $\delta_{11}$  component of the amide- $^{15}\text{N}$  CSA tensor with respect to the  $^{13}\text{C}$ – $^{15}\text{N}$  bond in the backbone by observing the dipolar-coupled  $^{15}\text{N}$  chemical shift powder patterns was suggested [198]. The amide- $^{15}\text{N}$  tensors of all 15 residues in gramicidin A have been determined from aligned lipid bilayer samples

[199] and used as orientational constraints to evaluate different models for the channel conformation of gramicidin A. Recently, the changes in amide  $^{15}\text{N}$  CSA of gramicidin A induced by cation binding were studied using aligned DMPC bilayers [200]. Upon cation binding, the  $\delta_{11}$  component of Trp-13 changed significantly, up to 6 ppm. It was demonstrated that the changes in chemical shift observables were primarily due to through-bond polarization by cations, while no significant change in dynamics was observed.

A new method employing the REDOR technique to obtain the orientation of a  $^{15}\text{N}$  chemical shift tensor relative to a  $^{15}\text{N}$ – $^{13}\text{C}$  bond has been proposed [201]. Using this method on a doubly  $^{15}\text{N}$  and  $^{13}\text{C}$  labeled polycrystalline acetanilide sample, the orientation of the  $^{15}\text{N}$  CSA tensors in the molecular frame with respect to the  $^{15}\text{N}$ – $^{13}\text{C}$  and  $^{15}\text{N}$ – $^1\text{H}$  bond vectors was obtained from a  $^{15}\text{N}$ – $^{13}\text{C}$  REDOR and  $^{15}\text{N}$ – $^1\text{H}$  dipolar-shift MAS experiments, respectively (see Table 6).

To resolve CSA line shapes of  $^{15}\text{N}$  in peptides labeled at multiple sites, multidimensional solid-state NMR experiments are highly desirable. A 2D MADMAT method was applied to polycrystalline



**Table 6**The amide  $^{15}\text{N}$  chemical shift tensors of peptides and proteins in the solid state.

| Peptides   | Angle between $\delta_{ii}$ and X–Y bond axis   | $\delta_{11}^a$ (ppm) | $\delta_{22}^a$ (ppm) | $\delta_{33}^a$ (ppm) | $\Delta\delta^b$ (ppm) | $\delta_{iso}$ (ppm) | Remarks  | Reference |
|--|---|-----------------------|-----------------------|-----------------------|------------------------|----------------------|--|-----------|
| Ac[ $^{1-13}\text{C}$ ]Ala [ $^{15}\text{N}$ ]AlaNH $_2$                         | $\delta_{11}$ : 100° from C'–N bond axis  | 229.4                 | 85.1                  | 44.6                  | 164.6                  | 119.7                | $^{15}\text{N}$ -dipole coupled powder                                     | [190]     |
| Ac[ $^{1-13}\text{C}$ ]Ala [ $^{15}\text{N}$ ]TyrNH $_2$                         | $\delta_{11}$ : 98° from C'–N bond axis   | 209.3                 | 77.1                  | 52.1                  | 144.7                  | 112.8                | $^{15}\text{N}$ -dipole coupled powder                                     | [190]     |
| [ $^{1-13}\text{C}$ ]Gly [ $^{15}\text{N}$ ]GlyHCl                               | $\delta_{11}$ : 20° from N–H bond axis  | 210.0                 | 59.8                  | 57.3                  | 151.5                  | 108.9                | $^{15}\text{N}$ -dipole coupled powder                                     | [190]     |
| Gly [ $^{15}\text{N}$ ]Gly   | $\delta_{11}$ : 21° from N–H bond axis  | 222.9                 | 79.7                  | 46.8                  | 159.6                  | 116.5                | Dipolar/CS   | [199]     |
| Gly [ $^{15}\text{N}$ ]GlyH $_2$ O   | $\delta_{11}$ : 25° from N–H bond axis  | 223.7                 | 78.9                  | 48.4                  | 160.0                  | 117.0                | 2D dipolar/CS  | [140]     |
| Gly [ $^{15}\text{N}$ ]GlyHClH $_2$ O  |   | 210.2                 | 64.8                  | 59.2                  | 148.2                  | 111.4                | 2D dipolar/CS  | [140]     |
| [ $^{1-13}\text{C}$ ]Gly [ $^{15}\text{N}$ ]GlyNH $_2$                           | $\delta_{11}$ : 100° from C'–N bond axis  | 210.6                 | 64.2                  | 40.7                  | 158.2                  | 105.2                | $^{15}\text{N}$ -dipole coupled powder                                     | [190]     |
| [ $^{1-13}\text{C}$ ]Gly [ $^{15}\text{N}$ ]GlyHCl H $_2$ O                      | $\delta_{11}$ : 21.3° from N–H bond axis  | 215.9<br>(188.6)      | 70.9<br>(43.6)        | 60.3<br>(33.0)        | 150.3                  | 115.7<br>(88.4)      | Single crystal. $\delta$ : converted                                       | [188]     |
| [ $^{13}\text{C}$ ]Ala [ $^{15}\text{N}$ ]Ala                                    | $\delta_{11}$ : 106° away from C'–N bond axis   | 215.5                 | 78.1                  | 65.3                  | 143.8                  | 119.6                | $^{15}\text{N}$ -dipole coupled powder.                                    | [182]     |
| Ac [ $^{13}\text{C}$ ]Gly [ $^{15}\text{N}$ ]AlaNH $_2$                          | $\delta_{11}$ : 100° away from C'–N bond axis   | 229.4                 | 85.1                  | 44.6                  | 164.6                  | 119.7                | $^{15}\text{N}$ -dipole coupled powder.                                    | [182]     |
| [ $^{13}\text{C}$ ]Gly [ $^{15}\text{N}$ ]GlyHCl                                 | $\delta_{11}$ : 99° away from C'–N bond axis  | 210.0                 | 59.8                  | 57.3                  | 151.5                  | 109.0                | $^{15}\text{N}$ -dipole coupled powder.                                    | [182]     |
| Ac [ $^{13}\text{C}$ ]Gly [ $^{15}\text{N}$ ]GlyNH $_2$                          | $\delta_{11}$ : 100° away from C'–N bond axis   | 210.6                 | 64.2                  | 40.7                  | 158.2                  | 105.2                | $^{15}\text{N}$ -dipole coupled powder                                     | [182]     |
| Ac [ $^{13}\text{C}$ ]Gly [ $^{15}\text{N}$ ]TyrNH $_2$                          | $\delta_{11}$ : 98° away from C'–N bond axis  | 209.3                 | 77.1                  | 52.1                  | 144.7                  | 112.8                | $^{15}\text{N}$ -dipole coupled powder.                                    | [182]     |
| BocGlyGly [ $^{15}\text{N}$ , $^2\text{H}$ ]GlyOBzl                              | 1. $\delta_{11}$ : 22° from N–H bond axis   | 227.2<br>(157.2)      | 66.3<br>(318.1)       | 59.3<br>(325.1)       | 164.4                  | 117.6                | Proton decoupled $^{15}\text{N}$ NMR. $\delta$ : converted                 | [191]     |
| 1. monoclinic form   |   |                       |                       |                       |                        |                      |  |           |
| 2. triclinic form  | 2. $\delta_{11}$ : 24° from N–H bond axis   | 224.6<br>(159.8)      | 87.6<br>(296.8)       | 40.6<br>(343.8)       | 160.5                  | 117.6                |  |           |
| Ala [ $^{15}\text{N}$ ]Leu   | $\delta_{11}$ : 17° from N–H bond axis  | 217                   | 77                    | 64                    | 83                     | 119.3                | $^{15}\text{N}$ -dipole coupled powder.                                    | [194]     |
| N-acetyl [ $^{15}\text{N}$ ]glycine  | $\delta_{11}$ : 25.5° or 154.5° from the N–H bond axis  | 220.4                 | 82.8                  | 37.0                  | 160.5                  | 113.4                | $^1\text{H}$ - $^{15}\text{N}$ dipolar $^{15}\text{N}$ chemical shift NMR  | [58]      |
| [ $^{15}\text{N}$ ] collagen powder  | $\delta_{11}$ : 24.5° or 155.5° from the N–H bond axis  | 223.4                 | 67.0                  | 42.3                  | 168.8                  | 110.9                | $^1\text{H}$ - $^{15}\text{N}$ dipolar $^{15}\text{N}$ chemical shift NMR  | [58]      |
| [ $^{15}\text{N}$ -Gly-18]magainin 2   | Angle $\beta$ : 22° $\pm$ 1°; $\alpha$ : 30° $\pm$ 19°  | 218.0                 | 75.4                  | 45.0                  | 157.8                  | 112.8                | $^1\text{H}$ - $^{15}\text{N}$ dipolar $^{15}\text{N}$ 7chemical shift NMR | [58]      |
| [ $^{15}\text{N}$ -Phe-16]magainin 2   | Angle $\beta$ : 22° $\pm$ 3°; $\alpha$ : 45° $\pm$ 15°  | 220                   | 80                    | 55                    | 148.9                  | 118                  | $^1\text{H}$ - $^{15}\text{N}$ dipolar $^{15}\text{N}$ chemical shift NMR  | [58]      |
| [ $^{15}\text{N}$ ] collagen oriented  | $\delta_{11}$ : 24.5° from the N–H bond axis  | 223.4                 | 67.0                  | 42.3                  | 168.8                  | 110.9                | $^1\text{H}$ - $^{15}\text{N}$ dipolar $^{15}\text{N}$ chemical shift NMR  | [58]      |
| [ $^{1-13}\text{C}$ ]glycyl [ $^{15}\text{N}$ ]alanyl $_3$ -gramicidin A         | $\delta_{11}$ : 104° from C'–N bond axis  | 228.8<br>(206)        | 85.4<br>(63)          | 59.4<br>(37)          | 156                    | 124.5                | $^{15}\text{N}$ chemical shift powder pattern. $\delta$ : Converted        | [198]     |
| [ $^{1-13}\text{C}$ ]alanyl $_3$ -d-[ $^{15}\text{N}$ ]leucyl $_4$ -gramicidin A | $\delta_{11}$ : 105° from C'–N bond axis  | 223.4<br>(201)        | 86.4<br>(64)          | 55.4<br>(33)          | 152.5                  | 121.7                | $^{15}\text{N}$ chemical shift powder pattern. $\delta$ : converted        | [198]     |
| [ $^{15}\text{N}$ ]Gly-d-Pro-Gly-[ $^{15}\text{N}$ ]Gly-1                        | Angle $\beta$ : 25°; angle $\alpha$ : 0°; angle $\beta$ : 18°; angle $\alpha$ : 0°  | 207                   | 77.3                  | 57                    | 139.8                  | 113.8                | 3D solid state NMR, $^1\text{H}$ homonuclear spin exchange                 | [62]      |
| Ala-d-Pro Ala-4  |   | 220                   | 80                    | 73                    | 143.5                  | 124.3                |  |           |
| GlyPro-d-Leu- [ $^{15}\text{N}$ ]Gly   | $\delta_{33}$ : parallel to C'–N bond axis  | 205.3                 | 39.7                  | 54.3                  | 158.3                  | 99.8                 | Dipolar coupled $^{15}\text{N}$ powder pattern                             | [140]     |
| Gly-[ $^{15}\text{N}$ ]Gly   | $\delta_{33}$ : parallel to C'–N bond axis  | 204.7                 | 56.5                  | 26.1                  | 163.4                  | 95.9                 | Dipolar coupled $^{15}\text{N}$ powder pattern                             | [140]     |
| Val-[ $^{15}\text{N}$ ]GlyGly  | $\delta_{33}$ : parallel to C'–N bond axis  | 199.6                 | 62.5                  | 19.9                  | 158.4                  | 94.0                 | Dipolar coupled $^{15}\text{N}$ powder pattern                             | [140]     |
| ValGly-[ $^{15}\text{N}$ ]Gly  | $\delta_{33}$ : parallel to C'–N bond axis  | 203.3                 | 54.9                  | 18.7                  | 166.5                  | 92.3                 | Dipolar coupled $^{15}\text{N}$ powder pattern                             | [140]     |
| Tyr-[ $^{15}\text{N}$ ]GlyGlyPheLeu  | $\delta_{33}$ : parallel to C'–N bond axis  | 194.2                 | 46.0                  | 10.0                  | 166.2                  | 83.4                 | Dipolar coupled $^{15}\text{N}$ powder pattern                             | [140]     |
| AcPro-[ $^{15}\text{N}$ ]GlyPhe  | $\delta_{33}$ : parallel to C'–N bond axis  | 190.7                 | 33.9                  | 20.5                  | 163.5                  | 81.7                 | Dipolar coupled $^{15}\text{N}$ powder pattern                             | [140]     |
| Ala-[ $^{15}\text{N}$ ]ProGly  | $\delta_{11}$ : 23° from C'–N bond axis   | 231                   | 127                   | 38                    | 148.5                  | 132                  | Single crystal. $^{15}\text{N}$ NMR  | [189]     |
| Ala-[ $^{15}\text{N}$ ]GlyGly  | $\delta_{11}$ : 11° out of peptide plane and $\delta_{22}$ : rotated by 15° from peptide plane normal. N–H bond vector deviates 12° from peptide plane. | 207                   | 59                    | 48                    | 153.5                  | 105                  | Single crystal. $^{15}\text{N}$ NMR  | [189]     |
| Gly-[ $^{15}\text{N}$ ]GlyVal  | $\delta_{11}$ : 23° from N–H bond axis  | 218                   | 63                    | 53                    | 160                    | 111                  | Single crystal. $^{15}\text{N}$ NMR  | [189]     |
| N-AcVal Leu  |   |                       |                       |                       |                        |                      | 2D magic angle decoupling and MAT  | [202]     |
| Val  | Angle $\beta$ : 20° $\pm$ 2°; $\alpha$ : 34° $\pm$ 12°  | 230.1                 | 87.1                  | 60.2                  | 156.0                  | 125.7                |  |           |
| Leu  | Angle $\beta$ : 18° $\pm$ 2°; $\alpha$ : 36° $\pm$ 11°  | 232.8                 | 93.7                  | 58.7                  | 156.5                  | 128.4                |  |           |
| [ $^{15}\text{N}$ -Leu-19]paradoxin  | Angle $\beta$ : 20° $\pm$ 3°; $\alpha$ : 30° $\pm$ 15°  | 224.4                 | 76.9                  | 52.3                  | 159.8                  | 117.4                | 2D magic angle decoupling and MAT  | [202]     |
| [ $^{15}\text{N}$ -Leu-19]SA peptide   | Angle $\beta$ : 20° $\pm$ 3°; $\alpha$ : 30° $\pm$ 15°  | 221.4                 | 76.9                  | 51.0                  | 156.0                  | 117.0                | 2D magic angle decoupling and MAT  | [202]     |

<sup>a</sup>  $\delta_{11} > \delta_{22} > \delta_{33}$ ,  $\delta_{11}$  is most deshielded component and  $\delta_{33}$  the most shielded component.  $\delta$ : Relative to liquid NH $_3$ .<sup>b</sup>  $\Delta\delta = \delta_{33} - (1/2)(\delta_{11} + \delta_{22})$ .



**Table 7**Conformation-dependent changes of  $^{15}\text{N}$  CSA for some polypeptides.

| Sample                             | Conformation      | $\delta_{11}$ (ppm) | $\delta_{22}$ (ppm) | $\delta_{33}$ (ppm) | $\Delta\delta$ (ppm) | $\delta_{\text{iso}}$ (ppm) | Remarks                    | Reference |
|------------------------------------|-------------------|---------------------|---------------------|---------------------|----------------------|-----------------------------|----------------------------|-----------|
| (Ala) $_n$                         | $\alpha$ -Helix   | 225                 | 75.5                | 50                  | 158                  | 119.9                       | Static, $^{15}\text{N}$ CP | [126]     |
| (Ala) $_5$                         | $\beta$ -Sheet    | 222                 | 82.8                | 65                  | 148                  | 123.3                       | Static, $^{15}\text{N}$ CP | [126]     |
| (Ala, $_{\text{Leu}}$ ) $_n$       | $\alpha$ -Helix   | 225                 | 78.                 | 56                  | 158                  | 119.7                       | Static, $^{15}\text{N}$ CP | [126]     |
| (Ala, $_{\text{Asp(OBzl)}}$ ) $_n$ | $\alpha$ -Helix   | 229                 | 79.8                | 59                  | 160                  | 122.6                       | Static, $^{15}\text{N}$ CP | [126]     |
| (Ala, $_{\text{Glu(OBzl)}}$ ) $_n$ | $\alpha$ -Helix   | 227                 | 77.8                | 60                  | 158                  | 121.5                       | Static, $^{15}\text{N}$ CP | [126]     |
| (Ala, $_{\text{Glu(OMe)}}$ ) $_n$  | $\alpha$ -Helix   | 226                 | 79.2                | 58                  | 157                  | 121.0                       | Static, $^{15}\text{N}$ CP | [126]     |
| (Ala, $_{\text{Val}}$ ) $_n$       | $\alpha$ -Helix   | 222                 | 74.2                | 63                  | 154                  | 119.7                       | Static, $^{15}\text{N}$ CP | [127]     |
| (Ala, $_{\text{Val}}$ ) $_n$       | $\beta$ -Sheet    | 223                 | 83.5                | 56                  | 153                  | 120.8                       | Static, $^{15}\text{N}$ CP | [126]     |
| (Ala, $_{\text{Ile}}$ ) $_n$       | $\beta$ -Sheet    | 221                 | 84.1                | 61                  | 149                  | 122.1                       | Static, $^{15}\text{N}$ CP | [126]     |
| (Ala, $_{\text{D-Ala}}$ ) $_n$     | $\alpha_L$ -Helix | 219                 | 76.2                | 57                  | 153                  | 117.6                       | Static, $^{15}\text{N}$ CP | [127]     |
| (Ala, $_{\text{Gly}}$ ) $_n$       | $\alpha$ -Helix   | 223                 | 78.5                | 57                  | 155                  | 119.7                       | Static, $^{15}\text{N}$ CP | [127]     |
| (Ala, $_{\text{Gly}}$ ) $_n$       | $\beta$ -Sheet    | 221                 | 80.7                | 58                  | 152                  | 119.9                       | Static, $^{15}\text{N}$ CP | [127]     |
| (Ala, $_{\text{Sar}}$ ) $_n$       |                   | 219                 | 83.3                | 58                  | 148                  | 120.1                       | Static, $^{15}\text{N}$ CP | [127]     |
| (Gly) $_n$                         | $\beta$ -Sheet    | 206                 | 61.4                | 46                  | 152                  | 104.2                       | Static, $^{15}\text{N}$ CP | [48]      |
| (Gly) $_n$                         | $3_1$ -Helix      | 215                 | 62.8                | 50                  | 158                  | 109.2                       | Static, $^{15}\text{N}$ CP | [48]      |
| (Gly, $_{\text{Ala}}$ ) $_n$       | $\alpha$ -Helix   | 213                 | 57.6                | 45                  | 162                  | 104.9                       | Static, $^{15}\text{N}$ CP | [48]      |
| (Gly, $_{\text{Leu}}$ ) $_n$       | $\alpha$ -Helix   | 211                 | 61.7                | 46                  | 157                  | 106.0                       | Static, $^{15}\text{N}$ CP | [48]      |
| (Gly, $_{\text{Glu(OBzl)}}$ ) $_n$ | $\alpha$ -Helix   | 211                 | 61.2                | 48                  | 156                  | 106.5                       | Static, $^{15}\text{N}$ CP | [48]      |
| (Gly, $_{\text{Lys(Z)}}$ ) $_n$    | $\alpha$ -Helix   | 209                 | 69.2                | 41                  | 154                  | 106.1                       | Static, $^{15}\text{N}$ CP | [48]      |
| (Gly, $_{\text{Leu}}$ ) $_n$       | $\beta$ -Sheet    | 207                 | 66.2                | 41                  | 153                  | 104.4                       | Static, $^{15}\text{N}$ CP | [48]      |
| (Gly, $_{\text{Val}}$ ) $_n$       | $\beta$ -Sheet    | 204                 | 74.6                | 40                  | 147                  | 105.8                       | Static, $^{15}\text{N}$ CP | [48]      |
| (Gly, $_{\text{Ile}}$ ) $_n$       | $\beta$ -Sheet    | 210                 | 68.3                | 46                  | 153                  | 108.5                       | Static, $^{15}\text{N}$ CP | [48]      |
| (Gly, $_{\text{Asp(OBzl)}}$ ) $_n$ | $\beta$ -Sheet    | 209                 | 71.5                | 40                  | 153                  | 106.7                       | Static, $^{15}\text{N}$ CP | [48]      |
| (Gly, $_{\text{Sar}}$ ) $_n$       |                   | 205                 | 65.8                | 39                  | 152                  | 103.1                       | Static, $^{15}\text{N}$ CP | [48]      |
| (Asp(OBzl)) $_n$                   | $\alpha_R$ -Helix | 205                 | 52.8                | 39                  | 159.1                | 98.9                        | Static, $^{15}\text{N}$ CP | [128]     |
|                                    | $\alpha_L$ -Helix | 201                 | 48.3                | 41                  | 156.4                | 96.8                        | Static, $^{15}\text{N}$ CP | [128]     |
|                                    | $\omega_L$ -Helix | 202                 | 47.4                | 40                  | 158.3                | 96.3                        | Static, $^{15}\text{N}$ CP | [128]     |
|                                    | $\beta$ -Sheet    | 203                 | 56.4                | 41                  | 154.3                | 100                         | Static, $^{15}\text{N}$ CP | [128]     |

*N*-acetylvaline (NAV) and *N*-acetylvalylleucine (NAVL) samples [202] to obtain a correlation of the  $^{15}\text{N}$  CSA with the isotropic chemical shift (Fig. 16). Another 2D method that correlates isotropic chemical shifts by fast MAS and amplified spinning sidebands by rotor synchronized  $\pi$  pulses has been developed [203]. This experiment has a high sensitivity due to the fast spinning, while the rotor-synchronized  $\pi$  pulses effectively reduce the effect of the spinning speed in the indirect dimension.

It is interesting to examine a possible conformation-dependent anisotropic  $^{15}\text{N}$  chemical shift of Ala- or Gly-residues involved in

either the  $\alpha$ -helix or  $\beta$ -sheet conformation of polypeptides as summarized in Table 7 [48,125,126]. It is noteworthy that the values of  $\delta_{22}$  of the  $^{15}\text{N}$  nuclei in  $\beta$ -sheets are more displaced downfield as compared with those in an  $\alpha$ -helix: they are 80–85 ppm ( $\beta$ -sheet) and 74–80 ppm ( $\alpha$ -helix) for Ala residues.  $^{15}\text{N}$  isotropic ( $\delta_{\text{iso}}$ ) and  $^{15}\text{N}$  CSA tensor components of  $^{15}\text{N}$ -labeled PBLA taking the  $\alpha_R$ -helix,  $\alpha_L$ -helix,  $\omega_L$ -helix and antiparallel  $\beta$ -sheet conformations in the solid-state have been reported. It was shown that  $\delta_{22}$  values are significantly changed depending on the conformation of the peptide [128].

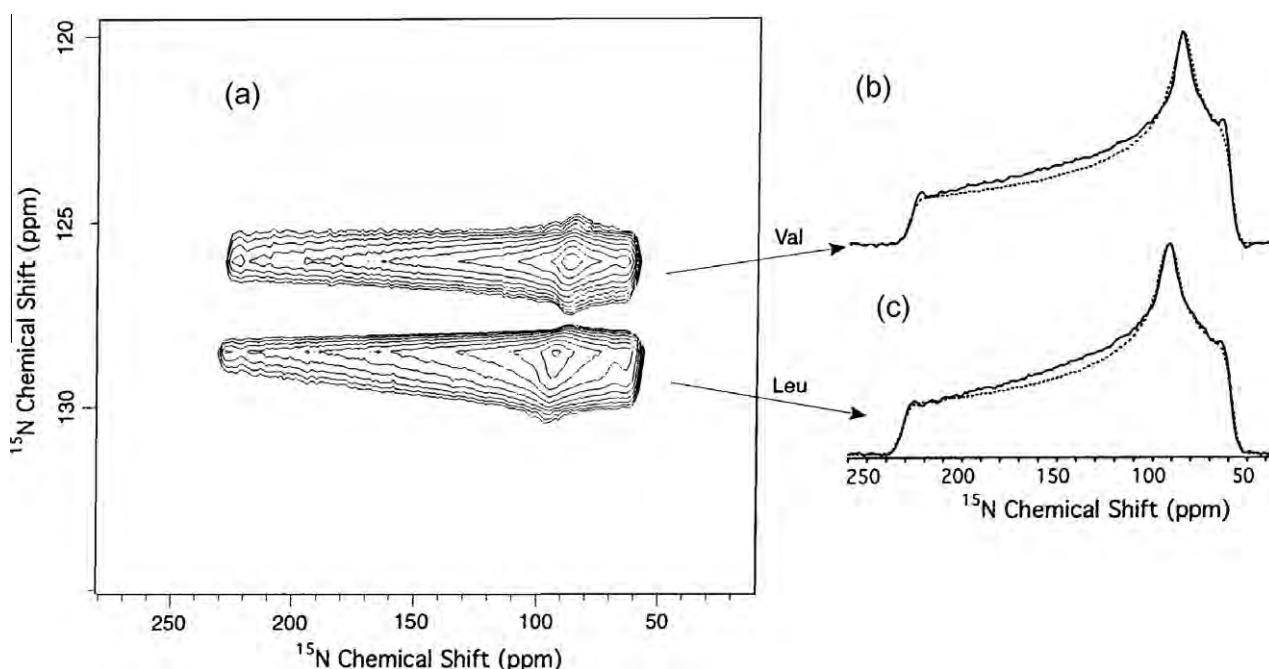


**Fig. 16.** (a) Correlation of  $^{15}\text{N}$  CSA and isotropic shifts of polycrystalline NAVL recorded by the 2D MADMAT method at 40.59 MHz. (b) and (c)  $^{15}\text{N}$  CSA powder patterns obtained from slices of the triple-echo MAT 2D spectrum at 9.4 T. Reproduced with permission from Lee et al. [202].

Amide- $^{15}\text{N}$  CSA tensors for several dipeptides, as well as for a series of model Ala-X and X-Ala sequences in both  $\alpha$ -helical and  $\beta$ -sheet conformations (where X is one of the naturally occurring amino acids) have been investigated by quantum chemical calculations [204]. The tensor of a  $^{15}\text{N}$  shifts in a given peptide residue is unaffected by residues other than those adjacent to it, which implies that the amide- $^{15}\text{N}$  CSA tensor should be considered in the context of tripeptide sequences. DFT-IGLO calculations have been performed for shielding tensors of a glycyl-glycine dipeptide [205]. The  $\delta_{11}$  component of the amide- $^{15}\text{N}$  CSA tensor is always tilted ( $18$ – $22^\circ$ ) from the N–H bond for a variety of selected conformations considered.

### 3.1.3. $^{17}\text{O}$ CSA

It is not easy to record the full  $^{17}\text{O}$  NMR spectrum of a solid, because of the widely spread signals produced by large quadrupolar interactions (spin quantum number 5/2), and its low natural abundance (0.037%), even if spectral regions arising from the central ( $1/2 \leftrightarrow -1/2$ ) transition alone are observed. Nevertheless, several attempts to record solid-state  $^{17}\text{O}$  NMR have been made with an emphasis on attempts to elucidate the hydrogen-bonded structure of peptides and polypeptides [206–218].  $^{17}\text{O}$  enrichment [206–211,216,217] together with higher-frequency solid-state NMR techniques are necessary to overcome the detection problems [219]. Indeed, acquisition of solid-state NMR spectra of quadrupolar nuclei at very high magnetic fields (25 and 40 T) has been shown to improve the spectral sensitivity and resolution substantially. Excellent review articles on this subject are available [33,213].

**3.1.3.1. CSAs and quadrupolar interaction.** To unambiguously determine eight NMR parameters in Eq. (23) from spectra with large CSA and quadrupolar interactions, it is essential to record  $^{17}\text{O}$  spectra for at least two different resonance frequencies. For instance, quite different spectral features are available from the static  $^{17}\text{O}$  cross-polarization spectra of [ $^{17}\text{O}$ ](Ala) $_n$  (Fig. 17) and [ $^{17}\text{O}$ ](Gly) $_n$ , taking the  $\alpha$ -helix,  $\beta$ -sheet or  $3_1$ -helix conformations recorded at 36.6 and 67.8 MHz [206,209,210]. The eight parameters were obtained by applying a curve-fitting procedure to the experimental spectra, and the results are summarized in Table 8. Static  $^{17}\text{O}$  NMR spectra of the central Gly residues in two single crystalline  $^{17}\text{O}$  labeled Gly $^*$ GlyVal (GGV) and Ala $^*$ GlyGly (AGG) were measured, where  $^*$ Gly indicates  $^{17}\text{O}$  labeled Gly [218]; the determined tensor orientations in the two peptides are very similar but the principal components are different. The most shielded CSA and smallest magnitude quadrupolar coupling (QC) components are normal to the peptide plane, while the most deshielded CSA and largest QC components are in the peptide plane either at an angle of  $17^\circ$  (CS) or perpendicular (QC) to the C=O bond (see Fig. 9). Comparisons of principal components from experiments and DFT calculations indicate that the smaller shielding tensor span in GGV (549 ppm) compared to that observed in AGG (606 ppm) is likely caused by two factors: a shorter “direct” H-bond distance to the peptide carbonyl oxygen and an “indirect” H-bond of the peptide NH to a carboxylate rather than a carbonyl oxygen. It was predicted by a FPT-MNDO-PM3 MO calculation that  $\delta_{22}$  lies approximately along the amide C=O bond, that  $\delta_{11}$  is aligned in the direction perpendicular to the C=O bond in the peptide plane, and that the most shielded component  $\delta_{33}$  is along the direction

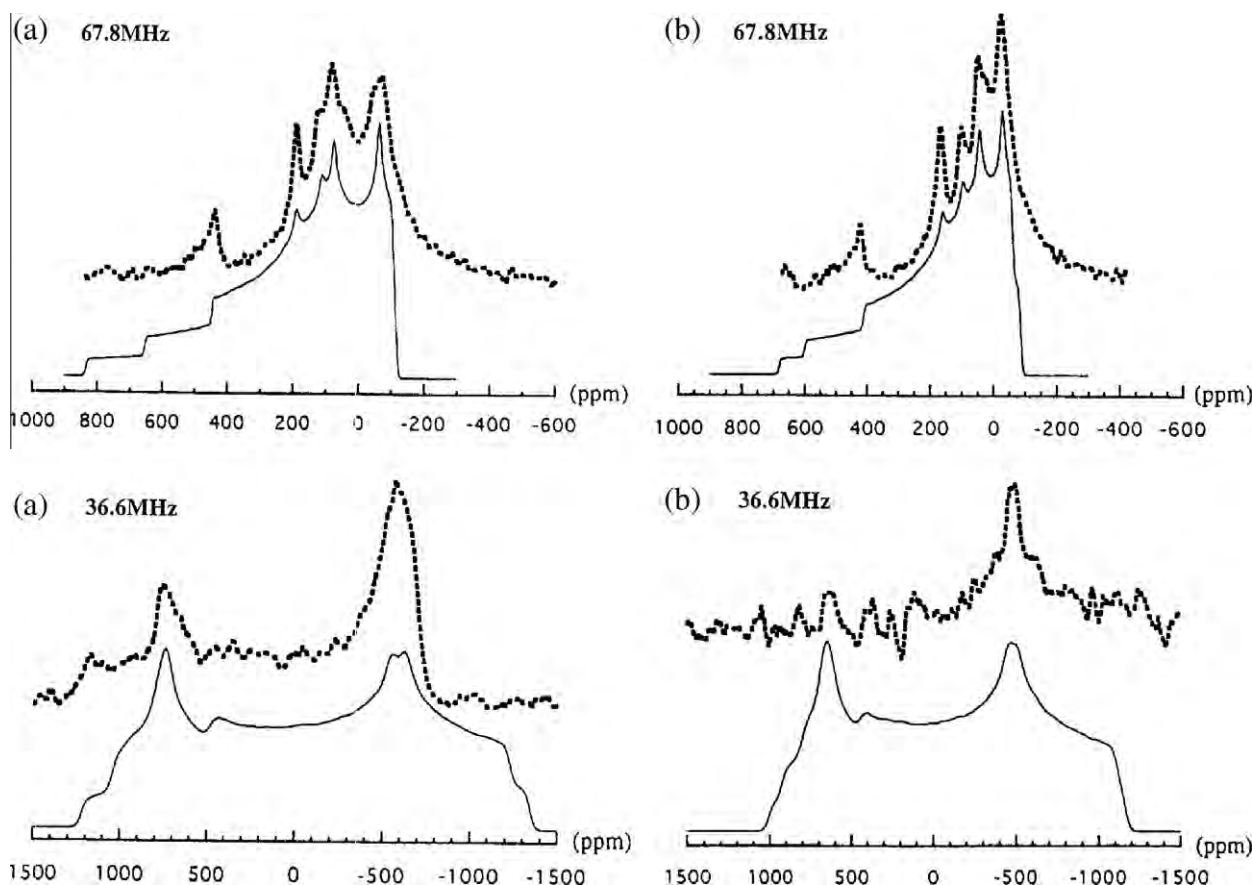


**Fig. 17.** Static 36.6 and 67.8 MHz  $^{17}\text{O}$  CP NMR spectra of (Ala) $_n$  (a) with the  $\alpha$ -helix form ( $n = 100$ ) and (b) the  $\beta$ -sheet form ( $n = 5$ ) in the solid state together with the computer simulations (bottom traces). Reproduced with permission from Takahashi et al. [209]. Copyright 1998 Elsevier.

**Table 8**  
The  $^{17}\text{O}$  chemical shift tensors of peptides and amino acids in the solid state.

|   |  | $\delta_{11}^a$ ppm | $\delta_{22}^a$ ppm | $\delta_{33}^a$ ppm | $\Delta\delta^b$ ppm | $\delta_{\text{iso}}$ ppm | $e^2qQ/h$ MHz | $\eta_Q$ | Remarks   | Reference |
|---|--|---------------------|---------------------|---------------------|----------------------|---------------------------|---------------|----------|---|-----------|
| <i>(Ala)<sub>n</sub> and oligopeptides</i>        |  |                     |                     |                     |                      |                           |               |          |   |           |
| (Ala) <sub>n</sub>                                | $\alpha$ -Helix                        | 595                 | 435                 | −121                | 438                  | 303                       | 9.28          | 0.38     | Static/ 36.6 & 67.8 MHz   | [209]     |
|   |  |                     |                     |                     |                      | 319                       | 8.59          | 0.28     | MAS/108.6 MHz   | [210]     |
|   | $\beta$ -Sheet                         | 514                 | 390                 | −110                | 373                  | 265                       | 8.65          | 0.41     | Static/ 36.6 & 67.8 MHz   | [209]     |
|   |  |                     |                     |                     |                      | 286                       | 8.04          | 0.28     | MAS/108.6 MHz   | [210]     |
| $[^{17}\text{O}]\text{-D-Ala}$                    | O1                                     |                     |                     |                     |                      | 275                       | 7.6           | 0.60     | MQMAS/ 67.78 MHz; $^{17}\text{O}$ in two different sites                  | [211]     |
|   | O2                                     |                     |                     |                     |                      | 262                       | 6.40          | 0.65     |   |           |
| L-Ala   | O1                                     |                     |                     |                     |                      | 284                       | 7.86          | 0.28     | MAS/ 81.345 MHz   | [214]     |
|   | O2                                     |                     |                     |                     |                      | 260                       | 6.53          | 0.70     |   |           |
| L-Ala HCl   | O1 (C=O)                               |                     |                     |                     |                      | 327.8                     | 8.31          | 0.0      | MAS/81.345 MHz  | [214]     |
|   | O2 (OH)                                |                     |                     |                     |                      | 176.7                     | 7.29          | 0.2      |   |           |
| fmoc-Ala  | O1                                     |                     |                     |                     |                      | 303.3                     | 7.89          | 0.16     | MAS/81.345 MHz  | [214]     |
|   | O2                                     |                     |                     |                     |                      | 175.7                     | 6.95          | 0.12     |   |           |
| $^{17}\text{O}$ -[Ala <sub>12</sub> ] WALP23      | lyophilized                            |                     |                     |                     |                      | 317                       | 8.45          | 0.21     | MAS/ 81.345 & 108.419 MHz   | [212]     |
|   | DSPC vesicle                           |                     |                     |                     |                      | 311                       | 8.42          | 0.21     | MAS/81.345 & 108.419 MHz  | [212]     |
|   | Hydrated DSPC vesicle                  |                     |                     |                     |                      | 315                       | 8.55          | 0.24     | MAS/81.345 & 108.419 MHz  | [212]     |
| Ala[ $^{17}\text{O}$ ]AlaAla                      | Anti-parallel $\beta$ -Sheet           |                     |                     |                     |                      | 302                       | 8.7           | 0.40     | MAS/126 MHz NMR. Two forms have two unique molecules in the unit cell.    | [226]     |
|   |  |                     |                     |                     |                      | 270                       | 8.7           | 0.35     |   |           |
|   | Parallel $\beta$ -sheet                |                     |                     |                     |                      | 293                       | 8.7           | 0.35     |   |           |
|   |  |                     |                     |                     |                      | 293                       | 8.7           | 0.35     |   |           |
| <i>(Gly)<sub>n</sub> and oligopeptides</i>        |  |                     |                     |                     |                      |                           |               |          |   |           |
| $[^{17}\text{O}]$ (Gly) <sub>n</sub>              | $\beta$ -Sheet                         | 574                 | 425                 | −101                | 412                  | 299                       | 8.55          | 0.26     | static 36.6, 54.2 & 67.8 MHz NMR  | [207]     |
|   |  |                     |                     |                     |                      | 304                       | 8.36          | 0.30     | MAS/108.6 MHz NMR   | [210]     |
|   | $3_1$ -Helix                           | 562                 | 410                 | −108                | 411                  | 288                       | 8.30          | 0.29     | static 36.6, 54.2 & 67.8 MHz NMR  | [207]     |
|   |  |                     |                     |                     |                      | 293                       | 8.21          | 0.33     | MAS 108.6 MHz NMR   | [210]     |
| Gly[ $^{17}\text{O}$ ]-Gy                         |  | 562                 | 382                 | −132                | 421                  | 265                       | 8.55          | 0.45     | static 36.6, 54.2 & 67.8 MHz NMR  | [207]     |
| Gly[ $^{17}\text{O}$ ]GlyHNO <sub>3</sub>         |  | 559                 | 408                 | −127                | 418.5                | 280                       | 8.75          | 0.47     | static 36.6, 54.2 & 67.8 MHz NMR  | [207]     |
| GlyHCl  | O1 (C=O)                               |                     |                     |                     |                      | 336                       | 8.4           | 0.0      | MAS 81.345 MHz NMR  | [214]     |
|   | O2 (OH)                                |                     |                     |                     |                      | 185                       | 7.6           | 0.25     |   |           |
| $^{17}\text{O}$ -[D-Leu] Gramicidin A lyophilized |  | 490                 | 400                 | −35                 | 307.5                | 285                       | 8.0           | 0.3      | MAS and static 122 MHz NMR  | [220]     |
| Gly[ $^{17}\text{O}$ ]-GlyGly                     |  | 533                 | 420                 | −50                 | 348                  | 301                       | 8.2           | 0.28     | MAS and static 113 MHz NMR  | [216]     |
| Gly[ $^{17}\text{O}$ ]-GlyGly CaCl <sub>2</sub>   |  | 427                 | 337                 | −24                 | 270.5                | 247                       | 7.4           | 0.70     | MAS and static 113 MHz NMR  | [216]     |
| Gly[ $^{17}\text{O}$ ]-GlyGly LiBr                |  | 453                 | 365                 | −43                 | 292                  | 258                       | 7.5           | 0.32     | MAS and static 113 MHz NMR  | [216]     |
| Gly[ $^{17}\text{O}$ ]-GlyGly HCl                 |  | 535                 | 395                 | −52                 | 363.5                | 293                       | 7.9           | 0.48     | MAS and static 113 MHz NMR  | [216]     |
| Gly-[ $^{17}\text{O}$ ]-GlyVal                    | $\delta_{11}$ : 17° from C=O bond axis | 526                 | 388                 | −23                 | 343.5                | 297                       |               |          | Single crystal. Static/ 67.15 MHz; Powder MAS/81 MHz & static 122 MHz NMR | [218]     |
| Ala-[ $^{17}\text{O}$ ]-GlyGly                    | $\delta_{11}$ : 17° from C=O bond axis | 546                 | 405                 | −60                 | 373.5                | 297                       |               |          | Single crystal; static/67.15 MHz; powder MAS/81 MHz & static 122 MHz NMR  | [218]     |

<sup>a</sup>  $\delta_{11} > \delta_{22} > \delta_{33}$ ,  $\delta_{11}$  is most deshielded component and  $\delta_{33}$  the most shielded component.  $\delta$ : relative to liquid water.

<sup>b</sup>  $\Delta\delta = \delta_{33} - 1/2(\delta_{11} + \delta_{22})$ .

perpendicular to the peptide plane [206,207]. This assignment for the directions of  $\delta_{11}$  and  $\delta_{22}$  is opposite to that determined from a single-crystal NMR measurement [219]. This shows that the MNDO-PM3 semi-empirical MO method for the prediction of the direction of the principal axes may be an insufficient approximation for the carbonyl oxygen with lone-pair electrons to obtain accurate direction for the principal axes [207].

**3.1.3.2. High field and fast-speed MAS.** By employing high-speed MAS at high field,  $^{17}\text{O}$  spectra can be obtained from which one can obtain three NMR parameters, namely, the isotropic chemical shift  $\delta_{\text{iso}}$ , the quadrupole coupling constant  $e^2qQ/h$  and  $\eta_Q$  (Eqs. (24) and (28)). It is easy to determine these three NMR parameters from a high speed MAS/high field  $^{17}\text{O}$  spectrum as compared with use of the static  $^{17}\text{O}$  spectrum, because the influence of quadrupolar interactions becomes extremely small in the high speed MAS/high field  $^{17}\text{O}$  spectrum. Indeed,  $^{17}\text{O}$  MAS spectra of a solid (Ala) $_n$

( $n = 100$ ;  $\alpha$ -helix) and (Ala) $_n$  ( $n = 5$ ;  $\beta$ -sheet) at 54.2 and 67.8 MHz spun at 15 kHz showed that the center-band signal is separated from the side-band signals at the latter frequency, allowing to determine more accurate values for the isotropic chemical shifts, quadrupole coupling constants and asymmetry parameter [207]. The center-band linewidth at 54.2 MHz is broadened compared with that at 67.8 MHz, because the center-band linewidth is proportional to  $\omega_Q^2/\omega_L^2$ , where  $\omega_L$  is the Larmor frequency and  $\omega_Q$  is proportional to the square of  $\omega_q (= e^2qQ/h)$  as shown in Eq. (23). Therefore, high-frequency NMR measurements are needed for a  $^{17}\text{O}$  MAS experiment, together with fast-speed MAS. The 108.6 MHz  $^{17}\text{O}$  MAS NMR spectra of a solid (Ala) $_n$  with  $\alpha$ -helix ( $n = 100$ ) and  $\beta$ -sheet form ( $n = 5$ ) and (Gly) $_n$  I ( $\beta$ -sheet) and II (3 $_1$  helix) were recorded using a spinning rate of 25 kHz [209,210].

High field/fast speed  $^{17}\text{O}$  MAS spectra of a selectively labeled transmembrane peptide ( $^{17}\text{O}$ -[Ala12]-WALP23) (examined as a lyophilized powder incorporated in hydrated vesicles) were recorded at frequencies 81.345 and 108.419 MHz, spun at 11–22 kHz, as illustrated in Fig. 18 [212]. Here, WALP23 is a synthetic peptide which represents a consensus sequence for transmembrane protein segments. A single resonance was centered at  $\sim 280$ –300 ppm from the single label at alanine-12. The decrease of the second-order quadrupole broadening and the associated increase in spectral resolution with increasing applied magnetic field is clearly evident. The observed  $^{17}\text{O}$  NMR parameters are consistent with those of poly(L-alanine) with the  $\alpha$ -helix conformation [210].

The effect of  $\text{Li}^+$  and  $\text{Ca}^{2+}$  binding to the carbonyl oxygen sites of a model Gly( $^{17}\text{O}$ -Gly)Gly peptide system was studied by a combination of stationary and fast MAS at a high magnetic field 19.6 T [216]. It was shown that the ion binding leads to significant upfield shift in  $\delta_{11}$  and  $\delta_{22}$  in the peptide plane and, thus, to significant upfield shift in the  $\delta_{\text{iso}}$ , together with a decrease in the quadrupole coupling constants of up to 1 MHz.  $^{17}\text{O}$  MAS and static NMR spectra of a lyophilized  $^{17}\text{O}$ -[D-Leu10]-gramicidin A (gA) sample were recorded and simulated with a set of parameters to elucidate the orientation of gA in uniformly aligned DMPC bilayers [220] (Fig. 19). It was found that the carbonyl  $^{17}\text{O}$  anisotropic chemical shift of Leu10, one of the three carbonyl oxygens contributing to the ion binding site in gramicidin A, is altered by 40 ppm when  $\text{K}^+$  ion binds to the channel, demonstrating a high sensitivity to such interactions. Moreover, considering the large range of the carbonyl  $^{17}\text{O}$  chemical shift ( $>500$  ppm), the recording of anisotropic  $^{17}\text{O}$  chemical shifts in bilayers aligned with respect to the magnetic field  $B_0$  offers high-quality structural restraints similar to  $^{15}\text{N}$  and  $^{13}\text{C}$  anisotropic chemical shifts.

2D  $^{17}\text{O}$  multiple quantum MAS (MQMAS) NMR spectra for amino acids, [ $^{17}\text{O}_2$ ]-D-alanine, [ $^{17}\text{O}_4$ ]-D,L-glutamic acid-HCl and other  $^{17}\text{O}$  labeled organic compounds, have been recorded at 67.78 MHz and 14.5 kHz MAS using rotor synchronized acquisition, were recorded [211] with a z-filter pulse sequence [221]. There are two magnetically distinct alanine oxygen sites (O1 and O2) sites in

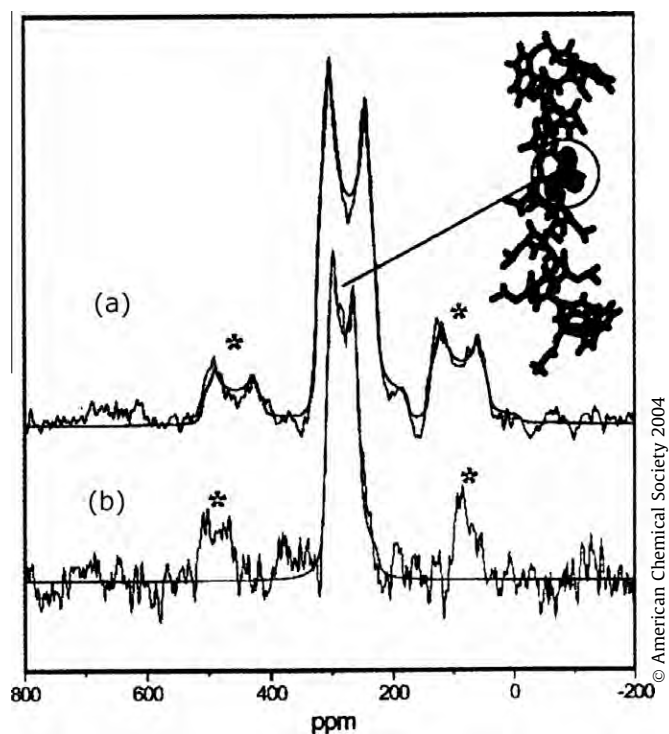


**Fig. 18.**  $^{17}\text{O}$  MAS NMR spectra of [ $^{17}\text{O}$ ]Ala12-WALP23 in hydrated DSPC vesicles at 14.1 and 18.8 T at room temperature. (a) At 14.1 T, spinning at  $\sim 15$  kHz with simulation (the continuous line). (b) at 18.8 T, spinning at  $\sim 22$  kHz with simulation (the continuous line). The spinning sidebands are marked by the asterisks. Reproduced with permission from Lemaître et al. [212].

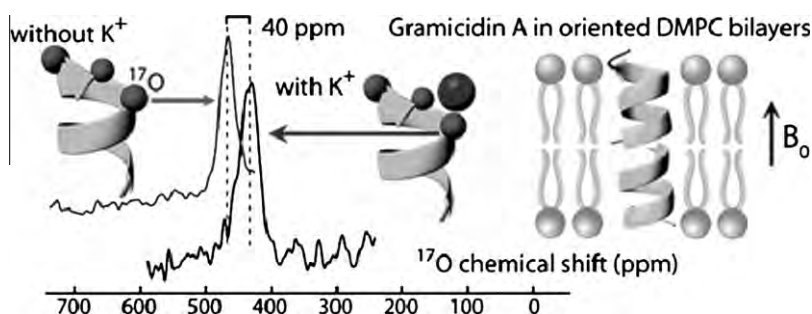


**Fig. 19.**  $^{17}\text{O}$  MAS NMR spectra of  $^{17}\text{O}$ -[p-Leu10]-gramicidin A uniformly aligned in DMPC bilayer at 21 T. Reproduced with permission from Hu et al. [220].



**Table 9**The amide  $^1\text{H}$  chemical shift tensors of peptides in the solid state.

| Peptides                   | Angle between $\delta_{ii}$ and N–H bond (degree)        | $\delta_{11}^a$ (ppm) | $\delta_{22}^a$ (ppm) | $\delta_{33}^a$ (ppm) | $\Delta\delta^b$ (ppm) | $\delta_{\text{iso}}$ (ppm) | Remarks  | Reference |
|----------------------------|--|-----------------------|-----------------------|-----------------------|------------------------|-----------------------------|--|-----------|
| Ac-D,L-Valine              | $\delta_{33}$ : Aligned with N–H bond axis               | 15.6<br>(14.9)        | 11.9<br>(18.6)        | 0.4<br>(30.1)         | 13.4                   | 9.3                         | Single crystal. $^2\text{H}$ NMR. $\delta$ in the brackets is absolute shielding | [227]     |
| Ala-[ $^{15}\text{N}$ ]Leu | $\delta_{33}$ : Collinear with N– $^1\text{H}$ bond axis | 17                    | 8                     | 3                     | 9.5                    | 9.3                         | 3D solid-state NMR   | [194]     |

<sup>a</sup>  $\delta_{11} > \delta_{22} > \delta_{33}$ ,  $\delta_{11}$  is most deshielded component and  $\delta_{33}$  the most shielded component,  $\delta$ : Relative to TMS.<sup>b</sup>  $\Delta\delta = \delta_{33} - (1/2)(\delta_{11} + \delta_{22})$ .

which O1 is involved in only one C=O...H–N hydrogen bond (hydrogen-bond length between O1 and H atoms ( $R_{\text{O} \dots \text{H}}$ ) = 1.242 Å) and O2 is involved in two hydrogen bonds ( $R_{\text{O} \dots \text{H}}$  = 1.258 Å). The NMR parameters for the examined amino acids show a wide variation of  $\delta_{\text{iso}}$ , from 83 to 353 ppm,  $e^2qQ/h$ , from 6.4 to 8.6 MHz,  $\eta_Q$ , from 0.0 to 0.9.  $^{17}\text{O}$  NMR spectra of L-alanine and Glycine-HCl with high resolution ( $\sim 1$  ppm) were obtained by combining  $^1\text{H}$ -decoupled double-rotation (DOR), which narrows the lines by a factor of  $\sim 100$  compared to conventional MAS, and manipulation of the satellite transition populations to transfer magnetization to the central transition, which produces a signal enhancement of  $\sim 2$  [222].  $^{17}\text{O}$  NMR of some other amino acids have also been examined [223–225].

$^{17}\text{O}$  MAS spectra at 21.8 T (126 MHz) and 20 kHz MAS have been reported for two kinds of Ala-[ $^{17}\text{O}$ ]Ala-Ala one with parallel (P) and the other with anti-parallel (AP)  $\beta$ -sheet structures [226]. The ( $\delta_{\text{iso}}$ ,  $e^2qQ/h$  and  $\eta_Q$ ) values are (O1: 302  $\pm$  5 ppm, 8.7  $\pm$  0.5 MHz, 0.40  $\pm$  0.1; O2: 270  $\pm$  5 ppm, 8.7  $\pm$  0.5 MHz, 0.35  $\pm$  0.1) and (O1: 293  $\pm$  5 ppm, 8.7  $\pm$  0.5 MHz, 0.30  $\pm$  0.1; O2: 293  $\pm$  5 ppm, 8.7  $\pm$  0.5 MHz, 0.30  $\pm$  0.1) for P and AP  $\beta$ -sheet structures, respectively. Calculated values of these parameters obtained using the DFT method were found to be in good agreement with those obtained from the spectra.

### 3.1.4. $^1\text{H}$ CSA

The principal values and axes for the amino- $^1\text{H}$  chemical shift tensor of Ac-D,L-valine single crystal have been reported [227]. They were obtained from the  $^2\text{H}$  amide CSA tensor obtained on a sample in which the amide and carboxyl protons had been exchanged with deuterons. The  $^1\text{H}$  shielding tensor was obtained by converting from the  $^2\text{H}$  amide chemical shift tensor and taking into account the isotope effect between proton and deuteron. The determined absolute  $^1\text{H}$  shielding tensor components summarized in Table 9 were obtained by converting the data relative to TMS by using a value for the absolute shielding of TMS of 30.5 ppm. The directions of the principal axes were also determined:  $\delta_{33}$  is aligned with the N–H bond axis with a deviation of 9° and  $\delta_{11}$  is perpendicular to the peptide plane with a deviation of 11° (see Fig. 9). The direction of

the most shielded amide  $^1\text{H}$   $\delta_{33}$  of  $^{15}\text{N}$  labeled Ala- $^{15}\text{N}$ -Leu is collinear with the N–H bond and the orientations of the  $^1\text{H}$  and  $^{15}\text{N}$  tensors are related by the Euler angles 45°, 90° and 75° from the analysis of the 2D  $^1\text{H}$  chemical shift– $^{15}\text{N}$  chemical shift correlation spectrum [194].

The flip-flop Lee–Goldburg (FFLG-2) homo-nuclear dipolar decoupling method combined with a 12-kHz MAS save signals with better resolution from amide-proton directly bonded to the amide- $^{14}\text{N}$  for Gly containing peptides [164]. By using the same method, high resolution  $^1\text{H}$  spectra of nylon 4 as a kind of polyamides have been measured by changing temperature to 214 °C and then the structural behavior has been studied [228]. The use of a continuously phase-modulated homonuclear decoupling sequence DUMBO-1 gave well resolved proton spectra both at slow and fast MAS conditions for L-alanine amino acid, Ala-Asp dipeptide and cyclosporin A [229]. In the case of L-alanine, a proton line width of less than 0.5 ppm was obtained under DUMBO-1 decoupling.

### 3.1.5. CSA can reveal the geometry of hydrogen bonding

The values of  $\delta_{22}$  for the amide  $^{13}\text{C}$  of Gly, Ala, Leu and Asp-containing peptides in the solid-state were found to vary with the hydrogen-bond length ( $R_{\text{N} \dots \text{O}}$ ), as illustrated in Fig. 20, by a similar relationship to that of the isotropic  $^{13}\text{C}$  chemical shift (Eq. (34)):

$$\delta_{22} \text{ (ppm)} = a - bR_{\text{N} \dots \text{O}} \text{ (Å)}, \quad (41)$$

where the coefficients  $a$  and  $b$  were readily estimated from plots of the experimental values of the  $\delta_{22}$  [42,114,115]; the  $\delta_{11}$  and  $\delta_{33}$  are insensitive to changes in  $R_{\text{N} \dots \text{O}}$ . This approach was extended to evaluate the  $R_{\text{N} \dots \text{O}}$  value for the guest  $^{13}\text{C}$ -labeled Gly residue as the 5–8% minor amount incorporated into host polypeptides (Ala, Gly) $_n$  taking the  $\alpha_R$ -helix as the major form [114,115,184]. The  $R_{\text{N} \dots \text{O}}$  values in the guest Gly residue in some host polypeptides have been determined using Eq. (41). The  $R_{\text{N} \dots \text{O}}$  values of the guest Gly residue in (Gly $^*$ ,Leu) $_n$  and (Gly $^*$ ,Ala) $_n$  are very close to those of the host polypeptides. This indicates that the guest Gly residue is completely incorporated into host polypeptides with an  $\alpha_R$ -helix or a  $\beta$ -sheet conformation.

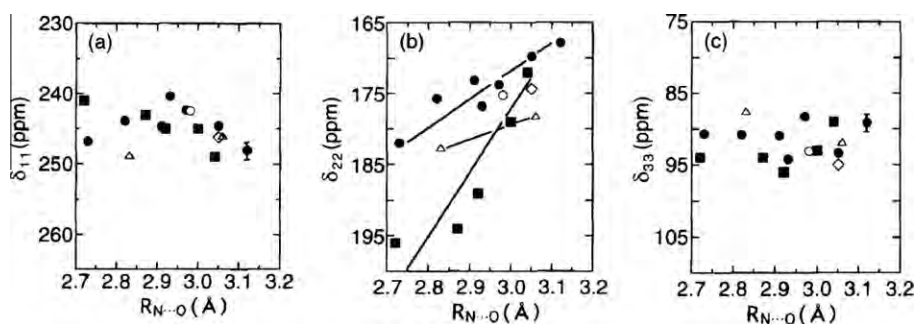


**Fig. 20.** Plots of the experimental  $^{13}\text{C}$  chemical shift tensor components for (a)  $\delta_{11}$ , (b)  $\delta_{22}$  and (c)  $\delta_{33}$  for the amide carbonyl carbon in Gly (●), Ala (■), Val (□), Leu (△) and Asp (○) residues in peptides against the hydrogen-bond length ( $R_{\text{N} \dots \text{O}}$ ). The experimental errors of  $\delta_{11}$  and  $\delta_{33}$  are indicated by an error bar. Reproduce with permission from Kameda et al. [114]. Copyright 1996 Elsevier.

Further, the conformational stability of the  $\alpha_R$ -helix and  $\omega_L$ -forms was analyzed through the  $R_{N...O}$  values in guest  $^{13}\text{C}$  labeled Gly residues that were incorporated into host ( $\beta$ -benzyl L-aspartate) $_n$  [PBLA; (Asp(OBzl)) $_n$ ] [114,115]. It was shown that the former is longer by 0.07 Å than the latter. This means that the hydrogen bond for the  $\alpha_R$ -helix form is somewhat stronger than that for the  $\omega_L$ -form, and thus the  $\alpha_R$  helical stability is somewhat higher than  $\omega_L$  helical stability. The  $^{13}\text{C}$ -labeled Ala residue incorporated into PBLA with various conformations [230–232] show displacement of the  $^{13}\text{C}$  chemical shift of the  $\text{C}_\beta$ -carbon on changing temperature, which indicates significant conformational changes of PBLA [233].

The diamagnetic contribution to  $\delta_{33}$  for Ala  $\text{C}_\alpha$  is mainly affected by changes in the main-chain torsion-angles but also by the hydrogen-bonding structure, especially in the comparison between the  $\alpha_R$ -helix and the  $\beta_A$ -sheet main-chain torsion-angles [117,186]. This comes from the interaction between the atomic-orbitals aligned to the  $\delta_{33}$  axis and the  $n$ -orbital (for lone-pair electrons) that is spread around the outside of the carbonyl bond.

The inclusion of intermolecular effects such as hydrogen bonding in the *ab initio* calculations of CSA tensors of  $^{13}\text{C}_\alpha$  in peptides provides a better agreement between the calculated and experimental values [234].

The protonation state of the amide carboxyl group of amino acids and peptides in the solid-state can easily be evaluated by  $^{13}\text{C}$  CSA tensors but not by isotropic shifts, and the substantial variation in the  $\delta_{22}$  element for both protonated and deprotonated forms is shown to be a result of the hydrogen bonding [235].

Behavior of the  $^{15}\text{N}$  isotropic shifts and  $^{15}\text{N}$  CSA tensors of the Gly amide nitrogen nuclei in various  $^{15}\text{N}$ -labeled glycylglycine ( $\text{X-Gly}^1\text{Gly}^2$ ) sequence peptides (where Gly $^1$  is  $^{15}\text{N}$ -labeled and X is some other amino acid) in the crystalline state have been studied [137], in order to relate the shift tensors with aspects of the hydrogen-bonded structure such as the hydrogen-bond length  $R_{N...O}$  and/or the N–H bond length. The  $^{15}\text{N}$  CSA components of  $^{15}\text{N}$ -labeled BocGlyY dipeptides (Y: amino acid residues other than Gly) with an  $R_{N...O}$  range of 2.95–3.08 Å were measured, in which some effect of the amino acid residues X on the  $^{15}\text{N}$  chemical shift of the amide-nitrogen for the Gly residue can be neglected [138]. The experimental values of  $\delta_{33}$  move linearly downfield with a decrease in  $R_{N...O}$ , while the experimental values of  $\delta_{11}$  and  $\delta_{22}$  are approximately independent of  $R_{N...O}$ . FPT INDO calculations were used to explore the effect of a change of the hydrogen bond angle  $\theta$ , and it was shown that the values of  $\delta_{33}$  are relatively insensitive to a change in  $\theta$ , but those of  $\delta_{11}$  and  $\delta_{22}$  are relatively sensitive to a change in  $\theta$ .

The N–H bond lengths of the fully  $^{15}\text{N}$ -labeled (Ala) $_n$  in the  $\beta$ -sheet form has been shown to be 0.03 Å longer than that in the  $\alpha$ -helix form from measurements of  $^{15}\text{N}$ – $^1\text{H}$  dipolar couplings obtained from  $^1\text{H}$  CRAMPS experiments [236].

### 3.2. CSA values of nuclei in solid-state globular and fibrous proteins

CSA recovery MAS experiments enable the measurement of CSA values of nuclei in individual amino acid residues in large molecular systems. The CSA values of  $^{13}\text{C}$  at multiple sites in selectively and extensively  $^{13}\text{C}$ -labeled and uniformly  $^{15}\text{N}$ -labeled ubiquitin (the 76 residue protein) have been measured by reintroducing them under MAS using a train of  $180^\circ$  pulses in which the second half of the pulse train is displaced with respect to the first half [237]. The 2D CSA-filtered  $^{15}\text{N}$ – $^{13}\text{C}$  2D correlation spectrum at a delay of half a rotor period corresponds predominantly to  $^{13}\text{C}$  nuclei in  $\alpha$ -helical residues which have smaller CSA values for  $\text{C}_\alpha$  CSAs than those in the sheet residues. The helical CSA values obtained in this way for  $^{13}\text{C}$  in helical structure are significantly larger than the values estimated by solution NMR studies [238].

The CSA values of  $^{13}\text{C}$  in several peptides and (Ala) $_n$  were determined by 1D CPMAS and 2D PASS NMR experiments [187]. The carbonyl  $^{13}\text{C}$  CSA tensor was found to correlate with the backbone hydrogen bond distance. The  $^{13}\text{C}_\alpha$  CSA tensors of alanine residues have a small dependency on the protein secondary structure and can vary from 20 to 30 ppm. For alanine and leucine, which are not branched at the  $\beta$ -carbon, the values of CSA span ( $\Omega$ ) are large, about 30 ppm, independent of whether the residues adopt a helical or a sheet conformation. In contrast, the CSA values ( $\Delta\sigma$ ) obtained from solution NMR data for alanine, valine and leucine residues in proteins show major differences, with helical residues having  $\Delta\sigma$  values of  $\sim 6$  ppm while sheet residues have  $\Delta\sigma \approx 27$  ppm.

The orientation of  $^{13}\text{C}_\alpha$  CSA tensors was obtained under MAS by modulating a recoupled CSA pattern with various dipolar couplings [239]. These dipolar coupling modulated CSA spectra are equivalent to the projection of a 2D static separated-local-field spectrum onto its chemical shift dimension [240], except that its dipolar coupling frequency dimension is multiplied with a modulation function. It was demonstrated that both  $^{13}\text{C}$ – $^1\text{H}$  and  $^{13}\text{C}$ – $^{15}\text{N}$  dipolar couplings can modulate the CSA spectra of the  $\text{C}_\alpha$  site in an amino acid and yield the orientations of the chemical shift principal axes relative to the C–H and C–N bonds. The magnitude of the  $\text{C}_\alpha$  chemical shift tensors in two peptides with  $\alpha$ -helical torsion angles was determined using the SUPER sequence under MAS [84] for the Ala residue in G\*AL ( $\phi = -65.7^\circ$ ,  $\psi = -40^\circ$ ) and Val residue in GG\*V ( $\phi = -81.5^\circ$ ,  $\psi = -50.7^\circ$ ) [241]. The helical Ala  $\text{C}_\alpha$  chemical shift tensor has a span of 36 ppm and an asymmetry parameter of 0.89. Its  $\sigma_{11}$  axis is  $116 \pm 5^\circ$  from the  $\text{C}_\alpha$ – $\text{H}_\alpha$  bond while the  $\delta_{22}$  axis is  $40 \pm 5^\circ$  from the  $\text{C}_\alpha$ –N bond. The  $^{13}\text{C}_\alpha$  CSA tensor of Val has an anisotropic span of 25 ppm and an asymmetry parameter of 0.33, both are much smaller than the values measured for a  $\beta$ -sheet Val [239]. The  $\delta_{33}$  axis in Val is tilted by  $115 \pm 50^\circ$  from the  $\text{C}_\alpha$ – $\text{H}_\alpha$  bond and  $98 \pm 5^\circ$  from the  $\text{C}_\alpha$ –N bond.

A recent study reported  $^{13}\text{C}$  and  $^{15}\text{N}$  CSA measurements from a uniformly  $^{15}\text{N}$ ,  $^{13}\text{C}$  labeled microcrystalline protein (the 56 residue  $\beta 1$  immunoglobulin binding domain of protein G, GB1) using a 3D experiment incorporating ROCSA [242–244]. This 3D experiment correlating CSA powder line shape with isotropic chemical shifts enabled 127 site-specific CSA measurements to be made [242]. The displayed “triple plot” illustrates the CSA tensor for the  $\text{C}_\alpha$  resonances of the Gly and Ala residues of GB1 (Fig. 21), and compares experimental values with calculated based on the GB1 crystal structure. While there is little change in the span of these tensors, there are important overall shifts of the principal elements. The residue G14, for example, resides in a turn, whereas G38 is positioned at the transition between the  $\alpha$ -helix and the  $\beta 3$ -strand, as clearly seen from the corresponding displaced principal values in the  $\delta_{11}$  and  $\delta_{22}$  (see Fig. 21b). The residue A20, in a reverse  $\beta$ -turn, displays an upfield  $\text{C}_\alpha$  isotropic shift due to  $\delta_{33}$ , which shows a larger variation relative to the helical Ala residues. Determination of 91 independent  $^{15}\text{N}$  CSA tensors at 51 of the 55 backbone amide sites was also achieved by ROCSA measurements based on resolved  $^{15}\text{N}$ – $^{13}\text{C}_\alpha$  and/or  $^{15}\text{N}$ – $^{13}\text{C}'$  cross peaks [243]. A systematic variation between  $\beta$ -sheet and  $\alpha$ -helix residues were also observed; the average value for the anisotropy parameter  $\delta$  for  $\alpha$ -helical residues is 6 ppm greater than that of  $\beta$ -sheet residues. High-quality slow-MAS spectra were acquired in a relatively simple experiment employing a diluted  $^{13}\text{C}$  labeling scheme for GB1, in combination with triple-resonance experiments based on a  $^{15}\text{N}$ – $^{13}\text{C}$  correlation method at a high magnetic field [244]. The average value of  $\delta$  ( $^{15}\text{N}$ ) analyzed by the Herzfeld-Berger method throughout the protein is  $-109$  ppm, slightly smaller in magnitude for  $\beta$ -sheet residues ( $-106$  ppm) and larger ( $-115$  ppm) for  $\alpha$ -helix (Fig. 22a). The measured values for the carbonyl CSA tensors show trends as a function of secondary structure and isotropic chemical shift, with an average  $\delta$  ( $^{13}\text{C}'$ ) over the entire protein of  $-79.3$  ppm,  $-83.5$  ppm

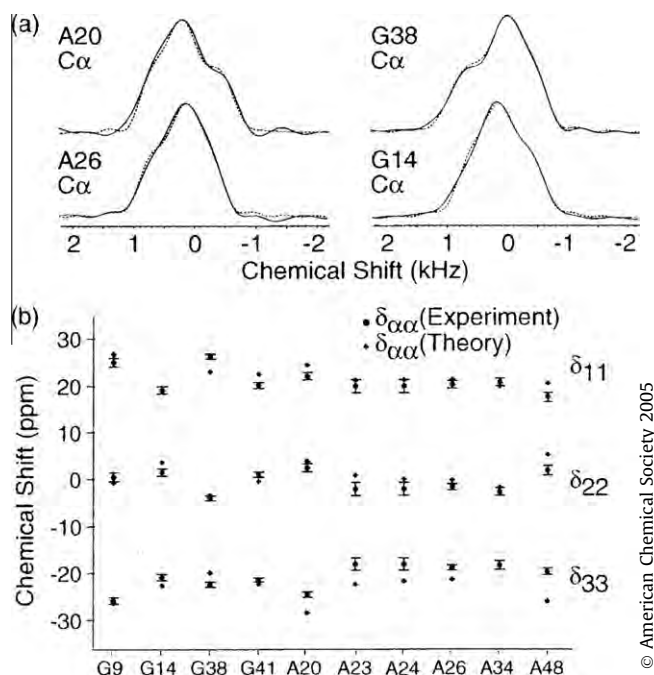


**Fig. 21.** (a) ROCSA  $C_\alpha$  powder patterns (solid line) obtained at 11.7 T with best simulations (dotted). (b) Plot of the principal components of  $C_\alpha$  CSA tensors for all Gly and Aa residues in GB1. Experimental and theoretical data are shown as closed circles and diamonds, respectively. Reproduced with permission from Wylie et al. [242].

for helical and  $-77.7$  for  $\beta$ -sheet residues (Fig. 22b). The asymmetry parameter  $\eta$  has a greater dependency on the secondary structure, with an average of  $0.53$  in  $\alpha$ -helical and  $0.72$  in  $\beta$ -sheet residues (Fig. 22c). Variations in the isotropic chemical shift are highly correlated with the  $\delta_{yy}$  tensor element (Fig. 22d).

### 3.3. CSA values for $^{13}\text{C}$ , $^{15}\text{N}$ and $^1\text{H}$ in globular proteins in solution

The residue-specific CSA data in proteins are also available from solution NMR:  $^{15}\text{N}$  relaxation times are utilized, based on a ratio of  $\eta/R_2$  of the cross correlation ( $\eta$ ) between  $^{15}\text{N}$  CSA and  $^{15}\text{N}$ – $^1\text{H}$  dipolar interaction and of the rate of  $^{15}\text{N}$  transverse relaxation ( $R_2$ ) [21,245–247], relying on a “model-free” approach for the interpretation of magnetic resonance relaxation [248]. Because the dependence of the spectral density function  $J(\omega)$  of the cross correlation rate,  $\eta$ , between  $^{15}\text{N}$  CSA and  $^{15}\text{N}$ – $^1\text{H}$  dipolar interaction,

$$\eta = dc[4J(0) + 3J(\omega_N)]P_2(\cos\theta), \quad (42)$$

and of the rate,  $R_2$ , of  $^{15}\text{N}$  transverse relaxation,

$$R_2 = (1/2)(d^2 + c^2)[4J(0) + 3J(\omega_N)] + P_{HF} + R_{ex}, \quad (43)$$

is similar, where  $P_{HF} \equiv (1/2)d^2[J(\omega_H - \omega_N) + 6J(\omega_H) + 6J(\omega_H + \omega_N)]$  denotes the contribution to  $R_2$  from high frequency motions, and  $R_{ex}$  corresponds to conformational exchange contribution, if any. Here,  $\omega_N$  and  $\omega_H$  are Larmor frequencies of the nitrogen and hydrogen, respectively.  $\theta$  is the angle between the N–H vector and the unique principal axis of the  $^{15}\text{N}$  CSA tensor;  $d = (\mu_0/(4\pi))\gamma_H\gamma_N\hbar/(4\pi r_{HN}^3)$ ,  $c = -\gamma_N B_0(\delta_{||} - \delta_{\perp})/3$ ;  $r_{HN}$  is the N–H bond length;  $\delta_{||} - \delta_{\perp}$  is the anisotropy of  $^{15}\text{N}$  CSA tensor, assuming axially symmetry;  $P_2(x) = (3x^2 - 1)/2$  is the second-rank Legendre polynomial; and  $h$  is the Planck's constant. For the majority of the amide-NH group  $J(\omega_H)$  is much smaller than  $J(\omega_N)$  and  $J(0)$ , which then allows  $P_{HF}$  to be safely neglected to first order. Assuming  $R_{ex}$  is negligible, Eq. (43) gives

$$R_2 \approx (1/2)(d^2 + c^2)[4J(0) + 3J(\omega_N)]. \quad (44)$$

The ratio

$$\eta/R_2 = [2dc/(d^2 + c^2)]P_2(\cos\theta), \quad (45)$$

is then independent of protein dynamics, and therefore contains only “structural” information, in the form of the  $^{15}\text{N}$  CSA and the angle  $\theta$  between the N–H vector and the unique principal axis of the  $^{15}\text{N}$  chemical shift tensor. The CSA is related to  $R_2$ ,  $\eta$  and  $\theta$ :

$$\delta_{||} - \delta_{\perp} = 3(\delta/\omega_N)[R_2 P_2(\cos\theta)/\eta][1 - \sqrt{1 - (\eta/R_2 P_2(\cos\theta))^2}]. \quad (46)$$

If the  $^{15}\text{N}$  CSA is known,  $\theta$  angle can be determined by the  $\eta/R_2$  ratio:

$$\theta = \cos^{-1}(\{[1 + (\eta/R_2)(d^2 + c^2)/(dc)]/3\}^{1/2}). \quad (47)$$

Usually, neither CSA nor  $\theta$  is known. Therefore, independent determination of both  $^{15}\text{N}$  CSA and the angle  $\theta$  is not possible from relaxation data at a single frequency, because  $\eta/R_2$  contains the product  $-(\delta_{||} - \delta_{\perp})P_2(\cos\theta)$ .

Determination of these parameters in ubiquitin is, therefore, feasible from the intersection of the curves representing loci of the CAS and  $\theta$  solutions to Eq. (46) at the three fields used, 360, 500 and 600 MHz, as shown in Fig. 23 [246]. The  $^{15}\text{N}$  CSA values thus obtained fall in the range 125 to 216 ppm, with the average value of  $157 \pm 19$  ppm; the average angle between the NH bond and the unique principal axis of the  $^{15}\text{N}$  CSA tensor was found to be  $15.7 \pm 5.0^\circ$  (range  $6$ – $26^\circ$ ) (Fig. 24). Assuming a Gaussian distribution of  $^{15}\text{N}$  CSA values, the mean anisotropy of  $^{15}\text{N}$  in the B3 domain of protein G measured at several fields as determined by this procedure is  $173.9$ – $177.2$  ppm (for  $1.02$ -Å N–H bond length) and the site-to-site CSA variability is  $\pm 17.6$  to  $\pm 21.4$  ppm, depending on the method used [247]. The  $\Delta\delta$  values for  $^{15}\text{N}$  in ribonuclease H are approximately  $172 \pm 13$  ppm, as determined by  $^1\text{H}$ – $^{15}\text{N}$  dipolar/ $^{15}\text{N}$  chemical shift anisotropy relaxation interference rate [249]. The standard deviation of the site-to-site variation is  $5.5$  ppm and a 95% confidence limit for this variation is  $9.6$  ppm. Variability in these CSA values is a significant factor in the interpretation of the spin relaxation rate especially at a high magnetic field. An average  $^{15}\text{N}$  CSA of  $-170$  ppm obtained with the assumption that  $\theta = 20^\circ$  was also demonstrated for ubiquitin by  $^{15}\text{N}$  CSA/ $^{15}\text{N}$ – $^1\text{H}$  dipolar correlation experiment [250]. It is pointed out that the above analysis of the magnetic field dependence of the  $^{15}\text{N}$  relaxation yielded a considerably (5–20%) higher CSA value (170–175 ppm) [246,252] than that observed in the solid-state ( $\sim 160$  ppm) [126,181,187,190,192,195,203]. The discrepancy between solid-state and solution NMR data has been attributed to the fact that the solution data have been corrected for the effects of internal motion, whereas solid-state values have been derived from the motionally narrowed powder pattern [251].

Further, the CSA data are available in solution from the model-dependent analysis of chemical shifts in the weakly oriented system [253,254]: the difference in apparent chemical shifts observed for weakly aligned ( $\delta_{aniso}$ ) and isotropic ( $\delta_{iso}$ ) samples is given by:

$$\Delta\delta = \delta_{aniso} - \delta_{iso} = \sum_{i=x,y,z} \sum_{j=x,y,z} A_{ij} \cos^2(\theta_{ij}) \delta_{ii}, \quad (48)$$

where  $A_{ij}$  are the principal components of the molecular alignment tensor,  $\delta_{ii}$  the principal components of the CSA tensor, and  $\theta_{ij}$  is the angle between the  $jj$  axis of the alignment tensor and  $ii$  axis of the CSA tensor. The dipolar coupling data  $D_{AB}$  between two nuclei, A and B, is also related to the traceless alignment tensor according to:

$$D_{AB} = \sum_{i=x,y,z} (\mu_0 h / 8\pi^3) \gamma_A \gamma_B \langle r_{AB}^{-3} \rangle \cos^2 \phi_i A_{ii}, \quad (49)$$

where  $\phi_i$  she angle between the A–B bond vector and the  $A_{ii}$  principal axis of the alignment tensor,  $\gamma_A$  and  $\gamma_B$  are the gyromagnetic



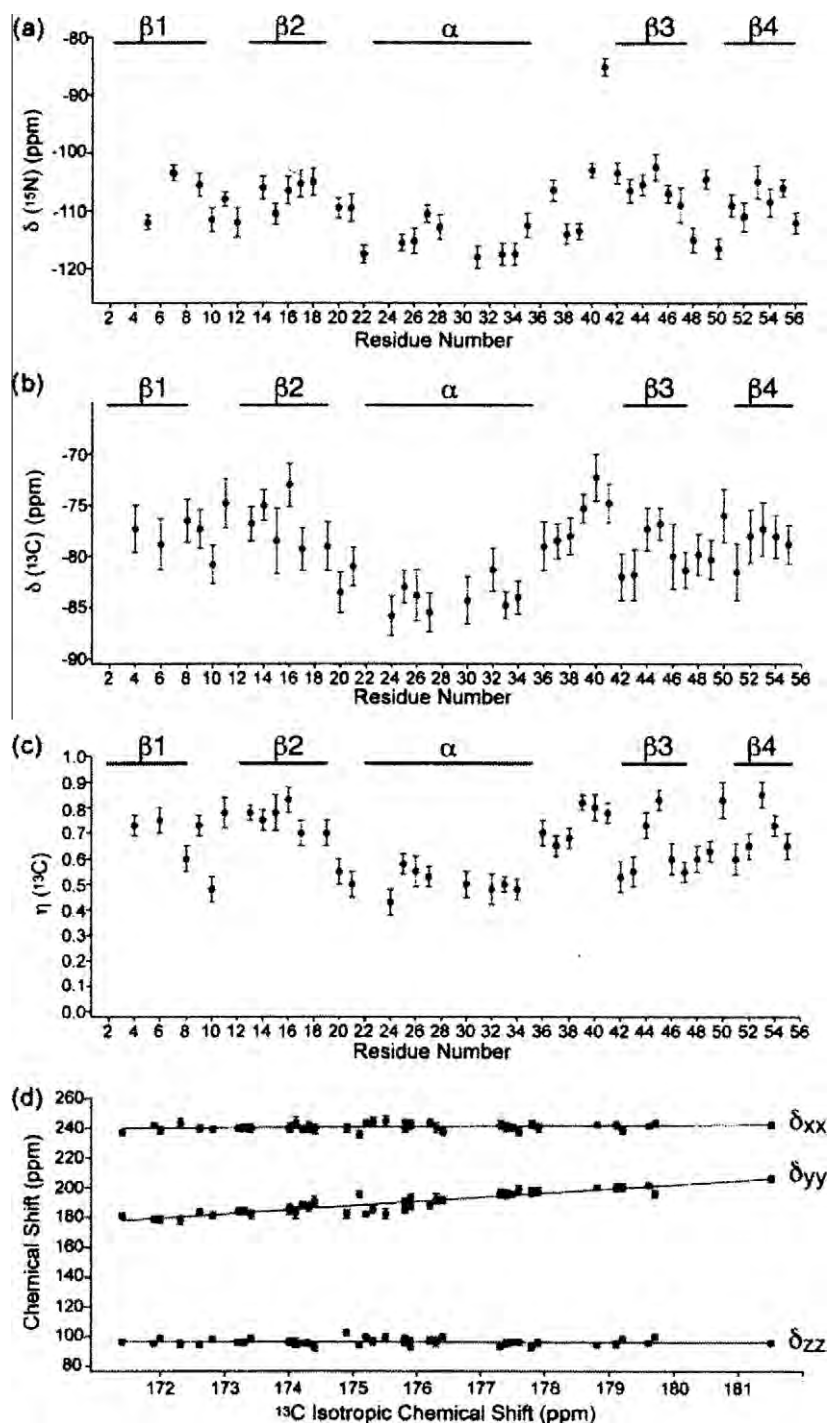


**Fig. 22.** Fitted CSA tensor parameters determined for GB1; (a)  $\delta(^{15}\text{N})$ ,  $^{15}\text{N}$  reduced anisotropy ( $\delta = \delta_{zz} - \delta_{\text{iso}}$ ), for backbone amide sites, (b)  $\delta(^{13}\text{C})$ , (c)  $\eta(^{13}\text{C})$  asymmetry parameter, (d)  $^{13}\text{C}$  principal elements as a function of the  $^{13}\text{C}$  isotropic chemical shift. Reproduced with permission from Wylie et al. [244].

ratios of the two nuclei and  $\langle r_{AB}^{-3} \rangle$  is the vibrationally averaged inverse cube of the distance between the two nuclei. The orientation and magnitude of the rhombic alignment tensor were obtained from fits of the dipolar coupling data to the X-ray diffraction structure of ubiquitin. For the magnitude of alignment typically used in biomolecular NMR,  $10^{-4}$  to  $10^{-3}$ , the measured  $\Delta\delta$  are on the order of parts per billion (ppb). The determined CSA tensors for  $^{13}\text{C}$  in ubiquitin have the average values  $\delta_{11} = 75$  ppm,  $\delta_{22} = 12$  ppm, and  $\delta_{33} = -87$  ppm with an angle between  $\delta_{11}$  and the C'–N bond of  $38^\circ$ , and  $\delta_{33}$  orthogonal to the peptide plane. For  $^{15}\text{N}$ ,  $\delta_{11} = 108$  ppm,  $\sigma_{22} = -46$  ppm, and  $\delta_{33} = -63$  ppm, with an angle

of  $19^\circ$  between the H–N vector and the  $\sigma_{11}$  axis, and  $\sigma_{22}$  orthogonal to the peptide plane. For  $\text{H}^{\text{N}}$ , the commonly used approximation of an axially symmetric shielding tensor was found to be invalid, and the best fit tensor values were found to be  $\delta_{11} = 6$  ppm,  $\delta_{22} = 0$  ppm, and  $\delta_{33} = -6$  ppm, with the  $\delta_{11}$  axis orthogonal to the peptide plane and  $\delta_{33}$  roughly parallel to the H–N bond axis [253]. The average  $^{15}\text{N}$  CSA was thus obtained to be  $163.4 \pm 4$  ppm.

The average  $^{15}\text{N}$  CSA tensor was determined for the residues in ubiquitin by an MAS experiment as  $\Delta\delta = 162.0 \pm 4.3$  ppm,  $\eta = 0.18 \pm 0.02$  and  $\beta = 18.6 \pm 0.5^\circ$ , assuming a  $^1\text{H}$ – $^{15}\text{N}$  bond length of  $1.02 \text{ \AA}$  [255]. Measurement of the relatively small  $^1\text{H}$  CSA is tech-

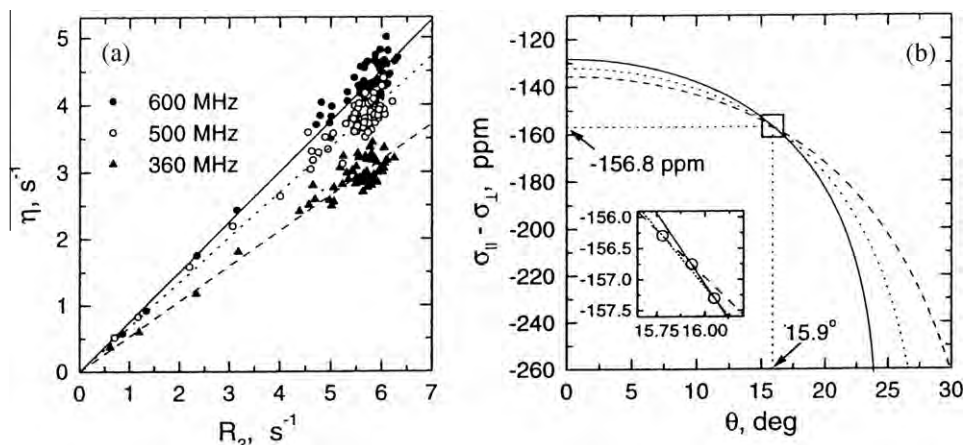


**Fig. 23.** (a) Correlation between the cross correlation term  $\eta$  and the rate of  $^{15}\text{N}$  transverse relaxation  $R_2$  in ubiquitin, from 600 MHz (solid circles), 500 MHz (open circles) and 360 MHz (solid triangles) data. (b) Graphical illustration for the deviation of CSA and  $\theta$  from  $\eta/R_2$  at multiple fields. The curves in (b) represent loci of CSA and  $\theta$  value solutions for the average values of  $\eta/R_2$  (from the linear fits in (a)). The intersection of any two curves provides a unique solution for a given pair of  $\eta/R_2$  values at two frequencies, as indicated in the inset. Reproduced with permission from Fushman et al. [246].

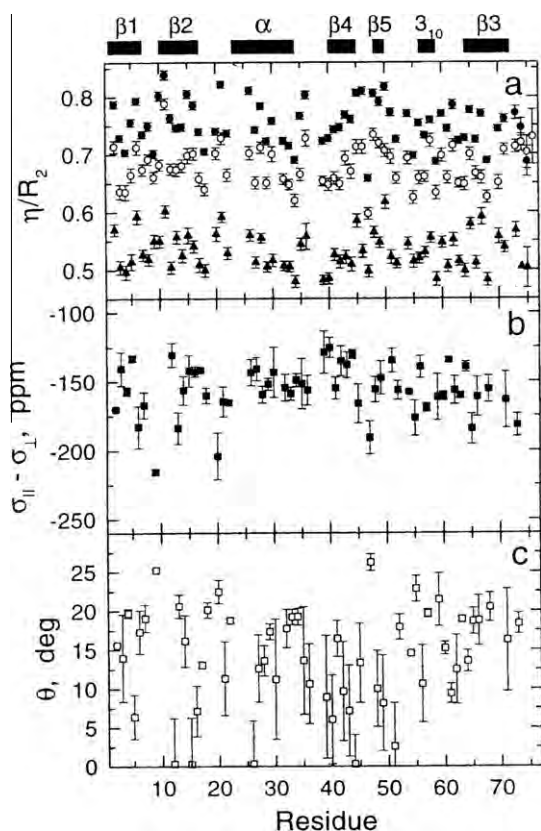


**Fig. 24.** A plot of (a)  $\eta/R_2$ , (b)  $\sigma_{||} - \sigma_{\perp}$  and (c)  $\theta$  versus residue number in human ubiquitin determined by  $^{15}\text{N}$  relaxation rates. Reproduced with permission from Fushman et al. [246].

nically challenging in the solid-state, as described already for Ala- $^{15}\text{N}$ -Leu [194], Ac-D,L-valine [227] and acetanilide [256]. The most shielded tensor component of the  $^1\text{H}^{\text{N}}$  CSA tensor ( $\delta_{33}$ ) is roughly collinear with the N-H bond. Amide  $^1\text{H}^{\text{N}}$  chemical shift anisotropies in  $^{15}\text{N}$ -enriched proteins, ubiquitin, HIV-protease and HU protein from *Bacillus stearothermophilus* have been determined in solution utilizing cross-correlation between  $^{15}\text{N}$ - $^1\text{H}$  dipolar interaction and  $^1\text{H}^{\text{N}}$  CSA [257,258]. The  $^1\text{H}^{\text{N}}$  transverse

relaxation rates for the two doublet components of a  $^1\text{H}^{\text{N}}$ - $^{15}\text{N}$  spin pair are given by [259]:

$$R_2 = \Delta + \lambda \pm \eta, \quad (50)$$

where the + sign applies to the upfield  $^1\text{H}^{\text{N}}$ - $^{15}\text{N}$  doublet component ( $^1J^{\text{NH}} < 0$ ), and  $\Delta$ ,  $\lambda$  and  $\eta$  correspond to homonuclear dipolar relaxation,  $\text{H}^{\text{N}}$ - $^{15}\text{N}$  dipolar relaxation and the cross correlation between the  $^1\text{H}$  CSA and the  $\text{H}^{\text{N}}$ - $^{15}\text{N}$  dipolar interaction, respectively. They are given by:

$$\Delta = q[5J(0) + 9J(\omega_{\text{H}}) + 6J(2\omega_{\text{H}})] \quad (51)$$

$$\lambda = d[4J^{\text{dd}}(0) + 4\alpha^2 J^{\text{cc}}(0) + 3J^{\text{dd}}(\omega_{\text{H}}) + 3\alpha^2 J^{\text{cc}}(\omega_{\text{H}}) + J^{\text{dd}}(\omega_{\text{H}} - \omega_{\text{N}}) + 3J^{\text{dd}}(\omega_{\text{N}}) + 6J^{\text{dd}}(\omega_{\text{H}} + \omega_{\text{N}})] \quad (52)$$

$$\eta = 2\alpha d[4J^{\text{cd}}(0) + 3J^{\text{cd}}(\omega_{\text{H}})], \quad (53)$$

where  $q = \sum_k \gamma_{\text{H}}^4 h^2 / (80\pi^2 r_{\text{Hk}}^6)$  and the summation extends over all protons  $k$  in the vicinity of the amide proton of interest with  $r_{\text{Hk}}$  being the interproton distance;  $d = \gamma_{\text{H}}^2 \gamma_{\text{N}}^2 h^2 / (80\pi^2 r_{\text{HN}}^6)$ ,  $\alpha = 4\pi B_0 (\delta_{||} - \delta_{\perp}) r_{\text{HN}}^3 / (3h\gamma_{\text{N}})$ , and  $r_{\text{HN}}$  is the  $^{15}\text{N}$ - $^1\text{H}$  distance, assumed to be 1.02 Å. The spectral densities  $J^{\text{dd}}(\omega)$ ,  $J^{\text{cc}}(\omega)$  and  $J^{\text{cd}}(\omega)$  are for dipolar coupling autocorrelation, CSA autocorrelation and dipolar coupling-CSA cross correlation, respectively. For the present case, where the angle  $\theta$  is assumed to be small ( $\theta \ll 1$ ) and the relative orientation of the dipolar coupling and CSA tensors was assumed to be independent of the internal motion, one has  $J^{\text{dd}}(\omega) = J^{\text{cd}}(\omega) / P_2(\cos \theta)$ . Thus, the superscript in the spectral density function may be dropped, and Eq. (53) can be rewritten as

$$\eta = 2\alpha d[4J(0) + 3J(\omega_{\text{H}})]P_2(\cos \theta). \quad (54)$$

In the absence of contribution to the spectral densities from slow conformational changes, values for  $J(0)$  and  $J(\omega_{\text{H}})$  can be obtained directly from the  $^{15}\text{N}$   $T_1$ ,  $T_2$  and  $^{15}\text{N}$ - $^1\text{H}$  NOE values:

$$J(\omega_{\text{H}}) = (2/5)(\text{NOE} - 1)(\gamma_{\text{N}}/\gamma_{\text{H}})/(dT_1); \quad (55)$$

$$J(0) = [1/(dT_2) - 10J(\omega_{\text{H}}) - 3(1 + \alpha^2)J(\omega_{\text{N}})]/(1 + \alpha^2), \quad (56)$$

with

$$J(\omega_{\text{N}}) = (1/6)[1/(dT_1) - 14J(\omega_{\text{H}})]/(1 + \alpha^2). \quad (57)$$

The values of  $\eta$  were determined based on the relaxation interference either by using a 2D experiment which is a simple modification of a HSQC or by a 3D HNH experiments. It was shown that CSA values of  $^1\text{H}$  in ubiquitin's five-stranded  $\beta$ -sheet

( $11 \pm 1.6$  ppm) are significantly larger than those in its  $\alpha$ -helix or its short  $3_{10}$  helix. Interestingly, Fig. 25 shows the correlation between the measured  $^1\text{H}$  CSA and the hydrogen bond length ( $R_{\text{H}\cdots\text{O}} - 1.3$ ) $^{-2}$ . The best agreement is given by the following equation:

$$\text{CSA} = 4.9 + 1.96/(R_{\text{H}\cdots\text{O}} - 1.3)^2. \quad (58)$$

#### 4. Insights into biological problems

##### 4.1. CSA versus secondary structure

###### 4.1.1. Unoriented samples

**Solution NMR.** A serious drawback to the study of conformation and dynamics of proteins in solution by conventional NMR is the molecular size limitation ( $\leq 30$  kDa). As discussed already in Section 2.2.3, the transverse relaxation rates for the two doublet components of a  $^1\text{H}_\text{N}$ – $^{15}\text{N}$  spin pair may differ due to the effect of interference between  $^1\text{H}_\text{N}$ – $^{15}\text{N}$  dipole–dipole relaxation and CSA of protons [257–260]. The TROSY (transverse relaxation-optimized spectroscopy) technique selects the slowly relaxing resonance line, eliminating the faster relaxing resonance [16,261]. The NMR assignment of a large  $^{13}\text{C}$ ,  $^{15}\text{N}$ -labeled protein is made feasible by a TROSY-type triple-resonance experiment [17,262] and indeed was extended to amide groups of a 110 kDa protein using polarization transfer by cross-correlated relaxation approach (CRINEPT) [18]. The optimal TROSY effect can be obtained by choosing an appropriate magnetic field strength, which, for amide protons, is about 23.5 T, corresponding to a proton resonance frequency of 1 GHz, since the dipole–dipole interaction is independent of the static magnetic field whereas the CSA increases with the magnetic field strength [19,20]. The  $^{15}\text{N}$  nuclei in an amide moiety also show interference between dipole–dipole relaxation and their CSA.

The  $^2\text{H}$ ,  $^{13}\text{C}$ ,  $^{15}\text{N}$ -labeled 148-residue integral membrane protein OmpX from *Escherichia coli* reconstituted with dihexanoyl phosphatidylcholine (DHPC) in mixed micelles of molecular mass of about 60 kDa has been studied by TROSY-type triple-resonance NMR experiments [263]. The  $^{13}\text{C}$  chemical shifts and the nuclear

Overhauser effect data enabled the identification of regular secondary structural elements of OmpX/DHPC in solution. The same type of polypeptide backbone fold is observed in the solution structure and a previously reported crystal structure of OmpX in the presence of the detergent *n*-octyltetraoxyethylene. Complete sequence-specific assignments of the 121-residue polypeptide chain in an octameric 110 kDa protein, uniformly  $^2\text{H}$ ,  $^{13}\text{C}$ ,  $^{15}\text{N}$ -labeled 7,8-dihydroopterin aldolase (DHNA) from *Staphylococcus aureus* were obtained using TROSY-type experiments in aqueous solution at 20 °C, and the regular secondary structures in the solution conformation were found to coincide nearly identically with those in the crystal structure of the DHNA octamer [264].

**NMR analysis of homotetradecameric chaperonin system GroEL–GroES** with a molecular weight of up to 900 kDa was achieved by TROSY/CRINEPT-based  $^{15}\text{N}$ – $^1\text{H}$  correlation experiments [265]. Most amino acid residues of GroES show the same resonance whether free in solution or in complex with chaperonin; however, residues 17–32 show a large chemical shift change on binding. It was also shown that the chemical shift mapping can be used to characterize such protein–protein interactions in large complexes.

**Solid-state NMR.** Application of the conformation-dependent  $^{13}\text{C}$  chemical shifts, as summarized in Table 3, to reveal secondary structures of proteins can be readily tested for a variety of fibrous proteins such as silk fibroin, collagen, etc. the amino acids of which consist of the limited numbers of major amino acid residues, and the resulting polymorphic structures in the solid can be mutually converted using a variety of physical treatments. Crystalline silk fibroins are known to exist in one of the polymorphs, either silk I or silk II ( $\beta$ -sheet) and either the  $\alpha$ -helix or  $\beta$ -sheet forms, depending on the species of silkworm, *Bombix mori* or *Philosophia Cynthia ricini*, respectively. It is straightforward to distinguish the two polymorphs of silk fibroin from *B. mori* by their  $^{13}\text{C}$  chemical shifts [95,96,266,267] with reference to the reference chemical shifts of the conformation-dependent  $^{13}\text{C}$  chemical shifts [22–24], because the variety of amino acid residues is limited to the following four kinds: Gly (42.9%), Ala (30.0%), Ser (12.2%) and Tyr (4.8%). The signals of  $\text{C}_\alpha$  in Ala and Ser residues of silk I are displaced downfield by about 2 ppm as compared with those of silk II, whereas the signals of  $\text{C}_\beta$  in silk I are displaced upfield by 3–4 ppm relative to that of silk II. The major advantage is to be able to estimate the relative proportion of the material that is not readily converted to each other (20–30%) [266]. Distinction of  $\alpha$ -helical and  $\beta$ -sheet signals in the Ala residue of *P. C. ricini* fibroin and the hydration-induced conformational change from the less stable  $\alpha$ -helix to  $\beta$ -sheet region are also very conveniently examined by the  $^{13}\text{C}$  NMR approach [95]. Most of the  $^{13}\text{C}$  NMR signals of the collagen fibril, arising from the major amino acid residues, which amount to approximately 65% (Gly,  $33 \pm 1.3\%$ ; Pro,  $11.8 \pm 0.9\%$ ; Ala,  $10.8 \pm 0.9\%$ ; Hyp,  $9.1 \pm 1.3\%$ ), can readily be assigned, with reference to the peak positions of Ala, Pro, Gly and Hyp from model polypeptides, (Pro-Ala-Gly) $_n$ , (Pro-Pro-Gly) $_{10}$  and (Hyp) $_n$ , taking the collagen-like triple helix conformation [95,96,104–106,268–270].

Conformational characterization is straightforward for synthesized peptides in which nuclei of desired residues are labeled with  $^{13}\text{C}$ , yielding ready distinction among  $\alpha$ -helix,  $\beta$ -sheet and random coil conformations, from their reference chemical shifts data [22,23,271–275]. This approach is also useful for conformational characterization of a variety of membrane proteins, once assignment of peaks to certain residues could be established. The following three types of approach are conceivable: (1) *region-specific assignment of peaks*, (2) *site-specific assignment of peaks based on site-specific mutagenesis and proteolysis* and (3) *sequential assignment*. The *region-specific assignment of peaks* is straightforward by differentiation of mobile C- or N-terminal peaks from less mobile

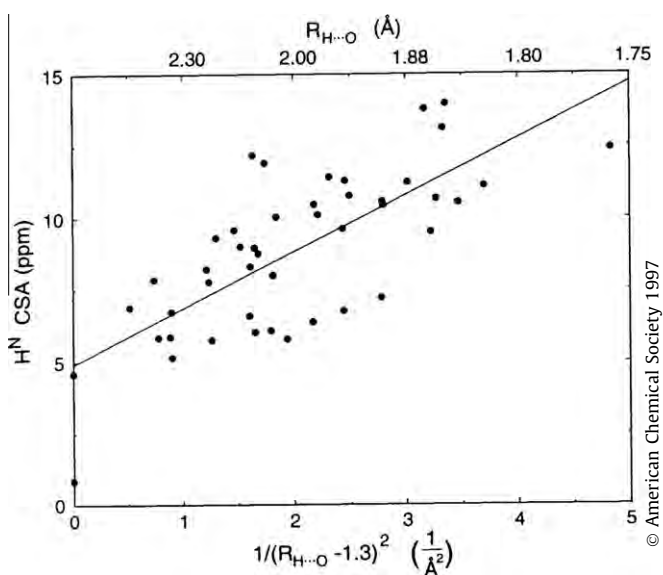


**Fig. 25.** Correlation between  $^1\text{H}$  CSA and hydrogen bond length ( $R_{\text{H}\cdots\text{O}}$ ) in human ubiquitin. Hydrogens were added to the X-ray crystal structure with the program X-PLOR. Amides with low order parameters ( $S^2 < 0.75$ ) and solvent exposed amides for which no hydrogen bonded water was observed in the crystal structure are not included. Reproduced with permission from Tjandra and Bax [257].



transmembrane peaks by comparative recording of peaks between CPMAS and DDMAS NMR spectra [276], together with the data of site-specific proteolytic enzymatic cleavage [277].

The  $^{13}\text{C}$  NMR spectral features of fully-hydrated  $[3-^{13}\text{C}]\text{Ala}$ -labeled bacteriorhodopsin (bR) in 2D crystals from purple membrane differ between the  $^{13}\text{C}$  DD and CPMAS NMR spectra recorded at ambient temperature, as demonstrated in Fig. 26 [276,277]. Several  $^{13}\text{C}$  NMR signals are suppressed in the CPMAS NMR, because the C-terminal  $\alpha$ -helix and its tail undergo fluctuation motions with correlation times of the order of  $10^{-6}$  to  $10^{-8}$  s, respectively. The three intense  $^{13}\text{C}$  NMR signals from the membrane surface (gray; top) in the DDMAS spectrum (consisting of contributions from a total 29 Ala residues) are unambiguously assigned to Ala 228 and 233 (C-terminal  $\alpha$ -helix), Ala 240, 244–246 (C-terminal tail taking random coil), and Ala 235 (at corner of the C-terminal  $\alpha$ -helix) from the upper to the lower field, with reference to the conformation-dependent  $^{13}\text{C}$  chemical shifts. The twelve Ala  $^{13}\text{C}$  NMR peaks in the CPMAS NMR (bottom) can be ascribed to 22 Ala residues present in the transmembrane  $\alpha$ -helices and loops. The assigned peaks indicated at the individual peaks were obtained in view of the selectively reduced  $^{13}\text{C}$  NMR peak-intensity of relevant mutant, in which an individual Ala residue was replaced by other amino acid residues (for instance, A196G, A126V, A215G, etc.) as compared with that of the wild-type, provided that a global conformational change is not induced. Such a  $^{13}\text{C}$  NMR peak from the transmembrane  $\alpha$ -helices can be identified as a single Ala residue by the difference  $^{13}\text{C}$  NMR spectrum between wild-type and a mutant, together with suppressed signals from residues located near the surface (within ca. 8.7 Å) by accelerated transverse relaxation due to surface-bound  $\text{Mn}^{2+}$  [278]. Site-specific assignments of  $^{13}\text{C}$  NMR signals have been attempted for  $[1-^{13}\text{C}]\text{Val}$ -, Pro-,

Trp- and, Ile-labeled bR [279–281].  $[3-^{13}\text{C}]\text{Ala}$ -,  $[1-^{13}\text{C}]\text{Val}$ -labeled ppR were also utilized for the resonance assignment [282,283].

The database of  $^{13}\text{C}$ ,  $^{15}\text{N}$  or  $^1\text{H}$  chemical shifts of various globular proteins of known crystalline structure [26,28,173] was utilized as a reference for sequential assignment of 2D correlation NMR studies on a uniformly  $^{13}\text{C}$ ,  $^{15}\text{N}$ -labeled 144 kDa membrane protein complex, *E. coli* cytochrome  $bo_3$  oxidase [284] and *Natromonas pharaonis* sensory rhodopsin II (NpSRII or ppR) uniformly labeled with the exception of the four dominant residue types (valine, leucine, phenylalanine and tyrosine), which occur in natural abundance  $U[^{13}\text{C}, ^{15}\text{N} (\text{V, L, F, Y})]\text{NpSRII}$  [285].

Resonance assignments based on the isotropic chemical shifts have also been accomplished on a uniformly- $^{13}\text{C}$ -labeled cytochrome-*b5* embedded in bicelles without having to freeze the sample [286]. Similar studies have also been reported for complex non-crystalline complex systems such as intact bovine cortical bone [287]. This MAS approach has been utilized to investigate the effect of the dehydration process in the intact bone. Tentative site-specific assignment of peaks was attempted for uniformly labeled  $\alpha$ -synuclein in a 3D  $^{15}\text{N}$ - $^{13}\text{C}$ - $^{13}\text{C}$  experiment at a low temperature ( $-40^\circ\text{C}$ ) in order to analyze the fibril structure [288]. Most of the signals, however, were not observed at  $0 \pm 3^\circ\text{C}$  and acquisition of spectra at a low temperature is essential for the assignment of chemical shifts. In such cases, it is essential to examine whether one is able or not to record all the expected  $^{13}\text{C}$  resonances without any suppressed peaks due to interference of the motional frequency, if any, with the frequency of either proton decoupling or MAS, as will be discussed in the next section. Conformational constraints based on isotropic or anisotropic chemical shifts have also been reviewed [289,290].

#### 4.1.2. Oriented samples

Secondary structure of peptides and proteins can be determined from orientational constraints such as dipole–dipole, CSA and quadrupolar interactions. These NMR parameters are routinely measured from mechanically (sandwiched between thin glass plates) or spontaneously, magnetically aligned systems. Indeed, orientational constraints from CSAs were utilized to study the polypeptide backbone of  $[^{13}\text{C}]$  or  $[^{15}\text{N}]\text{Ala}$  gramicidin A in oriented lipid bilayers [198–200,291–295]. In these samples, the observed chemical shifts vary with the relative orientation of the principal axes of the CSA at respective sites relative to the applied magnetic field. Orientational constraints for gramicidin A from  $^{15}\text{N}$  CSAs and  $^{15}\text{N}$ - $^1\text{H}$  dipole–dipole interactions were determined by recording SLF spectra [61,296]. The line widths in the dipolar coupling dimension of the 2D SLF spectrum are reduced by more than an order of magnitude by suppression of the broadening effects from inter-proton coupling by I-I homonuclear decoupling using the flip-flop Lee–Goldburg irradiation. The 2D PISEMA (Polarization Inversion Spin Exchange at the Magic Angle) spectrum has turned out to be indispensable for elucidating conformational feature of peptides and proteins in uniaxially oriented lipid bilayers. Details of the PISEMA pulse sequence, steps for the experimental set-up, data interpretation, effects of pulse imperfections and approaches to overcome such effects, and applications can be found in a recent review article [297].

The characteristic wheel-like patterns of resonances observed in these PISEMA spectra reflect helical wheel projections of residues in both transmembrane and in-plane helices called PISA (polarity index slant angle) without resonance assignments and hence provide direct indices of the secondary structure and topology of membrane proteins as viewed from the tilt angles of the transmembrane peptides relative to the bilayer normal [298,299]. Fig. 27a illustrates  $^{15}\text{N}$ - $^1\text{H}$  dipolar couplings observed from PISEMA spectra of multiple and single-site labeled preparations of a viral M2-TMP (transmembrane peptide) in hydrated lipid bilayers

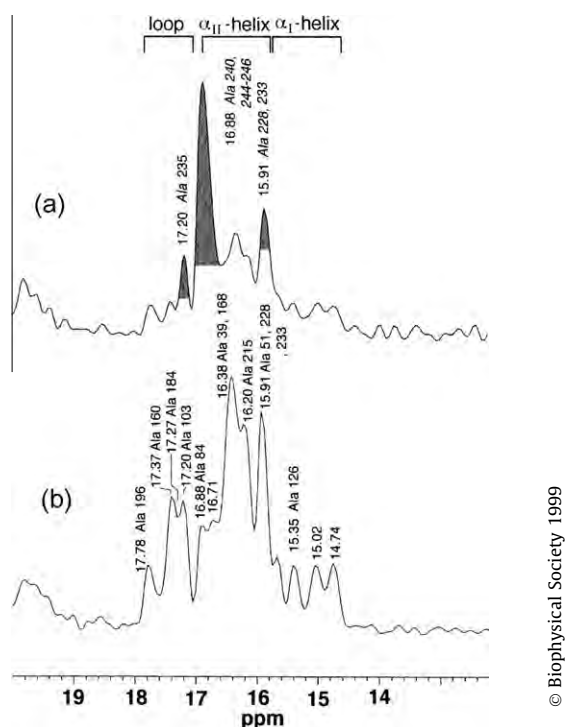


**Fig. 26.**  $^{13}\text{C}$  DDMAS (a) and CPMAS NMR (b) spectra at 100 MHz of  $[3-^{13}\text{C}]\text{Ala}$ -labeled bR from purple membrane. Peaks in gray from the C-terminus are preferentially suppressed by the CPMAS NMR, caused by a time-averaged  $^{13}\text{C}$ - $^1\text{H}$  dipolar interaction in the presence of isotropic motions in the C-terminus. Naturally, the remaining peaks in the DDMAS are identical to those of the CPMAS NMR, except for the reduced peak-intensities in the former. Reproduced with permission from Tuzi et al. [276].

aligned with the bilayer normal parallel to the magnetic field direction [299]. A mirror image pair of “PISA wheels” is immediately apparent as shown in Fig. 27b. The PISEMA spectra calculated for a full-range of possible orientations of an ideal 19-residue  $\alpha$ -helix, with 3.6 residues per turn and identical backbone dihedral angles ( $\phi = -65^\circ$  and  $\psi = -40^\circ$ ) for all residues are shown in Fig. 28 [300]. When the helical axis is parallel to the bilayer normal all of the amide sites have an identical orientation relative to the direction of the applied magnetic field and therefore all of the resonances overlap with the same  $^1\text{H}$ – $^{15}\text{N}$  dipolar coupling and  $^{15}\text{N}$  chemical shift frequencies. Tilting the helix away from the membrane normal breaks the symmetry, introducing variations in the orientations of the amide NH bond vectors relative to the field direction. This is manifested in the spectra as dispersions of both  $^1\text{H}$ – $^{15}\text{N}$  dipolar coupling and  $^{15}\text{N}$  chemical shift frequencies, as shown in Fig. 28j. No structural information, however, is available for the sites of the N- and C-terminal residues with isotropic resonances because of complete motional averaging of dipolar interactions. When the helical axis is parallel to the bilayer normal all of the amide sites have an identical orientation relative to the direction of the applied magnetic field and therefore all of the resonances overlap with the same  $^1\text{H}$ – $^{15}\text{N}$  dipolar coupling and  $^{15}\text{N}$  chemical shift frequencies.

An algorithm for fitting the protein structure to PISEMA spectra has been described [301] and its application to helical proteins in oriented samples was demonstrated using both simulated and experimental results. Although the algorithm can be applied in an “assignment-free” manner to spectra of uniformly labeled proteins, the precision of the structure fitting is improved by the addition of resonance assignment information, for example the identification of resonances by residue type from spectra of selectively labeled proteins. In addition, a simple, qualitative approach has been proposed for determination of a membrane protein secondary structure, including  $\beta$ -strands associated with membranes, and topology in lipid bilayers based on PISEMA and HETCOR spectra [302]. Indeed, PISA wheels are extremely sensitive to the tilt, rotation, and twist of  $\beta$ -strands in the membrane. A “shotgun” NMR approach relies solely on the spectra from one uniformly and several selectively labeled  $^{15}\text{N}$  samples, and on the fundamental symmetry properties of PISA wheels to enable the simultaneous sequential assignment of resonances and the measurement of the orientationally dependent frequencies [303]. The shotgun NMR ap-

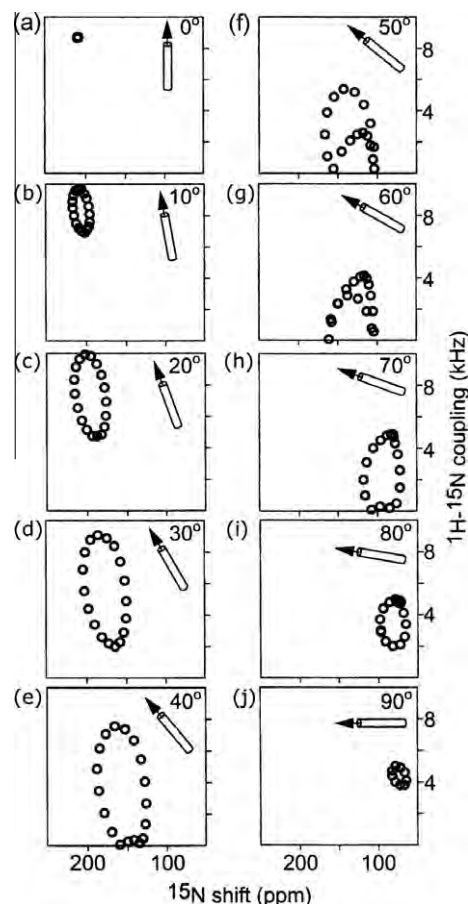


**Fig. 28.**  $^{15}\text{N}$  PISEMA spectra calculated for a 19-residue  $\alpha$ -helix with 3.6 residue per turn and uniform dihedral angles ( $\phi = -65^\circ$ , and  $\psi = -40^\circ$ ) at various tilt angles relative to the bilayer normal. (a)  $0^\circ$ , (b)  $10^\circ$ , (c)  $20^\circ$ , (d)  $30^\circ$ , (e)  $40^\circ$ , (f)  $50^\circ$ , (g)  $60^\circ$ , (h)  $70^\circ$ , (i)  $80^\circ$ , (j)  $90^\circ$ . The principal values and molecular orientation of the  $^{15}\text{N}$  tensor ( $\delta_{11} = 64$  ppm,  $\delta_{22} = 77$  ppm,  $\delta_{33} = 217$  ppm,  $\angle \delta_{33}\text{NH} = 17^\circ$ ). Reproduced with permission from Marassi and Opella [300]. Copyright 2000 Elsevier.

proach short-circuits the laborious and time-consuming process of obtaining complete sequential assignments prior to the calculation of a protein structure from the NMR data by taking advantage of

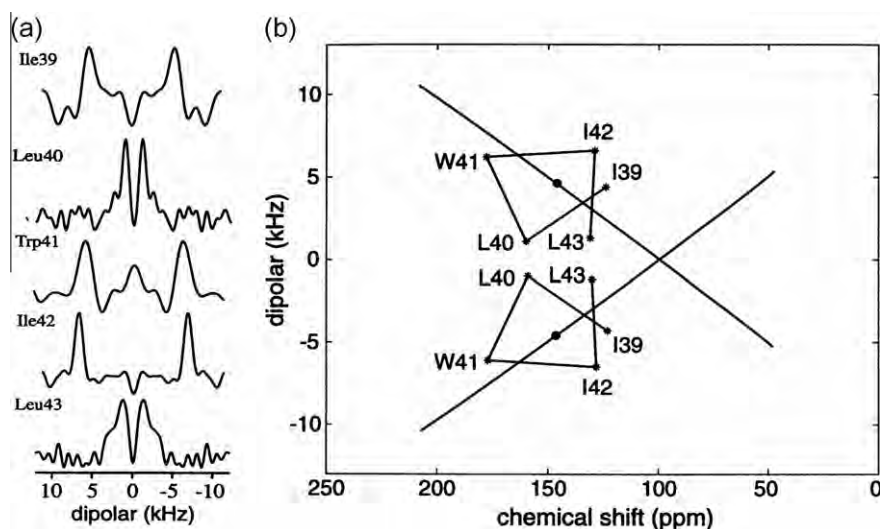


**Fig. 27.** (a) Dipolar splittings observed in the  $^{15}\text{N}$  PISEMA spectra of multiple and single site labeled preparations of M2-TMP in hydrated lipid bilayers aligned with the bilayer normal to the parallel to the magnetic field direction. (b) Display of the dipolar splittings (\*) at their observed chemical shift. The resonances are connected in helical wheel fashion. Reproduced with permission from Wang et al. [299]. Copyright 2000 Elsevier.

the orientational information inherent to the spectra of aligned proteins.

A total of five two-dimensional  $^1\text{H}/^{15}\text{N}$  PISEMA spectra, from one uniformly and four selectively  $^{15}\text{N}$ -labeled samples, were reported to be sufficient to determine the structure of the membrane-bound form of the 50 residue major pVIII coat protein of magnetically aligned fd filamentous bacteriophage, as shown in Fig. 29 [304]. The imperfections of the PISEMA sequence were overcome by the use of the HIMSELF or HERSELF sequence [305,306]. This method was utilized to determine the tilt of the transmembrane domain of the full-length uniformly- $^{15}\text{N}$ -labeled cytochrome-*b5* in aligned bicelles under physiologically-relevant experimental conditions [307]. This study demonstrated the spectral editing approach to distinguish resonances from the soluble and transmembrane domains based on dynamical differences among them. It should also be noted that the combination of SLF and using aligned lipid bilayers have been powerful in providing insights into the mechanism of membrane disruption by antimicrobial peptides [308,309].

Numerous studies have utilized these approaches to address biological questions and to obtain structural insights: for transmembrane domains of M2 protein from influenza A [310], phospholamban [311–313], membrane  $\beta$ -barrels [314], pore forming protein TatAd of the twin-arginine translocase [315], bacteriorhodopsin [316] and membrane-associated peptaibols ampuosporin A and alamethicin [317]. In all these applications, one could use CSA tensors accurately measured from model peptides to determine the structural parameters. These studies considerably benefit

from the investigation of the variation of CSA tensors in proteins in different environments. PISA spectra of uniformly  $^{15}\text{N}$ -labeled chemokine receptor, CXCR1 as a GPCR and selectively labeled *E. coli* diacylglycerol kinase (DAGK) were examined on the basis of PISEMA spectra recorded in magnetically aligned bicelles and liquid crystalline bilayers, respectively [318,319].

The determined torsion angles ( $\phi$ ,  $\psi$ ) of oriented silk II structure of *B. mori* silk fibroin, ( $-140^\circ$ ,  $142^\circ$ ) for the Ala residues and ( $-139^\circ$ ,  $135^\circ$ ) for the Gly residues [56,57], are very close to those proposed by X-ray diffraction [320,321]. Highly-oriented  $\alpha$ -helical chains of poly( $\gamma$ -benzyl L-glutamate) (PBLG) film can be prepared by evaporating slowly the solvent from the PBLG LC solution in a strong magnetic field of an NMR magnet [322]. It was demonstrated that there exists a linear relationship between the order parameter  $S$  of the  $\alpha$ -helical polypeptide chains with respect to the applied magnetic field and the observed main-chain carbonyl  $^{13}\text{C}$  chemical shift,  $\delta_{\text{obs}}$ , such that  $S = 0.024 \times \delta_{\text{obs}} - 3.758$ . Using the  $\delta_{\text{obs}}$  value and the  $S$ - $\delta_{\text{obs}}$  relation, the order parameter  $S$  of PBLG in the liquid crystalline state at 300 K was determined to be  $0.875 \pm 0.025$ .

## 4.2. CSA and dynamics

### 4.2.1. Solution NMR

Backbone fast *picosecond to nanosecond* dynamics for biomacromolecules in solution has been extensively analyzed by the examination of their nuclear relaxation times, utilizing the model-free approach [248,323] based on a generalized order parameter,  $S$ , which is a measure of the spatial restriction of motions, and an effective correlation time,  $\tau_e$ , which is a measure of the rate of motion. For the special case that the overall motion can be described by a single correlation time  $\tau_M$ , our approach to extracting the unique information (i.e.  $S$  and  $\tau_e$ ) is based on the following simple equation for the spectral density  $S$ :

$$J(\omega) = (2/5) \{ S^2 \tau_M / [1 + (\omega \tau_M)^2] + (1 - S^2) \tau / [1 + (\omega \tau)^2] \}, \quad (59)$$

with

$$\tau^{-1} = \tau_M^{-1} + \tau_e^{-1}, \quad (60)$$

In addition,  $S$  is a model-independent measure of the degree of spatial restriction of motion with the inequalities  $0 \leq S^2 \leq 1$ : if the internal motion is isotropic, then  $S = 0$ . If the motion is completely restricted, then  $S = 1$ .

The longitudinal relaxation rate ( $R_1$ ) for fast motions, as viewed from  $^{15}\text{N}$  or  $^{13}\text{C}$  nuclei, is the sum of the contributions of the dipole-dipole and CSA effects, and in the absence of the term of chemical exchange is given by:

$$R_1 = 3(d^2 + c^2)J(\omega_N) + d^2[3J(\omega_N) + J(\omega_H - \omega_N) + 6J(\omega_H + \omega_N)] \quad (61)$$

where  $d = -(\mu_0/(4\pi))\gamma_H\gamma_N\hbar/(4\pi r_{\text{NH}}^3)$  and  $c = -\omega_N(\delta_{\parallel} - \delta_{\perp})$  are dipole-dipole and CSA interactions, respectively. The relaxation data for  $^{15}\text{N}$ -enriched human ubiquitin are incompatible with isotropic rotational diffusion but agree well with an axially symmetric rotational diffusion with rotational diffusion anisotropy  $D_{\parallel}/D_{\perp}$  of 1.17, consistent with hydrodynamic calculations [324]. Anisotropic rotational diffusion of perdeuterated HIV protease complexed with the sub-nanomolar inhibitor DMP323 has been studied at two different magnetic field strengths [252].

Cross-correlation between  $^{15}\text{N}$ - $^1\text{H}$  dipolar and  $^{15}\text{N}$  CSA gives rise to different relaxation rates for the doublet components of  $^{15}\text{N}$ - $\{^1\text{H}\}$  backbone amides [250]. The relaxation interference is directly proportional to the generalized order parameter  $S^2$  of the N-H bonds in the peptide backbone, and this relation can be utilized to obtain approximate values for these order parameters. In

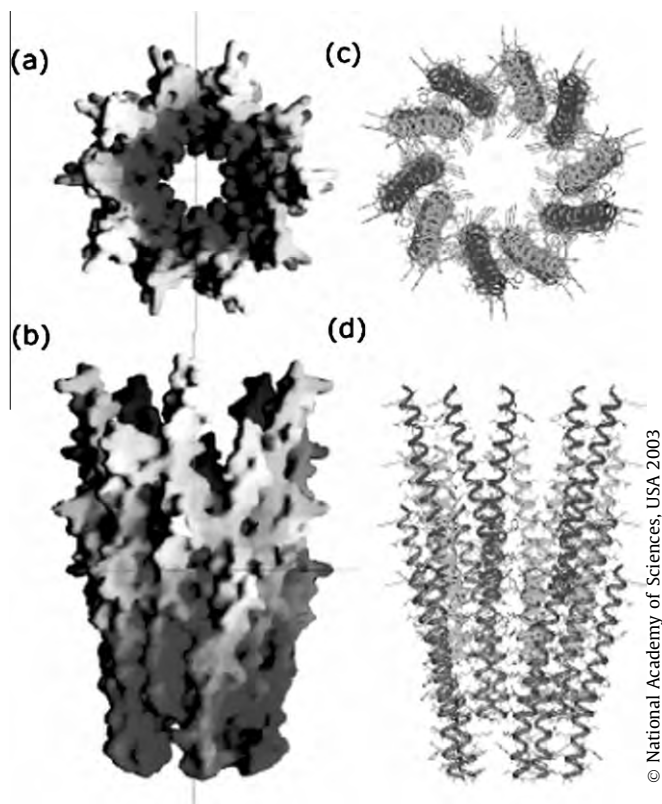


**Fig. 29.** Model of a section of the Y21M fd filamentous bacteriophage capsid built from the coat protein subunit structure, which was determined by PISEMA spectra. The symmetry was derived from fiber diffraction studies. ((a) and (b) Representations of the electrostatic potential on the molecular surface of the virus. ((a) is a bottom view and (b) is a side view along the virus axis). (c) and (d) Views of the capsid structure showing the arrangement of the coat proteins in pentamers and further assembly of the 2-fold helical structure. Reproduced with permission from Zeri et al. [304].



contrast, Engelke and Rüterjans examined the backbone dynamics of uniformly  $^{13}\text{C}/^{15}\text{N}$ -enriched ribonuclease  $T_1$  using carbonyl carbon relaxation times, to determine the order parameters ( $S^2$ ) and the effective internal correlation times ( $\tau_i$ ) [325]. Dayie and Wagner recorded proton-detected  $^{13}\text{C},^{15}\text{N}$  spectra of the N-terminal 14 kDa domain of the actin-binding protein, villin, at 9.4, 11.7 and 17.6 T [326]. Three rate measurements were used to obtain the values of the spectral density functions at zero  $J(0)$ , nitrogen  $J(\omega_N)$ , and carbonyl  $J(\omega_C)$  frequencies. In addition,  $^{13}\text{C}$  carbonyl NMR studies are potentially useful for probing hydrogen-bond dynamics, as significantly different average  $J(0)$  values are observed for hydrogen-bonded and solvent-exposed carbonyls. The anisotropy of rapid fluctuations of peptide planes in ubiquitin is explored by combined  $^{15}\text{N}$  and  $^{13}\text{C}$  nuclear spin relaxation measurements and molecular dynamics (MD) computer simulation [327]. They show that the dominant fluctuation axes for the backbone  $^{15}\text{N}$  and  $^{13}\text{C}$  spins are nearly parallel to the  $C_{i-1}^\alpha - C_i^\alpha$  axes.

In contrast, the presence of slow motions for backbone and side-chains with a time-scale of *millisecond to microsecond* is more biologically relevant than the fast motions detectable by relaxation parameters for a variety of globular proteins in relation to their specific activity including transient formation of ligand-binding-competent states and transitions coupled to enzyme catalysis [328–330]. In such cases, contribution of the last term  $R_{ex}$  in Eq. (43) should be taken into account. Indeed, the excess transverse relaxation rate ( $R_{ex}$ ) is expressed as a rate of the standard two site (A and B) exchange of nuclei between different conformations/states with different chemical shifts, which can be measured either by careful evaluation of  $R_2$  (see Eq. (43)) or by applying a train of  $180^\circ$  radio-frequency pulses separated by a delay of length  $\tau_{cp}$  in the CPMG (Carr–Purcell–Meiboom–Gill) experiment. The value of  $R_{ex}$  is given by [331]:

$$R_{ex} = \Delta\delta^2\gamma^2B_0^2p_ap_b(1/k_{ex})[1 - (2/\tau_{cp}k_{ex})\tanh(\tau_{cp}k_{ex}/2)] \quad (62)$$

where  $k_{ex}$  is the rate constant of the exchange process,  $\Delta\delta$  is the chemical shift difference between the two conformations, A and B, while  $p_a$  and  $p_b$  are the fractional populations of A and B, respectively.

The internal mobility in  $^{15}\text{N}$ -enriched protein eglin c was analyzed as a frequency spectrum of NH bonds from the spectral density mapping at multiple fields [332]. Here, dynamic heterogeneity along the protein backbone is manifested most clearly in spectral density values at low frequencies (<100 MHz), indicating slow exchange processes manifested as an increase of  $J_{eff}(0)$  with the spectrometer field strength.

The temperature dependence of backbone motions in *E. coli* ribonuclease HI was studied on a multi-time-scale by  $^{15}\text{N}$  spin relaxation [333,334]. Conformational exchange on a microsecond time-scale was observed for a large number of residues forming a continuous region of the protein that includes the coiled-coil formed by helices  $\alpha_A$  and  $\alpha_B$ . The temperature dependence of motion of the backbone N–H bond vectors on picoseconds to nanosecond time scales was characterized by the changes of the order parameter ( $S^2$ ), internal correlation time ( $\tau_e$ ), and phenomenological CPMG exchange rate constants ( $R_{ex}$ ) plotted versus residue number as shown in Fig. 30 [334].

Analysis of spin relaxation parameters of  $^{15}\text{N}$  in a homodimeric protein of HIV-protease showed that the flaps that cover the active sites of the protein have terminal loops undergoing large amplitude motions on the *ps* to *ns* time scale, while the tips of the flaps undergo a conformational exchange on the  $\mu\text{s}$  time scale [335]. This enforces the idea that the flaps of the proteinase are flexible structures that facilitate function by permitting substrate access to and product release from the active site of the enzyme.

Measurements of  $^{15}\text{N}$  relaxation parameters have been used to characterize the backbone dynamics of the folded and denatured states of the N-terminal SH3 domain from the adapter protein drk, in high salt or guanidium chloride, respectively [336]. The levels of backbone dynamics in the folded protein show little variation across the molecule and are of similar magnitude to those determined previously. The denatured state of the domain, however, exhibits both more extensive and more heterogeneous dynamics than the folded state.

Relaxation properties of the backbone  $^{15}\text{N}$  nuclei were measured to study the rotational correlations of the two domains and properties of the linker region for phosphotransfer and Che Y-binding domains of the histidine autokinase CheA [337] and cell binding region of fibronectin [338]. In the former, flexible domain linkers are extended and flexible terminal polypeptide chains can have significant effects on the motional properties of adjacent structured regions. In the latter, non-specific protein–protein interactions provide the bulk of the thermodynamic stabilization and the motional constraints of the two modules.

The structure of the C-terminal RNA recognition domain of ribosomal protein L11 has been solved by 3D NMR [339]. Although the structure can be considered to be high-resolution in the core, 15-residues between helix  $\alpha_1$  and strand  $\beta_1$  form an extended, unstructured loop. The loop is moving on a picosecond to nanosecond time scale in the free protein but not in the protein bound to RNA.

A strong correlation between phosphorylation-driven activation of the signaling protein NtrC, with two highly conserved components of histidine kinases and response regulators, and microsecond time-scale backbone dynamics as studied by  $^{15}\text{N}$  relaxation measurements has been reported [340]. The motions of NtrC in three functional states were characterized: unphosphorylated (inactive), phosphorylated (active) and a partially active mutant. These dynamics are indicative of exchange between inactive and active conformations.

Internal protein dynamics are intimately connected to enzyme catalysis. During catalytic action of the enzyme cyclophilin A, conformational fluctuations of the active site that occur on a time scale of hundreds of microseconds were detected by mapping the characteristic displacement of  $^{15}\text{N}$  chemical shifts and  $R_2$  relaxation rates [341]. The rates of conformational dynamics of the enzyme strongly correlate with the microscopic rates of substrate turnover.

The analysis of the exchange term in the  $R_2$  relaxation rates showed that the observed  $\mu\text{s}$ – $\text{ms}$  dynamics in plastocyanin from the cyanobacteria *Anabaena variabilis* (*A. v.* PCu) are caused primarily by the protonation/deprotonation process of two histidine residues, His92 and His61, with His92 being ligated to the Cu (I) ion [342].

Dynamic requirements for a functional protein hinge in triosephosphate isomerase (TIM) were analyzed for the wild-type and a mutant at loop 6, PGG/GGG, by means of  $^1\text{H}$ ,  $^{15}\text{N}$  and  $^{13}\text{C}$  chemical-shift differences,  $^{15}\text{N}$   $R_2$  measurements [343]. These experiments elucidate an important principle of catalytic hinge design in proteins.

The backbone dynamics of domain III of the envelope proteins (E-D3) of Langat virus (LGT-E-D3) was investigated using  $^{15}\text{N}$  relaxation measurements [344]. Solution structure and dynamics of LGT-E-D3 suggested potential residues that could form a surface for molecular recognition, and thereby represent a target site for antiviral therapeutics design.

Millisecond time scale dynamics plays an important role and relaxation dispersion NMR spectroscopy has been particularly informative [345,346]. The integral membrane enzyme PagP reconstituted in detergent exists in equilibrium between two states, relaxed (R) and tense (T). A comparison of  $^{15}\text{N}$  chemical shifts between the two states indicates that major structural



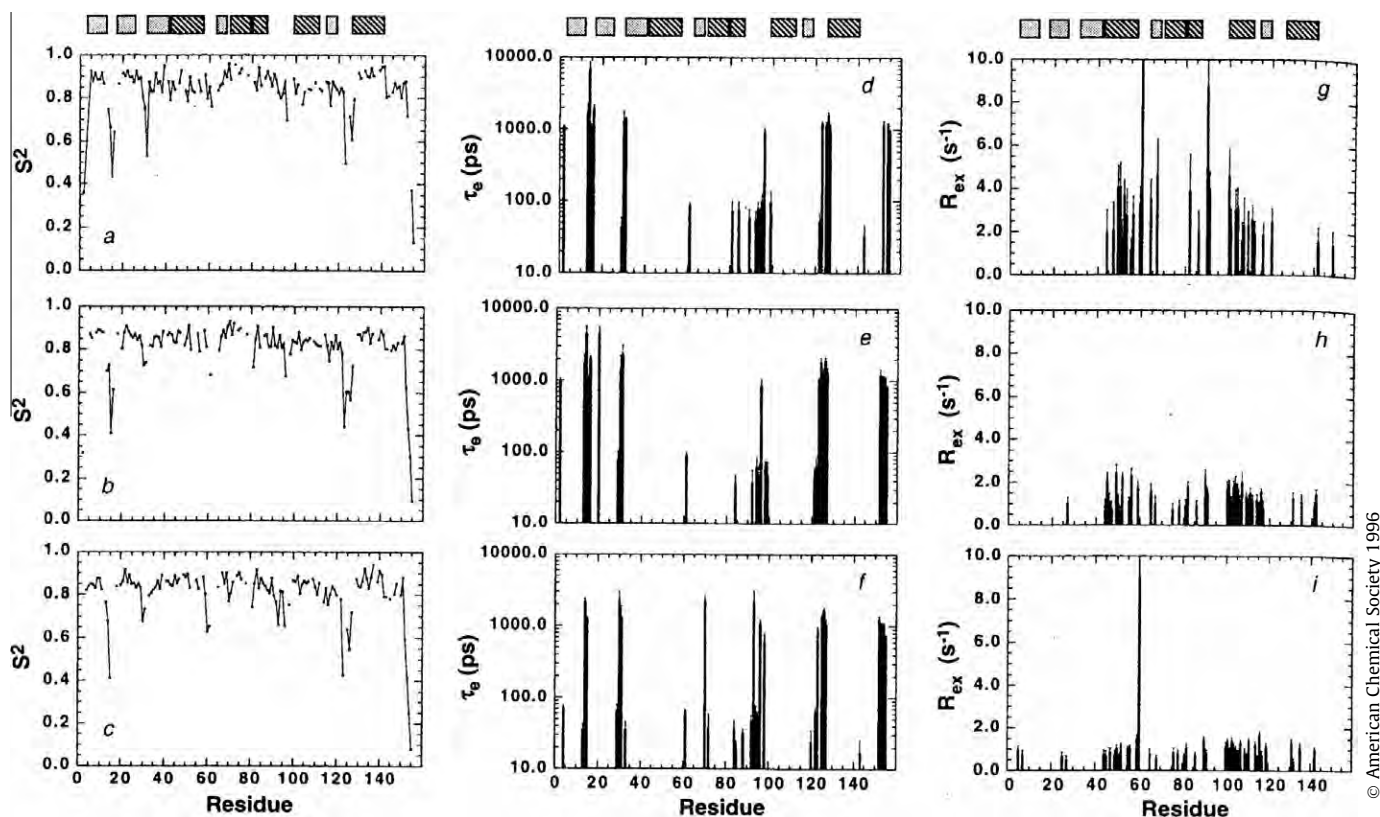


**Fig. 30.** Dynamical parameters obtained for RNase H from *E. coli*. Order parameters,  $S^2$ , of  $^{15}\text{N}$ -H bond vectors are plotted versus residue number at (a) 285 K, (b) 300 K and (c) 310 K; internal correlation times,  $\tau_e$ , are plotted at (d) 285 K, (e) 300 K and (f) 310 K; and phenomenological CPMG chemical exchange rate constants,  $R_{ex}$ , are plotted versus residue number at (g) 285 K, (h) 300 K and (i) 310 K. At 285 K, the value of  $R_{ex}$  for Lys 60 is  $23 \pm 4$ . At 300 K, the resonance for Lys 60 is overlapped with the resonance for Ile 7 and cannot be quantified. Error bars are not shown for (a)–(c) for clarity; average uncertainties in  $S^2$  are 0.024, 0.011 and 0.010 for 285, 300 and 310 K, respectively. Dark rectangles represent  $\beta$ -sheet regions and hatched rectangles represent  $\alpha$ -helical region of RNase H. Reproduced with permission from Mandel et al. [334].

changes occur in the large extracellular L1 loop and adjacent regions of the  $\beta$  barrel. In addition to the R/T interconversion, other conformational exchange processes are observed in the R state, showing it to be quite flexible. Thus a picture emerges in which substrate entry is facilitated by the mobility of the R state, whereas the relatively rigid T state adopts a radically different conformation in a region of the protein known to be essential for catalysis. It has also been demonstrated that relaxation dispersion experiments make available kinetic, thermodynamic and structural information on “excited” states that often comprise only a few percent of the total population of molecules in solution and that cannot be observed directly in even the most sensitive NMR experiments [345,347,348]. The relaxation dispersion curve, probing the backbone amide  $^{15}\text{N}$  linewidth for SH3 domain from Fyn tyrosine kinase, was fitted to a three state model including F, folded, U, unfolded and I, intermediate states, at temperatures, ranging from 15 to 35 °C, at spectrometer fields of 500, 600 and 800 MHz and for all residues in the protein with sizable dispersions. It is thus possible to characterize in some detail the kinetics and thermodynamics of this folding/unfolding reaction.

As a complementary means to the widely used  $^{15}\text{N}$   $T_2$  CPMG experiments, it was shown that slow motion in a protein can be detected by multiple refocusing of heteronuclear nitrogen/proton multiple quantum coherence, as demonstrated for I23 and T55 which are quite close in space although in different loops of ubiquitin [349].

#### 4.2.2. Solid-state NMR

**Peptides:** It is expected that the backbones of small peptides in the solid-state are considered static compared with side chains.

Nevertheless, it was shown that backbone dynamics of small peptides containing Gly-Gly residues can be detected by analyzing the  $^{15}\text{N}$  NMR line shapes powder pattern and the  $^{13}\text{C}$   $T_2$  obtained under proton decoupling [197]. It was found that by lowering the temperature from 40 to  $-120$  °C, the  $\delta_{11}$  and  $\delta_{22}$  values of Gly[ $^{15}\text{N}$ ]Gly shift to low and high field by 2.5 ppm, respectively, while the  $\delta_{33}$  value is unchanged. The observed displacement of the principal values of the  $^{15}\text{N}$  chemical shift tensor was interpreted by taking account of librational motion with small amplitudes. This librational motion was interpreted in terms of a two-site jump model about the  $\delta_{33}$  axis that is very close to the  $\text{C}_\alpha\text{C}_\alpha'$  carbons from the connecting two peptide units with a jump angle of  $17^\circ$  and a jump frequency higher than 1 kHz, as required by the simulated spectra. The correlation times of the librational motions of the peptide plane was estimated as  $2.3 \times 10^{-4}$  s at ambient temperature by analyzing  $^{13}\text{C}$   $T_2$  values in the presence of a  $^1\text{H}$  decoupling field of 50 kHz [350]. Here, it is noticed that the CSA for  $^{15}\text{N}$  amide and  $^{13}\text{C}$  carbonyl nuclei are of the order of  $10^3$  and  $10^4$  Hz, respectively, in view of the breadth of the respective tensors. This means that protein dynamics reflected in changes in CSA values are sensitive to the time scales of  $10^{-3}$  to  $10^{-4}$  s, respectively.

The dynamics of bee venom melittin, bound to magnetically oriented DMPC bilayers, can be visualized from the  $^{13}\text{C}$  NMR lineshapes of [ $1\text{-}^{13}\text{C}$ ]Gly<sup>3</sup>, Val<sup>5</sup>, Gly<sup>12</sup>, Leu<sup>16</sup> and Ile<sup>20</sup> labeled preparations recorded at various temperatures [351]. The  $^{13}\text{C}$  CSA values ( $\delta_{||} - \delta_{\perp}$ ) of the carbonyl carbons obtained from a slow MAS experiment indicate that melittin undergoes rotation or reorientation of the whole  $\alpha$ -helical rod about the average helical axis, parallel to the bilayer normal, rather than the helical axis.

The  $^{13}\text{C}$  and  $^{31}\text{P}$  NMR spectra of a transmembrane  $\alpha$ -helical peptide,  $[1-^{13}\text{C}]\text{Ala}^{14}$ -labeled A(6–34) of bacteriorhodopsin (bR), incorporated in DMPC bilayers or in a magnetically aligned system containing dynorphin [A(6–34):dynorphin:DMPC = 4:10:100] were examined to clarify its dynamics and orientation in the lipid bilayer [107]. This peptide undergoes rapid rigid-body rotation about the helical axis at ambient temperature to produce an axially symmetric  $^{13}\text{C}$  CSA, whereas this symmetric anisotropy changes to an asymmetric pattern at temperatures below  $10^\circ\text{C}$ .  $^{13}\text{C}$  NMR spectra of  $[3-^{13}\text{C}]$ -,  $[1-^{13}\text{C}]$ - or  $[1-^{13}\text{C}]\text{Val}$ -labeled transmembrane peptides of bR were also recorded in a lipid bilayer [273]. The  $^{13}\text{C}$  chemical shifts of the  $[3-^{13}\text{C}]\text{Ala}$ -labeled peptides in the bilayer were displaced downfield by 0.3–1.1 ppm, depending upon the amino-acid sequence, with respect to those in the solid-state, which were explained in terms of local conformational fluctuations ( $>10^2$  Hz) deviated from the torsion angles ( $\alpha_{\text{H}}$ -helix) from those of a standard  $\alpha$ -helix, in an anisotropic environment. The carbonyl  $^{13}\text{C}$  peaks, on the other hand, are not significantly displaced by such local anisotropy fluctuations. Instead, they are more sensitive to the manner of hydrogen bonding interactions than the local anisotropy fluctuations.

A variable temperature solid-state  $^{15}\text{N}$  NMR study on lipid vesicles containing magainin 2 revealed its backbone dynamics [352]. The backbone dynamics of a channel-forming second-transmembrane segment of GABA receptor in lipid bilayers has been determined using PISEMA experiments [353]. The effect of whole-body motion on the peptide orientations obtained from calculated PISEMA spectra was analyzed [354]. It was shown that wheel-like patterns are still preserved, and it is possible to determine the average peptide tilt and azimuthal rotation angles using simple static models for the spectral fitting, as demonstrated for the model peptide, WLP23, in a lipid membrane.

The effects of cholesterol on the dynamics of pardaxin and its ability to form ion-channels and disrupt bacterial cell membranes have been investigated using PISEMA experiments [355].

The dynamic structure of disulfide-removed linear analogs of tachyplesin-I (TP-I), where four Cys residues were replaced by aromatic and aliphatic residues, in bacteria-mimetic POPE/POPG bilayer have been studied by solid-state NMR [356]. The active TP-I and TPF4 are both highly mobile in the liquid crystalline phase of the membrane while the inactive TPA4 is completely immobilized. The different mobilities are revealed by the temperature-dependent  $^{13}\text{C}$  and  $^{15}\text{N}$  spectra,  $^{13}\text{C}$ -H and  $^{15}\text{N}$ -H dipolar couplings and  $^1\text{H}$  rotating frame spin-lattice relaxation times.

**Fibrous proteins.** The data obtained from proton decoupled  $^{13}\text{C}$  NMR spectra of reconstituted fibrils of chick calvaria collagen enriched at the glycine  $\text{C}_\alpha$  and  $\text{C}'$  positions are consistent with a model in which collagen molecules reorient about the long axis of the helix with a rotational diffusion constant ( $R_1$ ) of  $\sim 10^7 \text{ s}^{-1}$  [357]. The full-width of the glycolyl carbonyl powder pattern is 103 ppm which is substantially smaller than the rigid lattice value 144 ppm, which provides further evidence for motion in the fibril [358]. The powder line width of  $[1-^{13}\text{C}]\text{Gly}$ -labeled collagen,  $\Delta = \delta_{\text{zz}} - \delta_{\text{xx}}$  at  $22^\circ\text{C}$  for the uncross-linked reconstituted collagen fibril is 108 ppm, whereas the maximum value of delta (140 ppm) is observed for the cross-linked and mineralized collagen fibrils in rat calvaria [359]. The line shapes were analyzed using a model in which azimuthal orientation of the collagen backbone is assumed to fluctuate as a consequence of reorientation about the helix axis. Fluctuations in azimuthal orientation are smaller in cross-linked tendon and demineralized calvaria collagen fibers than in reconstituted collagen fibers. It was shown that slow motions having large amplitudes will be sensed by the line shape but not the relaxation times [360].

Characterization of slow segmental dynamics in solids has been developed by the centerband-only detection of exchange (CODEX)

NMR experiment which employs recoupling of the CSA under MAS before and after a long mixing time during which molecular reorientations may occur [361,362]. By an analysis in terms of the difference tensor of the chemical shifts before and after the mixing time, the dependence on the reorientation angle is obtained analytically for uniaxial interactions, and a relation to 2D exchange NMR patterns has been established. This technique was applied to a triblock hydrogel protein ACA [363]. Its CODEX mixing time dependence revealed a detectable decaying component with a correlation time of about 80 ms.

Fast and slow dynamics of collagen fibrils at various hydration levels were examined by  $^{13}\text{C}$  CPMAS experiments [270,364]. Fast motions with correlation times much shorter than  $40 \mu\text{s}$  were detected by dipolar couplings measured by the DIPSHIFT experiment [365], and by the CSA values of the carbon sites in collagen. These motionally averaged anisotropic interactions provide a measure of the amplitudes of the segmental motions as described by a segmental order parameter. The data reveal that increasing hydration has a much stronger effect on the amplitude of the molecular processes than increasing temperature. In particular, the CODEX experiment showed that the Hyp residues in the hydrated state have an appreciable level of mobility in the millisecond range.

$^2\text{H}$ ,  $^{13}\text{C}$  and  $^{15}\text{N}$  NMR spectra of the fd bacteriophage coat protein were used to analyze the motions of their aromatic amino acids [366]. The presence of background signals from natural abundant nuclei in the  $^{13}\text{C}$ -labeled sample, however, represents a serious obstacle to line shape analysis, as illustrated in the  $^{13}\text{C}$  NMR spectra of  $[^{13}\text{C}_\alpha]\text{Tyr}$ -labeled fd. The slow MAS spectrum (0.38 kHz) arising from the narrow sidebands from Tyr residues was recorded to distinguish the powder pattern from the natural abundance background. The calculated powder pattern from the sideband intensities is consistent with the difference spectrum between the labeled and unlabeled static samples and indicates that the Phe and Tyr rings undergo  $180^\circ$  flips about the  $\text{C}_\beta$ - $\text{C}_\gamma$  bond axis at a rate greater than  $10^6 \text{ Hz}$ , as well as small-amplitude rapid motions in other directions. The dynamics of the coat protein in fd bacteriophage has also been studied by  $^{15}\text{N}$  and  $^2\text{H}$  NMR experiments [367,368], which showed that the virus particles and the coat protein subunits are immobile on the time scales of the  $^{15}\text{N}$  CSA ( $10^3 \text{ Hz}$ ) and  $^2\text{H}$  quadrupole ( $10^6 \text{ Hz}$ ) interactions. PISEMA spectra of the Pf1 bacteriophage indicate that at  $30^\circ\text{C}$ , some of the coat protein subunits assume a single, fully structured conformation, and some have a few mobile residues that provide a break between two helical segments, in agreement with structural models from X-ray fiber and neutron diffraction [369]. The structural basis of the temperature-dependent transition of Pf1 was also examined [370]. The dynamics in this protein as revealed by studies of order parameters characterizing bond vector dynamics [371] show that the subunit backbone is static. In contrast to the backbone, several side-chains reveal large-amplitude angular motions. Side-chains on the virion exterior that interact with solvent are highly mobile, but the side chains of residues arginine 44 and lysine 45 near the DNA deep in the interior of the virion are also highly mobile.

**Membrane proteins.** The presence of fast motions with a  $ps$  to  $ns$  time-scale can readily be identified in the solid-state by observing that certain NMR peaks in spectra recorded by CPMAS are appreciably suppressed as compared with those in spectra recorded by DDMAS (direct detection or dipolar decoupled magic angle spinning). For instance, fully-hydrated membrane proteins which are arranged on a 2D lattice in bilayers (2D crystals) are far from being rigid bodies at ambient temperature, in spite of 3D pictures currently available from X-ray diffraction studies at very low temperature [372–374], as demonstrated by extensive studies on  $[3-^{13}\text{C}]\text{Ala}$ - or  $[1-^{13}\text{C}]\text{Val}$ -labeled bacteriorhodopsin (bR) as a typical membrane protein from the purple membrane (PM) of *Halobac-*

*terium salinarum* [107,279,375–379]. Indeed,  $^{13}\text{C}$  NMR studies on specifically  $^{13}\text{C}$  amino-acid labeled bR showed that bR undergoes several types of motion even in a 2D crystal at ambient temperature, depending upon the site of interest, revealing fast ( $>10^8$  Hz), slow ( $\mu\text{s}$ – $\text{ms}$ ) ( $10^4$ – $10^5$  Hz) or very slow ( $10^2$  Hz) motions, as described below [24,107,281,376,377]. Well-separated  $^{15}\text{N}$  NMR spectra of green variant of [ $^{15}\text{N}$ - $\zeta$ -Lys]proteorhodopsin (GPR), a photoactive retinylidene protein in marine bacterioplanktons, were recorded from 2D crystals formed with a hexagonal packing in DOPC bilayer, due to efficient cross-polarization in the non-freezing state (280K) [380]. In contrast, it is noted that additional conformational fluctuations with frequencies of the order of  $10^4$  to  $10^5$  Hz are induced when monomeric bR is reconstituted in a lipid bilayer in the absence of 2D crystalline lattice, leading to strongly modified spectral features [381].

The presence of the fast motion is ascribed to the N- and C-terminal portions of [3- $^{13}\text{C}$ ]Ala-bR even in 2D crystal, undergoing isotropic motion which leads to suppression of cross-polarization from the protons, as demonstrated by the gray peaks in Fig. 26 [107,382]. This portion of the spectrum includes the peaks from the C-terminal  $\alpha$ -helix protruding from the membrane surface [383–385] with reference to the peak-positions of the conformation-dependent  $^{13}\text{C}$  chemical shifts [23,24]. In a similar manner,  $^{13}\text{C}$  signals from the surface area turned out to be visible only in DDMAS spectra for a variety of fully-hydrated membrane proteins, including *pharaonis* phoborhodopsin (ppR) (or sensory rhodopsin SRII) [285,386], its truncated transducer pHtrII (1–159) [387], and *E. coli* diacylglycerol kinase (DGK) [388].

In contrast, it is expected that CPMAS NMR signals from  $^{13}\text{C}$  labeled sites in portions of hydrophobic [1- $^{13}\text{C}$ ]Val or Ile residues are free from such suppression of peaks caused by fast motion, because they are not always located at such flexible positions in the surface area of lipid bilayers [281]. However, there may be additional reasons for suppressed NMR signals, such as the failure of peak-narrowing caused by interference of a slow motional frequency with either proton decoupling [350] or MAS [389]. Such slow motions on the  $\mu\text{s}$ – $\text{ms}$  time scale, if encountered in proteins in solution can be readily identified also in the solid, by observations of suppressed or recovered peak-intensities (SRI) by both CPMAS or DDMAS experiments [350,389]. Indeed, a  $^{13}\text{C}$  NMR line width  $1/\pi T_2^C$  of the residue under consideration could be considerably broadened, when a motional frequency of an incoherent random fluctuation motion interferes with either the coherent frequency of the proton decoupling or MAS. In such cases, the overall transverse relaxation rate  $1/T_2^C$  given by [197]

$$1/T_2^C = (1/T_2^S)^2 + (1/T_2^{CD})^2 + (1/T_2^{CS})^2, \quad (63)$$

can be dominated by the second or third terms, where  $(1/T_2^S)^2$  which is the transverse component due to static C–H dipolar interactions, and  $(1/T_2^{CD})^2$  and  $(1/T_2^{CS})^2$  are the transverse components due to the fluctuation of dipolar coupling and chemical shift interactions in the presence of internal fluctuation motions, respectively. The latter two terms are given as a function of the correlation time  $\tau_c$  by:

$$(1/T_2^{CD})^2 = \Sigma(4\gamma_I^2\gamma_S^2\hbar^2/15r^6)I(I+1)[\tau_c/(1+\omega_I^2\tau_c^2)], \quad (64)$$

$$(1/T_2^{CS})^2 = (\omega_0^2\delta^2\eta^2/45)[\tau_c/(1+4\omega_r^2\tau_c^2) + 2\tau_c/(1+\omega_r^2\tau_c^2)]. \quad (65)$$

Here,  $\gamma_I$  and  $\gamma_S$  are the gyromagnetic ratios of  $I$  (proton) and  $S$  (carbon) nuclei, respectively, and  $r$  is the internuclear distance between spins  $I$  and  $S$ , and the summation is over pairs of  $I$ – $S$  nuclei. The angular frequencies  $\omega_0$  and  $\omega_I$  are the carbon resonance frequency and the amplitude of the proton decoupling RF field, respectively.  $\omega_r$  is the rate of spinner rotation.  $\delta$  is the CSA and  $\eta$  is the asymmetric parameter of the chemical shift tensor. It is expected that a decoupling field of 50 kHz is sufficient to reduce the static compo-

nent and the  $(1/T_2^{CS})^2$  term will be dominant in the overall  $1/T_2^C$ , as far as the carbonyl signals with larger chemical shift anisotropies are concerned. Consequently, the maximum of the line-broadening occurs when the frequency of the incoherent motion is near  $\omega_r$ , and thus effect is called interference of motional frequency with the MAS frequency. Of course, it is possible to avoid this interference from frequency in the order of typically  $10^4$  Hz by increasing the spinning rate up to as fast as 20 kHz. In such case, however, one should take special precaution to prevent unnecessary heating of samples as well as dehydration due to a centrifuging effect on fully hydrated membrane proteins. In this connection, it was demonstrated, on the basis of  $^{15}\text{N}$  chemical shifts of [ $\zeta$ - $^{15}\text{N}$ ]Lys of a Schiff's base, that pressure-induced isomerization of retinal on bR occurs at an increased MAS frequency of 12 kHz, corresponding to the sample pressure of 63 bar, resulting in the decreased equilibrium constant of [all trans-bR]/[13-cis bR] leading to structural change in the vicinity of retinal [390]. This finding was explained in terms of a disrupted or distorted hydrogen bond network by means of a constantly applied pressure. The presence of the two backbone conformations at Tyr185 caused by such a retinal configuration in the dark, light and pressure adapted bR has been extensively studied by REDOR filtered experiments [391].

It is more practical to observe the expected intensity change as a function of temperature or pH which might indirectly vary with the frequency dispersion as expressed in Eqs (64) or (65). A typical example for such suppressed or recovered peak-intensities (SRI) is shown in the  $^{13}\text{C}$  CPMAS NMR spectra of the [ $^{13}\text{C}$ ]Val-labeled D85N mutant of bR recorded at various pH [392–394]. As shown in Fig. 31, raising the pH of this mutant from 7 to 10 (leading to the M-like state, mimicking the M photo-intermediate without photo-illumination) resulted in additional spectral changes in which several peaks were suppressed together when raising pH to 10, while the others were recovered. In particular, the intensities of the five peaks in D85N, 177.31 ppm (V213), 175.69 ppm (unassigned), 174.98 ppm (V217), 173.2 ppm (unassigned), and 172.3 ppm (V49), decreased with the raised pH, while the intensities of the two peaks, 171.8 ppm (V69,130) and 172.8 ppm (V34), increased, as demonstrated in Fig. 32, by taking into account that raising pH is related to accelerate fluctuation as a result of conformational change from the L to M-like state of bR. This situation occurs in the M-like state of D85N at higher pH or bacteriorhodopsin (bO) [383] in which specific retinal-protein interaction is partly or completely removed by neutralization of the negative charge at Asp 85 or its absence, respectively.

A similar SRI change was more clearly visualized for synthetic hydrophilic polymers, poly(acrylate)s, by plotting their DDMAS peak-intensities as a function of temperature [395]. Several intensity minima were noted at different temperatures for the different individual sites in the polymer side-chains, indicating the presence of fluctuation motions with correlation times of the order of  $10^{-5}$  s at particular temperatures.

Bacteriorhodopsin (bR) from purple membrane (PM) is packed to form a trimeric unit which is further assembled into a hexagonal lattice as a native 2D (liquid) crystal [396]. As demonstrated already,  $^{13}\text{C}$  NMR signals of [3- $^{13}\text{C}$ ]Ala- (Fig. 26) or [1- $^{13}\text{C}$ ]Val-labeled bR preparation adopting such 2D crystal are well resolved in DDMAS NMR spectra or CPMAS spectra at ambient temperature. Nevertheless, it was found that several  $^{13}\text{C}$  NMR signals from the surface areas are suppressed for [1- $^{13}\text{C}$ ]Gly-, Ala-, Leu-, Phe- and Trp-labeled bR from PM, owing to the presence of conformational fluctuations with a correlation time of the order of  $10^{-4}$  s interfering with frequency of magic angle spinning (4 kHz) [377,384]. This is related to a possible conformational fluctuation, in 2D crystal, around the  $\text{C}_\alpha$ – $\text{C}_\beta$  bond in the side-chains of amino-acid residues as expressed by  $\text{C}_\alpha$ – $\text{C}_\beta\text{H}_2\text{X}$  system. The conformational space allowed for fluctuation is limited to a very narrow area for Val or



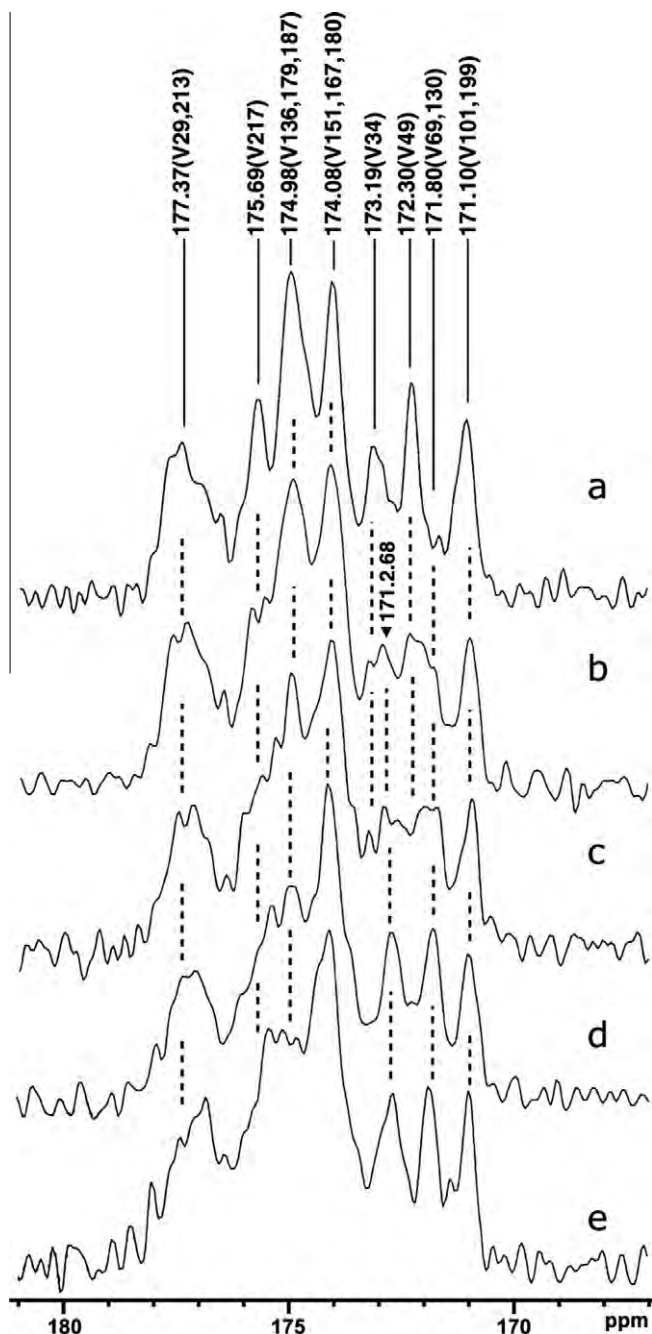


**Fig. 31.** 100.6 MHz  $^{13}\text{C}$  CPMAS NMR spectra of  $[1-^{13}\text{C}]\text{Val}$ -labeled D85N mutant at various pH values: (a) pH 6, (b) 8, (c) 9, (d) 10 and (e) 11. The assignment of peaks is based on newly performed experiments [377], and also corrected ones from older spectra [401]. Reproduced with permission from Saitô et al. [394]. Copyright 2010 Elsevier.

Ile residues with a bulky side-chain at  $\text{C}_\beta$ , leading to a limited range for  $\chi_1$ , the rotation angle around the  $\text{C}_\alpha\text{--C}_\beta$  bond, as demonstrated by  $\text{C}_\alpha\text{--C}_\beta\text{HYZ}$  where Y and Z are  $\text{CH}_3$  and  $\text{CH}_3$  or  $\text{CH}_2\text{CH}_3$ , respectively [228]. This is the reason why the  $^{13}\text{C}$  NMR signals are observed from  $[1-^{13}\text{C}]\text{Val}$ - or Ile-labeled bR preparations in 2D crystal, but partially suppressed for other types of  $[1-^{13}\text{C}]\text{amino-acid}$  labeled preparations. This surface dynamics was also examined by measurements of site-specific  $^{13}\text{C}$ –H dipolar coupling of  $[3-^{13}\text{C}]\text{Ala}$ -bR by 2D dipolar and chemical shift (DIPSHIFT) correlation techniques [397]. Dynamic feature of  $[1-^{13}\text{C}]\text{Pro}$ -labeled bR together with the kinked structure has been investigated by  $^{13}\text{C}$  NMR [398]. The contribution of Glu residues at the extracellular site to

the conformation and dynamics was extensively investigated by examination of a variety of  $[3-^{13}\text{C}]\text{Ala}$ - or  $[1-^{13}\text{C}]\text{Val}$ - mutants, E9Q, E74Q, E194Q/E204Q (2Glu), E9Q/E194Q/E204Q (3Glu), E9Q/E74Q/E194Q/E204Q (4Glu) [399]. Significant dynamic changes were induced for the triple- or quadruple mutants by acquisition of global fluctuation motions with correlation times  $10^{-4}$  or  $10^{-5}$  s in the disorganized trimeric form. The dynamic aspects of the extracellular loop region as a proton release pathway of bR were studied by measuring a variety of relaxation times [400]. The  $^{13}\text{C}$  and  $^{15}\text{N}$   $T_1$  values of V199/P200 indicate that the long FG loop has a fast fluctuation motion with a frequency of  $10^8$  Hz. However, the  $^{13}\text{C}$  and  $^{15}\text{N}$   $T_2$  values of V69/P70 indicate that the BC loop (connecting the B and C transmembrane  $\alpha$ -helices) of bR is involved in a rigid  $\beta$ -sheet structure in spite of possessing large amplitude motions.

In contrast, it is noteworthy that several Ala  $\text{C}_\beta$   $^{13}\text{C}$  NMR signals arising from the surface areas (8.7 Å depth), including the most downfield peaks in the loops (Ala 196,160 and 103) and the low-field region of the transmembrane  $\alpha$  helices (16–17 ppm) are almost completely or partially suppressed, respectively, when 2D crystals were disrupted or disorganized as in W80L and W12L mutants, caused by the absence of Trp 80 or 12 located at the key positions for specific lipid–helix interaction, leading to modified lipid–helix and helix–helix interactions [401], or monomer in regenerated lipid bilayers [402,403]. At the same time, the carbonyl  $^{13}\text{C}$  NMR signals from the transmembrane  $\alpha$ -helices and loops of monomeric bR were also almost completely suppressed in preparations including  $[1-^{13}\text{C}]\text{Gly}$ -, Ala-, Val-labeled bR because of fluctuation motions with correlation times in the order of  $10^{-4}$  s [377,381,402].

$^{15}\text{N}$  spectral peaks of fully-hydrated  $[^{15}\text{N}]\text{Gly}$ -bR obtained via cross-polarization are suppressed at 293 K due to interference with proton decoupling frequency, and also because of short values of  $T_2$  in the loops [403]. The motion of the transmembrane  $\alpha$ -helices in bR is strongly affected by the freezing of excess water at low temperatures. It was shown that motions in the 10  $\mu\text{s}$  correlation regime may be functionally important for the photocycle of bR, and protein–lipid interactions are motionally coupled in this dynamic regime.

Pharaois phoborhodopsin ppR (or sensory rhodopsin II) is also a heptahelical transmembrane retinylidene protein, and active as a sensor for negative phototaxis on binding with the cognate transducer pHtrII. It was demonstrated that the surface structure of ppR near the E–F loop plays a dominant role to regulate membrane surface dynamics when ppR is complexed with truncated pHtrII (1–159) through direct interaction of the C-terminal  $\alpha$ -helix in the former with the cytoplasmic  $\alpha$ -helical region of the latter [404]. Assuming that the break of the hydrogen bonding between C and G helices is a trigger of phototaxis signal, the D75N mutant of ppR was used as a “quasi”-activated receptor [405]. Clear dynamical changes of the C-terminal tip portion of the receptor ( $10^4$ – $10^5$  Hz) were observed when the receptor bound to the transducer and the complex changed to the “quasi”-signaling state. This can be named as a “switch model” as shown in Fig. 33: the cytoplasmic  $\alpha$ -helix in the transducer interacts with the C-terminal helices of the receptor, leading to the activation of the receptor. The interaction site at the linker switches to the linker region of the paired transducer. This formation of a paired transducer may further relay the signals to phosphorylation cascade.

Interestingly, a preparation of non-crystalline green-absorbing proteorhodopsin (GP) with higher lipid to protein ratio of 0.5:1 (w/w) gave well-resolved multi-dimensional solid-state NMR spectra in samples with different patterns of reverse labeling [406,407], even though 2D (liquid) crystalline preparation at a very low lipid to protein ratio of  $\sim 0.25$  (w/w) was shown to be more favorable for its solid-state NMR studies [380,408]. The assigned

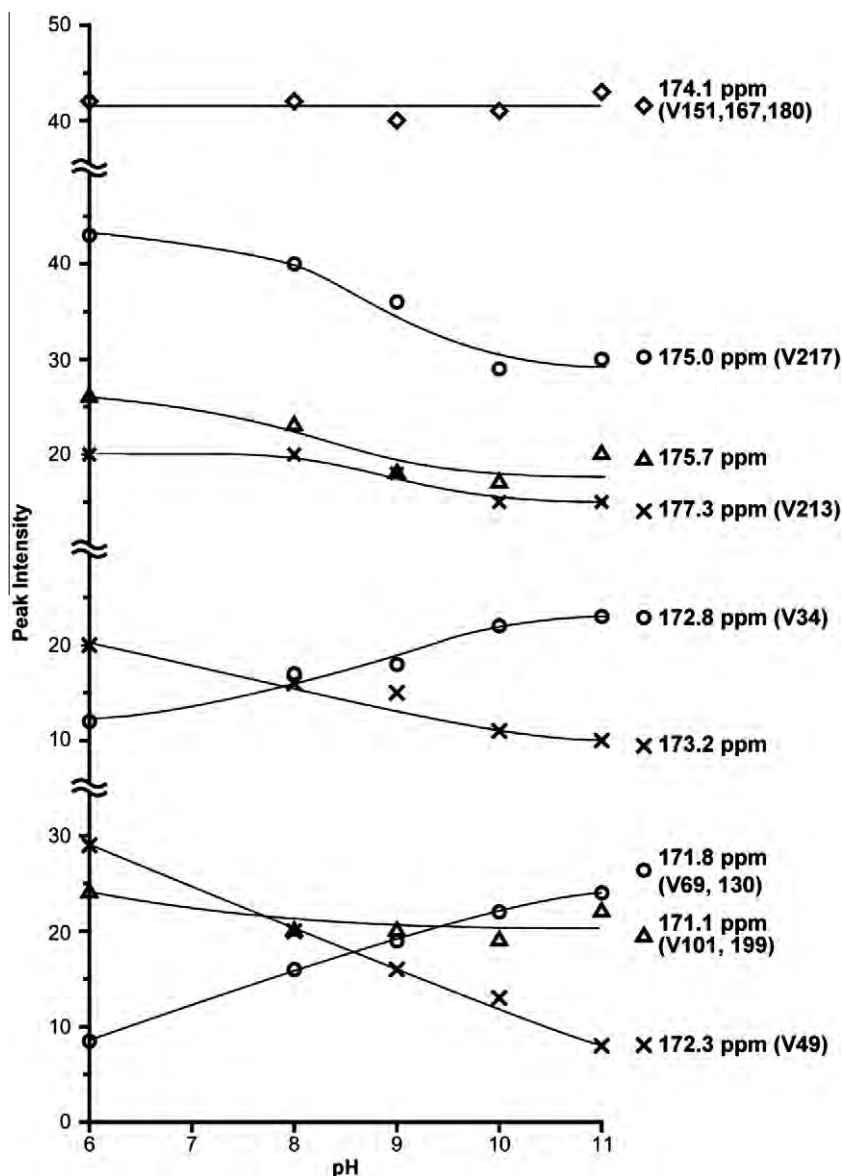


**Fig. 32.** Suppressed or recovered intensities (SRI) plots for D85N mutant against pH. The peak intensities are either increased or decreased with increased pH, depending upon the respective peaks, except for the peak V151, 167, 180 whose intensity is unchanged. Reproduced with permission from Saitô et al. [394]. Copyright 2010 Elsevier.

peaks of  $^{13}\text{C}$  and  $^{15}\text{N}$  nuclei for 153 residues, with a particularly high density in the transmembrane regions ( $\sim 75\%$  of residues), based on 3D and 4D sequential chemical shift assignments permitted a detailed examination of the secondary structure and dynamics of GPR [407]. Experimental evidence of mobility was shown for proteorhodopsin in the lipid environment at the protein's termini and of the A–B, C–D and F–G loops, the latter being possibly coupled to the GPR ion-transporting function. Further, it appears that use of high-field NMR (at 800 MHz for  $^1\text{H}$ ) together with fast-MAS might be a favorable procedure to minimize the number of  $^{13}\text{C}$  or  $^{15}\text{N}$  suppressed peaks caused by interference between the frequency of fluctuation motions and MAS frequency occurring at intermediate magnetic field (400 MHz for  $^1\text{H}$ ) as observed for reconstituted non-crystalline bR [381], leading to strong protein–protein interactions [408].

**Globular proteins.** The signal intensities and linewidths of  $^{13}\text{C}$  and  $^{15}\text{N}$  nuclei in 56 residues in  $\beta 1$  immunoglobulin binding domain of protein G (GB1) vary as a function of amino acid position and temperature [409]. High-resolution spectra have been ob-

served near room temperature (280 K) and at  $< 180$  K, whereas resolution and sensitivity greatly degrade near 210 K; the magnitude of this effect is greatest among the side chains of residues at the intermolecular interface of the microcrystal lattice, which can be attributed to intermediate-rate translational diffusion of solvent molecules near the glass transition.

Multidimensional SLF experiments have been used to study the backbone and side chain conformational dynamics of ubiquitin, a globular microcrystalline protein [410]. Molecular conformational order parameters were obtained from heteronuclear dipolar couplings, and they were correlated to assigned chemical shifts, to obtain a global perspective on the sub-microsecond dynamics in microcrystalline ubiquitin. A total of 38  $C_\alpha$ , 35  $C_\beta$  and multiple side chain unique order parameters were collected, and the high mobility of ubiquitin in the microcrystalline state is revealed. In general the side chains show elevated motion in comparison with the backbone sites. Two review articles on the structure and dynamics of membrane-associated peptides [411] and protein dynamics [412] have appeared.

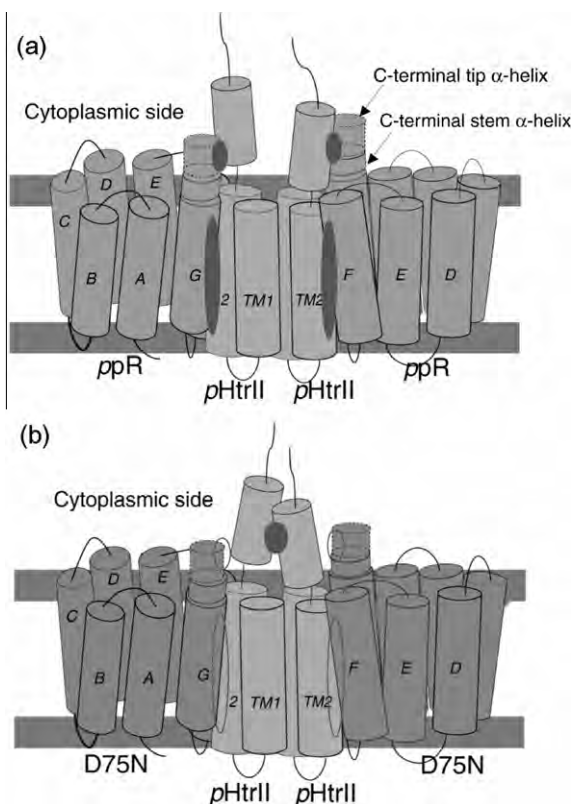


**Fig. 33.** Schematic representation of the manner of interaction of the C-terminal  $\alpha$ -helical tip region in ppR (a) and D75N (b) with the transmembrane and cytoplasmic  $\alpha$ -helices of pHtrII (1–159). The helix–helix interactions between the cytoplasmic  $\alpha$ -helices are also presented. Elliptical dark gray areas and open areas show the enhanced and weakened interaction parts, respectively. Reproduced with permission from Kawamura et al. [405].

The averaging of  $^{15}\text{NH}^{\alpha/\beta}$  multiplet components by  $^1\text{H}$  decoupling induces effective relaxation of the  $^{15}\text{N}$  coherence when the N–H spin pair undergoes significant motion. High resolution  $^{15}\text{N}$  solid-state NMR spectra can then only be recorded by application of TROSY type techniques which select the narrow component of the multiplet pattern, as demonstrated for solid-state  $^{15}\text{N}$  spectra of chicken  $\alpha$ -spectrin SH3 domain [413]. It was speculated that this averaging effect has been the major obstacle to successful NMR spectroscopic characterization of many membrane proteins and fibrillar aggregates examined so far.

#### 4.3. $^{31}\text{P}$ CSA of phospholipids in biomembranes

The 100% natural abundance, high gyromagnetic ratio, and the presence of phosphorus-31 in the phosphate group of phospholipids present in the biological cell membrane make this nucleus as an excellent probe for NMR investigation of the structure and dynamics of lipid bilayer model membranes, as well as for studies of ligand–membrane interactions. As discussed below, the  $^{31}\text{P}$  CSA is highly sensitive to hydration, temperature, the presence of ions, and ligand–lipid interactions.

##### 4.3.1. Unoriented lipid bilayers

Phospholipids in biomembranes of living cells are predominantly organized as a bilayer structure which provides a barrier between the cell interior and its environment. Membrane proteins embedded therein mediate various functions such as transport of appropriate molecules into or out of the cell, catalysis of chemical reactions, receiving and transducing chemical signals from the cell

environment, etc. Proton-decoupled  $^{31}\text{P}$  NMR spectra of 1,2-dipalmitoyl-*sn*-glycero-3-phosphocholine (DPPC), for instance, exhibit quite different spectral patterns depending upon its water content [414]. At 0 wt%  $\text{H}_2\text{O}$ , a static phosphodiester moiety of this phospholipid yields the  $^{31}\text{P}$  NMR powder pattern typical of axial asymmetry, with the three principal components,  $\delta_{11}$ ,  $\delta_{22}$  and  $\delta_{33}$ , which span some 190 ppm, and which have almost identical values for various phospholipids [415]. This spectrum collapses from the axial asymmetric to an axial symmetric pattern, due to the onset of molecular motion at a water content over 10 wt %  $\text{H}_2\text{O}$ , when the sample enters a micellar liquid crystalline state [414]. The molecules move within the micelles, which have a bilayer structure, such that a symmetry axis is created perpendicular to the bilayer surface, yielding an axially symmetric  $^{31}\text{P}$  NMR powder pattern, consisting of a peak at the high field ( $\delta_{\perp}$ ) with a low field shoulder ( $\delta_{\parallel}$ ) with  $\Delta\delta = |\delta_{\parallel} - \delta_{\perp}| \sim 47$  ppm [416]. Here,  $\delta_{\parallel}$  and  $\delta_{\perp}$  are the peak-positions corresponding to the components of the shift tensor parallel and perpendicular to the symmetry axis, respectively. The values of  $\Delta\delta$  for both saturated and unsaturated phosphatidylcholines in the liquid crystalline state are very similar (in the range of 43–47 ppm) and do not vary appreciably ( $\leq 5\%$ ) over the temperature range investigated. The largest change in  $\Delta\delta$  rises on the addition of an equimolecular concentration of cholesterol to 16:0/16:0-phosphatidylcholine, for which  $\Delta\delta$  is decreased from about 45 to 36 ppm [416]. Thus, the  $^{31}\text{P}$  NMR powder patterns of all phospholipids can be used as a characteristic feature of liquid crystalline lipid bilayers in addition to measure the orientation and average fluctuation of the phosphate segment [417–419].

It is also noted that with the possible exception of phosphatidic acid [420], all glycerol-based phospholipids, as well as the most abundant mammalian phosphosphingolipid and sphingomyelin, have similar values of  $\Delta\delta$ , resulting in almost equivalent lineshapes for these different species when in the liquid crystalline bilayer phase [417]. At low temperature, however, the rotation is expected to slow or cease (gel phase lipids) resulting in the axially asymmetric pattern again, as seen in the temperature-dependent  $^{31}\text{P}$  NMR spectra of DPPC, together with the simulated spectra described by two diffusion coefficients  $R_{\parallel}$  (fast motion) and  $R_{\perp}$  (net slow motion) [421]. It is obvious that the spectral feature varies strongly with the value of fast diffusion coefficient. For relatively small membrane fragments ( $< 10,000$  Å), however, the rate of overall isotropic diffusion is also important, leading to further averaging of spectral components [422].

Biomembranes are thought to contain functional domains (lipid rafts) made up in particular of sphingomyelin and cholesterol, glycolipids and certain proteins, as detergent-resistant membranes in Triton X-100. They are discussed in terms of liquid-ordered ( $l_o$ ) and -disordered ( $l_d$ ) bilayer and micellar phases [423]. Distinguishing individual lipid headgroup mobility and phase transitions in raft-forming lipid mixtures has been examined by using  $^{31}\text{P}$  CSA measurements [423,424].

##### 4.3.2. Oriented lipid bilayers

Revealing the secondary structure of  $^{13}\text{C}$ - or  $^{15}\text{N}$ -labeled peptides or proteins embedded in lipid bilayers is feasible by careful analysis of the orientational constraints of the dipolar interaction or chemical shift anisotropies with respect to the applied magnetic field via bilayer normal [425–428]. Three types of oriented lipid bilayers have been increasingly utilized: (1) mechanically oriented lipid bilayers obtained by shear between glass plates [429,430]; (2) magnetically oriented bicelles consisting of lipid–detergent aggregates [431–433]; (3) magnetically oriented large unilamellar vesicles [434,435]. Aluminum oxide nanotubes have also been used for oriented samples in solid-state NMR studies. The unique advantage of this approach was recently utilized to identify the islet amyloid



polypeptide (IAPP or amylin) induced membrane fragmentation by solid-state NMR spectroscopy [436].

The sample preparation protocol for mechanically oriented bilayers was improved to achieve a minimal dispersion of the bilayer normal and minimal amounts of unoriented sample, as viewed from both the  $^{31}\text{P}$  CSA, which is very sensitive to such orientation, and optical microscopy [437]. It was demonstrated that adding sublimable solid such as naphthalene or para-dichloro benzene to a lipid–peptide solution in  $\text{CHCl}_3/\text{CH}_2\text{OH}$  (1:1 molar ratio) and its removal yielded significantly enhanced alignment of all sorts of lipids, including palmitoylphosphatidylethanolamine (POPE) [438]. Optimizing the alignment of oriented lipid samples has been achieved for bilayer and hexagonal phases on a mica surface [439].

Bicelles are lipid–detergent aggregates of DMPC with certain detergents [440,441], either short-chain phosphatidylcholine, dihexanoyl-phosphatidylcholine (DHPC), or a zwitter ion bile salt derivative, CHAPSO. The function of the short-chain molecules is to coat the edges of the bilayered sections to protect the longer phospholipid chains from exposure to water. Bicellar size varies as a function of the molar ratio [DMPC]/[DHPC] (with a diameter  $\approx 10$ – $100$  nm). The anisotropy of the magnetic susceptibility  $\Delta\chi$  of the bicelles when  $2 < [\text{DMPC}]/[\text{DHPC}] < 6$  leads to their alignment in the spectrometer magnetic field with the bilayer normal orthogonal to the field [440,442]. The phospholipid bicelles possess great potential as membrane mimetics for structural studies. The addition of small amounts of paramagnetic ions change the sign of  $\Delta\chi$  and as the effect of flipping the alignment of the phospholipids bicelles, making NMR measurements possible for the two types of orientations, parallel and perpendicular, to the magnetic field. The presence of bulk water enables proper folding of membrane proteins especially for the loops and C- or N-terminal regions exposed to aqueous phase, even though major transmembrane helical regions are embedded within the lipid bilayers. Therefore, these model membranes are considered to be highly valuable for NMR studies. In addition, the variation of the lipid:detergent ratio can be utilized to prepare near-isotropic to rigid bicelles for solution-like to solid-state-like NMR experiments [306].

A DMPC bilayer containing a moderately high concentration of melittin (DMPC: melittin = 10:1 molar ratio) is subject to lysis and fusion at temperatures lower and higher than the gel to liquid crystalline phase transition temperature,  $T_c$ , respectively [434]. The magnetically aligned, elongated vesicles are formed at a temperature above  $T_c$  as shown from  $^{31}\text{P}$  NMR and microscopic observation. Opioid peptide dynorphin A (1–17) is also shown to strongly interact with DMPC bilayer to cause fusion and lysis across the phase transition temperature between the gel and liquid crystalline temperature and results in subsequent magnetic ordering at a temperature above  $T_c$  [435].

#### 4.3.3. Polymorphism: non-bilayer lipids

Besides the bilayer, lamellar phase lipids can form other phases, such as hexagonal  $H_{11}$  and cubic phases, depending upon the lipid type and molecular shape, the presence of other lipid molecules, water content, temperature, etc. [417,443–446]. If the lipid phase changes from lamellar to hexagonal, the  $^{31}\text{P}$  CSA,  $\Delta\delta$ , changes its sign and is reduced by exactly a factor of two [414,417,419]. The cylinders in a hexagonal phase have a very small radius, and therefore lateral diffusion about the cylinder axis can cause further averaging of tensor components.

Lipids assuming the hexagonal ( $H_{11}$ ) phase may be considered to exhibit a “cone” shape, where the polar headgroup region is at the smaller end of the cone [417]. Lysophospholipids to display an “inverted cone” shape where the cross sectional area of the polar group is larger than that subtended toward the end of the acyl chain. This shape has been suggested as the reason why the  $^{31}\text{P}$  sig-

nal is that typical of an isotropic environment in these micellar phases. Indeed, the smaller headgroup of phosphatidylethanolamines as compared to phosphatidylcholine would be expected to result in a reduced area per molecule at the lipid–water interface, thus producing a cone shaped molecule compatible with the  $H_{11}$  phase [417]. Alternatively, increased unsaturation in the acyl chain region leads to a more pronounced cone shape, fully compatible with the requirement for a minimal degree of unsaturation for  $H_{11}$  phase phosphatidylethanolamine [447]. Further, increased amplitude of the thermal motion of the acyl chains at elevated temperature leads to a cone shape compatible with that  $H_{11}$  structure, as seen in both pure phosphatidylethanolamines [447] and mixed lipid systems [448,449]. The ability of cholesterol to induce  $H_{11}$  phase formation in certain mixed lipid systems [448,449] is also consistent with a cone shape for cholesterol [450,451].

The integrity of membranes as bilayers is maintained by a balance of intermolecular forces in the acyl and headgroup regions of lipids. The geometric packing properties of different lipids may be conveniently expressed in terms of the dimensionless *critical packing parameter* [452,453],

$$f = v/a_0l_c, \quad (66)$$

where  $v$  and  $l_0$  are their hydrocarbon volume and critical (or maximum) length that the chains can assume, respectively, and  $a_0$  is their optimal surface area of the headgroup (minimum at a certain head-group area). If  $f < 0.5$  such lipids normally form micelles and are entropically and energetically unlikely to form bilayers. If  $f > 1$  such lipids cannot even pack into bilayers since their headgroup area is too small; instead, they form inverted micellar structures. If  $0.5 < f < 1$  these lipids are packed into bilayers. Support for this shape concept of lipid structure was shown to depend on the effects of lipid packing [454], additivity of the packing parameter [455], and headgroup volume [456,457].

The phase behavior is largely the result of a delicate balance of forces in the headgroup and acyl-chain regions. Mismatches in packing in either region induce a tendency toward membrane curvature which is offset by similar changes in the apposed leaflet in lipids; consequently, the curvature is not expressed (frustrated curvature stress), but is stored as potential energy with a latent ability to destabilize the bilayer structure [458]. The frustration of lipid layer curvature is measured calorimetrically [459] or shown to reflect in the acyl chain order measured by  $^2\text{H}$  NMR in the  $L_\alpha$  phase [460]. In the latter, for a given temperature, increased order is observed when the curling tendencies of the lipid plane are more pronounced. The effects of membrane constituents, such as drugs, detergent or hydrocarbons on the  $L_\alpha \rightarrow H_{11}$  transition temperature,  $T_H$ , were examined to provide a quantitative, widely applicable, index of the ability of membrane constituents to induce curvature stress in model bilayers [458,461–463]. The phase transition can be conveniently monitored by recording  $^{31}\text{P}$  chemical shift spectra as illustrated in Fig. 34 [461]. It was shown that *n*-dodecane induces the formation of the reversed hexagonal ( $H_{11}$ ) phase of diolelphosphatidylcholine (DOPC)-*n*-dodecane- $\text{H}_2\text{O}$  system at low and high water concentrations, and a cubic phase (giving rise to an isotropic  $^{31}\text{P}$  NMR peak) at low water content [464]. The translational diffusion coefficient of DOPC in the cubic phase is more than an order of magnitude smaller than the lateral diffusion coefficient of DOPC in an oriented lipid bilayer which can be attributed to restricted lipid translational motion caused by closed lipid aggregates [465]. A membrane-mimicking system consisting of a lipid cubic phase containing a membrane protein which allowed the formation of three-dimensional protein crystals amenable to X-ray crystallography has been reported [466,467].

Membrane fusion, in which two separate membranes merge into a single bilayer is mediated by certain lipids or proteins, and is involved in various biological processes such as fertilization,

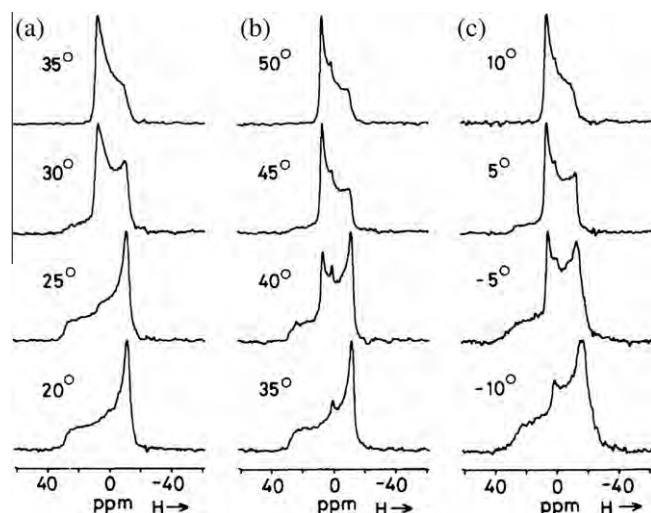


**Fig. 34.**  $^{31}\text{P}$  NMR spectra recorded at 81.0 MHz of egg phosphatidylethanolamine at the indicated temperatures. (a) in the absence of alcohol, (b) in the presence of ethanol (ethanol to phospholipid molar ratio = 4.5), (c) in the presence of decanol (decanol to phospholipid molar ratio = 0.45). Reproduced with permission from Hornby and Cullis [461]. Copyright 1981 Elsevier.

endo- or exocytosis, viral infection, etc. Fusion of erythrocyte ghosts was shown to proceed through formation of  $H_{11}$  phase, in the presence of oleic acid as “fusogenic” agent, by changes in the  $^{31}\text{P}$  NMR spectra change [454]. The fact that many lipid species can adopt or induce such bilayer destabilization suggested that this may be a general mechanism of fusion in *in vivo* [417]. Segments of viral fusion proteins play an important role in viral fusion where viral infection proceeds with aid of fusion proteins [468]. A common property of a number of fusion peptides is that they lower the bilayer to hexagonal phase transition temperature ( $T_H$ ) of phosphatidylethanolamine, indicating that they promote negative curvature [469]. This property is well correlated with conditions that lead to membrane fusion. For example, the fusion peptide from influenza virus lowers  $T_H$  at acidic pH where the virus is fusogenic, but not at neutral pH where the rate of fusion is slow [470]. There is also a correlation between the fusion activity of viral mutants and the ability to lower  $T_H$  of the influenza virus [471]. The promotion of negative curvature by fusion peptides is in accord with the requirement to increase the negative curvature of the contacting monolayers to form the hemifusion intermediate [472,473].

#### 4.3.4. Lipid–protein or peptide interactions

Even though biomembranes are predominantly arranged as bilayers, some lipid components of biomembranes spontaneously form non-lamellar phase of inverted hexagonal as well as cubic phases [469,474,475]. In addition, proteins and peptides can influence the tendency of lipids to form bilayer or non-lamellar forms. Indeed, a possible role of rhodopsin in maintaining bilayer structure has been demonstrated: the  $^{31}\text{P}$  NMR spectra of extracted lipids from rhodopsin are characteristic of the hexagonal  $H_{11}$  phase and an isotropic phase, although the lipids in the photo-receptor membrane are almost exclusively organized in a bilayer [476]. The integral membrane protein, cytochrome c oxidase, has a stabilization effect on the bilayer organization of cardiolipin, in that it inhibits the formation of the  $\text{Ca}^{2+}$ -induced,  $H_{11}$  phase of this lipid for  $\text{Ca}^{2+}$ /cardiolipin molar ratios of 1–10 [477]. Further, it is interesting to note that hydrophobic mismatch in length between the hydrophobic part of membrane spanning proteins and the hydrophobic bilayer thickness affects both lipid and protein sides, either phase transition temperature or formation of non-lamellar phases

for the former, or protein activity and stability, protein aggregation, tilt, localization at membrane surface, protein/peptide backbone conformation, etc for the latter [474,475]. For instance, gramicidin A is able to convert the stable bilayer form of dioleoylphosphatidylcholine (DOPC) into an  $H_{11}$  phase at high concentration [478]. The localization of the  $\alpha$ -helical peptides in the  $H_{11}$  phase was proposed to be similar to that for gramicidin [479]. When a 17 amino acid residue long peptide (WALP17) was incorporated in a 1/10 molar ratio of peptide to diacylphosphatidylcholine, a bilayer was maintained in saturated phospholipids containing acyl chains of 12 and 14 C atoms, an isotropic phase was formed at 16 C atoms, and an inverted hexagonal phase at 18 and 20 C atoms. Further, it is proposed that this ability of the peptides to induce non-bilayer structures in phosphatidylcholine model membranes is due to the presence of tryptophans at both sides of the membrane/water interface, which prevent the peptide from aggregation when the mismatch is increased.

Lipid modulation of protein activity is also a very interesting issue: the activity of protein kinase C (PKC), when bound to membranes in a cubic phase prepared from monoolein with 1-palmitoyl-2-oleoyl-3-phosphatidylserine (MO/PS) or dielaidoylphosphatidylethanolamine/alamethicin (EEPE/alamethicin), has a higher specific activity than that bound to vesicle bilayers [480]. It was proposed that there being little or no curvature strain in the cubic phase might be responsible for the activation of PKC, in addition to its physiological relevance due to the apparent presence of the cubic phase in certain biological structures. The photochemical process of rhodopsin in membrane is coupled with a conformational change associated with the conversion of metarhodopsin I (MI) to metarhodopsin II (MII). This transition is favored in membrane by relatively small headgroup of the lipid which produce a condensed bilayer surface of a comparatively small interfacial areas as in the case of phosphatidylethanolamine (PE), giving rise to a curvature stress of the lipid/water interface of the reverse hexagonal  $H_{11}$  phase at slightly higher temperature [481].

Any peptide that greatly changes the spontaneous monolayer curvature of a stable bilayer will promote vesicle leakage: peptides which promote either positive or negative curvature can be hemolytic [469]. In particular, the antimicrobial peptide, magainin, can induce the formation of pores in phospholipid bilayers with a high curvature [482].  $^{31}\text{P}$  NMR spectra of mechanically aligned bilayers containing the amphipathic, helical peptide MSI-78, an analogue of magainin, in 1-palmitoyl-2-oleoyl-phosphatidylcholine (POPC),

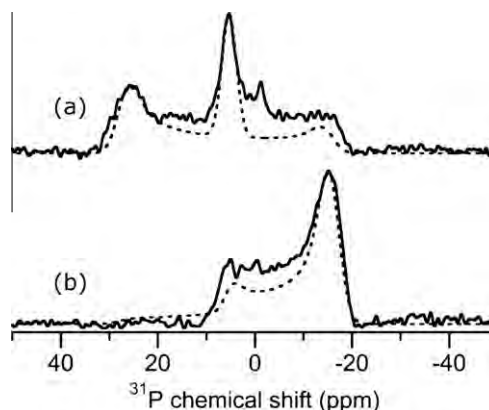


**Fig. 35.** Experimental and simulated 161.979 MHz  $^{31}\text{P}$ -chemical shift spectra of POPC bilayers containing 10% MSI-78. (a) Parallel orientation, (b) perpendicular orientation. The best-fitting simulations combined lipids in toroidal pores (73%) in an  $H_1$  phase (27%). The spectral parameters for the simulation of the toroidal pore component:  $\sigma_{\parallel} = 26\text{ ppm}$ ,  $\sigma_{\perp} = -15\text{ ppm}$ , 2 ppm linebroadening; for the  $H_1$  phase component,  $\sigma_{\parallel} = -15\text{ ppm}$ ,  $\sigma_{\perp} = 5.3\text{ ppm}$ , and 1.5 ppm line broadening. The experiments were performed at 30 °C. Reproduced with permission from Hallock et al. [483].

have been recorded to reveal its cell membrane permeation mechanism [483]. In POPC bilayer, unusual  $^{31}\text{P}$  NMR spectra were obtained from mechanically aligned samples containing 1–5% peptide, consistent with the formation of toroidal pores similar to the pores formed by magainin2. The toroidal pore geometry was characterized using  $^{31}\text{P}$  NMR experiments. Similar studies have recently been extended to other bilayers containing antimicrobial peptides [484]. At a higher concentration (>10 mol% peptide), the formation of a peptide-induced  $H_1$  phase (27%) was observed besides toroidal pore (73%) in POPC bilayer, from the experimental and simulated spectra as seen in Fig. 35a and b, corresponding to the parallel and perpendicular orientations, respectively.

Secondary structure and alignment of lysine-anchored hydrophobic model peptides in phosphatidylcholine have been examined as a function of hydrophobic mismatch [485]. When the helix is much longer than the width of the membrane, both the lipid and the peptide order are perturbed, while sequences that are much shorter show little effect on the phospholipid headgroup order, but the peptides exhibit a wide range of orientational distributions but which are predominantly close to being parallel to the membrane surface. The influence of an antimicrobial peptide, protegrin-1 (PG-1), on the curvature and lateral diffusion coefficient of phosphocholine bilayers has been investigated using 1D and 2D  $^{31}\text{P}$  exchange NMR [486]. PG-1 maintains the structural integrity of the dilaurylphosphatidylcholine (DLPC) bilayer and only reduces the lateral diffusion coefficient due to its binding. In contrast, PG-1 fragments the POPC vesicles, reducing the vesicle radius by about a factor of 3. Simulations of the 2D exchange spectra yielded quantitative reorientation-angle distributions that are consistent with the bimodal distributions of the vesicle curvature and the effects of the peptide on the two types of lipid bilayers. The membrane lysing mechanism of the carboxy-amide of pardaxin (Pla), of a 33-amino-acid residues, on bilayers of various composition was also studied by  $^{31}\text{P}$  NMR [487]. It was shown that Pla significantly disrupts bilayers composed of only zwitterionic lipids, particularly bilayers composed of POPC. Pla also reduces the lamellar to hexagonal phase-transition temperature  $T_H$  very low concentrations (1:50,000), which is interpreted as the formation of a cubic phase and not micellization of the membrane.

RTD-1 from rhesus macaque leukocytes is an 18-residue cyclic peptide taking a  $\beta$ -hairpin structure, and exhibiting broad-spectrum antimicrobial activity. It was shown to cause moderate orientational disorder when incorporated into PC bilayers, independent of the bilayer thickness, suggesting that this peptide binds to the surface of PC bilayers without perturbing the hydrophobic core [488].

Amyloid  $\beta$ -peptide ( $\text{A}\beta$ ) is a major component of plaques in Alzheimer's disease, and formation of senile plaques has been suggested to originate from regions of neuronal membrane rich in gangliosides. In this connection, it was demonstrated that  $\text{A}\beta$  (1–40) strongly perturbs the bilayer structure of mechanically oriented dimyristoylphosphatidylcholine (DMPC), leading to three lipid phases, namely a lamellar phase, a hexagonal phase and non-oriented lipids in the DMPC/ $\text{A}\beta$  and DMPC/GM1/ $\text{A}\beta$  systems [489]. The latter two phases are induced by the presence of the  $\text{A}\beta$  peptide, and facilitated by GM1.

## 5. Concluding remarks

In the present article, we have covered experimental and theoretical aspects of the complete set of chemical shifts for peptides and proteins. They include isotropic ( $\delta_{\text{iso}}$ ) and anisotropic ( $\delta_{11}$ ,  $\delta_{22}$  and  $\delta_{33}$ ) shifts and the asymmetric factor ( $\eta$ ), which are undoubtedly some of the most important NMR parameters for characteriza-

tion of a given molecular system, including structural and dynamical characterization. The isotropic shifts alone occur in solution NMR, leaving the others as hidden parameters. Currently, however, a knowledge of the CSA parameters is becoming increasingly important for solution NMR studies of larger proteins at higher magnetic field strength, where such parameters allow one for optimized experimental conditions. In the present article, we have covered a wide range of topics both in the solid-state and solution NMR, reported over a rather a long time-span from 1960 to present, and dealing with problems associated with measuring and interpreting the isotropic and chemical shifts. We feel that the interpretation of the CSA data is still undeveloped as compared to the data of isotropic chemical shifts, which has achieved greater success for application to various problems. NMR studies involving the measurement and utilization of CSA parameters are increasingly being used to tackle greater challenging biological problems related to protein–protein complexes and other biopolymers like DNA and RNA. We believe that the development such as use of higher magnetic field spectrometers and ultrafast spinning MAS probes will continue to broaden the scope of application of chemical shift parameters.

## Acknowledgements

The authors are grateful to their current and former colleagues and students for their excellent contributions and stimulating discussions during their research studies cited herein. A.R acknowledges the funding support from NIH.

## References

- [1] J.A. Pople, W.G. Schneider, H.J. Bernstein, High-resolution Nuclear Magnetic Resonance, McGraw-Hill, 1959.
- [2] C.P. Slichter, Principles of Magnetic Resonance, 1963, Harper & Row; 1989, Springer.
- [3] R.K. Harris, Nuclear Magnetic Resonance Spectroscopy, Longman Scientific and Technical, 1983.
- [4] E.D. Becker, High Resolution NMR, Theory and Chemical Applications, Academic Press, 1969, 1980, 2000.
- [5] R.R. Ernst, G. Bodenhausen, A. Wokaun, Principles of Nuclear Magnetic Resonance in One and Two Dimensions, Oxford, 1987.
- [6] M.H. Levitt, Spin Dynamics, Basics of Nuclear Magnetic Resonance, Wiley, 2002.
- [7] R.K. Harris, E.D. Becker, S.M.C. de Menezes, P. Granger, R.E. Hoffman, K.W. Zilm, Pure Appl. Chem. 80 (2008) 59–84.
- [8] U. Haeberlen, High Resolution NMR in Solids, Selective Averaging, Academic Press, 1976.
- [9] M. Mehring, High Resolution NMR in Solids, Springer, 1983.
- [10] J. Mason, Solid State NMR 2 (1993) 285–288.
- [11] A. Abragam, Principles of Nuclear Magnetism, Clarendon Press, 1962.
- [12] C.A. Fyfe, Solid State NMR for Chemists, CFC Press, 1983.
- [13] B.C. Gerstein, C.R. Dybowski, Transient Techniques in NMR of Solids, An Introduction to Theory and Practice, Academic Press, 1985.
- [14] G. Engelhardt, D. Michel, High-resolution Solid-state NMR of Silicates and Zeolites, John Wiley & Sons, 1987.
- [15] K. Schmidt-Rohr, H.W. Spiess, Multidimensional Solid-state NMR and Polymers, Academic Press, 1994.
- [16] K. Pervushin, R. Riek, G. Wider, K. Wüthrich, Proc. Natl. Acad. Sci. USA 94 (1997) 12366–12371.
- [17] M. Salzmann, K. Pervushin, G. Wider, H. Senn, K. Wüthrich, Proc. Natl. Acad. Sci. USA 95 (1998) 13585–13590.
- [18] R. Riek, G. Wider, K. Pervushin, K. Wüthrich, Proc. Natl. Acad. Sci. USA 96 (1999) 4918–4923.
- [19] K. Pervushin, Q. Rev. Biophys. 33 (2000) 161–197.
- [20] C. Fernandez, G. Wider, Curr. Opin. Struct. Biol. 13 (2003) 570–580.
- [21] D. Fushman, D. Cowburn, Meth. Enzymol. 339 (2001) 109–126.
- [22] H. Saitô, Magn. Reson. Chem. 24 (1986) 835–852.
- [23] H. Saitô, I. Ando, Ann. Rept. NMR Spectrosc. 21 (1989) 210–290.
- [24] H. Saitô, I. Ando, A. Naito, Solid State NMR Spectroscopy for Biopolymers, Principles and Applications, Springer, 2006.
- [25] S. Spera, A. Bax, J. Am. Chem. Soc. 113 (1991) 5490–5492.
- [26] D.S. Wishart, B.D. Sykes, F.M. Richards, J. Mol. Biol. 222 (1991) 311–333.
- [27] L. Szilágyi, Prog. NMR Spectrosc. 27 (1995) 325–443.
- [28] D.S. Wishart, B.D. Sykes, Meth. Enzymol. 239 (1994) 363–392.
- [29] B.J. Wylie, C.M. Rienstra, J. Chem. Phys. 128 (2008) 052077.



- [30] A. Shoji, S. Ando, S. Kuroki, I. Ando, G.A. Webb, *Annu. Rep. NMR Spectrosc.* 26 (1993) 55–98.
- [31] W.S. Veeman, *Prog. NMR Spectrosc.* 16 (1984) 193–235.
- [32] L. Shao, J.J. Titman, *Prog. NMR Spectrosc.* 51 (2007) 103–137.
- [33] G. Wu, *Prog. NMR Spectrosc.* 52 (2008) 118–169.
- [34] I. Ando, T. Asakura (Eds.), *Solid State NMR of Polymers*, Elsevier Science, Amsterdam, 1998.
- [35] O.N. Antzutkin, in: M.J. Duer (Ed.), *Solid-state NMR Spectroscopy: Principles and Applications*, Blackwell Sciences, Oxford, 2002, p. 280.
- [36] A. Ramamoorthy (Ed.), *NMR Spectroscopy of Biological Solids*, CRC Press, Cleveland, 2005.
- [37] B.C. Gerstein, C.R. Dybowski, *Transient Techniques in NMR of Solids, An Introduction to Theory and Practice*, Academic Press, Orlando, 1985.
- [38] O.N. Antzutkin, *Prog. NMR Spectrosc.* 35 (1999) 203–266.
- [39] T.M. Duncan, *A Compilation of Chemical Shift Anisotropies*, The Farragut Press, Chicago, 1990.
- [40] I. Ando, G.A. Webb, *Theory of NMR Parameters*, Academic Press, London, 1983.
- [41] I. Ando, H. Saitô, R. Tabeta, A. Shoji, T. Ozaki, *Macromolecules* 17 (1984) 457–461.
- [42] N. Asakawa, S. Kuroki, H. Kurosu, I. Ando, A. Shoji, T. Ozaki, *J. Am. Chem. Soc.* 114 (1992) 3261–3265.
- [43] A.C. de Dios, J.G. Pearson, E. Oldfield, *Science* 260 (1993) 1491–1495.
- [44] D. Jiao, M. Barfield, V.J. Hruby, *J. Am. Chem. Soc.* 115 (1993) 10883–10887.
- [45] A.C. de Dios, E. Oldfield, *J. Am. Chem. Soc.* 116 (1994) 11485–11488.
- [46] A.C. de Dios, *Prog. NMR Spectrosc.* 29 (1996) 229–278.
- [47] H. Fukui, *Prog. NMR Spectrosc.* 31 (1997) 317–342.
- [48] A. Shoji, T. Ozaki, T. Fujito, K. Deguchi, I. Ando, J. Magoshi, *J. Mol. Struct.* 441 (1998) 251–266.
- [49] N. Asakawa, T. Kameda, S. Kuroki, H. Kurosu, S. Ando, I. Ando, A. Shoji, *Annu. Rep. NMR Spectrosc.* 35 (1998) 55–135.
- [50] I. Ando, T. Asakura, *NMR chemical shift map*, in: G.A. Webb (Ed.), *Modern Magnetic Resonance*, vol. 1, Springer, Dordrecht, 2006, pp. 33–38.
- [51] D. Sitkoff, D.A. Case, *Prog. NMR Spectrosc.* 32 (1998) 165–190.
- [52] I. Ando, S. Kuroki, H. Kurosu, T. Yamanobe, *Prog. NMR Spectrosc.* 39 (2001) 79–133.
- [53] S. Kuroki, K. Yamauchi, I. Ando, A. Shoji, T. Ozaki, *Curr. Org. Chem.* 5 (2001) 1001–1016.
- [54] X.-P. Xu, D.A. Case, *Biopolymers* 65 (2002) 408–423.
- [55] A. Naito, S. Ganapathy, K. Akasaka, C.A. McDowell, *J. Chem. Phys.* 74 (1981) 3190–3197.
- [56] L.K. Nicholson, T. Asakura, M. Demura, T.A. Cross, *Biopolymers* 33 (1993) 847–861.
- [57] M. Demura, M. Minami, T. Asakura, T.A. Cross, *J. Am. Chem. Soc.* 120 (1998) 1300–1308.
- [58] D.K. Lee, R.J. Witterbort, A. Ramamoorthy, *J. Am. Chem. Soc.* 120 (1998) 8868–8874.
- [59] S.C. Shekar, A. Ramamoorthy, R.J. Wittebort, *J. Magn. Reson.* 155 (2002) 257–262.
- [60] N. Bloembergen, J.A. Rowland, *Acta Metall.* 1 (1953) 731–746.
- [61] C.H. Wu, A. Ramamoorthy, S.J. Opella, *J. Magn. Reson. A* 109 (1994) 270–272.
- [62] A. Ramamoorthy, L.M. Gierasch, S.J. Opella, *J. Magn. Reson. B* 110 (1996) 102–106.
- [63] D.K. Lee, A. Ramamoorthy, *J. Magn. Reson.* 133 (1998) 204–206.
- [64] Y.F. Wei, D.K. Lee, A. Ramamoorthy, *Chem. Phys. Lett.* 324 (2000) 20–24.
- [65] C.J. Hartzell, T.K. Pratum, G.P. Drobny, *J. Chem. Phys.* 87 (1987) 4324–4331.
- [66] M.M. Maricq, J.S. Waugh, *J. Chem. Phys.* 70 (1979) 3300–3316.
- [67] J.H. Van Vleck, *Phys. Rev.* 74 (1948) 1168–1183.
- [68] J. Herzfeld, A.E. Berger, *J. Chem. Phys.* 73 (1980) 6021–6030.
- [69] J. Fenzke, B. Maess, H. Pfeifer, *J. Magn. Reson.* 88 (1990) 172–176.
- [70] H.J.M. de Groot, S.O. Smith, A.C. Kolbert, J.M.L. Courtin, C. Winkel, J. Lugtenburg, J. Herzfeld, R.G. Griffin, *J. Magn. Reson.* 91 (1991) 30–38.
- [71] P. Hodgkinson, L. Emsley, *J. Chem. Phys.* 107 (1997) 4808–4816.
- [72] A. Bax, N.M. Szeveny, G.E. Maciel, *J. Magn. Reson.* 52 (1983) 147–152.
- [73] Z. Gan, *J. Am. Chem. Soc.* 114 (1992) 8307–8309.
- [74] T. Terao, T. Fujito, T. Onodera, A. Saika, *Chem. Phys. Lett.* 107 (1984) 145–148.
- [75] J.Z. Hu, W. Wang, F. Liu, M.S. Solum, D.W. Alderman, R.J. Pugmire, D.M. Grant, *J. Magn. Reson.* 113 (1995) 21–222.
- [76] W.T. Dixon, *J. Chem. Phys.* 77 (1982) 1800–1809.
- [77] A.C. Kolbert, R.G. Griffin, *Chem. Phys. Lett.* 166 (1990) 87–91.
- [78] O.N. Antzutkin, S.C. Shekar, M.H. Levitt, *J. Magn. Reson. A* 115 (1995) 7–19.
- [79] O.N. Antzutkin, Y.K. Lee, M.H. Levitt, *J. Magn. Reson.* 135 (1998) 144–155.
- [80] R. Tycko, G. Dabbagh, P.A. Mirau, *J. Magn. Reson.* 85 (1989) 265–274.
- [81] R. Witter, S. Hesse, U. Sternberg, *J. Magn. Reson.* 161 (2003) 35–42.
- [82] R. Witter, U. Sternberg, A.S. Ulrich, *J. Am. Chem. Soc.* 128 (2006) 2236–2243.
- [83] R.M. Orr, M.J. Duer, *J. Magn. Reson.* 181 (2006) 1–8.
- [84] S.F. Liu, J.D. Mao, K. Schmidt-Rohr, *J. Magn. Reson.* 155 (2002) 15–28.
- [85] M. Hong, X.L. Yao, *J. Magn. Reson.* 160 (2003) 114–119.
- [86] J.C.C. Chan, R. Tycko, *J. Chem. Phys.* 118 (2004) 8378–8389.
- [87] J.C. Facelli, A.C. de Dios (Eds.), *Modeling NMR Chemical Shifts, Gaining Insights into Structure and Environment*, ACS Symp. Ser. vol. 732, 1999.
- [88] P. Karadakov, *Ab initio calculation of NMR shielding constants*, in: G.A. Webb (Ed.), *Modern Magnetic Resonance*, vol. 1, Springer, Dordrecht, 2006, pp. 59–66.
- [89] R.K. Harris, E.D. Becker, S.M.C. de Menezes, R. Goodfellow, P. Granger, *Pure Appl. Chem.* 73 (2001) 1795–1818.
- [90] H. Saitô, A. Naito, *Biochim. Biophys. Acta* 1768 (2007) 3145–3161.
- [91] C.R. Morcombe, K.W. Zilm, *J. Magn. Reson.* 162 (2003) 479–486.
- [92] T. Taki, S. Yamashita, M. Satoh, A. Shibata, T. Yamashita, R. Tabeta, H. Saitô, *Chem. Lett.* (1981) 1803–1806.
- [93] D. Müller, H.R. Kricheldorf, *Polym. Bull.* 6 (1981) 101–108.
- [94] H.R. Kricheldorf, D. Müller, *Macromolecules* 16 (1983) 615–623.
- [95] H. Saitô, R. Tabeta, A. Shoji, T. Ozaki, I. Ando, *Macromolecules* 16 (1983) 1050–1057.
- [96] H.R. Kricheldorf, M. Mutter, D. Müller, D. Forster, *Biopolymers* 22 (1983) 1357–1382.
- [97] H. Saitô, Y. Iwanaga, R. Tabeta, M. Narita, T. Asakura, *Chem. Lett.* (1983) 427–430.
- [98] A. Shoji, T. Ozaki, H. Saitô, R. Tabeta, I. Ando, *Macromolecules* 17 (1984) 1472–1479.
- [99] D.-K. Lee, A. Ramamoorthy, *J. Phys. Chem. B* 103 (1999) 271–275.
- [100] K.A.H. Wildman, D.K. Lee, A. Ramamoorthy, *Biopolymers* 64 (2002) 246–254.
- [101] K.A.H. Wildman, E.E. Wilson, D.-K. Lee, A. Ramamoorthy, *Solid State NMR* 24 (2003) 94–109.
- [102] H. Saitô, R. Tabeta, T. Asakura, Y. Iwanaga, A. Shoji, T. Ozaki, I. Ando, *Macromolecules* 17 (1984) 1405–1412.
- [103] M. Ishida, T. Asakura, M. Yokoi, H. Saitô, *Macromolecules* 23 (1990) 88–94.
- [104] H. Saitô, R. Tabeta, A. Shoji, T. Ozaki, I. Ando, T. Miyata, *Biopolymers* 23 (1984) 2279–2297.
- [105] H. Saitô, M. Yokoi, *J. Biochem. (Tokyo)* 111 (1992) 376–382.
- [106] D. Huster, J. Schiller, K. Arnold, *Magn. Reson. Med.* 48 (2002) 624–632.
- [107] S. Kimura, A. Naito, S. Tuzi, H. Saitô, *Biopolymers* 63 (2002) 122–131.
- [108] H. Saitô, S. Tuzi, S. Yamaguchi, M. Tanio, A. Naito, *Biochim. Biophys. Acta* 1460 (2000) 39–48.
- [109] L. Pauling, R.B. Corey, *Proc. Natl. Acad. Sci. USA* 37 (1951) 729–740.
- [110] A. Hempel, N. Camerman, A. Camerman, *Biopolymers* 31 (1991) 187–192.
- [111] R. Tycko, *Meth. Enzymol.* 413 (2006) 103–122.
- [112] T. Asakura, M. Okonogi, Y. Nakazawa, K. Yamauchi, *J. Am. Chem. Soc.* 128 (2006) 6231–6238.
- [113] S. Ando, I. Ando, A. Shoji, T. Ozaki, *J. Am. Chem. Soc.* 110 (1988) 3380–3386.
- [114] T. Kameda, N. Takeda, S. Kuroki, H. Kurosu, S. Ando, I. Ando, A. Shoji, T. Ozaki, *J. Mol. Struct.* 384 (1996) 17–23.
- [115] K. Tsuchiya, A. Takahashi, N. Takeda, N. Asakawa, S. Kuroki, I. Ando, A. Shoji, T. Ozaki, *J. Mol. Struct.* 350 (1995) 233–240.
- [116] T. Yamanobe, I. Ando, H. Saitô, R. Tabeta, A. Shoji, T. Ozaki, *Bull. Chem. Soc. Jpn.* 58 (1985) 23–29.
- [117] T. Yamanobe, I. Ando, H. Saitô, R. Tabeta, A. Shoji, T. Ozaki, *Chem. Phys.* 99 (1985) 259–264.
- [118] N. Asakawa, H. Kurosu, I. Ando, *J. Mol. Struct.* 323 (1994) 279–285.
- [119] N. Asakawa, H. Kurosu, I. Ando, S. Shoji, T. Ozaki, *J. Mol. Struct.* 317 (1994) 119–129.
- [120] D.S. Wishart, B.D. Sykes, F.M. Richards, *J. Mol. Biol.* 222 (1991) 211–333.
- [121] D.S. Wishart, F.M. Richards, B.D. Sykes, *Biochemistry* 31 (1992) 1647–1651.
- [122] D.S. Wishart, B.D. Sykes, *J. Biomol. NMR* 4 (1994) 171–180.
- [123] R. Powers, D.S. Garrett, C.J. March, E.A. Frieden, A.M. Gronenborn, G.M. Clore, *Biochemistry* 31 (1992) 4334–4346.
- [124] M. Iwadate, T. Asakura, M.P. Williamson, *J. Biomol. NMR* 13 (1999) 199–211.
- [125] A. Shoji, T. Ozaki, T. Fujito, K. Deguchi, I. Ando, *Macromolecules* 20 (1987) 2441–2445.
- [126] A. Shoji, T. Ozaki, T. Fujito, K. Deguchi, S. Ando, I. Ando, *Macromolecules* 22 (1989) 2860–2863.
- [127] A. Shoji, T. Ozaki, T. Fujito, K. Deguchi, S. Ando, I. Ando, *J. Am. Chem. Soc.* 112 (1990) 4693–4697.
- [128] M. Ashikawa, A. Shoji, T. Ozaki, I. Ando, *Macromolecules* 32 (1999) 2288–2292.
- [129] J. Glushka, M. Lee, S. Coffin, D. Cowburn, *J. Am. Chem. Soc.* 111 (1989) 7716–7722.
- [130] H. Le, E. Oldfield, *J. Biomol. NMR* 4 (1994) 341–348.
- [131] H. Le, E. Oldfield, *J. Phys. Chem.* 100 (1996) 16423–16428.
- [132] H. Saitô, K. Nukada, H. Kato, T. Yonezawa, K. Fukui, *Tetrahedron Lett.* (1965) 111–117.
- [133] H. Saitô, K. Nukada, *J. Am. Chem. Soc.* 93 (1971) 1072–1076.
- [134] H. Saitô, Y. Tanaka, K. Nukada, *J. Am. Chem. Soc.* 93 (1971) 1077–1081.
- [135] M. Witkowski, G.A. Webb, *Nitrogen NMR*, Plenum, London and New York, 1973.
- [136] G.C. Levy, R.L. Lichter, *Nitrogen-15 Nuclear Magnetic Resonance Spectroscopy*, John Wiley & Sons, New York, 1979.
- [137] S. Kuroki, S. Ando, I. Ando, A. Shoji, T. Ozaki, G.A. Webb, *J. Mol. Struct.* 240 (1990) 19–29.
- [138] S. Kuroki, N. Asakawa, S. Ando, I. Ando, A. Shoji, T. Ozaki, *J. Mol. Struct.* 245 (1991) 69–81.
- [139] A. Naito, S. Tuzi, H. Saitô, *Eur. J. Biochem.* 224 (1994) 729–734.
- [140] A. Fukutani, A. Naito, S. Tuzi, H. Saitô, *J. Mol. Struct.* 602–603 (2002) 491–503.
- [141] G.S. Harbison, J. Herzfeld, R.G. Griffin, *Biochemistry* 22 (1983) 1–5.
- [142] H.J.M. de Groot, S.O. Smith, J. Courtin, E. van den Berg, C. Winkel, J. Lugtenburg, R.G. Griffin, *J. Herzfeld, Biochemistry* 29 (1990) 6873–6883.
- [143] J.G. Hu, B.Q. Sun, A.T. Petkova, R.G. Griffin, *J. Herzfeld, Biochemistry* 36 (1997) 9316–9322.
- [144] J.G. Hu, R.G. Griffin, J. Herzfeld, *J. Am. Chem. Soc.* 119 (1997) 9495–9498.
- [145] M.L. Mark-Jurkauskas, V.S. Bajaj, M.K. Hornstein, M. Belenky, R.G. Griffin, J. Herzfeld, *Proc. Natl. Acad. Sci. USA* 105 (2008) 883–888.

- [146] M. Eilers, P.J. Reeves, W. Ying, H.G. Khorana, S.O. Smith, *Proc. Natl. Acad. Sci. USA* 96 (1999) 487–492.
- [147] N.J. Clayden, R.J.P. Williams, *J. Magn. Reson.* 49 (1982) 383–396.
- [148] D.C. Dalgarno, B.A. Levine, R.J.P. Williams, *Biosci. Rept.* 3 (1983) 443–452.
- [149] A. Pardi, G. Wagner, K. Wüthrich, *Eur. J. Biochem.* 137 (1983) 445–454.
- [150] T. Asakura, I. Ando, A. Nishioka, *Makromol. Chem.* 178 (1977) 1111–1132.
- [151] T. Asakura, E. Nakamura, H. Asakawa, M. Demura, *J. Magn. Reson.* 93 (1991) 355–360.
- [152] K. Ōsabay, D.A. Case, *J. Am. Chem. Soc.* 113 (1991) 9436–9444.
- [153] M.P. Williamson, T. Asakura, E. Nakamura, M. Demura, *J. Biomol. NMR* 2 (1992) 83–98.
- [154] K. Ōsabay, D.A. Case, *J. Biomol. NMR* 4 (1994) 213–230.
- [155] D.S. Wishart, C.G. Bigam, A. Holm, R.S. Hodges, B.D. Sykes, *J. Biomol. NMR* 5 (1995) 67–81.
- [156] C.W. Haigh, R.B. Mallion, *Prog. NMR Spectrosc.* 13 (1980) 303–344.
- [157] H.M. McConnell, *J. Chem. Phys.* 27 (1957) 226–229.
- [158] H.L. Tigelaar, W.H. Flygare, *J. Am. Chem. Soc.* 94 (1972) 343–346.
- [159] M.P. Williamson, T. Asakura, *J. Magn. Reson. B* 101 (1993) 63–71.
- [160] A. Shoji, H. Kimura, T. Ozaki, H. Sugisawa, K. Deguchi, *J. Am. Chem. Soc.* 118 (1996) 7604–7607.
- [161] A. Shoji, H. Kimura, H. Sugisawa, *Annu. Rep. NMR Spectrosc.* 45 (2002) 69–150.
- [162] H. Kimura, T. Ozaki, H. Sugisawa, K. Deguchi, A. Shoji, *Macromolecules* 31 (1998) 7398–7408.
- [163] K. Yamauchi, S. Kuroki, K. Fujii, I. Ando, *Chem. Phys. Lett.* 324 (2000) 435–439.
- [164] K. Yamauchi, S. Kuroki, I. Ando, *J. Mol. Struct.* 602–603 (2002) 9–16.
- [165] Y. Suzuki, M. Okonogi, K. Yamauchi, H. Kurosu, M. Tansho, T. Shimizu, H. Saitô, T. Asakura, *J. Phys. Chem. B* 111 (2007) 9172–9178.
- [166] A. Naito, S.G. Ganapathy, C.A. McDowell, *J. Magn. Reson.* 48 (1982) 367–381.
- [167] S. Hori, K. Yamauchi, S. Kuroki, I. Ando, *Int. J. Mol. Sci.* 3 (2002) 907–913.
- [168] J. Kuszewski, A.M. Gronenborn, G.M. Clore, *J. Magn. Reson. B* 102 (1995) 293–297.
- [169] J.G. Pearson, J.-F. Wang, J.L. Markley, H. Le, E. Oldfield, *J. Am. Chem. Soc.* 117 (1995) 8823–8829.
- [170] R.D. Beger, P.H. Bolton, *J. Biomol. NMR* 10 (1997) 129–142.
- [171] D.W. Wishart, D.A. Case, *Meth. Enzymol.* 338 (2001) 3–34.
- [172] D.S. Wishart, M.S. Watson, R.F. Boyko, B.D. Sykes, *J. Biomol. NMR* 10 (1997) 319–336.
- [173] G. Cornilescu, F. Delaglio, A. Bax, *J. Biomol. NMR* 13 (1999) 289–302.
- [174] S. Neal, A.M. Nip, H. Zhang, D.S. Wishart, *J. Biomol. NMR* 26 (2003) 215–240.
- [175] Y. Shen, A. Bax, *J. Biomol. NMR* 38 (2007) 289–302.
- [176] A. Cavalli, X. Salvatella, C.M. Dobson, M. Vendruscolo, *Proc. Natl. Acad. Sci. USA* 104 (2007) 9615–9620.
- [177] Y. Shen, O. Lange, F. Delaglio, P. Rossi, J.M. Aramini, G. Liu, A. Eletsky, Y. Wu, K.K. Singarapu, A. Lemak, A. Ignatchenko, C.H. Arrowsmith, T. Szyperski, G.T. Montelione, D. Baker, A. Bax, *Proc. Natl. Acad. Sci. USA* 105 (2008) 4685–4690.
- [178] D.S. Wishart, D. Arndt, B. Berjanski, P. Tang, J. Zhou, G. Lin, *Nucleic Acid Res.* 36 (2008) W496–W502.
- [179] R.E. Stark, L.W. Jelinski, D.L. Ruben, D.A. Torchia, R.G. Griffin, *J. Magn. Reson.* 55 (1983) 266–273.
- [180] N. Takeda, S. Kuroki, H. Kurosu, I. Ando, *Biopolymers* 50 (1999) 61–69.
- [181] T.G. Oas, C.J. Hartzell, T.J. McMahon, G.P. Drobny, F.W. Dahlquist, *J. Am. Chem. Soc.* 109 (1987) 5956–5962.
- [182] C.J. Hartzell, M. Whitfield, T.G. Oas, G.P. Drobny, *J. Am. Chem. Soc.* 109 (1987) 5966–5969.
- [183] S. Ando, T. Yamanobe, I. Ando, A. Shoji, T. Ozaki, R. Tabeta, H. Saitô, *J. Am. Chem. Soc.* 107 (1985) 7648–7652.
- [184] S. Ando, I. Ando, A. Shoji, T. Ozaki, *J. Mol. Struct.* 192 (1989) 153–161.
- [185] Y.F. Wei, D.-K. Lee, A. Ramamoorthy, *J. Am. Chem. Soc.* 123 (2001) 6118–6126.
- [186] N. Asakawa, M. Takenori, D. Sato, M. Sakurai, Y. Inoue, *Magn. Reson. Chem.* 37 (1999) 303–311.
- [187] R.H. Havlin, D.D. Laws, H.-M.L. Bitter, L.K. Sanders, H. Sun, J.S. Grimley, D.E. Wemmer, A. Pines, E. Oldfield, *J. Am. Chem. Soc.* 123 (2001) 10362–10369.
- [188] G.S. Harbison, L.W. Jelinski, R.E. Stark, D.A. Torchia, J. Herzfeld, R.G. Griffin, *J. Magn. Reson.* 60 (1984) 79–82.
- [189] K.W. Waddell, E.Y. Chekmenev, R.J. Wittebort, *J. Am. Chem. Soc.* 127 (2005) 9030–9035.
- [190] T.G. Oas, C.J. Hartzell, F.W. Dahlquist, G.P. Drobny, *J. Am. Chem. Soc.* 109 (1987) 5962–5966.
- [191] Y. Hiyama, C.H. Niu, J.V. Silverton, A. Bavo, D.A. Torchia, *J. Am. Chem. Soc.* 110 (1988) 2378–2383.
- [192] J.E. Roberts, G.S. Harbison, M.G. Munowitz, J. Herzfeld, R.G. Griffin, *J. Am. Chem. Soc.* 109 (1987) 4163–4169.
- [193] S. Kuroki, N. Asakawa, S. Ando, I. Ando, A. Shoji, T. Ozaki, *J. Mol. Struct.* 245 (1991) 69–80.
- [194] C.H. Wu, A. Ramamoorthy, L.M. Gierasch, S.J. Opella, *J. Am. Chem. Soc.* 117 (1995) 6148–6149.
- [195] D.K. Lee, J.S. Santos, A. Ramamoorthy, *Chem. Phys. Lett.* 309 (1999) 209–214.
- [196] M.D. Lumsden, R.E. Wasylshen, K. Eichele, M. Schindler, G.H. Penner, W.P. Power, R.D. Curtis, *J. Am. Chem. Soc.* 116 (1994) 1403–1413.
- [197] A. Naito, A. Fukutani, M. Uidehaag, S. Tuzi, H. Saitô, *J. Mol. Struct.* 441 (1998) 231–241.
- [198] Q. Teng, T.A. Cross, *J. Magn. Reson.* 85 (1989) 439–447.
- [199] W. Mai, W. Hu, C. Wang, T.A. Cross, *Protein Sci.* 2 (1993) 532–542.
- [200] F. Tian, T.A. Cross, *J. Magn. Reson.* 135 (1998) 535–540.
- [201] B. Heise, J. Leppert, R. Ramachandran, *Solid State NMR* 16 (2000) 177–187.
- [202] D.K. Lee, Y.F. Wei, A. Ramamoorthy, *J. Phys. Chem. B* 105 (2001) 4752–4762.
- [203] Y.F. Wei, D.K. Lee, A.E. McDermott, A. Ramamoorthy, *J. Magn. Reson.* 158 (2002) 23–35.
- [204] A. Poon, J. Birn, A. Ramamoorthy, *J. Phys. Chem. B* 108 (2004) 16577–16584.
- [205] A.E. Walling, R.E. Pargas, A.C. de Dios, *J. Phys. Chem. A* 101 (1997) 7299–7303.
- [206] S. Kuroki, I. Ando, A. Shoji, T. Ozaki, *J. Chem. Soc. Chem. Commun.* (1992) 433–434.
- [207] S. Kuroki, A. Takahashi, I. Ando, A. Shoji, T. Ozaki, *J. Mol. Struct.* 323 (1994) 197–208.
- [208] S. Kuroki, S. Ando, I. Ando, *Chem. Phys.* 195 (1995) 107–116.
- [209] A. Takahashi, S. Kuroki, I. Ando, T. Ozaki, A. Shoji, *J. Mol. Struct.* 442 (1998) 195–199.
- [210] K. Yamauchi, S. Kuroki, I. Ando, *J. Mol. Struct.* 602–603 (2002) 171–175.
- [211] G. Wu, S. Dong, *J. Am. Chem. Soc.* 123 (2001) 9119–9125.
- [212] V. Lemaître, M.R.R. de Planque, A.P. Howes, M.E. Smith, R. Dupree, A. Watts, *J. Am. Chem. Soc.* 126 (2004) 15320–15321.
- [213] V. Lemaître, M.E. Smith, A. Watts, *Solid State NMR* 26 (2004) 215–235.
- [214] K.J. Pike, V. Lemaître, A. Kukol, T. Anupold, A. Samoson, A.P. Howes, A. Watts, M.E. Smith, R. Dupree, *J. Phys. Chem. B* 108 (2004) 9256–9263.
- [215] R. Fu, W.W. Brey, K. Shetty, P. Gor'kov, S. Saha, J.R. Long, S.C. Grant, E.Y. Chekmenev, J. Ha, Z. Gan, M. Sharma, F. Zhang, T.M. Logan, R. Brüschweiler, A. Edison, A. Blue, I.R. Dixon, W.D. Markiewicz, T.A. Cross, *J. Magn. Reson.* 177 (2005) 1–8.
- [216] E.Y. Chekmenev, K.W. Waddell, J. Hu, Z. Gan, R.J. Wittebort, T.A. Cross, *J. Am. Chem. Soc.* 128 (2006) 9849–9855.
- [217] V. Lemaître, K.J. Pike, A. Watts, T. Anupold, A. Samoson, M.E. Smith, R. Dupree, *Chem. Phys. Lett.* 371 (2003) 91–97.
- [218] K.W. Waddell, E.Y. Chekmenev, R.J. Wittebort, *J. Phys. Chem. B* 110 (2006) 22935–22941.
- [219] Z. Gan, P. Gor'kov, T.A. Cross, A. Samoson, D. Massiot, *J. Am. Chem. Soc.* 124 (2002) 5634–5635.
- [220] J. Hu, E.Y. Chekmenev, Z. Gan, P.L. Gor'kov, S. Saha, W.W. Brey, T.A. Cross, *J. Am. Chem. Soc.* 127 (2005) 11922–11923.
- [221] J.-P. Amoureux, C. Fernandez, S. Steuernagel, *J. Magn. Reson. A* 123 (1996) 116–118.
- [222] A.P. Howes, T. Anupold, V. Lemaître, A. Kukol, A. Watts, A. Samoson, M.E. Smith, R. Dupree, *Chem. Phys. Lett.* 421 (2006) 42–46.
- [223] S. Prasad, T.M. Clark, R. Sharma, H.-T. Kwak, P.J. Grandinetti, H. Zimmermann, *Solid State NMR* 29 (2006) 119–124.
- [224] K. Yamada, T. Nemoto, M. Asanuma, H. Honda, T. Yamazaki, H. Hirota, *Solid State NMR* 30 (2006) 182–191.
- [225] K. Yamada, T. Shimizu, T. Yamazaki, S. Ohki, *Solid State NMR* 33 (2008) 88–94.
- [226] K. Yamauchi, M. Okonogi, H. Kurosu, M. Tansho, T. Shimizu, T. Gullion, T. Asakura, *J. Magn. Reson.* 190 (2008) 327–333.
- [227] R. Gerald II, T. Bernhard, U. Haeblerlen, J. Rendell, S. Opella, *J. Am. Chem. Soc.* 115 (1993) 777–782.
- [228] K. Yamauchi, S. Kuroki, I. Ando, *Polymer* 43 (2002) 3331–3333.
- [229] A. Lesage, D. Sakellariou, S. Hediger, B. Elena, P. Charmont, S. Steuernagel, L. Emsley, *J. Magn. Reson.* 163 (2003) 105–113.
- [230] H. Saitô, R. Tabeta, I. Ando, T. Ozaki, A. Shoji, *Chem. Lett.* (1983) 1437–1440.
- [231] T. Akieda, H. Mimura, S. Kuroki, H. Kurosu, I. Ando, *Macromolecules* 25 (1992) 5794–5797.
- [232] K. Murata, E. Katoh, S. Kuroki, I. Ando, *J. Mol. Struct.* 689 (2004) 223–235.
- [233] S. Tuzi, T. Komoto, I. Ando, H. Saitô, A. Shoji, T. Ozaki, *Biopolymers* 26 (1987) 1983–1992.
- [234] J. Birn, A. Poon, Y. Mao, A. Ramamoorthy, *J. Am. Chem. Soc.* 126 (2004) 8529–8534.
- [235] Z. Gu, R. Zambrano, A. McDermott, *J. Am. Chem. Soc.* 116 (1994) 6368–6372.
- [236] H. Kimura, A. Shoji, H. Sugisawa, K. Deguchi, A. Naito, H. Saitô, *Macromolecules* 33 (2000) 6627–6629.
- [237] M. Hong, *J. Am. Chem. Soc.* 122 (2000) 3762–3770.
- [238] N. Tjandra, A. Bax, *J. Am. Chem. Soc.* 119 (1997) 9576–9577.
- [239] X. Yao, M. Hong, *J. Am. Chem. Soc.* 124 (2002) 2730–2738.
- [240] Y. Ishii, T. Terao, M. Kainosho, *Chem. Phys. Lett.* 256 (1996) 133–140.
- [241] X. Yao, S. Yamaguchi, M. Hong, *J. Biomol. NMR* 24 (2002) 51–62.
- [242] B.J. Wylie, W.T. Franks, D.T. Graesser, C.M. Rienstra, *J. Am. Chem. Soc.* 127 (2005) 11946–11947.
- [243] B.J. Wylie, W.T. Franks, C.M. Rienstra, *J. Phys. Chem. B* 110 (2006) 10926–10936.
- [244] B.J. Wylie, L.J. Sperling, H.L. Frericks, G. J. Shah, W.T. Franks, C.M. Rienstra, *J. Am. Chem. Soc.* 129 (2007) 5318–5319.
- [245] D. Fushman, D. Cowburn, *J. Am. Chem. Soc.* 120 (1998) 7109–7110.
- [246] D. Fushman, N. Tjandra, D. Cowburn, *J. Am. Chem. Soc.* 120 (1998) 10947–10952.
- [247] J.B. Hall, D. Fushman, *J. Am. Chem. Soc.* 128 (2006) 7855–7870.
- [248] G. Lipari, A. Szabo, *J. Am. Chem. Soc.* 104 (1982) 4546–4559.
- [249] C.D. Kroenke, M. Rance, A.G. Palmer III, *J. Am. Chem. Soc.* 121 (1999) 10119–10125.
- [250] N. Tjandra, A. Szabo, A. Bax, *J. Am. Chem. Soc.* 118 (1996) 6986–6991.
- [251] S.F. Lienin, T. Bremi, B. Brutscher, R. Brüschweiler, R.R. Ernst, *J. Am. Chem. Soc.* 120 (1998) 9870–9879.
- [252] N. Tjandra, P. Wingfield, S. Stahl, A. Bax, *J. Biomol. NMR* 8 (1996) 273–284.

- [253] G. Cornilescu, A. Bax, *J. Am. Chem. Soc.* 122 (2000) 10143–10154.
- [254] D.L. Bryce, A. Grishaev, A. Bax, *J. Am. Chem. Soc.* 127 (2005) 7387–7396.
- [255] J. Kurita, H. Shimahara, N. Utsunomiya-Tate, S. Tate, *J. Magn. Reson.* 163 (2003) 163–173.
- [256] J.A. Reimer, R.W. Vaughan, *J. Magn. Reson.* 41 (1980) 483–491.
- [257] N. Tjandra, A. Bax, *J. Am. Chem. Soc.* 119 (1997) 8076–8082.
- [258] M. Tessari, H. Vis, R. Boelens, R. Kaptein, G.W. Vuister, *J. Am. Chem. Soc.* 119 (1997) 8985–8990.
- [259] M. Goldman, *J. Magn. Reson.* 60 (1984) 437–452.
- [260] H. Shimizu, *J. Chem. Phys.* 40 (1964) 3357–3364.
- [261] K. Wüthrich, *Nat. Struct. Biol.* 5 (1998) 492–495.
- [262] K. Pervushin, G. Wider, R. Riek, K. Wüthrich, *Proc. Natl. Acad. Sci. USA* 96 (1999) 9607–9612.
- [263] C. Fernández, K. Adeishvili, K. Wüthrich, *Proc. Natl. Acad. Sci. USA* 98 (2001) 2358–2363.
- [264] M. Salzmann, K. Pervushin, G. Wider, H. Senn, K. Wüthrich, *J. Am. Chem. Soc.* 122 (2000) 7543–7548.
- [265] J. Fiaux, E.B. Bertelsen, A.L. Horwich, K. Wüthrich, *Nature* 418 (2002) 207–211.
- [266] T. Asakura, A. Kuzuhara, R. Tabeta, H. Saitô, *Macromolecules* 18 (1985) 1841–1845.
- [267] H. Saitô, M. Ishida, M. Yokoi, T. Asakura, *Macromolecules* 23 (1990) 83–88.
- [268] D. Huster, J. Schiller, K. Arnold, *Magn. Reson. Med.* 48 (2002) 624–632.
- [269] M. Sackervitz, H.A. Scheidt, G. Lodderstedt, A. Schierhorn, E. Schwarz, D. Huster, *J. Am. Chem. Soc.* 130 (2008) 7172–7173.
- [270] D. Huster, *Annu. Rep. NMR Spectrosc.* 64 (2008) 127–159.
- [271] A. Naito, T. Nagao, K. Norisada, T. Mizuno, S. Tuzi, H. Saitô, *Biophys. J.* 78 (2000) 2405–2417.
- [272] M. Kamihira, A. Naito, S. Tuzi, A.Y. Nosaka, H. Saitô, *Protein Sci.* 9 (2000) 5867–5877.
- [273] S. Kimura, A. Naito, S. Tuzi, H. Saitô, *Biopolymers* 58 (2001) 78–88.
- [274] S. Kimura, A. Naito, H. Saitô, K. Ogawa, A. Shoji, *J. Mol. Struct.* 562 (2001) 197–203.
- [275] M. Kamihira, Y. Oshiro, S. Tuzi, A.Y. Nosaka, H. Saitô, A. Naito, *J. Biol. Chem.* 278 (2003) 2859–2865.
- [276] S. Tuzi, S. Yamaguchi, M. Tanio, H. Konishi, S. Inoue, A. Naito, R. Needleman, J.K. Lanyi, H. Saitô, *Biophys. J.* 76 (1999) 1523–1531.
- [277] S. Tuzi, A. Naito, H. Saitô, *Biochemistry* 33 (1994) 15046–15052.
- [278] H. Saitô, J. Mikami, S. Yamaguchi, M. Tanio, A. Kira, T. Arakawa, K. Yamamoto, S. Tuzi, *Magn. Reson. Chem.* 204 (2004) 218–230.
- [279] H. Saitô, S. Tuzi, M. Tanio, A. Naito, *Annu. Rep. NMR Spectrosc.* 47 (2002) 39–108.
- [280] S. Tuzi, A. Naito, H. Saitô, *J. Mol. Struct.* 654 (2003) 205–214.
- [281] H. Saitô, *Annu. Rep. NMR Spectrosc.* 57 (2006) 99–175.
- [282] I. Kawamura, Y. Ikeda, Y. Sudo, M. Iwamoto, K. Shimono, S. Yamaguchi, S. Tuzi, H. Saitô, N. Kamo, A. Naito, *Photochem. Photobiol.* 83 (2007) 339–345.
- [283] I. Kawamura, H. Yoshida, Y. Ikeda, S. Yamaguchi, S. Tuzi, H. Saitô, N. Kamo, A. Naito, *Photochem. Photobiol.* 84 (2008) 921–930.
- [284] H.L. Frericks, D.H. Zhou, L.L. Yap, R.B. Gennis, C.M. Rienstra, *J. Biomol. NMR* 36 (2006) 55–71.
- [285] M. Etzkorn, S. Martell, O.C. Andronesi, K. Seidel, M. Engelhard, M. Baldus, *Angew. Chem. Int. Ed.* 46 (2006) 459–462.
- [286] J. Xu, U.H. Dürr, S.C. Im, Z. Gan, L. Waskell, A. Ramamoorthy, *Angew. Chem. Int. Ed. Engl.* 47 (2008) 7864–7867.
- [287] P. Zhu, J. Xu, N. Sahar, M.D. Morris, D.H. Kohn, A. Ramamoorthy, *J. Am. Chem. Soc.* 131 (2009) 17064–17065.
- [288] K.D. Kloepper, D.H. Zhou, Y. Li, K.A. Winter, J.M. George, C.M. Rienstra, *J. Biomol. NMR* 39 (2007) 197–211.
- [289] R. Tycko, *Prog. NMR Spectrosc.* 42 (2003) 53–68.
- [290] M. Baldus, *Prog. NMR Spectrosc.* 41 (2002) 1–47.
- [291] L.K. Nicholson, F. Moll, T.E. Mizon, P.V. LoGrasso, J.C. Lay, T.A. Cross, *Biochemistry* 26 (1987) 6621–6626.
- [292] G.B. Fields, C.G. Fields, J. Petefish, H.E. van Wart, T.A. Cross, *Proc. Natl. Acad. Sci. USA* 85 (1988) 1384–1388.
- [293] C. Wang, Q. Teng, T.A. Cross, *Biophys. J.* 61 (1992) 1550–1556.
- [294] W. Hu, K.C. Lee, T.A. Cross, *Biochemistry* 32 (1993) 7035–7047.
- [295] R.R. Ketchum, W. Hu, T.A. Cross, *Science* 261 (1993) 1457–1460.
- [296] A. Ramamoorthy, C.H. Wu, S.J. Opella, *J. Magn. Reson.* 140 (1999) 131–140.
- [297] A. Ramamoorthy, Y. Wei, D.-K. Lee, *Annu. Rep. NMR Spectrosc.* 52 (2004) 1–52.
- [298] F.M. Marassi, S.J. Opella, *J. Magn. Reson.* 144 (2000) 155–159.
- [299] J. Wang, J. Denny, C. Tian, S. Kim, Y. Mo, F. Kovacs, Z. Song, K. Nishimura, Z. Gan, R. Fu, J.R. Quine, T.A. Cross, *J. Magn. Reson.* 144 (2000) 162–167.
- [300] F. Marassi, S.J. Opella, *J. Magn. Reson.* 144 (2000) 150–155.
- [301] A.A. Nevzorov, S.J. Opella, *J. Magn. Reson.* 160 (2003) 33–39.
- [302] F.M. Marassi, *Biophys. J.* 80 (2001) 994–1003.
- [303] F.M. Marassi, S.J. Opella, *Protein Sci.* 12 (2003) 403–411.
- [304] A.C. Zeri, M.F. Mesle, A.A. Nevzorov, S.J. Opella, *Proc. Natl. Acad. Sci. USA* 100 (2003) 6458–6463.
- [305] K. Yamamoto, S.V. Dvinskikh, A. Ramamoorthy, *Chem. Phys. Lett.* 419 (2006) 533–536.
- [306] K. Yamamoto, R. Soong, A. Ramamoorthy, *Langmuir* 25 (2009) 7010–7018.
- [307] U.H. Dürr, K. Yamamoto, S.C. Im, L. Waskell, A. Ramamoorthy, *J. Am. Chem. Soc.* 129 (2007) 6670–6671.
- [308] A. Ramamoorthy, *Solid State Nucl. Magn. Reson.* 35 (2009) 201–207.
- [309] A. Ramamoorthy, S. Thennarasu, D.K. Lee, A. Tan, L. Maloy, *Biophys. J.* 91 (2006) 206–216.
- [310] Z. Song, F.A. Kovacs, J. Wang, J.K. Denny, S.C. Shekar, J.R. Quine, T.A. Cross, *Biophys. J.* 79 (2000) 767–775.
- [311] E.K. Tiburu, E.S. Karp, P.C. Dave, K. Damodran, G.A. Lorigan, *Biochemistry* 43 (2004) 13899–13909.
- [312] N.J. Traaseth, J.J. Buffy, J. Zamoan, G. Veglia, *Biochemistry* 45 (2006) 13827–13834.
- [313] S. Abu-Baker, J.-X. Lu, S. Chu, K.N. Shetty, P.L. Gor'kov, G.A. Lorigan, *Protein Sci.* 16 (2007) 2345–2349.
- [314] D.W. Bleile, W.R. Scott, S.K. Straus, *J. Biomol. NMR* 32 (2005) 101–111.
- [315] S.D. Müller, A.A. De Angelis, T.H. Walther, S.L. Grage, C. Lange, S.J. Opella, A.S. Ulrich, *Biochim. Biophys. Acta* 1786 (2007) 3071–3079.
- [316] T. Vosegaard, M. Kamihira-Ishijima, A. Watts, N.C. Nielsen, *Biophys. J.* 94 (2008) 242–250.
- [317] E.S. Salnikov, H. Friedrich, X. Li, P. Bertani, S. Reissmann, C. Hertweck, J.D.J. O'Neil, J. Raap, B. Bechinger, *Biophys. J.* 96 (2009) 86–100.
- [318] S.H. Park, S. Prytulla, A.A. De Angelis, J.M. Brown, H. Kiefer, S.J. Opella, *J. Am. Chem. Soc.* 128 (2006) 7402–7403.
- [319] C. Li, P. Gao, H. Qin, R. Chase, P.L. Gor'kov, W.W. Brey, T.A. Cross, *J. Am. Chem. Soc.* 129 (2007) 5304–5305.
- [320] R.E. Marsh, R.B. Corey, L. Pauling, *Biochim. Biophys. Acta* 16 (1955) 1–34.
- [321] Y. Takahashi, M. Gehoh, K. Yuzuriha, *J. Polym. Sci. Polym. Phys.* 29 (1991) 889–891.
- [322] C. Zhao, H. Zhang, T. Yamanobe, S. Kuroki, I. Ando, *Macromolecules* 32 (1999) 3389–3394.
- [323] G. Lipari, A. Szabo, *J. Am. Chem. Soc.* 104 (1982) 4559–4570.
- [324] N. Tjandra, S.E. Feller, R.W. Pastor, A. Bax, *J. Am. Chem. Soc.* 117 (1995) 12562–12566.
- [325] J. Engelke, H. Rüterjans, *J. Biomol. NMR* 9 (1997) 63–78.
- [326] K.T. Dayie, G. Wagner, *J. Am. Chem. Soc.* 119 (1997) 7797–7806.
- [327] S.F. Lienin, T. Bremi, B. Brutscher, R. Brüschweiler, R.R. Ernst, *J. Am. Chem. Soc.* 120 (1998) 9870–9879.
- [328] A.G. Palmer III, *Curr. Opin. Struct. Biol.* 7 (1997) 732–737.
- [329] A.G. Palmer III, C.D. Kroenke, J.P. Loria, *Meth. Enzymol.* 339 (2001) 204–238.
- [330] M. Akke, *Curr. Opin. Struct. Biol.* 12 (2002) 642–647.
- [331] Z. Luz, S. Meiboom, *J. Chem. Phys.* 39 (1963) 366–370.
- [332] J.W. Peng, G. Wagner, *Biochemistry* 34 (1995) 16752–16773.
- [333] A.M. Mandel, M. Akke, A.G. Palmer III, *J. Mol. Biol.* 246 (1995) 14–163.
- [334] A.M. Mandel, M. Akke, A.G. Palmer III, *Biochemistry* 35 (1996) 16009–16023.
- [335] L.K. Nicholson, T. Yamazaki, D.A. Torchia, S. Grzesiek, A. Bax, S.J. Stahl, J.D. Kaufman, P.T. Wingfield, P.Y.S. Lam, P.K. Jadhav, C.N. Hodge, P.J. Dommelle, C.-H. Chang, *Nat. Struct. Biol.* 2 (1995) 274–280.
- [336] N.A. Farrow, O. Zhang, J.D. Forman-Kay, L.E. Kay, *Biochemistry* 36 (1997) 2390–2402.
- [337] H. Zhou, M.M. McEvoy, D.F. Lowry, R.V. Swanson, M.I. Simon, F.W. Dahlquist, *Biochemistry* 35 (1996) 433–443.
- [338] C. Spitzfagen, R.P. Grant, H.J. Mardon, I.D. Campbell, *J. Mol. Biol.* 265 (1997) 565–579.
- [339] M.A. Markus, A.P. Hinck, S. Huang, D.E. Draper, D.A. Torchia, *Nat. Struct. Biol.* 4 (1997) 70–77.
- [340] B.F. Volkman, D. Lipson, D.E. Wemmer, D. Kern, *Science* 291 (2001) 2429–2433.
- [341] E.Z. Eisenmesser, D.A. Bosco, M. Akke, D. Kern, *Science* 295 (2002) 1520–1523.
- [342] M.A.S. Haas, M.H. Thuesen, H.E.M. Christensen, J.J. Led, *J. Am. Chem. Soc.* 126 (2004) 753–765.
- [343] J.G. Kempf, J. Jung, C. Ragain, N.S. Sampson, J.P. Loria, *J. Mol. Biol.* 368 (2007) 131–149.
- [344] M. Mukherjee, K. Dutta, M.A. White, D. Cowburn, R.O. Fox, *Protein Sci.* 15 (2006) 1342–1355.
- [345] L.E. Kay, *J. Magn. Reson.* 173 (2005) 193–207.
- [346] P.M. Hwang, R.E. Bishop, Lewis E. Kay, *Proc. Natl. Acad. Sci. USA* 101 (2004) 9618–9623.
- [347] A.A. Di Nardo, D.M. Korzhnev, P.J. Stogios, A. Zarrine-Afsar, L.E. Kay, A.R. Davidson, *Proc. Natl. Acad. Sci. USA* 101 (2004) 7954–7959.
- [348] D. M Korzhnev, X. Salvatella, M. Vendruscolo, A.A. Di Nardo, A.R. Davidson, C.M. Dobson, L.E. Kay, *Nature* 430 (2004) 586–590.
- [349] J. Dittmer, G. Bodenhausen, *J. Am. Chem. Soc.* 126 (2004) 1314–1315.
- [350] W.P. Rothwell, J.S. Waugh, *J. Chem. Phys.* 75 (1981) 2721–2732.
- [351] A. Naito, T. Nagao, K. Norisada, T. Mizuno, S. Tuzi, H. Saitô, *Biophys. J.* 78 (2000) 2405–2417.
- [352] D.K. Lee, J.S. Santos, A. Ramamoorthy, *J. Phys. Chem. B* 103 (1999) 8383–8390.
- [353] S.K. Kandasamy, D.K. Lee, R.P. Nanga, J. Xu, J.S. Santos, R.G. Larson, A. Ramamoorthy, *Biochim. Biophys. Acta* 1788 (2009) 686–695.
- [354] S. Esteban-Martín, E. Strandberg, G. Fuertes, A.S. Ulrich, J. Salgado, *Biophys. J.* 96 (2009) 3233–3241.
- [355] A. Ramamoorthy, D.K. Lee, T. Narasimhaswamy, R.P. Nanga, *Biochim. Biophys. Acta* 1798 (2010) 223–227.
- [356] T. Doherty, A.J. Waring, M. Hong, *Biochemistry* 47 (2008) 1105–1116.
- [357] D.A. Torchia, D.L. VanderHart, *J. Mol. Biol.* 104 (1976) 315–321.
- [358] L.W. Jelinski, D.A. Torchia, *J. Mol. Biol.* 133 (1979) 45–63.
- [359] S.K. Sarkar, C.E. Sullivan, D.A. Torchia, *J. Biol. Chem.* 258 (1983) 9762–9767.
- [360] S.K. Sarkar, C.E. Sullivan, D.A. Torchia, *Biochemistry* 24 (1985) 2348–2354.
- [361] E.R. deAzevedo, W.G. Hu, T.J. Bonagamba, K. Schmidt-Rohr, *J. Am. Chem. Soc.* 121 (1999) 8411–8412.



- [362] E.R. deAzevedo, W. -G. Hu, T.J. Bonagamba, K. Schmidt-Rohr, J. Chem. Phys. 112 (2000) 8988–9001.
- [363] E.R. deAzevedo, S.B. Kennedy, M. Hong, Chem. Phys. Lett. 321 (2000) 43–48.
- [364] D. Reichert, O. Pascui, E.R. deAzevedo, T.J. Bonagamba, K. Arnold, D. Huster, Magn. Reson. Chem. 42 (2004) 276–284.
- [365] M. Hong, J.D. Gross, R.G. Griffin, J. Phys. Chem. 101 (1997) 5869–5874.
- [366] C.M. Gall, T.A. Cross, J.A. DiVerdi, S.J. Opella, Proc. Natl. Acad. Sci. USA 79 (1982) 101–105.
- [367] T.A. Cross, S.J. Opella, J. Mol. Biol. 159 (1982) 543–549.
- [368] L.A. Colnago, K.G. Valentine, S.J. Opella, Biochemistry 26 (1987) 847–854.
- [369] D.S. Thiriot, A.A. Nevzorov, L. Zagayanskiy, C.H. Wu, S.J. Opella, J. Mol. Biol. 341 (2004) 869–879.
- [370] D.S. Thiriot, A.A. Nevzorov, S.J. Opella, Protein Sci. 14 (2005) 1064–1070.
- [371] J.L. Lorieau, L.A. Day, A.E. McDermott, Proc. Natl. Acad. Sci. 105 (2008) 10366–10371.
- [372] N. Grigorieff, T.A. Ceska, K.H. Downing, J.M. Baldwin, R. Henderson, J. Mol. Biol. 259 (1996) 393–421.
- [373] E. Pebay-Peyroula, G. Rummel, J.P. Rosenbusch, E.M. Landau, Science 277 (1997) 1676–1681.
- [374] H. Luecke, H.T. Richter, J.K. Lanyi, Science 280 (1998) 1934–1937.
- [375] H. Saitô, S. Tuzi, A. Naito, Annu. Rep. NMR Spectrosc. 36 (1998) 79–121.
- [376] H. Saitô, Chem. Phys. Lipids 132 (2004) 101–112.
- [377] H. Saitô, in: G.A. Webb (Ed.), Modern Magnetic Resonance, Springer, 2006, pp. 287–293.
- [378] H. Saitô, A. Naito, Biochim. Biophys. Acta 1768 (2007) 3090–3097.
- [379] H. Saitô, Y. Kawase, A. Kira, K. Yamamoto, M. Tanio, S. Yamaguchi, S. Tuzi, A. Naito, Photochem. Photobiol. 83 (2007) 253–262.
- [380] S. Shastri, J. Vonck, N. Pfefer, W. Haase, W. Kuehlbrandt, C. Glaubit, Biochim. Biophys. Acta 1768 (2007) 3012–3019.
- [381] H. Saitô, K. Yamamoto, S. Tuzi, S. Yamaguchi, Biochim. Biophys. Acta 1616 (2003) 127–136.
- [382] S. Tuzi, S. Yamaguchi, M. Tanio, H. Konishi, S. Inoue, A. Naito, R. Needleman, J.K. Lanyi, H. Saitô, Biophys. J. 76 (1999) 1523–1531.
- [383] S. Yamaguchi, S. Tuzi, M. Tanio, A. Naito, J.K. Lanyi, R. Needleman, H. Saitô, J. Biochem. (Tokyo) 127 (2000) 861–869.
- [384] S. Yamaguchi, S. Tuzi, K. Yonebayashi, A. Naito, R. Needleman, J.K. Lanyi, H. Saitô, J. Biochem. (Tokyo) 129 (2001) 373–382.
- [385] S. Yamaguchi, K. Yonebayashi, H. Konishi, S. Tuzi, A. Naito, J.K. Lanyi, R. Needleman, H. Saitô, Eur. J. Biochem. 268 (2001) 2218–2228.
- [386] T. Arakawa, K. Shimono, S. Yamaguchi, S. Tuzi, Y. Sudo, N. Kamo, H. Saitô, FEBS Lett. 536 (2003) 237–240.
- [387] S. Yamaguchi, K. Shimono, Y. Sudo, S. Tuzi, A. Naito, N. Kamo, H. Saitô, Biophys. J. 86 (2004) 3131–3140.
- [388] S. Yamaguchi, S. Tuzi, J.U. Bowie, H. Saitô, Biochim. Biophys. Acta 1698 (2004) 97–105.
- [389] D. Suwelack, W.P. Rothwell, J.S. Waugh, J. Chem. Phys. 73 (1980) 2559–2569.
- [390] I. Kawamura, Y. Degawa, S. Yamaguchi, K. Nishimura, S. Tuzi, H. Saitô, A. Naito, Photochem. Photobiol. 83 (2007) 346–350.
- [391] I. Kawamura, N. Kihara, M. Ohmine, K. Nishimura, S. Tuzi, H. Saitô, A. Naito, J. Am. Chem. Soc. 129 (2007) 1016–1017.
- [392] Y. Kawase, M. Tanio, A. Kira, S. Yamaguchi, S. Tuzi, A. Naito, M. Kataoka, J.K. Lanyi, R. Needleman, H. Saitô, Biochemistry 39 (2000) 14472–14480.
- [393] A. Kira, M. Tanio, S. Tuzi, H. Saitô, Eur. Biophys. J. 33 (2004) 580–588.
- [394] H. Saitô, A. Kira, T. Arakawa, M. Tanio, S. Tuzi, A. Naito, Biochim. Biophys. Acta 1798 (2010) 167–176.
- [395] Y. Miwa, H. Ishida, H. Saitô, M. Tanaka, A. Mochizuki, Polymer 50 (2009) 6091–6099.
- [396] C. Sternberg, C. L'Hostis, C.A. Whiteway, A. Watts, Biochim. Biophys. Acta 1108 (1992) 21–30.
- [397] P. Barré, S. Yamaguchi, S. Tuzi, H. Saitô, Eur. Biophys. J. 32 (2003) 578–584.
- [398] S. Tuzi, A. Naito, H. Saitô, J. Mol. Struct. 654 (2003) 205–214.
- [399] H. Saitô, S. Yamaguchi, K. Ogawa, S. Tuzi, M. Márquez, C. Sanz, E. Padrós, Biophys. J. 86 (2004) 1673–1681.
- [400] I. Kawamura, M. Ohmine, J. Tanabe, S. Tuzi, H. Saitô, A. Naito, Biochim. Biophys. Acta 1768 (2007) 3090–3097.
- [401] H. Saitô, T. Tsuchida, K. Ogawa, T. Arakawa, S. Yamaguchi, S. Tuzi, Biochim. Biophys. Acta 1565 (2002) 97–106.
- [402] K. Yamamoto, S. Tuzi, H. Saitô, I. Kawamura, A. Naito, Biochim. Biophys. Acta 1758 (2006) 181–189.
- [403] M. Kamihira, A. Watts, Biochemistry 45 (2006) 4304–4313.
- [404] I. Kawamura, Y. Ikeda, Y. Sudo, M. Iwamoto, K. Shimono, S. Yamaguchi, S. Tuzi, H. Saitô, N. Kamo, A. Naito, Photochem. Photobiol. 83 (2007) 339–345.
- [405] I. Kawamura, H. Yoshida, Y. Ikeda, S. Yamaguchi, S. Tuzi, H. Saitô, N. Kamo, A. Naito, Photochem. Photobiol. 84 (2008) 921–930.
- [406] L. Shi, M.A.M. Ahmed, W. Zhang, G. Whited, L.S. Brown, V. Ladizhansky, J. Mol. Biol. 386 (2009) 1078–1093.
- [407] L. Shi, E.M.R. Lake, M.A.M. Ahmed, L.S. Brown, V. Ladizhansky, Biochim. Biophys. Acta 1788 (2009) 2563–2574.
- [408] N. Pfefer, A.C. Wörner, J. Yang, S. Shastri, U.A. Hellmich, L. Aslimovska, M.S.M. Marier, C. Glaubit, Biochim. Biophys. Acta 1787 (2009) 697–705.
- [409] W.T. Franks, D.H. Zhou, B.J. Wylie, B.G. Money, D.T. Graesser, H.L. Frericks, G. Sahota, C.M. Rienstra, J. Am. Chem. Soc. 127 (2005) 12291–12305.
- [410] J.L. Lorieau, A.E. McDermott, J. Am. Chem. Soc. 128 (2006) 11505–11512.
- [411] D. Huster, Prog. NMR Spectrosc. 46 (2005) 79–107.
- [412] A. Krushelnitsky, D. Reichert, Prog. NMR Spectrosc. 47 (2005) 1–25.
- [413] V. Chevelkov, K. Faelber, A. Schrey, K. Rehbein, A. Diehl, B. Reif, J. Am. Chem. Soc. 129 (2007) 10195–10200.
- [414] R.G. Griffin, J. Am. Chem. Soc. 98 (1976) 851–853.
- [415] J. Seelig, Biochim. Biophys. Acta 515 (1978) 105–140.
- [416] P.R. Cullis, B. de Kruijff, R.E. Richards, Biochim. Biophys. Acta 426 (1976) 433–446.
- [417] J. Seelig, A. Seelig, Quart. Rev. Biophys. 13 (1980) 19–61.
- [418] P.R. Cullis, B. de Kruijff, Biochim. Biophys. Acta 559 (1979) 399–420.
- [419] I.C.P. Smith, I.H. Ekiel, in: D.G. Gorenstein (Ed.), Phosphorous-31 NMR. Principles and Applications, Academic Press, 1984, pp. 447–475.
- [420] P.R. Cullis, B. de Kruijff, Biochim. Biophys. Acta 436 (1976) 523–540.
- [421] R.F. Campbell, E. Meirovitch, J.H. Freed, J. Phys. Chem. 83 (1979) 525–533.
- [422] E.E. Burnell, P.R. Cullis, B. de Kruijff, Biochim. Biophys. Acta 603 (1980) 63–69.
- [423] H. Heerklotz, Biophys. J. 83 (2002) 2693–2701.
- [424] G.P. Holland, S.K. McIntyre, T.M. Alam, Biophys. J. 90 (2006) 4248–4260.
- [425] S.J. Opella, P.L. Stewart, Methods Enzymol. 176 (1989) 242–275.
- [426] T. Cross, Methods Enzymol. 289 (1997) 672–697.
- [427] S.J. Opella, C. Ma, F.M. Marassi, Methods Enzymol. 339 (2001) 285–313.
- [428] S.J. Opella, F.M. Marassi, Chem. Rev. 104 (2004) 3587–3606.
- [429] J. Seelig, H. Gally, Biochemistry 15 (1976) 5199–5204.
- [430] N.A. Clark, K.J. Rothchild, D. Luippold, B.A. Simon, Biophys. J. 31 (1980) 65–96.
- [431] C.R. Sanders, G.C. Landis, Biochemistry 34 (1995) 4030–4040.
- [432] C.R. Sanders, B.J. Hare, K.P. Howard, J.H. Prestegard, Prog. Nucl. Magn. Reson. Spectrosc. 26 (1994) 421–432.
- [433] C.R. Sanders, in: G.A. Webb (Ed.), Modern Magnetic Resonance, Springer, 2006, pp. 229–235.
- [434] A. Naito, T. Nagao, K. Norisada, T. Mizuno, S. Tuzi, H. Saitô, Biophys. J. 78 (2000) 2405–2417.
- [435] S. Kimura, A. Naito, S. Tuzi, H. Saitô, Biopolymers 63 (2002) 122–131.
- [436] J.R. Brender, E.L. Lee, M.A. Cavitt, A. Gafni, D.G. Steel, A. Ramamoorthy, J. Am. Chem. Soc. 130 (2008) 6424–6429.
- [437] F. Moll III, T.A. Cross, Biophys. J. 57 (1990) 351–362.
- [438] K.J. Hallock, K.H. Wildman, D. -K. Lee, A. Ramamoorthy, Biophys. J. 82 (2002) 2499–2503.
- [439] J.K. Rainey, B.D. Sykes, Biophys. J. 89 (2005) 2792–2805.
- [440] C.R. Sanders, J.P. Schwonek, Biochemistry 31 (1992) 8898–8905.
- [441] C.R. Sanders, J.H. Prestegard, Biophys. J. 58 (1990) 447–460.
- [442] R.R. Vold, R.S. Prosser, J. Magn. Reson. Ser. B 113 (1996) 267–271.
- [443] V. Luzzatti, T. Gulik-Krzywicki, A. Tardieu, Nature 218 (1968) 1031–1034.
- [444] V. Luzzatti, A. Tardieu, Ann. Rev. Phys. Chem. 25 (1974) 79–94.
- [445] P.R. Cullis, M.J. Hope, Nature 271 (1978) 672–674.
- [446] N. Janes, Chem. Phys. Lipids 81 (1996) 133–150.
- [447] P.R. Cullis, B. de Kruijff, Biochim. Biophys. Acta 513 (1978) 31–42.
- [448] P.R. Cullis, B. de Kruijff, Biochim. Biophys. Acta 507 (1978) 207–218.
- [449] P.R. Cullis, P.W.M. van Dijk, B. de Kruijff, J. de Gier, Biochim. Biophys. Acta 513 (1978) 20–21.
- [450] J.N. Israelachvili, D.J. Mitchell, Biochim. Biophys. Acta 389 (1975) 13–19.
- [451] B. de Kruijff, P.R. Cullis, G.K. Radda, Biochim. Biophys. Acta 436 (1976) 729–740.
- [452] J.N. Israelachvili, D.J. Mitchell, B.W. Ninham, J. Chem. Soc. Faraday Trans. II 72 (1976) 1525–1568.
- [453] J.N. Israelachvili, S. Marčelja, R.G. Horn, Quart. Rev. Biophys. 13 (1980) 121–200.
- [454] S.-W. Hui, A. Sen, Proc. Natl. Acad. Sci. USA 86 (1989) 5825–5829.
- [455] V.V. Kumar, Proc. Natl. Acad. Sci. USA 88 (1991) 444–448.
- [456] Y.-C. Lee, T.F. Taraschi, N. Janes, Biophys. J. 65 (1993) 1429–1432.
- [457] Y.-C. Lee, Y.O. Zheng, T.F. Taraschi, N. Janes, Biochemistry 35 (1996) 2677–2684.
- [458] N. Janes, Chem. Phys. Lipids 81 (1996) 133–150.
- [459] R.M. Epand, R.F. Epand, Biophys. J. 66 (1994) 1450–1456.
- [460] M. Lafleur, M. Bloom, E.F. Eikenberry, S.M. Gruner, Y. Han, P.R. Cullis, Biophys. J. 70 (1996) 2747–2757.
- [461] A.P. Hornby, P.R. Cullis, Biochim. Biophys. Acta 647 (1981) 285–292.
- [462] T.D. Madden, P.R. Cullis, Biochim. Biophys. Acta 684 (1982) 149–153.
- [463] R.M. Epand, Biochemistry 24 (1985) 7092–7095.
- [464] M. Sjölund, G. Lindblom, L. Rilfors, G. Arvidson, Biophys. J. 52 (1987) 145–153.
- [465] S. Orädd, G. Lindblom, K. Fontell, H. Ljusberg-Wahren, Biophys. J. 68 (1995) 1856–1863.
- [466] E.M. Landau, J.P. Rosenbush, Proc. Natl. Acad. Sci. USA 93 (1996) 14532–14535.
- [467] B. de Kruijff, Nature 386 (1997) 129–130.
- [468] R.M. Epand, Biochim. Biophys. Acta 1614 (2003) 116–121.
- [469] R.M. Epand, Biochim. Biophys. Acta 1376 (1998) 353–368.
- [470] R.M. Epand, R.F. Epand, Biochem. Biophys. Res. Commun. 02 (1994) 1420–1425.
- [471] R.M. Epand, R.F. Epand, I. Martin, J.-M. Ruysschaert, Biochemistry 40 (2001) 8800–8807.
- [472] D.P. Siegel, Biophys. J. 76 (1999) 291–313.
- [473] L. Chernomordik, Chem. Phys. Lipids 81 (1996) 203–213.
- [474] B. de Kruijff, Nature 329 (1987) 587–588.
- [475] B. de Kruijff, Curr. Opin. Chem. Biol. 1 (1997) 564–569.
- [476] W.J. de Grip, E.H. Drenth, C.J. van Echteld, B. de Kruijff, A.J. Verkleij, Biochim. Biophys. Acta 558 (1979) 330–337.
- [477] A. Rietveld, T.J.J.M. van Kemenade, T. Hak, A.J. Verkleij, B. de Kruijff, Eur. J. Biochem. 164 (1987) 137–140.

- [478] J.A. Killian, B. de Kruijff, *Biochemistry* 24 (1985) 7890–7898.
- [479] J.A. Killian, I. Salemink, M.R.R. de Planque, G. Lindblom, R.E. Koeppe II, D.V. Greathouse, *Biochemistry* 35 (1996) 1037–1045.
- [480] J.R. Giorgione, Z. Huang, R.M. Epand, *Biochemistry* 37 (1998) 2384–2392.
- [481] M.F. Brown, *Chem. Phys. Lipids* 73 (1994) 159–180.
- [482] K. Matsuzaki, O. Murase, T. Tokuda, S. Funakoshi, N. Fujii, K. Miyajima, *Biochemistry* 33 (1994) 3342–3349.
- [483] K.J. Hallock, D.-K. Lee, A. Ramamoorthy, *Biophys. J.* 84 (2003) 3052–3060.
- [484] S. Wi, C. Kim, *J. Phys. Chem. B* 112 (2008) 11402–11414.
- [485] U. Harzer, B. Bechinger, *Biochemistry* 39 (2000) 13106–13114.
- [486] P.A.B. Marasinghe, J.J. Buffy, K. Schmidt-Rohr, M. Hong, *J. Phys. Chem.* 109 (2005) 22036–22044.
- [487] K.J. Hallock, D.-K. Lee, J. Omnaas, H.I. Mosberg, A. Ramamoorthy, *Biophys. J.* 83 (2002) 1004–1013.
- [488] J.J. Buffy, M.J. McCormick, S. Wi, A. Waring, R.I. Lehrer, M. Hong, *Biochemistry* 43 (2004) 9800–9812.
- [489] Y. Nakazawa, Y. Suzuki, M.P. Williamson, H. Saitô, T. Asakura, *Chem. Phys. Lipids* 158 (2009) 54–60.